CRANFIELD UNIVERSITY

N. W. BRESSLOFF

CFD PREDICTION OF COUPLED RADIATION HEAT TRANSFER AND SOOT PRODUCTION IN TURBULENT FLAMES

School of Mechanical Engineering

Ph. D. Thesis

CRANFIELD UNIVERSITY

School of Mechanical Engineering

Ph. D. Thesis

1996-1997

N. W. BRESSLOFF

CFD PREDICTION OF COUPLED RADIATION HEAT TRANSFER AND SOOT PRODUCTION IN TURBULENT FLAMES

Supervisor : Professor J. B. Moss

June 1996

This thesis is submitted for the degree of
Doctor of Philosophy

Abstract

The mechanisms governing the formation and destruction of soot in turbulent combustion are intimately coupled to thermal radiation due to the strong dependence of sooting processes and radiative loss on temperature. Detailed computational fluid dynamics (CFD) predictions of the radiative and soot output from turbulent non-premixed flames are normally performed by parabolic algorithms. However, the modelling of combustion systems, such as furnaces and unwanted enclosure fires, often require a fully elliptic description of the flow field and its related physical phenomena. Thus, this thesis investigates the intimate coupling between radiative energy exchange and the mechanisms governing soot formation and destruction within a three-dimensional, general curvilinear CFD code.

Thermal radiation is modelled by the discrete transfer radiation model (DTRM). Special emphasis is given to approximate solutions to the radiative transfer equation encompassing various models for the radiative properties of gases and soot. A new algorithm is presented, entitled the differential total absorptivity (DTA) solution, which, unlike alternative solutions, incorporates the source temperature dependence of absorption. Additionally, a weighted sum of gray gases (WSGG) solution is described which includes the treatment of gray boundaries. Whilst the DTA solution is particularly recommended for systems comprising large temperature differences, the WSGG solution is deemed most appropriate for numerical simulation of lower temperature diffusion flames, due to its significant time advantage.

The coupling between radiative loss and soot concentration is investigated via a multiple laminar flamelet concept applied within the CFD simulation of confined turbulent diffusion flames burning methane in air at 1 and 3 atm. Flamelet families are employed relating individual sooting mechanisms to the level of radiative loss, which is evaluated by the DTRM formulated for emitting-absorbing mixtures of soot, CO_2 and H_2O. Combustion heat release is described by an eddy break-up concept linked to the $k-\varepsilon$ turbulence model, whilst temperature is evaluated from the solved enthalpy field. Detailed comparisons between prediction and experiment for the critical properties of mixture fraction, temperature and soot volume fraction demonstrate the effectiveness of this novel, coupled strategy within an elliptic flow field calculation.

Acknowledgements

The author would like to extend his thanks to Professor J. B. Moss, Dr. P. A. Rubini and, of course, SOFIE.

The Engineering and Physical Sciences Research Council is also acknowledged for their financial support through research grant GR/H80088.

Finally, a hand-shake in thought to my family, especially my wife, Jo.

Contents

List of Tables

List of Figures

Nomenclature

$a_{m,n,n'}, a_j$	Gray gas polynomial weighting coefficient
A, B	Constants in Magnussen's eddy break-up model
c_p	Specific heat at constant pressure, J/kg/K
C_1, C_2	Planck's first and second constants
C_μ	Constant in $k-\varepsilon$ turbulence model
D	Diffusion coefficient
E	Mean percentage absolute error
F	Black body fraction
g	Gravitational acceleration, m/s^2
h	Specific sensible enthalpy, J/kg
h_f^0	Specific enthalpy of formation, J/kg
H	Specific total enthalpy, J/kg
i	Radiative intensity, kW/m^2/sr
i_ν	Spectral radiative intensity, kW-cm/m^2/sr
k	Absorption coefficient, m^{-1}, or turbulent kinetic energy, m^2/s^2
l, L	Path length, m
m	Ray number
M	Total number of rays
n	Total number of cells in a path
p	Partial pressure, atm.
P	Probability density function or Total Pressure, atm.
q	Radiative flux, kW/m^2
q^-	Incident radiative flux, kW/m^2
Q_R	Radiative heat loss fraction
R_0	Universal gas constant, J/kg-mole/K
s	Stoichiometric ratio
s , s', s''	Distance, m

S	Volumetric source term
Sc	Schmidt number
t	Time, s
T	Temperature, K
$T_w^{'}$	Effective wall temperature, K
u	Velocity, ms^{-1}
w	Weighting of radiative intensity
$\dot{w}$	Chemical source term, $kg/m^3/s$
W	Relative molecular mass, kg
x	Distance, m
X	Mole fraction
Y	Mass fraction

Greek symbols

α	Absorptivity
α, β	Exponents of beta function
ΔA	Area of a surface element, m^2
δ	Direction cosine
δ_{ij}	Dirac's delta function
ε	Emissivity or turbulent dissipation rate, m^2/s^3
ϕ	Azimuthal angle or conserved quantitiy
Φ	Soot volume fraction
$\overline{\phi}$	Reynolds mean
ϕ'	Reynolds fluctuation
$\widetilde{\phi}$	Favre mean
ϕ''	Favre fluctuation
λ	Wavelength, m
μ	Dynamic viscosity, Ns/m^2
Ω	Solid angle, sr
ν	Wave number, m^{-1}

θ	Polar angle
ρ	Density, kg/m^3
ξ	Mixture fraction
σ	Stefan-Boltzman constant, kW/m^2/K^4 or Prandtl-Schmidt number
τ	Transmissivity

Subscripts

a	Adiabatic
b	Black body quantities
c	Carbon dioxide
fu	Fuel
g	Gas
h	Water
i	Species or ambient
j	Spectral band or gray gas component
L	Laminar quantity
m	Mixture
n,*r* ,*r'*	Computational grid cell
o	Oxidant
p	Soot or species products
s	Source temperature
T	Turbulent quantity
ν	Wave number
0	Origin of path

Superscripts

c	Correlated solution
T	Total property

Chapter 1

Introduction

Thermal radiation plays a crucial role in the coupling between combustion, heat transfer and fluid dynamics in a wide range of combustion environments. Temperature changes due to radiation ultimately affect the yield of combustion products, and the concentrations of species and particulates influence the further emission, absorption and scattering of radiation. Simultaneously, the fluid flow varies due to changes in thermodynamic properties, especially density. Radiative effects are also influenced by turbulence-radiation interaction. Due to the non-linear relationship between temperature and emission, relatively small fluctuations in temperature can yield significant variations in radiative exchange. Furthermore, turbulence governs all the processes referred to above.

Clearly, accurate computational modelling of turbulent reacting flows represents a formidable task. The researcher is constrained by his apprehension of the physical processes involved, by his ability to model them accurately, and by the computing capabilities at his disposal. Generally, a balance has to be struck between the demand for greater resolution of physical modelling, and the need to generate solutions on an acceptable time-scale. Additionally, the modelling process is guided by the objectives of the combustion scenario under consideration.

In furnaces and combustors, it is desirable to optimise the radiant output from flames to increase the efficiency of operation. Simultaneously, control of the very different and complex temperature dependencies of pollutant formation - particularly NO_x and soot - require a clear understanding of the radiative energy transfer accompanying

these processes. In open fires, radiation to neighbouring structures is the principal means by which they spread. Enclosure fires present an additional set of particularly challenging problems all strongly influenced by radiation. Irradiation of combustible surfaces may eventually cause them to ignite producing rapid fire spread. However, prior to this, vaporisation of the material augments a particularly volatile mixture which thickens downwards from the ceiling. If the right conditions are satisfied, ignition of other surfaces may be superseded by flash-over of this explosive layer. Indeed, fire-fighters are only recently recognising the need to douse the layer of combustible gases, as well as directing water at the fire source.

Most fatalities occur in enclosure fires due to asphyxiation. One of the main components of smoke is soot, and this is produced in abundance due to favourable conditions of long residence times in fuel rich, high temperature combustion zones. Radiative loss, particularly from the luminous part of flames, may then quench the process of soot oxidation. Consequently, unburned matter is buoyantly carried up through the plume, and then spreads outwards as it reaches an upper surface. It is the coupling between radiation and soot formation (and destruction) which forms the focus of this thesis.

Until recently, radiation in combustion has been modelled in a fairly limited fashion. Either, it has been effectively decoupled from other combustion processes, or the modelling of radiative properties has been considerably simplified. In the present context, emphasis is given to predicting radiative exchange in a three-dimensional elliptic CFD calculation from turbulent flames, and how radiative loss may be coupled to the formation of combustion products, especially soot.

In non-premixed combustion, the fast chemistry assumption implies that chemical reaction occurs instantaneously when fuel and oxidant meet. Thus, combustion is governed by the rate of turbulent mixing. Whilst theoretical models have been developed, such as the various

conserved scalar approaches, which are able to predict turbulence-chemistry interaction in this way, the processes of soot formation and destruction demand more sophisticated modelling strategies. Conserved scalar approaches are capable of successfully modelling heat release and gaseous species formation, but they cannot be extended to the relatively slow processes of soot formation and oxidation. Nonetheless, one of the most popular conserved scalar approaches, the laminar flamelet model, can be manipulated to yield soot predictions via a set of flamelets generated to account for different proportions of radiative loss. Essentially, sets of flamelets are required to represent each of the key mechanisms of nucleation, surface growth, coagulation and oxidation, which are then combined in an empirically based soot model adapted for application in the multiple flamelet approach. A transport equation is solved for enthalpy, and local values are compared against expected values generated by integrating the set of enthalpy flamelets for a probability density function with respect to mixture fraction. The coupling of radiation and soot formation is then realised by the effect that the calculated radiative loss has on the location of the local enthalpy relative to the values obtained from the integrated flamelets. Adjustment to predictions of soot volume fraction then feed back into the evaluation of radiative loss via the modelling of radiative properties.

Thermal radiation is modelled by the discrete transfer radiation model (DTRM) due to Lockwood and Shah (1980). Being a ray-tracing procedure, the DTRM lends itself to a wide range of solutions to the RTE. These algorithms, based on a variety of different radiative property models, have been established as approximations to the high resolution correlations which exist between radiative intensity and absorption. With current levels of computing power, it is not feasible to apply high resolution property modelling within a typical CFD calculation. Therefore, approximate techniques are required to yield adequate accuracy without excessive computational cost.

Radiative property modelling is further complicated by the very different characteristics of gaseous and particulate radiation. Whereas molecular gases radiate in particular regions of the spectrum, soot radiates in a continuous spectrum primarily in the visible and near infra-red. Additionally, for gas-soot mixtures, it is inaccurate to sum contributions from the separate components. The general approach is to adopt a solution for the molecular gases, and then modify it to account for the presence of soot. This strategy has been applied in developing a new algorithm, designed to model the source temperature dependence of absorption without the need for spectral integration. The differential total absorptivity solution, as it is called, requires a method to evaluate total radiative properties. For gases, this is accomplished by curve-fits to experimentally or spectrally derived data, and for soot, a number of relatively straightforward analytical expressions are available. Since, gaseous radiation is dominated by CO_2 and H_2O, radiative property modelling is confined to mixtures of CO_2, H_2O and soot.

One of the attractions of the DTRM is the relative ease with which it can be linked to three-dimensional curvilinear CFD codes. The DTRM has been incorporated into the finite-volume code, SOFIE (Simulation Of Fires In Enclosures), currently being developed at Cranfield University, and used here for the analysis of confined jet diffusion flames. The time-averaged Navier-Stokes equations are solved on a co-located grid for velocities and pressure. The SIMPLEC pressure correction method is employed with momentum interpolation. Turbulence is modelled by the standard $k-\varepsilon$ model.

The structure of this thesis is as follows.

Chapter 2 commences with a review of coupled soot, radiation modelling in combustion. Then, a general discussion is presented of turbulent reacting flows. Special attention is given to appropriate methods for modelling non-premixed combustion in three-dimensional, finite-volume; general curvilinear CFD codes. In particular, issues of

turbulence and chemical reaction closure are addressed. Methods for predicting the distribution of combustion products, especially soot, are discussed and the chapter concludes with a summary of the CFD code, SOFIE.

In chapter 3, numerical modelling of radiation by the discrete transfer radiation model (DTRM) due to Lockwood and Shah (1980) is described in detail. A number of methods for optimising the DTRM are considered. Emphasis is given to discretisation of the solid angle hemisphere which defines the directions in which rays are launched from solid surfaces. Alternative methods of discretisation are presented with the intention of improving the distribution of rays throughout a domain.

Energy exchange due to radiation is evaluated by solving the radiative transfer equation (RTE) along each ray. This procedure is capable of incorporating the radiative properties of gases and particulates into a range of solutions to the RTE. Following a discussion of the radiative properties of typical combustion media, the more approximate, but relatively fast, algorithms are compared across a variety of configurations characteristic of diffusion flames. The analysis incorporates the molecular gases, CO_2 and H_2O, soot and mixtures of these combustion products.

Chapter 4 focuses upon differential solutions to the RTE. A new algorithm, the differential total absorptivity solution, is presented and compared against other techniques. With current levels of computer resources, these methods are generally too slow for radiation prediction in typical engineering problems, but they are expected to become more viable as computing power continues to expand.

Coupling between the soot formation and radiation sub-models is investigated as applied to confined turbulent methane jet flames in chapter 5. Computational predictions are compared against experimental data of temperature and soot volume fraction obtained for two flames, one burning at atmospheric pressure, and the other at a total pressure of

three atmosphere. Initially, various attributes of the overall methodology are assessed in simulations of the lower pressure flame. Subsequently, for both flames, the effects of including oxidation and turbulence-radiation interaction are appraised, and comparisons are made between the radiation solutions previously discussed. Also, the complex dependence of radiative energy exchange on contributions from the gaseous and particulate phases is analysed.

Finally, in chapter 6, the important consequences of this work are presented, and some recommendations for future research are made.

Chapter 2

Turbulent Reacting Flows

2.1 INTRODUCTION

In turbulent reacting flows, there are numerous inter-dependent physical phenomena which influence the combustion process. Two of them, radiation and soot formation, are intimately coupled. Therefore, the interaction between them has a significant effect on various aspects of practical combustion devices, including the emissions from combustors and furnaces. Radiation from soot also represents a central component of fire spread.

Within the general analysis of flames, the development of accurate soot prediction techniques has provided the principal inspiration for many researchers. The importance of radiation in the mechanisms governing soot growth (and burnout) has been widely recognised, but has been modelled in varying degrees of detail. This initial discussion contextualises the status of coupled radiation and soot formation in turbulent combustion.

Radiative energy exchange affects flame structure in the following way. Net radiative emission from regions of high temperature and concentration reduces local temperature. As a consequence, reaction and chemical heat release rates are reduced leading to lower volumetric expansion. Additionally, density changes affect all transported quantities. Ultimately, the influence of these processes on the distribution of soot and gas species thus determines the level of radiative loss. In the present context, it is the effect of radiative loss (and lower temperatures) on the mechanisms governing soot formation and destruction, which is central to the discussion.

Much research into soot-radiation coupling has focused on heavily

sooting fuels such as ethylene and acetylene. In these cases, there is some justification for ignoring the radiative effects of gaseous species, but a complete and general treatment should not. However, the distribution of gaseous species is only weakly coupled to radiative loss (cf. Gore and Faeth, 1988), primarily through the influence of density.

The laminar flamelet combustion model for non-premixed flames, (cf. Liew et al, 1981), has been the main vehicle by which researchers have attempted to initiate a modelling strategy for luminous turbulent flames which accounts for radiative loss. The laminar flamelet concept is based on the observation that scalar properties in non-luminous laminar diffusion flames are nearly universal functions of mixture fraction, a conserved scalar, representing the fraction of mass at a point which originated in the fuel stream. These functions are called state relationships; they are generally determined from experiment (cf. Gore and Faeth, 1986) or from partial equilibrium analysis (cf. Jeng and Faeth, 1984). Turbulent flames are then viewed as an ensemble of wrinkled laminar flamelets having the same properties.

State relationships were successfully applied in a number of studies for estimating scalar properties in non-luminous diffusion flames (cf. Jeng and Faeth, 1984 and Gore and Faeth, 1986) and in a buoyant fire (cf. Crauford et al., 1985). Significantly, the buoyant fire study, which is discussed in more detail below, employed an adiabatic temperature flamelet perturbed by an illustrative fraction to represent radiative loss. The use of a single, experimentally determined temperature flamelet, also accounts for radiative loss in a global sense.

The extension of the laminar flamelet concept to soot volume fraction has attracted considerable attention due to the appeal of circumventing the complexities of soot chemistry in turbulent environments. Gore and Faeth (1986) attempted to construct a flamelet for soot volume fraction in ethylene flames. However, they concluded that effects of finite-rate chemistry and hydrodynamics resulted in poorer universality of soot volume fraction, in

comparison to gas species concentrations. A slightly different approach by Kent and Honnery (1987), demonstrated, again for ethylene flames, that soot volume fraction cannot be simply modelled as a unique function of mixture fraction. By correlating soot volume fraction with mean mixture fraction at a number of heights in a series of flames, a state relationship for soot volume fraction severely under-predicted the measured soot growth with increasing height, and failed to capture the shift in the mean mixture fraction at which the peak soot volume fraction occurred. An important feature of their analysis was the inclusion of a modelled radiative heat loss, albeit through a fairly simple expression, manifested as a sink term in an enthalpy equation. Mean temperatures were evaluated from enthalpy. Consequently, radiation and soot concentration were effectively coupled via the influence of temperature on the density field, and the resultant effect of density on the transport equation for mixture fraction. However, the authors conceded that this coupling was relatively weak, since large errors in predicted temperatures (between 200 and 300 K) had little effect on the profiles of mixture fraction.

Despite the non-universality of a laminar flamelet prescription for soot volume fraction, Gore and Faeth (1986) revealed that the performance of structure and radiation predictions employing this approach in ethylene flames, were similar to earlier results for non-luminous flames. Also, Bhattacharjee and Grosshandler (1989) performed a parabolic analysis of a non-premixed methane flame with a steady state soot model relating soot volume fraction to mixture fraction, and coupled to the effective angle/total transmittance non-homogeneous radiation model. However, they were only using a crude soot formation model as a vehicle to demonstrate features of the radiation model. Gore and Faeth, (1988) reapplied some of their previous analysis of ethylene flames to acetylene, but found poor agreement for radiative emission between prediction and experiment. The authors concluded that the discrepancy between the different fuels resulted from a much higher radiative heat loss fraction - approximately, 60 % of the

chemical energy release - for acetylene, compared to ethylene. This, they suggested, implied significant radiative energy exchange within acetylene flames, which demands a coupled radiation and structure analysis.

Notwithstanding the implications of the above discussion relative to a detailed analysis of a particular flames propensity to soot, there is considerable justification for relating soot volume fraction directly to mixture fraction in regions outside the immediate fuel source. From their experimental observations of the overfire region in a range of turbulent diffusion flames, Sivathanu and Faeth (1990) demonstrated the validity of state relationships for soot volume fraction. Thus, in the wider sense of furnaces and unwanted fires, it is not unreasonable to determine the distribution of soot from the laminar flamelet concept. Fletcher et al. (1994) employed this approach in their numerical simulation of smoke movement from a pool fire in a ventilated tunnel. They constructed a simple state relationship in which soot fraction peaked at the stoichiometric mixture fraction, and followed a linear variation with mixture fraction, with no soot at values of zero and unity. Once the processes of soot formation and destruction have been quenched external to a fire source, the distribution of soot is governed by transport phenomena. Therefore, an alternative strategy for predicting soot concentration is facilitated by solving a separate balance equation for soot volume fraction, provided the output from the fire source can be prescribed.

Another uncoupled approach which has developed out of the laminar flamelet concept entails the perturbation of an adiabatic temperature flamelet by a fixed fraction to represent radiative loss. This can then be used in conjunction with species concentration flamelets to model separate mechanisms of soot kinetics. Such a strategy was adopted by Syed et al. (1990) and by Leung et al. (1991) in developing their respective soot models. Previously, Crauford et al. (1985) had employed a perturbed temperature flamelet in the numerical simulation of a buoyant fire. Whilst they recognised that a "fixed loss" flamelet only crudely represented the radiative

loss throughout the flame, this approach provided a simplified means for assessing the possible effects of radiative loss on flame structure. Analysis of the same fire was extended by Syed et al. (1990) to include predictions of soot volume fraction, again using perturbed temperature (and density) flamelets. Since the focus of their work was the extension of a soot model, initially established from a laminar flame analysis, the temperature, density and fuel concentration fields were post processed in evaluating the different soot formation mechanisms. Radiation was similarly de-coupled from the energy equation, and the soot formation processes, by Leung et al. (1991), Fairweather et al. (1992a) - in the prediction of soot formation in an axisymmetric turbulent propane diffusion flame - and by Fairweather et al. (1992b) who analysed a turbulent jet in a cross-wind. In the context of the present work, this last reference is significant since it comprised a three-dimensional, finite-volume flow field simulation. Soot, chemical species and temperature predictions were post processed in a discrete transfer radiation model estimation of the radiative flux received external to the flame.

Although uncoupled descriptions of radiative loss are capable of yielding qualitatively good results, they fail to adequately describe the distribution of soot, and the effect of radiation on flames. Consequently, Gore et al. (1992) revisited the earlier acetylene flame studies with a coupled calculation similar to that employed by Kent and Honnery (1987). However, Gore et al. (1992) evaluated separate source terms to represent radiative emission and absorption. The former was modelled using a joint probability density function of mixture fraction and enthalpy, whilst a multiray method, devised for the parabolic GENMIX code (cf. Spalding, 1977), was used to calculate absorbed energy. Soot volume fraction was still evaluated by the laminar flamelet concept. The authors offered some justification for this, based on earlier findings by Sivathanu and Faeth (1990) for soot volume fraction state relationships in flames with long residence times. However, Gore et al. (1992) conceded that the approach was used in the absence of alternatives at the time. Nonetheless, the

coupled calculations demonstrated far better performance than the uncoupled calculations, when predicting mean emission temperatures and visible radiation intensities.

An important feature of the analysis by Gore et al. (1992) was the inclusion of turbulence-radiation interaction. The need to incorporate this phenomenon into turbulent reacting flow analysis has been recognised for some time (cf. Williams and Fuhs, 1957). Cox (1977) showed that fluctuating temperature intensities higher than 40 percent yielded radiance values which were more than twice those predicted using mean temperatures. Kabashnikov and Kmit (1979), who treated combined effects of fluctuating absorption coefficient and temperature, also concluded that mean property predictions under-estimated radiation properties.

Early attempts to incorporate turbulence-radiation interaction into turbulent flame analysis - through a stochastic model proposed by Jeng et al. (1984) - yielded inferior predictions of spectral intensity from non-luminous flames relative to those based on mean properties. Additionally, fluctuations had considerably different effects between fuels. When applied to luminous flames, the stochastic method produced a considerably greater effect on continuum radiation from soot, than that from the non-luminous gaseous bands, but in all cases, the method failed to always demonstrate superior accuracy relative to the mean property approach (cf. Gore and Faeth, 1986 and 1988). Kounalakis et al. (1988 and 1991) and Sivathanu et al. (1990) extended the stochastic method to include temporal and spatial variations of mixture fraction applied to non-luminous and luminous flames, respectively. Although radiation statistics were reasonably well predicted, relatively large differences were still evident between prediction and experiment for spectrally resolved radiation intensities. Improved performance in this respect has been recently demonstrated by Chan et al. (1994) who have further extended the method to include cross correlations of mixture fraction in time and space. All of these investigations of spectrally resolved turbulence-radiation interaction cannot be practicably

incorporated into a full three-dimensional CFD simulation due to the computational expense they would incur. Nonetheless, Gore et al. (1992) successfully adopted an alternative approach for including turbulent fluctuations into their parabolic calculation whereby radiative properties were expressed as functions of mixture fraction and enthalpy, and integrated across the joint pdf. Spectral and spatial integration then yielded approximations for locally emitted and absorbed energy.

Adams and Smith (1995) followed a broadly similar strategy in an elliptic CFD simulation of an industrial-scale furnace. However, they performed their statistical analysis on total radiative properties for incorporation into the discrete ordinates radiation model, thus avoiding the need for spectral integration. Their overall approach was somewhat weakened by an extremely crude soot model based on a single empirical expression relating soot formation to the mass fraction of volatile fuel carbon which forms soot.

In contrast to the laminar flamelet concept, other researchers have developed soot formation models by solving a transport equation for enthalpy, combined with a model describing the accompanying chemical reaction, in order to calculate temperature. In this way, energy loss due to radiation can be coupled to soot formation, if a radiative source/sink term is included in the enthalpy equation.

Holen et al. (1990) have developed an overall strategy on this basis for their predictions of heat loads, smoke concentrations and fire development of pool fires in enclosures. Soot was modelled by the approach recommended by Magnussen (1974 and 1979), combustion was represented by the eddy dissipation concept (cf. Magnussen, 1989), and the discrete transfer radiation model was used to evaluate radiative exchange. The overall strategy was similar to that adopted in this thesis, but differs most notably in the soot formation model and in the treatment of radiative properties.

Honnery and Kent (1992) have employed an enthalpy equation based methodology in developing a soot formation model for laminar diffusion flames in which a transport equation for soot particles was solved with empirically based source terms describing formation and oxidation. Species composition was derived from the partial equilibrium model due to Bilger and Starner (1983); and radiative loss was evaluated by the discrete ordinates radiation model, first proposed by Chandrasekhar (1960). Radiation was assumed to be dominated by soot, so gaseous contributions were ignored. A gray absorption coefficient was evaluated as a function of local temperature and soot volume fraction.

Kaplan et al. (1994) also analysed an ethylene diffusion flame by solving a transport equation for enthalpy with radiative source terms evaluated by the discrete ordinates model. Additionally, they included an absorption coefficient which accounted for gaseous and particulate contributions to radiation. Via a fairly comprehensive set of flame property contours, they reinforced the notion that soot dominates emission and absorption of thermal radiation in such flames. Radiative loss was shown to maximise in the region of maximum soot concentration, and then to decrease rapidly with radial distance across the remainder of the soot zone. However, a direct comparison of radiation due to the gaseous and particulate components was not presented.

Notwithstanding the merits of these ethylene flame studies, there is still considerable uncertainty concerning the predictions of soot distribution. Kaplan et al. (1994), who used the soot model due to Moss et al. (1988), described predictions of flame shrinkage but without validation against experiment. The qualitative details of reduced temperature, soot volume fraction and chemical heat release rate, all resulting from radiative heat loss, and subsequently reducing the volumetric expansion of the flame, are not unexpected. Indeed, these characteristics are implicit in many flame studies, including the Honnery and Kent flame just described. In this case, predictions of soot volume fraction were compared against experimental

data, and significant inaccuracies were encountered, especially in the oxidation regions of the flames. The authors indicated potential weaknesses in their prediction of the oxidation rate. Kaplan et al. (1994) only considered oxidation due to O_2 which is questionable in light of other recent work (cf. Puri et al., 1992, Moss et al., 1995 and Coelho and Carvalho, 1995).

Additional uncertainties exist due to the neglect of turbulence-radiation interaction, and due to the possibility of less obvious flame structure properties. For example, Klassen et al. (1992) reinforced the findings of Sivathanu et al. (1991) that, for strongly sooting flames, soot particles at individual locations have different temperatures. Greater insight into the nature of these temperature differences is needed before such a phenomenon can be incorporated into numerical simulations, but in common with turbulence-radiation interaction, this effect has important implications for the accurate prediction of radiative exchange.

Further flame structure characteristics have been revealed by the coupled radiation and soot kinetics study reported by Sivathanu and Gore (1994). Although their claim of being the first workers to report research into the coupling between radiation and soot formation and oxidation was, perhaps unwarranted, there were considerable differences between their analysis of laminar acetylene/air flames and those studies previously described. In particular, the mass fraction of soot was accounted for in the conservation of overall mixture fraction, source terms were included in the enthalpy equation due to energy exchanges associated with soot formation and oxidation, and radiation was modelled by source terms described by Gore et al. (1992). Gaseous radiation was neglected and soot oxidation by OH radicals was not included. Correlations of temperature, radiative fraction and soot volume fraction against mixture fraction at different heights, revealed inflection points in the temperature profiles not observed in weakly radiating flames. The inflection points coincided with regions of maximum soot concentration in which the radiative fraction was maximised

as well. Due to the sensitivity of the individual soot kinetic mechanisms to temperature, and radiative loss, it was also concluded that the use of a constant radiative fraction was ineffective for predicting observed trends in axial and radial distributions of soot volume fraction.

Extension to turbulent flames of the coupled radiation, soot kinetics modelling techniques applied to laminar flames represents the current state of the art. A multiple flamelet approach, developed by Young and Moss (1995) in the simulation of turbulent ethylene flames, has also been used in the coupled analysis presented in chapter 5. Unlike most previously reported coupled studies, the soot predictions are performed in a three-dimensional elliptic calculation. However, in common with previous work, coupling between the soot kinetic mechanisms and radiation is accomplished by the solution of an enthalpy equation, but now the radiative source term is calculated by the discrete transfer radiation model.

The following section, appraises the issues of turbulence and chemical source term closure in the context of CFD simulation of turbulent non-premixed combustion. Subsequently, soot formation models are considered, including a detailed description of the multiple flamelet approach employed in the analysis of turbulent jet diffusion flames in chapter 5. Finally, an overview is presented of the CFD code, SOFIE, which provides the framework for linking the soot formation and radiation sub-models.

2.2 TURBULENCE MODELLING AND CHEMICAL SOURCE TERM CLOSURE

The complexity associated with numerical modelling of turbulence is significantly compounded when chemical reaction occurs. The interaction between turbulence and combustion is principally manifested by the effect of turbulent fluctuations on chemical source terms in the species conservation equations. The following discussion identifies the key

modelling strategies employed in turbulent non-premixed combustion without segregating the issue of chemical source term closure from that pertaining to turbulence.

For all types of flows, conservation equations are derived by balancing the fluxes across boundaries of a small volume with volumetric sources, both internal and external. In low Mach number turbulent flows, using standard tensor notation for Cartesian co-ordinates, these equations take the following forms :

(i) mass conservation

$$\frac{\partial \rho}{\partial t} + \frac{\partial (\rho u_i)}{\partial x_i} = 0 \qquad (2.1)$$

(ii) momentum conservation

$$\frac{\partial (\rho u_i)}{\partial t} + \frac{\partial (\rho u_j u_i)}{\partial x_j} = -\frac{\partial P}{\partial x_i} + \frac{\partial \tau_{ij}}{\partial x_j} + F_i \qquad (2.2)$$

where, if the fluid is considered Newtonian, the shear stress tensor is

$$\tau_{ij} = \mu \left(\frac{\partial u_i}{\partial x_j} + \frac{\partial u_j}{\partial x_i} - \frac{2}{3} \frac{\partial u_k}{\partial x_k} \delta_{ij} \right) \qquad (2.3)$$

and buoyancy is included in the body force term, F_i.

(iii) energy conservation

$$\frac{\partial (\rho H)}{\partial t} + \frac{\partial (\rho u_j H)}{\partial x_j} = \frac{\partial}{\partial x_j} \left[\frac{\mu}{\sigma} \frac{\partial H}{\partial x_j} + \mu \sum_{i=1}^{N} \left(\frac{1}{Sc_i} - \frac{1}{\sigma} \right) H_i \frac{\partial Y_i}{\partial x_j} \right] + S_R \qquad (2.4)$$

which is considerably simplified if equal diffusivities are assumed, and if the single Lewis number, Sc/σ, thus derived, is unity. Then, the specific enthalpy, H, is represented by a standard convective-diffusive balance equation with a source term due to radiative exchange, S_R.

(iv) species conservation

$$\frac{\partial(\rho Y_i)}{\partial t}+\frac{\partial\left(\rho u_j Y_i\right)}{\partial x_j} = \frac{\partial}{\partial x_j}\left(\rho D_i \frac{\partial Y_i}{\partial x_j}\right)+\dot{w}_i \tag{2.5}$$

where Fick's law has been adopted to describe the mass molecular flux of species, this being justifiable due to the secondary importance of molecular transport at high turbulence Reynolds number.

In order to solve these equations, it is necessary to define an equation of state, which for ideal gases is given by

$$p = \rho R_0 T \sum_{i=1}^{N} \frac{Y_i}{W_i} \tag{2.6}$$

and to relate specific total enthalpy to temperature,

$$H = \sum_{i=1}^{N} Y_i \left(h_{f,i}^0 + \int_{T_0}^{T} c_{p,i}(T) dT \right) \tag{2.7}$$

Finally, closure is accomplished via sub-models necessary to derive the source terms occurring in the conservation equations. When the conservation equations are written in the generic form,

$$\frac{\partial(\rho\phi)}{\partial t}+\frac{\partial\left(\rho u_j\phi\right)}{\partial x_j} = \frac{\partial}{\partial x_j}\left(\Gamma_\phi \frac{\partial\phi}{\partial x_j}\right)+S_\phi \tag{2.8}$$

the source terms, S_ϕ, comprise : (i) for momentum, pressure differences due to the pressure gradient, a buoyancy contribution constituting the only body force, and components of the shear stress tensor, all of which are derived in the CFD algorithm; (ii) for energy, radiative exchange which forms the focus of this entire work; and (iii) for species, chemical source terms, $\dot{w}_i$, describing the rate of creation and destruction of the respective chemical species. When a non-orthogonal grid is transformed to Cartesian co-ordinates, additional terms arise which are accumulated in the respective source terms, thus preserving the generic form of Eq. (2.16). Brief details of the finite volume CFD approach, including these transformations, are provided in section 2.4. Γ_ϕ represents the ratio of a diffusion coefficient and a Prandtl-Schmidt number.

The effect of turbulence on radiative and chemical source terms introduces considerable complexity into the analysis of turbulent reacting flows due to the non-linear nature of these expressions. Turbulence-radiation interaction is only briefly addressed in the present work, since in the three-dimensional calculations presented in chapter 5, attention is focused on the coupling between radiative exchange and the formation of combustion products, especially soot. A detailed discussion of the explicit evaluation of radiative exchange is presented in chapters 3 and 4.

Historically, evaluation of radiative source terms has been approached by appending appropriate sub-models to the energy equation, whereas chemical source term closure has stimulated research into multifarious strategies for incorporating turbulence and chemical kinetic effects into complete turbulent reacting flow analysis. Reaction rates are highly non-linear functions of concentration, and, more importantly, temperature. Thus, mean reaction rates cannot be determined from the mean values of

the variables on which they depend (cf. Borghi, 1988). Also, it is not possible to decompose concentrations and temperature into mean and fluctuating components, and model the resulting correlations in a simple way, unless the fluctuations are small. Therefore, alternative means have been established to represent the effect of turbulence on chemical reaction.

Two distinct approaches have emerged. In the first, turbulence and chemical source term closure are modelled by essentially separate techniques, but are linked by the inclusion of turbulence quantities in the combustion model, and by the influence of chemical kinetic effects on thermodynamic properties. This strategy is exemplified in non premixed combustion by parallel solution of modelled equations for turbulence quantities with a fast chemistry model, such as the laminar flamelet concept or an eddy break-up mechanism, both of which effectively circumvent direct treatment of the chemical source terms for all species. This methodology is adopted in the present work, but before describing it in more detail, a brief consideration is given to the alternative strand of approach, in which chemical reaction is treated as one component of a global procedure. Second moment closure and pdf methods are the principal techniques which are able to accommodate the evaluation of reaction rates in this way, and there is expanding interest in model free approaches also categorised as direct numerical simulations (DNS).

2.2.1 Model Free Approaches

Direct numerical simulation aims to solve the governing equations numerically for all types of flows without employing modelling assumptions (cf. Givi, 1989). The attraction of a model free approach is self evident, but the level of computing power required to resolve all the necessary length scales is less obvious, particularly in turbulent reacting flows. It can be shown (cf. Libby and Williams, 1994), for non-reacting turbulence, that the number of grid points required to capture features of the large, geometrically determined length scales, as well as the small Kolmogorov

scales associated with molecular stresses and molecular transport, increases as $Re_t^{9/4}$. Additionally, when DNS is extended to reacting flows, uncertainty is engendered due to the thinness of reaction flame sheets relative to the Kolmogorov length scales. Consequently, computational limitations have restricted DNS calculations to low Reynolds numbers, simple geometries and simple reactions unrepresentative of practical problems. Nonetheless, hope exists that expanding computing power will eventually make it possible to resolve turbulent chemical reaction. Sekar et al. (1990) have achieved a certain degree of success in this respect following their study of a two-dimensional mixing layer of combusting air and hydrogen. A direct numerical simulation of a diffusion flame in a shear flow by Riley et al. (1986) revealed some interesting results concerning the effect of heat release on turbulence quantities. From predictions of Reynolds stresses and other transported turbulence quantities, they demonstrated that thermal expansion through heat release reduces turbulent intensity. Other examples of the current status are provided by Mell et al. (1993) who applied a DNS calculation to the conditional moment closure model for non-premixed turbulent reacting flows, and by Davis et al. (1994) who successfully reproduced experimentally observed dynamic features typical of buoyant jet diffusion flames.

In an attempt to avoid the difficulties associated with simulating all turbulent length scales, a hybrid technique has been developed entitled large eddy simulation (LES). This entails direct simulation of the large turbulence scales, specified by a process of filtering the conservation equations combined with closure approximations needed to model the approximately universal small scales. Consequently, LES is able to model higher Reynolds numbers than complete DNS. Germano et al. (1991) significantly advanced the application of LES to non-reacting flows by replacing the *ad hoc* filter procedure with one calculated on the basis of the local resolved sub-grid Reynolds stresses. However, the accuracy of LES is

questionable for reacting turbulent flows, again because of the length scales of reaction zones, and due to the uncertainty accompanying closure. A detailed discussion of DNS and LES is provided by Reynolds (1990).

Historically, failure to model turbulence exactly, as is now being attempted by DNS, has led to the development of two principal modelling strategies. The first, categorised as pdf methods, solve a transport equation for a pdf containing all relevant statistical information. In contrast, moment methods re-express the instantaneous conservation equations in terms of mean values, and then employ approximations to unresolved turbulence correlations (cf. Tennekes and Lumley, 1972). Common to both of these methodologies is a statistical representation of the physical variables which, in conjunction with appropriate transport equations, prognosticate the approximate behaviour of the flow field.

2.2.2 Pdf Methods

Pdf methods applied to reacting flows were developed from techniques previously applied to the analysis of velocity fluctuations in the field of classical turbulence (cf. Borghi 1988). The general approach develops a balance equation for a pdf from the conservation equations describing the flow under consideration. When chemical reaction is included, species mass fractions appear in the multi-dimensional pdf, and, more significantly, the reaction term in the balance equation is exact and does not require closure. Indeed, complete closure of turbulent combustion is provided if all the velocity, composition and dissipation fields are incorporated in the joint pdf (Pope, 1991). Consequently, the pdf method is applicable to premixed and non-premixed combustion for any chemical scheme. However, difficulties surrounding closure of terms representing pressure fluctuations, molecular stresses and molecular diffusion, still occupy many researchers (Dopazo, 1994), as does the complicated issue of numerical solution of the modelled pdf equations. The high number of independent variables in these equations render the classical finite-difference, finite-volume or finite-

element strategies unfeasible. Stochastic or deterministic models in combination with particle tracking techniques require considerably less computational work. Pope (1981, 1985) provided a good example of a Monte Carlo technique for the solution of a multi-dimensional pdf. Generally, pdf methods adopt a reduced kinetic scheme (involving 5 or fewer compositions) and employ, for example, a table-look-up procedure to integrate the composition equation (cf. Chen et al., 1989). A more detailed chemical description is computationally impracticable.

As an alternative to pdf methods, the assumed pdf approach avoids the need to solve a complex balance equation. Instead, the shape of a 'presumed' pdf is parameterised in terms of its moments, for which modelled conservation equations are solved. The elegant laminar flamelet concept is based on this strategy, but when conditions do not permit representation of the pdf in terms of only its first two moments, modelling of the joint statistics thus required is a formidable task. Additionally, unlike the two-parameter form of the pdf (which has been substantiated experimentally (cf. Kent and Bilger, 1976), the assumed pdf shape may not be sufficiently accurate when it is dependent on a larger number of moments. Nonetheless, some success has been achieved from an assumed joint pdf of two reactant concentrations and temperature (cf. Bockhorn, 1989).

2.2.3 Moment Methods

In moment methods, the governing equations of turbulent flows are derived by time averaging the momentum and scalar equations for laminar flows in a procedure known as Reynolds averaging. For a general conserved quantity, ϕ, the Reynolds averaging procedure decomposes the instantaneous value of ϕ into a mean and fluctuating part :

$$\phi = \bar{\phi} + \phi' \qquad (2.9)$$

where the time averaged value of ϕ is defined as

$$\bar{\phi} = \frac{1}{\Delta t}\int_{t}^{t+\Delta t} \phi\, dt \tag{2.10}$$

and Δt is a time-scale much larger than the largest time-scale of turbulent fluctuations. Time-averaged equations are then obtained by substituting Eq. (2.9) into Eq. (2.8) and integrating over a sufficiently large time interval. The resulting expressions are considerably simplified if density fluctuations are negligible or zero. However, this is not the case in turbulent reacting flows, and a slightly different approach is required. If, instead of decomposing ϕ as described above, it is decomposed into density weighted (or Favre) components (cf. Jones, 1980),

$$\phi = \tilde{\phi} + \phi'' \tag{2.11}$$

where

$$\tilde{\phi} = \frac{1}{\bar{\rho}}\frac{1}{\Delta t}\int_{t}^{t+\Delta t} \rho(t)\phi(t)\, dt \tag{2.12}$$

the same procedure of substitution and integration leads to Favre averaged balance equations of the form

$$\frac{\partial(\bar{\rho}\tilde{\phi})}{\partial t} + \frac{\partial(\bar{\rho}\tilde{u}_j\tilde{\phi})}{\partial x_j} = \frac{\partial}{\partial x_j}\left(\overline{\Gamma_\phi}\frac{\partial\tilde{\phi}}{\partial x_j} - \overline{\rho u_j''\phi''}\right) + \bar{S}_\phi \tag{2.13}$$

which are similar to the constant density, Reynolds averaged counterparts. The flux terms, $\overline{\rho u_j''\phi''}$, represent transport of ϕ due to turbulent

fluctuations. In the momentum equations, they are commonly referred to as the Reynolds stresses and comprise six unique terms.

So, turbulence closure in moment methods concerns evaluation of the turbulent fluxes. Originally, they were modelled by the eddy viscosity concept employing gradient approximations akin to those of molecular theory. In these models, the individual Reynolds stresses are related to a single velocity scale characterising the local state of turbulence. However, when turbulence is non-isotropic, such an assumption fails to account for the different development of each stress and their subsequent transport. Consequently, more complex techniques have emerged which attempt to solve transport equations for each of the Reynolds stresses.

In the Reynolds stress model (RSM), stress equations are derived from the instantaneous momentum equation. For each correlation, the time dependent equation in terms of one velocity is cross multiplied by the fluctuating component of the other, and the resulting equations are averaged and added. A similar procedure is followed for the Reynolds fluxes whereby the scalar equation and its corresponding fluctuating term replace one of the velocity fields. The generation of these second moment equations yields a number of terms, including third order correlations, which require modelling. Consequently, a vast array of equations has to be solved. Numerous closure techniques have been devised as described by Dibble et al. (1986) and Vandromme and Kollmann (1982).

An important advantage of the RSM is that the derivation of its equations automatically introduces terms accounting for buoyancy, rotational and other special effects (Rodi, 1993). Another feature of the RSM is that it is possible to simplify the equations into algebraic expressions which retain these basic features. The so-called algebraic stress model (ASM), in its most general form, is derived by assuming the transport of Reynolds stresses is proportional to the transport of the turbulent kinetic energy (Rodi, 1972). The algebraic expressions comprise many of the modelled terms in the RSM including dependencies on turbulence intensity

and dissipation. An extension to Rodi's ASM is the $k-\varepsilon-g$ model due to Gibson and Launder (1978) in which Reynolds stresses and fluxes are expressed in terms of an additional parameter, g, representing the mean square fluctuations of a composition parameter. Thus, balance equations are required for k, ε and g.

2.2.3.1 The $k-\varepsilon$ Turbulence Model

The oldest proposal for Reynolds stress closure, Boussinesq's (1877) eddy-viscosity concept, still underpins a large proportion of practical turbulence modelling. By analogy with the viscous stresses in laminar flows, Boussinesq established a gradient transport approximation whereby the turbulent stresses were proportional to the mean velocity gradients. In Favre averaged form (Jones, 1980) the Reynolds stresses are

$$-\overline{\rho u_j'' u_i''} = \mu_T\left(\frac{\partial \tilde{u}_i}{\partial x_j}+\frac{\partial \tilde{u}_j}{\partial x_i}\right)-\frac{2}{3}\left(\bar{\rho}k+\mu_T\frac{\partial \tilde{u}_k}{\partial x_k}\right)\delta_{ij} \qquad (2.14)$$

where k represents the turbulent intensity (or kinetic energy), $\frac{1}{2}\left(\tilde{u}_i''\right)^2$. If it is assumed that the same length scale characterises the transport of momentum and all scalars, the gradient assumption for Reynolds fluxes yields

$$-\overline{\rho u_j'' \phi''} = \frac{\mu_T}{\sigma_T}\frac{\partial \tilde{\phi}}{\partial x_j} \qquad (2.15)$$

When the turbulent fluxes represented by Eqs. (2.14) and (2.15) are substituted into Eq. (2.13), the Favre-averaged balance equations take the form

$$\frac{\partial(\bar{\rho}\tilde{\phi})}{\partial t} + \frac{\partial(\bar{\rho}\tilde{u}_j\tilde{\phi})}{\partial x_j} = \frac{\partial}{\partial x_j}\left(\frac{\mu_e}{\sigma_\phi}\frac{\partial\tilde{\phi}}{\partial x_j}\right) + \bar{S}_\phi \qquad (2.16)$$

where the effective viscosity is given by $\mu_e = \mu_L + \mu_T$. The eddy-viscosity concept thus establishes a framework for constructing a turbulence model, which is then required to provide the distribution of μ_T. Rodi (1993) lucidly reviewed the various approaches to this problem. They are all based on the notion, again derived by analogy with molecular theory, that the eddy viscosity is proportional to a velocity characterising the (large-scale) fluctuating motion, and to a typical length of this motion which Prandtl called the "mixing length". The semi-empirical $k-\varepsilon$ model, due to Jones and Launder (1972), has become established as the most popular method for evaluating μ_T. Additionally, it has become the basis of much analysis in turbulent reacting flows, although it was originally devised to describe inert constant density turbulence.

In the $k-\varepsilon$ model, the eddy viscosity is given by

$$\mu_T = C_\mu \bar{\rho}\frac{k^2}{\varepsilon} \qquad (2.17)$$

where the velocity and length scales are assumed to be $k^{1/2}$ and $k^{3/2}/\varepsilon$, respectively. Since μ_T is dependent on the turbulent kinetic energy, k, and on the viscous dissipation, ε, the $k-\varepsilon$ model is expected to encapsulate a satisfactory level of sensitivity to turbulence intensity and length scales. When treating Favre averaged quantities, the form of Eq. (2.17) remains unchanged. The values of k and ε are obtained by separate conservation equations in the form of Eq. (2.16). The k-equation is derived in a similar manner to the Reynolds stress equations based on a summation of each velocity fluctuation. The source term is

$$\overline{S}_k = \overline{P} + \overline{G} - \overline{\rho}\varepsilon \tag{2.18}$$

where the rate of production of turbulent kinetic energy due to shear is

$$\overline{P} = \mu_T\left(\frac{\partial\tilde{u}_i}{\partial x_j}+\frac{\partial\tilde{u}_j}{\partial x_i}\right)\frac{\partial\tilde{u}_i}{\partial x_i} \tag{2.19}$$

and $\overline{G}$ represents mean generation of turbulence due to buoyancy :

$$\overline{G} = g_i\frac{\mu_T}{\sigma_h}\frac{1}{\overline{\rho}}\frac{\partial\overline{\rho}}{\partial x_i} \tag{2.20}$$

The last term in Eq. (2.18) denotes the dissipation rate of turbulence, for which an essentially *ad hoc* balance equation is solved, again having the generic form of Eq. (2.16), with a source term modelled as

$$\overline{S}_\varepsilon = \frac{\varepsilon}{k}\left(C_{1\varepsilon}\left(\overline{P}+\overline{G}\right) - C_{2\varepsilon}\overline{\rho}\varepsilon\right) \tag{2.21}$$

The empirical constants, $C_{1\varepsilon}$ and $C_{2\varepsilon}$, were originally evaluated for cold planar jets as 1.44 and 1.92, respectively. Liew (1983), amongst others, has demonstrated that the same values can be applied to high Reynolds number reacting flows. However, some modification is required when modelling round turbulent jets as discussed in chapter 5.

The Favre averaged form of the $k-\varepsilon$ equations have been successfully applied by several researchers including Lockwood and Naguib (1975), Kent and Bilger (1976) and Jones and Whitelaw (1982). More recently, Young and Moss (1995) and Fletcher et al. (1994) have, respectively, applied the $k-\varepsilon$ model in the analysis of sooting turbulent axisymmetric jet flames, and in the simulation of smoke movement from a pool fire in a ventilated tunnel. Despite yielding good engineering accuracy in these, and other studies, the

$k-\varepsilon$ model has limited general applicability. The assumption of local isotropy is reasonably well founded in high Reynolds number flows. However, eddy viscosity models cannot account for Reynolds stress anisotropies, nor can they deal with streamline curvature and rotational strains (Speziale, 1991). Additionally, counter-gradient diffusion, which can occur in reacting flow systems (Libby and Bray, 1981), is unlikely to be predicted by a gradient transport concept. Another problem has been encountered concerning the universality of the constants, especially those in the ε-equation. This matter is considered further in chapter 5. Libby and Williams (1994) discuss the general applicability of the model in variable density flows.

Notwithstanding the criticisms above, many researchers are still using the standard $k-\varepsilon$ model to simulate turbulence in combusting flows since it is relatively simple to implement, and provides reasonable predictions without excessive computational expense. However, second moment closure methods possess greater generality and physical realism, and have attracted increasing attention in recent years. Therefore, they are expected to become more widely used as expanding computing power is able to accommodate the method's heavy computational demand. One of the main uncertainties in second moment closure methods, concerns the modelling of turbulent dissipation, ε. Jones (1994) presented a good account of the status of ε-equation modelling. There is also uncertainty regarding the treatment of chemical reaction. Unlike the $k-\varepsilon$ model, which solely addresses the fluid mechanical aspects of turbulence, the RSM includes mean reaction rate terms, arising from the derivation of Reynolds fluxes for species mass fractions. Thus, despite the existence of many impressive results for constant density flows (cf. Launder, 1989), the additional complexity associated with modelling chemical reaction has not yet yielded a well established extension to variable density flows and turbulent flames (Jones, 1994). Nonetheless, various chemical closure techniques are attracting considerable attention as evidenced by Chen and Kollman (1994).

Of these, the conditional moment approach suggested by Bilger (1993) has produced promising results for flows near chemical equilibrium. Essentially, dependent variables, and hence, mean reaction rates, are statistically described by moments conditioned on mixture fraction.

When the $k-\varepsilon$ model is applied in combustion problems, a separate model is required to represent chemical reaction. Considerable simplification in this respect is made possible if chemical reaction is assumed to occur at a much faster rate than reactant mixing. The main fast chemistry models are either based on the laminar flamelet concept, which completely circumvents consideration of reaction rates, or on a set of approaches which directly model the rate of fuel consumption. Whereas fast chemistry models have proven validity when predicting heat release and concentrations of the major species, they become non-physical if applied to processes which are controlled by relatively slow chemical mechanisms. For example, the formation of particulates, NO_x and CO are all governed by slow chemistry. However, despite the expectation that pdf methods, particularly, will be able to successfully address finite rate kinetics in the near future (cf. Dopazo, 1994), their accompanying complexity will, most likely, render them unusable in practical combusting applications for some time. Consequently, extensions to fast chemistry models have recently been explored which are able to simulate relatively slow processes. In particular, the laminar flamelet concept for predicting soot formation in turbulent flames (Young and Moss, 1995 and Bressloff et al., 1996b).

2.2.4 Fast chemistry models for turbulent non-premixed combustion.

The main premise of fast chemistry models is that the combustion rate is entirely turbulent-mixing controlled. Explicit application of this principle permits the reaction rate, $\dot{w}$, to be related to the rate of dissipation of the reactant and product containing eddies. Then, the evaluation of $\dot{w}$, and the subsequent solution of balance equations for all species, is reduced to the

solution of a balance equation for mass fraction of fuel including a simple source term describing the rate of fuel consumption. Other mass fractions are then evaluated from combustion stoichiometry. Spalding (1971a) and Magnussen and Hjertager (1976) developed distinct models of this type. Spalding's eddy break-up model related the dissipation of eddies to the fluctuations in concentrations of intermittent reactants, whereas Magnussen and Hjertager's version related them to the mean concentrations. Both models are fairly crude, so the latter approach is popularised by its avoidance of concentration fluctuations; it is the one used here in a slightly modified form.

In contrast to the eddy break-up approach, Bilger (1976) established the framework for the laminar flamelet concept by deriving an expression relating the mean reaction rate to the local scalar dissipation rate given by

$$\chi = 2D\overline{\left(\frac{\partial \xi''}{\partial x_i}\right)^2} \tag{2.22}$$

having assumed unity Lewis number, equal diffusivities, D, of species as well as infinitely fast chemistry. It then follows that concentrations and other chemistry dependent scalars can be related to a single conserved scalar, the mixture fraction. Turbulence interaction is incorporated by integration of the scalar functions of mixture fraction across a pdf of mixture fraction as explained below. Thus, reacting flows are entirely represented by the evolution of mixture fraction (which is governed, in large part, by the rate of mixing), and chemical source term closure is elegantly circumvented.

The strategies for modelling turbulent non-premixed combustion encompassing these distinct fast chemistry models, are described in the following sub-sections. Common to both of them, is the solution of balance equations for momentum, overall mass, turbulence intensity, k, turbulence

dissipation, ε, and mixture fraction. All but the last of these variables are discussed in earlier sections. It is appropriate, therefore, to here delineate the principal characteristics of mixture fraction.

In non-premixed combustion, mixture fraction, ξ, represents the fraction of a mixture originating from the fuel stream. Thus, for the conserved property, $\phi = Y_f - Y_o/s$, mixture fraction is defined as

$$\xi = \frac{\phi - \phi_{o,inlet}}{\phi_{f,inlet} - \phi_{o,inlet}} \tag{2.23}$$

which is naturally bounded between 0 and 1. The balance equation for ξ is represented by Eq. (2.16) with $\overline{S}_\xi = 0$.

2.2.4.1 The eddy break-up model

In the eddy break-up model due to Magnussen and Hjertager (1976), chemical reaction occurs by a one-step mechanism in which fuel and oxidant react to generate a mixture of simple products. Fast chemistry is assumed along with unity Lewis number and equal diffusivities of heat and mass. The simplest implementation of the eddy break-up model for turbulent flows requires separate balance equations for mixture fraction and mass fraction of fuel with the consumption rate of fuel represented by

$$\overline{S}_{fu} = -A\overline{\rho}\frac{\overline{\varepsilon}}{k} min\left(\tilde{Y}_{fu}, \frac{\tilde{Y}_o}{s}, B\frac{\tilde{Y}_p}{1+s}\right) \tag{2.24}$$

Thus, if intermittency of a species is assumed to be proportional to the mean concentration of that species, fuel consumption is determined by the rate of intermittency on a molecular scale of fuel, oxygen and hot product eddies, such that the reactant (or product) with the most marked intermittency governs the rate of combustion. Mixture fraction is needed in order to

determine the mass fractions of oxidant, $\tilde{Y}_o$ and products, $\tilde{Y}_p$ occurring in Eq. (2.24), as well as the mass fraction of diluent (cf. Kuo, 1986), all of which are required to evaluate the mixture temperature. Indeed, combustion is coupled to all transported properties via the effect of heat release on temperature, and hence on radiative loss and density.

The constants, A and B (equal to 4.0 and 0.5, respectively) were originally established for premixed combustion, but were also deemed appropriate for non-premixed combustion. However, variation of A has a significant effect on temperature in fuel rich regions of diffusion flames as investigated in chapter 5.

Despite its simplified representation of combustion, the eddy break-up model still commands interest in the CFD community, largely due to its cost effectiveness. Benim (1989) successfully applied the same implementation as that adopted here, to the finite element solution of an enclosed turbulent diffusion flame, and, more recently, Bai and Fuchs (1993) investigated various aspects of the eddy break-up methodology in simulations of turbulent propane flames in furnaces.

2.2.4.2 The laminar flamelet concept

In common with the eddy break-up model, the laminar flamelet concept is limited to processes of fast chemistry, having unity Lewis number and equal diffusivities of all species and heat. However, it accommodates turbulence-chemistry interaction in a rather more sophisticated manner.

Numerous results from laminar flame experiments have demonstrated the validity of using state relationships to describe chemistry dependent scalars as a function of mixture fraction (cf. Kent and Bilger, 1976 and Liew et al., 1983). However, in turbulent reacting flows, highly non-linear functional relationships invalidate the evaluation of mean scalar properties from state relationships using the mean value of mixture fraction. Thus, a statistical representation of turbulence-chemistry interaction is adopted to

establish a framework in which it is possible to predict the distribution of the same scalars without having to instigate complex closure procedures. Peters (1986) provided a detailed pictorial description of turbulent combustion pertaining to an ensemble of wrinkled flamelets, and it is this widely accepted view which validates a point to point statistical integration of unique state relationships.

Therefore, a pdf is required to describe the effect of turbulence on the distribution of possible values of each property. The laminar flamelet concept capitulates on the mathematics of evaluating a pdf in terms of the first two moments of its independent variable. Hence, the pdf of mixture fraction is completely defined if balance equations are solved for the mixture fraction, $\tilde{\xi}$, and its variance, ξ''^2. Both are represented by the generic convective-diffusive equation (cf. Eq. (2.16)), the first with a zero source term, whereas the balance equation for variance contains a modelled source due to turbulent generation and dissipation :

$$\overline{S_g} = C_{g1}\mu_T\left(\frac{\partial\tilde{\xi}}{\partial x_i}\right)^2 - C_{g2}\frac{\varepsilon}{k}\xi''^2 \qquad (2.26)$$

The values of the constants, C_{g1} and C_{g2} were originally recommended by Spalding (1971b) to be 2.97 and 1.9, respectively. However, despite various suggestions for alternative values, (cf. Spalding, 1979), the values of 2.8 and 2.0 have been widely adopted in recent years.

Since, for variable density flows, Favre-averaged equations are employed to represent the transport of the first two moments of mixture fraction, the pdf of mixture fraction is also a Favre-averaged expression. Thus, mixture fraction dependent scalars are given by

$$\tilde{\phi} = \int_0^1 \phi(\xi)\tilde{P}(\xi)d\xi \qquad (2.27)$$

If Reynolds mean values are required, then

$$\bar{\phi} = \int_0^1 \frac{\bar{\rho}\phi(\xi)}{\rho} \tilde{P}(\xi) d\xi \tag{2.28}$$

where Reynolds averaged density is obtained from

$$\bar{\rho} = \left(\int_0^1 \frac{1}{\rho} \tilde{P}(\xi) d\xi \right)^{-1} \tag{2.29}$$

since integration from zero to unity of the Reynolds-averaged pdf is unity.

Having established a framework for incorporating turbulence-chemistry interaction into the evaluation of mean mixture fraction dependent scalars, all that remains is to determine the shape of the pdf. The most commonly used shapes are the beta function (cf. Jones and Priddin, 1979) and the clipped Gaussian (Lockwood and Naguib, 1975). Chen et al. (1991) have explored the influence of the shape of the presumed pdf in calculations of a diffusion flame in a boundary layer, and found that profiles of mean velocity, enthalpy, mixture fraction and its variance are little affected by the pdf shape. The beta function (cf. Abramowitz and Stegun, 1968) is used here, and defined by

$$\tilde{P}(\xi) = \xi^{\alpha-1}(1-\xi)^{\beta-1} \Big/ \int_0^1 \xi^{\alpha-1}(1-\xi)^{\beta-1} d\xi \tag{2.30}$$

where

$$\alpha = \tilde{\xi}\left(\frac{\tilde{\xi}(1-\tilde{\xi})}{\widetilde{\xi''^2}} - 1 \right) \tag{2.31}$$

and

$$\beta = \alpha(1-\tilde{\xi}) / \tilde{\xi} \tag{2.32}$$

The beta function is normalised by its area between *0* and *1* so that integration of the pdf is unity in the same range.

Although the laminar flamelet concept incorporates turbulent fluctuations into the evaluation of enthalpy and temperature, it cannot accomodate heat transfer at boundaries. Furthermore, its elegance lacks generality once state relationships become functions of more than variable; for example, when the chemistry is not fast, and under conditions of significantly varying heat loss. Although some workers have attempted to represent joint pdfs as the product of marginal pdfs, having assumed statistical independence (cf. Liew et al., 1984), such a simplification is not generally applicable. Consequently, either the computation of a mult-variate pdf is necessary, or an alternative strategy must be sought.

In a manner reminiscent of the circumvention of chemical source term closure, the laminar flamelet concept has ably side-stepped the complicated issue of coupled soot formation and radiation by an extended flamelet approach which allows for local levels of radiative loss in the evaluation of soot formation mechanisms. Before describing this strategy in more detail, an overview is presented of recent advances in soot formation predictive techniques.

2.3 SOOT FORMATION MODELLING

Prediction of soot concentration in turbulent combustion has been arousing increasing levels of interest in recent years (cf. Bockhorn, 1994). The reasons for this are manifold. Legislation and performance criteria

necessitate a clear understanding of the processes governing combustor emissions in both the gas turbine and internal combustion engine industries. The design of industrial furnaces has to satisfy a partially conflicting set of requirements. High levels of soot in flames improve operating efficiencies, through an enhancement of radiative exchange, whilst emissions standards do not permit unbounded efflux of pollutants. In enclosure fires, soot represents a critical component of fire spread including the flash-over phenomenon (cf. Lockwood and Malalasekera, 1988), and produces a considerable human hazard due to asphyxiation and reduced visibility. Unfortunately, unwanted fires produce copious amounts of soot as they are characterised by poor mixing and long residence times.

Experimental observations confirm that soot is primarily formed when a mixture is richer than stoichiometric (cf. Kent and Honnery, 1987). Thus, in non-premixed combustion, considerable quantities of soot can be produced at particular locations despite a low overall equivalence ratio of the complete system. If this soot is not subsequently oxidised, it is either deposited on solid surfaces or is emitted as smoke. In combustors and furnaces, partially burnt fuel additionally represents a loss of efficiency.

The mechanisms governing soot formation are extremely complex, and although some researchers have attempted to develop detailed models based upon the fundamental chemical processes occurring in flames (cf. Weissman and Benson, 1989, Frenklach and Wang, 1990 and Miller et al., 1992), no unifying theory has yet been proven. Even if such a theory was available, the complexity associated with its extension to turbulent reacting flows would preclude feasible computational application. Consequently, computationally tractable approaches to modelling soot formation under turbulent conditions have been developed which attempt to represent experimentally observed features in laminar flames by global expressions.

The most straightforward approach entails representation of soot formation by a single empirical rate expression exemplified by Kahn and Greaves (1974). Originally devised for diesel engines, it has also been

applied to turbulent jet diffusion flames (cf. Abbas and Lockwood, 1985). However, a recent comparison of the Kahn and Greaves model with more sophisticated two-step models (Coelho and Carvalho, 1995) has demonstrated that the former fails to capture some important features of a turbulent propane jet diffusion flame. A review of one-step soot formation models is provided by Mullins et al. (1987), whilst Coelho and Carvalho (1995) present a general discussion of two-step models suitable for incorporation into CFD codes.

The one-step approach is fairly bold in that it completely circumvents treatment of the individual mechanisms governing soot formation. In contrast, two-step approaches explicitly model these distinct processes. The first, nucleation, describes the initial creation of particles on the fuel side of the flame close to the reaction zone. Subsequently, intense mass growth - particularly on the surface of particles - increases the soot volume fraction while coagulation serves to reduce the particle number density. Following their formation, burnout of soot particles may occur near and beyond the flame reaction zone due to oxidation. If the strongly temperature dependent oxidation reactions are sufficiently quenched by radiative energy loss at the flame tip, the remaining soot is emitted as smoke (cf. Kent and Wagner, 1984). Oxidation is considered further below.

In recent years, two contrasting approaches have emerged for incorporating distinct formation mechanisms into the evaluation of soot concentration. The first, which employs approximations for the number density in the solution of a balance equation for mass concentration, thus only requires modelled expressions for nucleation and surface growth. Kennedy and co-workers (1990 and 1992) and Honnery and Kent (1992), respectively, approximated number density from measured average values, and from a relationship between surface area and volume fraction. Common to these methodologies is an emphasis on surface growth rates. This is not surprising since it has been shown by a comparison between the evolution of soot volume fraction and number density that surface growth is

the dominant component in the overall formation of soot (cf. Glassman, 1988). An older model, due to Tesner et al. (1971), also requires an approximation for number density, but it differs from the more recent models of this kind due to the necessity of solving an additional scalar equation for the concentration of radical nuclei. Nonetheless, the Tesner model maintains a certain level of popularity evidenced by its inclusion in commercial CFD codes (FLUENT, 1993). It has also been used fairly recently to model soot formation - via the approach recommended by Magnussen (1976 and 1979) - in the simulation of pool fires in enclosures (cf. Holen et al., 1990).

In their study of a laminar ethylene diffusion flame, Kennedy et al. (1990) compared predictions based upon an assumed number density, with those obtained by solving a separate equation for number density. They concluded that the additional detail provided by the latter approach did not yield significant change in the predicted structure of the sooting region. However, the solution of balance equations for number density as well as mass concentration has been attracting considerable interest in the analysis of turbulent diffusion flames. It is this approach which characterises the second methodology for incorporating global formation mechanisms into the derivation of soot volume fraction. Capitulating on the work of Gilyazetdinov (1972), it requires consideration of coagulation of soot particles in addition to the processes of nucleation and surface growth.

Moss and co-workers (1988, 1990 and 1991) have developed expressions for all three formation mechanisms in relation to volume fraction and number density based on laminar flame experiment for a number of fuels including ethylene, methane and kerosene. Fairweather et al. (1992a) have followed a broadly similar strategy, but in contrast, have employed a detailed chemical kinetic scheme (Leung et al., 1991) to determine the laminar flame soot source terms in propane jet flames. Another significant difference between these approaches concerns the species used as a precursor to nucleation and surface growth rates.

Originally, Moss et al. (1988) used the parent fuel, but evidence now suggests (Missaghi et al., 1993 and Coelho and Carvalho, 1995) that it is more realistic to use a characteristic pyrolysis product such as acetylene as proposed by Fairweather et al. (1992a). Indeed, more recently, Moss et al. (1995) employed the total hydrocarbon concentration - conceded to be primarily acetylene - as the fuel driving nucleation and surface growth in the study of an ethylene laminar diffusion flame burning under oxygen-enriched conditions.

Most of the studies mentioned above include a term to represent soot burnout, generally adopting O_2 as the principal oxidising species. However, a number of recent works (cf. Puri et al., 1992) have emphasised the combined importance of OH and O_2 in soot oxidation, and it is possible that other species such as O, H, NO, H_2O and CO_2 may also play a significant role (Bradley et al., 1984). Recently, Moss et al. (1995) compared the oxidation rate expressions due to Nagle and Strickland-Constable (1962), Lee et al. (1962) and Fenimore and Jones (1967) in an laminar ethylene flame and concluded that the Fenimore and Jones expression yielded the best predictions. It is the one employed here.

The soot model used in the present work is a variant of the one due to Moss et al. and is described in more detail by Brookes (1996). In order to facilitate the representation of soot number density, n, and soot volume fraction, f_v in Favre-averaged balance equations, n and f_v are replaced by $\phi_n = n/\rho N_0$ and $\phi_f = \rho_p f_v/\rho$, respectively; N_0 denotes Avogadro's number (6×10^{26}) and ρ_p signifies soot density (assumed to be 1800 kgm^{-3}). The equations for ϕ_n and ϕ_f, are of the same form as Eq. (2.16) with source terms given by (cf. Brookes, 1996)

$$\overline{S}_n = \overline{\alpha} - \overline{\rho}^2 \overline{\beta}\, \tilde{\phi}_n^{7/3} \tilde{\phi}_f^{-1/3} \tag{2.33}$$

and

$$\overline{S}_f = \overline{\delta} + \overline{\rho}\,\overline{\gamma}\,\tilde{\phi}_n^{1/3}\,\tilde{\phi}_f^{2/3} \tag{2.34}$$

α and δ represent the influence of nucleation on the number density and soot volume fraction, whilst β and γ characterise the processes of coagulation and surface growth, respectively. These soot formation parameters are all modelled in terms of properties describable by state relationships. Acetylene is used as the soot precursor, and the state relationship for the mass fraction of acetylene is considered invariant with radiative loss. Further details are provided by Brookes (1996).

Soot oxidation can be viewed as a sink of soot mass whilst the number density is little affected. Thus, Brookes (1996) incorporated a negative mean oxidation rate into the balance equation for mass concentration. Equation (2.34) then becomes

$$\overline{S}_f = \overline{\delta} + \overline{\rho}\,\overline{\gamma}\,\tilde{\phi}_n^{1/3}\,\tilde{\phi}_f^{2/3} - \overline{\rho}\,\overline{\omega}\,\tilde{\phi}_n^{1/3}\,\tilde{\phi}_f^{2/3} \tag{2.35}$$

In common with the soot formation mechanisms, the oxidation parameter, ω, can be represented by a single state relationship in terms of mixture fraction.

Having established a means for describing soot formation and destruction in laminar flames, incorporation into turbulent flame prediction has drawn on the flamelet concept of integration across a pdf with respect to mixture fraction. Thus, if the global mechanisms of nucleation, surface growth, coagulation and oxidation are reduced to functions of mixture fraction, balance equations for mass concentration and/or number density can be established with mean source terms determined via Eq. (2.28). However, since these kinetic processes are strongly dependent on temperature and density, the considerable effect of radiative loss on the corresponding state relationships precludes using a single flamelet to

represent all levels of radiative loss. Consequently, a scheme has now been established to couple the individual source terms to the level of heat loss by radiation (cf. Young and Moss, 1995). The methodology is an extension of the laminar flamelet concept in that turbulence-chemistry interaction is incorporated by statistical integration of state relationships, but now, a library of flamelets are employed to map the joint dependence of state variables on mixture fraction and heat loss. Such an approach circumvents the need to statistically integrate across a joint pdf

$$\tilde{\phi} = \int_0^1 \phi(\xi, Q_R)\tilde{P}(\xi, Q_R)d\xi \tag{2.36}$$

but requires, in its place, a fairly cumbersome procedure to identify which flamelets describe local levels of radiative loss. Soot source term flamelets are derived, like density, form state relationships for temperature which, themselves, are inferred from specific enthalpy using the caloric equation of state

$$\bar{h} = \sum_{i=1}^{N} \overline{Y_i h_i}(T) \approx \sum_{i=1}^{N} \overline{Y}_i h_i(\overline{T}) \tag{2.37}$$

and species composition-mixture fraction relationships derived from an adiabatic flame calculation. Likewise, an adiabatic flamelet for acetylene concentration is used for the nucleation and surface growth terms in Eqs. (2.33) and (2.35). The family of enthalpy flamelets are derived from the expression

$$h(\xi; Q_R) = h_i(\xi) + (1 - Q_R)(h_a(\xi) - h_i(\xi)) \tag{2.38}$$

which prescribes the fraction of sensible enthalpy, relative to ambient, lost

from a linearly approximated adiabatic profile.

It is via the perturbative effect of heat loss on the enthalpy field (and hence temperature) that the derived soot source term flamelets are linked to radiative loss, the latter being manifested as a source term to the enthalpy balance equation. Hence, it is possible to identify a local level of radiative loss by comparing the mean total enthalpy derived from solution of its balance equation with the statistically integrated values

$$\tilde{H} = \int_0^1 H(\xi; Q_R)\tilde{P}(\xi)d\xi \tag{2.39}$$

obtained from the flamelet library. It is then a simple matter to interpolate between adjacent flamelets which bracket the computed value. Finally, soot source terms are evaluated by interpolation between the corresponding pair of flamelets derived as described above. In all cases, statistical integration is performed with a beta function pdf determined from the Favre-averaged values of mixture fraction and its variance.

In the finite volume method, matrices generated by discretisation of the transport equations are ill-conditioned if source terms become too large. As a consequence, converged solutions may not be achieved. In order to avoid such a scenario, source term linearisation is employed to the coagulation expression in Eq. (2.33) and to the oxidation term in Eq. (2.35).

2.4 THE CFD CODE SOFIE

Computational simulation is performed using a finite volume, general curvilinear CFD code called SOFIE (Simulation of Fires In Enclosures) currently being developed at Cranfield for wide-ranging combustion applications. A SIMPLEC pressure correction algorithm (Patankar, 1980)

for co-located velocities and pressure is used to evaluate the flow field (Melaaen, 1992). Momentum interpolation (Majumdar, 1988) and a second order TVD discretisation scheme (van Leer, 1974) are employed to ensure a numerically stable solution without non-physical oscillations and false diffusion.

The axisymmetric flames analysed in chapter 5 are modelled by a prismatic sector of a cylinder with mirror symmetry boundary conditions imposed on the two longitudinal faces thus produced. In Cartesian co-ordinates, these non-orthogonal faces require the governing equations to be transformed to general curvi-linear co-ordinates. The basis of the transformation from physical space, (x,y,z), to computational space, $(\varepsilon,\mu,\varsigma)$, is given by

$$\frac{\partial\phi}{\partial x_j} = \frac{1}{J}\frac{\partial}{\partial\varepsilon_i}\left(J\frac{\partial\varepsilon_i}{\partial x_j}\phi\right) \tag{2.40}$$

where J denotes the Jacobian of the transformation. The generic balance equation (cf. Eq. 2.16) maintains its basic convective-diffusive form once Cartesian velocities are manipulated into their contravariant counterparts, and provided the additional cross diffusion terms are added to the source term. Then,

$$J\frac{\partial(\bar{\rho}\tilde{\phi})}{\partial t}+\frac{\partial(\bar{\rho}\tilde{U}_j\tilde{\phi})}{\partial\varepsilon_j} = \frac{\partial}{\partial\varepsilon_j}\left(\frac{\mu_e}{\sigma_\phi}J\,g_{jj}\frac{\partial\tilde{\phi}}{\partial\varepsilon_j}\right)+J\,\bar{S}_\phi \tag{2.41}$$

where contravariant velocity components (scaled by the Jacobian) are given by

$$U_j = J\frac{\partial\varepsilon_j}{\partial x_i}u_i \tag{2.42}$$

and the grid metric g_{jj} is defined by

$$g_{jk} = \frac{\partial \varepsilon_j}{\partial x_k} \frac{\partial \varepsilon_k}{\partial x_j} \tag{2.43}$$

Being of the same form as the partial differential equations in Cartesian coordinates, the transformed equations can be discretised and solved by identical methods. Consequently, the finite volume method applied to Eq. (2.41) yields the general algebraic expression

$$a_p \phi_p = \sum_{all\ faces} a_f \phi_f + S\delta V \tag{2.44}$$

where ϕ_p denotes the value of the variable at the central node of the computational molecule. The coefficients, a_f, comprise the convective and diffusive fluxes across each face, and are determined by the interpolation scheme employed to evaluate face velocities. The discretised equations are solved using a line-by-line tri-diagonal matrix algorithm. Further details concerning all these techniques are available in the cited literature, and salient features of the computational simulations are discussed in chapter 5.

2.5 CONCLUDING REMARKS

There now exists a vast body of work relating to the accurate prediction of turbulent reacting flows. Substantial effort is still being expended on developing second moment and pdf methods, but these more sophisticated approaches demand considerable computer expense. They are likely to acquire greater viability due to a continual expansion in computing power.

Likewise, model free approaches are expected to gain in popularity.

Many simpler techniques are also available which are capable of generating adequate accuracy at low computational cost. It is appropriate, therefore, to adopt less sophisticated techniques when developing other sub-models for incorporation into CFD simulation of turbulence, chemical reaction and heat transfer. Specifically, the $k-\varepsilon$ model of turbulence, and the eddy break-up model of combustion are adopted in this thesis as vehicles for investigating the important interaction between soot formation and radiation in turbulent flames.

Having introduced the multiple flamelet model for soot formation and burnout, the next two chapters focus upon various aspects of radiation modelling. Then, in chapter 5, the soot and radiation sub-models are coupled together in the simulation of confined jet diffusion flames operating under different total pressures.

Chapter 3

Numerical Modelling of Thermal Radiation in Combustion

3.1 INTRODUCTION

Radiation modelling is a critical component in the prediction of highly temperature-dependent pollutant formation and wall heat transfer in complex combustion systems. The nature of solution is especially important in coupled CFD heat transfer calculations in which it is necessary to strike a balance between generality, accuracy and computational effort.

Early attempts to incorporate radiation in computational flow/heat transfer prediction largely relied upon the zone model (Hottel and Sarofim, 1967), the various flux models (Lockwood and Shah, 1976) and the Monte Carlo method (Steward and Cannon, 1971). Although these models possess considerable merit in a number of applications, especially in terms of their accuracy, they do not ideally satisfy the aforementioned balance.

The zone model demands excessively high storage, since the exchange areas between all surface and volume elements need to be evaluated. It becomes particularly uneconomic in complex geometries. The Monte Carlo method avoids these shortcomings by automatically calculating exchange areas as part of the process in which randomly generated energy bundles are traced across an enclosure. However, traditionally, the method has tended to be slow - as the energy bundles are traced to extinction - and it suffers from statistical error dependent on the quality of the random number generator employed.

Common to the wide variety of flux models is a procedure which reduces the integro-differential radiative transport equation to a series of

coupled linear differential equations. Although flux models produce a high level of computational economy, they tend to suffer from the mathematical complexity that is engendered when transforming to more complex co-ordinate systems (including general curvilinear co-ordinates).

With the intention of combining the advantages of the older zone, Monte Carlo and flux models in an exact model capable of producing sufficient accuracy at low computational cost, and easily applied to complex geometries (such as those found in most combustors), Lockwood and Shah (1981) developed the discrete transfer radiation model (DTRM). The method employs a ray tracing procedure which solves the radiative transfer equation, RTE, along a discrete set of representative directions from fixed points on solid surfaces. Internal radiative energy exchange is thus represented by a summation of the contributions due to each ray that traverses individual control volumes. Consequently, the physical nature of radiation is not obscured by over-elaborate mathematics.

Before considering the DTRM in more detail, it is appropriate to assess the current status of radiation modelling in general. Additional information is available in the reviews by Sarofim (1986), Viskanta and Menguc (1987) and Howell (1988), in the more recent publications by Siegel and Howell (1992) and Modest (1993), and in the cited literature.

Of the older radiation models, the Monte Carlo approach represents the most popular method for model validation. For example, four out of five authors who participated in a comparison exercise of different radiation solution methods co-ordinated by Tong and Skocypec (1992), also used the Monte Carlo method as a means of validation. Interestingly though, in a fairly simple three-dimensional enclosure, differences as large as a factor of 2 were observed for heat fluxes, and a factor of 3 for the divergence of heat flux.

Flux models have generated the largest number of alternative approaches to solving the radiative transfer equation. Spherical harmonics (also known as the differential approximation), moment methods and

discrete ordinates can all be classified as flux models since they solve the RTE in specific directions, only differing in the derivation of weighting coefficients for the radiative intensities in each direction. Additionally, a number of hybrid models have been developed such as those which combine spherical harmonics and discrete ordinates. Borkowski and Kaminski (1994) provide a recent summary of many flux based models with special attention to the P-1 spherical harmonics solution. Most analyses normally make comparisons in relatively simple, non-practical geometries. Recently, however, Adams and Smith (1993) reported an impressive assessment of the discrete-ordinates method applied to a geometrically complex furnace including multiple shadowing effects. The DTRM has been applied to a number of complex geometries as described below.

In terms of coupling radiative heat transfer calculation to CFD codes, the discrete-ordinates method has proved popular in parabolic flame studies (cf. Kaplan et al, 1994), whereas the relatively simple formulation of the DTRM makes it well suited to three-dimensional calculation (cf. Fletcher et al., 1994). Recently, Giridharan et al. (1995) reported a body-fitted co-ordinates version of discrete-ordinates which is considerably more complex than the DTRM. A particularly simple model suitable for parabolic type flows is the effective angle model due to Bhattacharjee and Grosshandler (1990) which has been successfully applied in a coupled radiation soot formation simulation of a turbulent diffusion flame (cf. Bhattacharjee and Grosshandler, 1989). Finally, a number of approaches have been developed which apply a particular CFD methodology to solution of the RTE. The finite-volume methods of Raithby and Chui (1989) and Chai et al. (1994), and the finite-element method of Schneider and Raw (1987) are noteworthy in this respect. Notwithstanding their mathematical elegance, these are all characterised by considerable complexity relative to the DTRM.

In section 3.2, the discrete transfer radiation model is described in detail. Then, models for the radiative properties of combustion products are discussed in section 3.3, and finally, methods traditionally employed to

solve the radiative transfer equation in the DTRM are compared in section 3.4.

3.2 THE DISCRETE TRANSFER RADIATION MODEL

3.2.1 Introduction

The DTRM represents one of the most popular methods used for the modelling of radiation in a variety of combustion situations including furnaces (Abbas and Lockwood, 1984) combustors (Carvalho and Coelho, 1989), flames (Fairweather et al., 1992b) and fires (Fletcher et al., 1994). Its popularity is enhanced by its inclusion in many commercially available CFD codes (FLUENT, 1993). It is also being used in the three-dimensional general curvilinear co-ordinates CFD code, SOFIE, being developed at Cranfield University for wide-ranging combustion applications.

Two of the key attractions of the DTRM, its relatively simple formulation, and its straightforward implementation in general curvi-linear co-ordinates, are described in the first two sub-sections. Then, in sub-section 3.2.4, issues relating to optimisation of the method are considered. Particular attention is paid to strategies of angular discretisation defining the directions relative to a surface in which the RTE is solved.

3.2.2 Theoretical Formulation

The ray tracing procedure in the DTRM, is based upon a directional discretisation of the hemispherical solid angle representing the "field of vision" of a surface. In its original formulation, the solid angle hemisphere is discretised using divisions of the polar and azimuthal angles, θ and ϕ, as shown in Fig. (3.1). It is customary to launch sets of rays from the boundary faces of the CFD grid. Once ray directions are established, each ray is traversed both towards and away from its originating surface. Incident radiation is evaluated from the incoming traverse so that the hemispherical

solid angle of a surface is completely mapped. Similarly, the outward traverse fully represents the output from a surface which is communicated throughout the domain. The changes in intensity along outgoing rays is used to evaluate the radiative loss or gain of control volumes in the CFD grid. It is the modelling of this volumetric flux, and its manifestation as a source term in the energy equation, which is critical in the predictive techniques discussed in chapter 5.

The DTRM employs a direct solution to the radiative transfer equation, RTE, the fundamental equation describing spectrally resolved transfer of thermal radiation. The RTE is derived by balancing the rate of change of intensity across an elemental path with the changes due to absorption, emission and scattering. For a purely absorbing-emitting medium the radiative transfer equation is

$$\frac{di_\nu}{ds} = -k_\nu i_\nu + k_\nu i_{b,\nu} \tag{3.1}$$

Following the approach of Siegel and Howell (1992), integration of Eq. (3.1) along a single line of sight yields the monochromatic intensity

$$i_\nu(s) = i_\nu(0)\,exp\left(-\int_0^s k_\nu(s'')ds''\right) + \int_0^s i_{b,\nu}(s')k_\nu(s'\rightarrow s)\,exp\left(-\int_{s'}^s k_\nu(s'')ds''\right)ds' \tag{3.2}$$

The first term represents radiance at the start of a path length that is transmitted across s. The second term is the sum of energy emitted from intermediate points, s', that is then transmitted across the remaining path to s. Integrating Eq. (3.2) across the spectrum and substituting for transmissivity,

$$\tau_\nu(s' \rightarrow s) \;=\; exp\left(-\int_{s'}^{s} k_\nu(s'')ds''\right) \tag{3.3}$$

yields the integro-differential equation

$$i(s) \;=\; \int_0^\infty i_\nu(0)\tau_\nu(0 \rightarrow s)d\nu \;+\; \int_0^\infty\int_0^s i_{b,\nu}(s')\frac{\delta\tau_\nu(s' \rightarrow s)}{\delta s'}ds'd\nu \tag{3.4}$$

For a gray, homogenous medium, Eq. (3.4) simplifies to a recurrence relation expressing the intensity at the end of a path in terms of that at the start :

$$i_n \;=\; i_{n-1}\tau_N \;+\; i_{b,N}\left(1-\tau_N\right) \tag{3.5}$$

The total transmissivity, τ_N, and the black body intensity, $i_{b,N}$, are assumed constant for the N^{th} control volume.

If Eq. (3.5) is expanded back to the origin of its path, the intensity at a point is expressed as

$$i_n \;=\; i_0\prod_{r=1}^{n}\tau_r \;+\; \sum_{r=1}^{n} i_{b,r}\varepsilon_r\prod_{r'=r+1}^{n}\tau_{r'} \tag{3.6}$$

Eq. (3.6) represents a constant absorption coefficient (CAC) solution to the RTE such that, for constant values of k, the transmissivity is given by $\tau_r = exp(-kl) = \left(1-\varepsilon_r\right)$. As a new cell in a path is traversed, the transmissivity product for each upstream cell is multiplied by the transmissivity of the new cell. The initial intensity at the origin of every path is given by

$$i_0 = \left[\varepsilon_0 \sigma T_0^4 + \left[1-\varepsilon_0\right] q^-\right] / \pi \tag{3.7}$$

where, for gray boundaries, the second term makes all values of i_0 dependent on the initial intensities from other solid locations within the domain. Therefore, the ray tracing procedure is iterative (other than for black walls with prescribed temperatures).

The intensity variation along each ray is assumed constant for the associated solid angle. Angular fluxes are then evaluated as the product of the radiative intensity, and a weighting factor dependent on the method of directional discretisation. When the inward ray tracing traverse is performed, summation of these products finally yields the total incident radiative flux

$$q^- = \sum_{m=1}^{M} w_m i_m \tag{3.8}$$

i_m represent the final values from Eq. (3.6) along each ray of the solid angle hemisphere. Once all rays have been traced to and from a particular face, both the incident flux and the radiance from the face - Eq. (3.7) - are updated. Radiative source terms

$$S_R = \sum_{all\ rays} w \Delta i \Delta A \tag{3.9}$$

are evaluated from the outgoing traverse where Δi represents the change in intensity of a ray which crosses the control volume. Each ray is assumed to occupy a "pencil" equal to the projection of the area, ΔA, of the surface element from which it originates. It is also assumed that the "pencil" completely overlaps every control volume that it intersects. These

assumptions were justified by Lockwood and Shah (1981) in terms of the expensive cpu penalties that are incurred, for a small improvement in accuracy, when the source terms are calculated according to the proportion of a control volume overlapped by a ray. Source terms are continually updated during the course of a complete sweep of all rays from every surface.

The weighting coefficients, w, in Eqs. (3.8) and (3.9) are functions of ray directions and the solid angles represented by each ray. They are also dependent upon the alignment of the axes used to discretise the hemispherical solid angle relative to a solid surface. The evaluation of weighting coefficients is discussed in section 3.2.4.

To summarise, the ray tracing procedure in the discrete transfer radiation model is performed for each surface in turn, surface and volumetric radiative fluxes are updated, and a convergence criterion is tested at the end of a complete sweep based upon the absolute change in the net wall heat flux.

3.2.3 Implementation in General Curvilinear Co-ordinates

One of the principal advantages of the DTRM is its simple application to complex geometries. Therefore, the method is extremely well suited to finite volume CFD codes written in general curvilinear co-ordinates (GCC). Details concerning the transformation of CFD transport equations in GCC was addressed in the previous chapter, and further information is available in the cited literature. Less readily available, however, are descriptions of the coupling of the DTRM to GCC CFD codes. Therefore, an outline is presented below. Within this discussion, emphasis is given to the computational issue of storage versus cpu cost.

In the DTRM, it is standard practice to maintain a fixed set of ray tracing directions. Therefore, it is particularly wasteful of cpu time to repeat the initial ray tracing sequence which determines the history of each ray. However, the storage penalty incurred by storing path lengths and

connectivities can be severe, especially if large numbers of rays are employed on fine CFD grids. Notwithstanding the problem of storage, it is preferable to pre-process and store this ray tracing information thus improving the efficiency of the radiation calculation. Furthermore, when the gray gas approximation is made it is prudent to store individual path transmissivities, instead of path lengths, thus avoiding repeated exponential calculations at run time. Finally, storage requirements can be reduced if integer offsets are used to record the sequence of traversed control volumes.

In order to determine a complete description of a ray, which is specified relative to a surface of arbitrary orientation, it is necessary to know the ray's origin and a Cartesian vector describing its direction. All faces are defined by covariant base vectors, $\hat{e}_1$, $\hat{e}_2$ and $\hat{e}_3$ simply determined from the co-ordinates of cell corners and centres of the CFD grid. These base vectors provide the basis for orientating the polar and azimuthal axes of the surface's solid angle hemisphere. Conventionally, $\hat{\theta}$ is aligned with the surface normal, $\hat{e}_2$ as shown in Fig. (3.1), and $\hat{\phi}$ is aligned with one of the planar base vectors. Also, the polar and azimuthal angles are subdivided equally.

Now, ray directions relative to a surface are defined by vectors passing through the centre of the solid angle polygons produced by discretising the solid angle hemisphere. A typical ray is shown in Fig. (3.1). Relative to a surface, ray vectors are

$$\vec{r}_{rel} = (\vec{\theta},\vec{\phi}) \tag{3.10}$$

or, in terms of the base vectors,

$$\vec{r}_{rel} = (sin\theta cos\phi)\hat{e}_1 + (cos\theta)\hat{e}_2 + (sin\theta sin\phi)\hat{e}_3 \tag{3.11}$$

Therefore, in an external, Cartesian reference frame, rays are given by

$$\vec{r} = \begin{pmatrix} r_1 e_{1x} + r_2 e_{2x} + r_3 e_{3x} \\ r_1 e_{1y} + r_2 e_{2y} + r_3 e_{3y} \\ r_1 e_{1z} + r_2 e_{2z} + r_3 e_{3z} \end{pmatrix} \tag{3.12}$$

where,

$$\begin{aligned} r_1 &= \sin\theta\cos\phi \\ r_2 &= \cos\theta \\ r_3 &= \sin\theta\sin\phi \end{aligned} \tag{3.13}$$

and where (e_{1x}, e_{1y}, e_{1z}), (e_{2x}, e_{2y}, e_{2z}) and (e_{3x}, e_{3y}, e_{3z}) denote the Cartesian components of $\hat{e}_1$, $\hat{e}_2$ and $\hat{e}_3$, respectively.

The suitability of the DTRM to a general curvilinear co-ordinates CFD code is clearly confirmed by the way in which the directions of ray tracing are simply represented using Cartesian co-ordinates in equation (3.12).

Having completely defined a ray vector, the distance traversed across successive control volumes is calculated using a sequence that minimises the distance between the point previously reached at the control volume, and the next intersected face. This is achieved by determination of the minimum perpendicular distance from the current point to planes containing other cell faces. Alternatively, path lengths can be evaluated by a process which identifies an intersected face by minimising the sum of triangular areas produced by joining each face vertex with the intersection point of the ray and the plane containing the face (cf. FLUENT, 1993). The disadvantage of this approach is that once an intersected face has been identified, a further calculation is required to obtain the path length. Malalasekera and James (1995) have assessed two further alternatives developed in the field of computer graphics.

One of the optimisation issues discussed in sub-section 3.2.4 concerns the possibility of launching rays in less restricted directions as demanded by a fixed directional discretisation relative to all faces. However, a single set of weightings derived from a pre-selected orientation and discretisation of the solid angle hemisphere, is computationally attractive due to the relatively small demand made on storage. For all the calculations presented in later chapters, a single weighting set is always pre-calculated and stored.

Since a complete mapping of the ray tracing web is established before a flow/heat transfer calculation commences, the solution algorithm only has to solve the RTE and its associated fluxes. Four embedded loops are required. The outermost loop controls iterations towards a converged solution. The next two loops step through all radiating faces and launch rays from each one. Finally, at the algorithm's heart, is the repeated solution to the RTE.

Coupling of the DTRM to a CFD calculation is established through the volumetric radiative source terms to the energy equation, and by the treatment of boundary fluxes. In common with general procedures of source term manipulation (cf. Patankar, 1980), Eq. (3.9) is re-expressed as

$$S_R = L_1 - L_2 T^3 T \tag{3.14}$$

where

$$L_1 = \sum_{all\ rays} w \Delta A \left[1 - exp(-kl)\right] i_{n-1} \tag{3.15a}$$

$$L_2 = \frac{\sigma}{\pi} \sum_{all\ rays} w \Delta A \left[1 - exp(-kl)\right] \tag{3.15b}$$

L_1 and L_2 are derived by extracting Δi from Eq. (3.5). The second term in Eq. (3.14) can now be expressed in terms of enthalpy and added to the centre

coefficient in the algebraic equation for enthalpy.

Radiative fluxes at boundary surfaces also couple to the energy equation, but in a way dependent on the type of boundary condition. Additionally, boundary temperatures are evaluated based upon a total balance between conductive, convective and radiative fluxes.

3.2.4 Optimisation of the DTRM

The issue of optimisation in the DTRM relates to the computational expediency of obtaining acceptable accuracy at low cpu cost. Unfortunately, it is not feasible in most engineering problems to use thousands of rays to yield ray number independent solutions. For example, Fairweather et al. (1992b) settled upon 1024 rays, but only in a post-processed calculation of the radiation received external to a turbulent jet in a cross flow. Generally, therefore, it is necessary to determine the minimum number of rays that can deliver a particular level of accuracy without incurring excessive expense. However, the quality of solution is dependent not only on the number of rays, but also the directions in which they are traced, the resolution of the grid and the intimate link between these parameters. If an acceptable number of rays are to cross all control volumes in a particular geometry, problem specific optimisation is required.

Originally, Lockwood and Shah (1981) did not report on an extensive assessment of the sensitivity of accurate prediction to grid and ray number resolution. Since then, various articles have alluded to the issue (cf. Carvalho et al., 1991), and some have presented comparisons (cf. Bressloff et al., 1995 and Meng et al., 1993), but none have provided general guidelines. This is not unexpected as accuracy is very problem specific. For example, Shah (1979) presented highly accurate predictions using 64 rays per boundary face in some relatively simple infinite cavity test cases. However, in the more challenging cavities used below for the comparisons of different weighting sets, 64 rays do not yield the same level of accuracy.

The problem of ray number selection is exacerbated by the fact that the

DTRM suffers from the "ray effect" (cf. Lathrop, 1968) - in which incomplete information may be received by a surface due to the inability of a finite number of rays to intersect all control volumes and all surfaces. Additionally, this becomes more prominent and problematic when scattering is included (Carvalho et al., 1991). The main optimisation issue confronted during the course of this work concerned the selection of ray directions in the hope of mitigating the "ray effect". Thus, discretisation of the solid angle hemisphere is considered in some detail below, and other optimisation possibilities are alluded to at the end of the section.

3.2.4.1 Alternative methods for discretising the solid angle hemisphere

The set of weighting coefficients in Eqs. (3.8) and (3.9) are functions of ray direction and the solid angles represented by each ray. They also depend upon the alignment of the axes (used to discretise the hemispherical solid angle) relative to a surface. Hence, the specification of ray directions completely determines a weighting set. A new weighting set has been derived which aims to mitigate the "ray effect" through a more uniform distribution of rays.

The conventional method of discretising the solid angle hemisphere is based upon the equal division of polar and azimuthal angles as shown in Fig. (3.1). Integration of the differential radiative flux,

$$dq_m = i_m \cos\theta_m d\Omega_m \tag{3.16}$$

for the elemental solid angle, $d\Omega_m$, yields

$$q_m = i_m \sin\theta_m \cos\theta_m \sin\Delta\theta_m \Delta\phi_m \tag{3.17}$$

where i_m is assumed constant in each solid angle. θ_m is the angle between

the m^{th} ray and the surface normal, and $\Delta\theta_m$ and $\Delta\phi_m$ specify the solid angle polygon. When the radiative recurrence relation, Eq. (3.5), is solved across all intersected cells from the hit surface back to the firing surface, the total incident flux is given by Eq. (3.8) with weightings determined from

$$w_m = \sin\theta_m \cos\theta_m \sin\Delta\theta_m \Delta\phi_m \tag{3.18}$$

Eq. (3.18) is such that, for constant $\Delta\theta$ and $\Delta\phi$, weightings are proportional to $\sin 2\theta$ producing a bias towards rays closest to $\theta = \pi/4$. Additionally, rays making a shallow angle to a surface have the same weighting as rays making the same angle with the surface normal. This is in contrast to what is expected from Eq. (3.16) since, if elemental solid angles are equal, the distribution of weightings is given by the cosine function which is single valued for $0 \leq \theta \leq \pi/2$.

A better representation of the elemental flux equation is obtained if a more even distribution of ray directions is established. There are a number of sophisticated grid generation techniques available to do this, such as Delaunay triangulation (cf. Delaunay, 1934). However, an important feature of the DTRM concerns the simplicity of the integral calculation for the incident flux from Eq. (3.16) which is based upon the use of local spherical co-ordinates. Cumber (1985) also recognised this characteristic in his development of alternative weighting sets based on numerical quadrature techniques applied to Shah's discretisation of the solid angle hemisphere. Cumber's principal weighting set was derived from a formula for numerical integration on an interval having assumed a bilinear distribution of the incident intensity evaluated at the corners of each hemispherical element. Although he demonstrated superior accuracy relative to that obtained using Eq. (3.18), Cumber presented results for very few different numbers of rays. A more thorough analysis should include comparisons across a range of ray numbers (cf. Bressloff et al., 1995).

The weighting set considered in greater detail here has been devised in an attempt to generate a more uniform distribution of ray directions whilst still working in spherical polar co-ordinates. It involves a realignment of the co-ordinate axes (in order to move the poles away from the surface normal), combined with a discretisation of the solid angle hemisphere which produces approximately equal areas. A schematic of this angular discretisation is shown in Fig. (3.2). The polar axis, $\hat{\theta}$, is now aligned with a planar base vector, $\hat{e}_1$, and the $\hat{\phi}$ axis is aligned with the normal base vector, $\hat{e}_2$. Consequently, the ray vector relative to a surface becomes

$$\vec{r}_{rel} = (cos\theta)\hat{e}_1 + (sin\theta cos\phi)\hat{e}_2 + (sin\theta sin\phi)\hat{e}_3 \tag{3.19}$$

Division of the hemispherical solid angle into equal areas is restricted by the requirement of fitting an integer number of areas into individual theta bands. (A theta band is defined as the surface area of the hemisphere contained between two values of θ for all values of ϕ). Therefore, each band comprises identical areas, but a slight variation in areas exists between bands. The number of theta bands described throughout the text are in addition to the polar areas. These areas are kept as complete solid angles since a slight improvement in performance is observed when they are not subdivided.

Since, in the original weighting set, the angle between a ray and the surface normal is equal to θ, the direction cosine in Eq. (3.16) is only dependent on θ. For the transformed axes, the direction cosine becomes dependent on both θ and ϕ, and is defined by

$$cos\delta = sin\theta cos\phi \tag{3.20}$$

Integration of Eq. (3.16) and summation for all rays then yields Eq. (3.8) with a weighting set given by

$$w_m = \sin(\Delta\phi_m/2)\cos\phi_m[\Delta\theta_m - \sin\Delta\theta_m\cos 2\theta_m] \quad (3.21)$$

One of the main criticisms of the original weighting set made by Bressloff et al. (1995) concerned the uncertainty associated with selecting the number of divisions in each polar direction. The new weighting set aims to overcome this problem by fixing the number of "theta bands" across ranges of ray numbers based upon extensive validation. Although further testing is still required, Table (3.1) shows preliminary recommendations for the number of "theta bands" for up to 128 rays. Another disadvantage of the original weighting set concerns the restriction imposed by having to divide each spherical direction into the mathematical factors of the total number of rays. The quasi-equal area weighting set is not restricted in this way.

In the analysis of turbulent jet flames presented in chapter 5, both methods of discretisation discussed so far were unable to generate rays which traversed control volumes close to the centre-line. Consequently, a third method of discretisation was employed as shown in Fig. (3.3). In this case, a ray is always launched perpendicular to solid surfaces, thus ensuring information is transmitted to and from the centre-line of a cylindrical polar grid. The remaining solid angle is then discretised by equal polar and azimuthal angles. The weighting for the normal ray is

$$w_m = \pi\sin(\Delta\phi_m)^2 \quad (3.22)$$

The weighting sets are now compared in four very different test cases, each having been selected, not only as a vehicle for the comparisons, but also to test various aspects of the discrete transfer radiation model. The specifications of the test cases are described first before presenting a general discussion of the comparisons, all of which are performed for 16, 32, 64 and 128 rays. Within the accompanying figures, ws1, ws2 and ws3

denote, respectively, the original weighting set, the quasi-equal area weighting set, and the discretisation which launches a ray perpendicular to a surface. For ws1 and ws3, the number of divisions in the θ and ϕ directions are 2x8, 4x8, 4x16 and 4x32.

3.2.4.2 Radiative flux to a side wall in an isothermal cavity

The first test case comprises a 10 cm square infinite cavity containing an isothermal gas. The black body intensity and the absorption coefficient of the gas are both equal to unity. All the walls are cold ($T_w = 0K$), the side walls have an emissivity of 0.5 and the top and bottom walls have an emissivity of 0.99 (cf. Fig. (3.4)). This problem specification represents one of the most challenging of the analytical solutions produced by Thynell and Lin (1989) due to the short optical lengths involved, and due to the discontinuities in wall emissivities at the corners. The net radiative flux at a side wall is shown for a half of its length in Fig. (3.5).

3.2.4.3 Radiative flux to the top wall of a cavity in radiative equilibrium

Whereas the Thynell and Lin test case comprises a distributed source of energy, the gas, analytical results are available (cf. Crosbie and Schrenker, 1984) for infinite cavities incorporating a localised source of energy. A 1 metre square infinite cavity (containing a gas in radiative equilibrium) has three of the four walls at 0K; therefore, the bottom wall, which has a black body intensity of unity, is the only source of energy. All the walls are black, and the gas is purely absorbing with an absorption coefficient of 0.25 (cf. Fig. (3.4)). This problem is additionally challenging since there are two discontinuities in the leaving intensities at the corners of the top and side walls. Also, unlike the previous test case, the temperature field has to be calculated. For a gas in radiative equilibrium the volumetric source terms must be zero. Therefore, from Eq. (3.14)

$$T = \left(\frac{L_1}{L_2}\right)^{0.25} \tag{3.23}$$

The heat flux to the top wall is the most difficult to calculate accurately due to the fact that it faces the two intensity discontinuities. It is expected, therefore, that this heat flux is very sensitive to the "ray effect". Fig. (3.6) shows the radiative flux to the top wall non-dimensionalised by the flux leaving the bottom wall.

3.2.4.4 Floor and ceiling fluxes in a three-dimensional rectangular furnace

Ultimately, optimum performance of DTRM is required in three-dimensional calculations. Therefore, it is appropriate to compare the weighting sets in post-processed calculations of available data.

The furnace model described by Hyde and Truelove (1977) is based upon an experimental 3MW natural gas fired furnace of the International Flame Research Foundation, IFRF, M3A (flame 10) trials. This has been regularly used for testing radiation models (cf. Carvalho et al. (1991)), comparisons being made against zone model results. All input data is shown in Fig. (3.7), and predictions are compared in Fig. (3.8) for the radiative flux to the floor and roof. The roof flux appears to be more sensitive to changes in the number of rays most probably because it faces the temperature and emissivity discontinuities at the floor corners.

3.2.4.5 Radiative source terms in an analytically solved three-dimensional furnace

Selcuk (1985) presented exact analytical solutions for the distribution of radiative wall fluxes and radiative energy source terms applied to a large-scale experimental tunnel type furnace. Typical of the conditions encountered in industrial furnaces, the temperature field is highly non-

uniform; its cross-sectional and axial variation is generated from non-dimensionalised expressions derived from experimental data.

This problem is particularly useful for validating the discrete transfer radiation model since the evaluation of volumetric source terms is assessed in a fully three-dimensional geometry with symmetry planes on two adjacent edges. Fig. (3.9) shows the dimensionless volumetric source term along nodes closest to the axis. In accordance with analytical results presented by Selcuk, a 24x2x2 grid has been used in 1/4 of the furnace.

3.2.4.6 Discussion of results

Four main conclusions can be drawn from the results presented in Figs. (3.5), (3.6), (3.8) and (3.9). First, all three weighting sets generally perform quite poorly for 16 rays. Surprisingly, the Selcuk furnace is an exception here in that very small errors are generated for all ray numbers across its whole length, including the initial steep temperature gradient region. Second, it is important not to be misled by good performance of a given weighting set for a particular number of rays. For example, in the infinite cavity test cases, the original weighting set (ws1) demonstrates negligible improvement in performance between 16 and 32 rays, and the new, quasi-equal angle weighting set (ws2) performs particularly well for 32 rays with inferior performance for 64 rays. Third, for 64 and 128 rays, greatest accuracy is obtained by ws3, the weighting set with a ray launched normal to a surface. Finally, the main aspects of the discrete transfer radiation model (i.e. the evaluation of boundary fluxes and volumetric source terms, and the incorporation of reflection at symmetry planes) have been successfully tested under widely varying conditions.

3.2.4.7 Further optimisation of the DTRM

A number of strategies for optimising the DTRM, in addition to those discussed in the previous sub-sections, have been identified as warranting further research. Their common purpose is to maximise accuracy whilst

minimising storage and cpu demands. The expectation is that "intelligent feedback" from a solution would drive the optimisation process.

The importance of radiation in combustion is well established. However, less certainty accompanies the priority which should be given to the radiation algorithm within a CFD combustion calculation. Assuming that a converged solution to a particular problem is attainable, optimum performance is achieved if radiative energy transfer is recalculated at a low frequency - relative to the CFD solver - early in a calculation, and then at an increasingly higher frequency as convergence proceeds. Even when a low number of rays are employed, the radiation routine can be more expensive than the complete CFD solver. Thus, it is too costly, and in most cases unnecessary, to adopt a high frequency at all times. However, if a low frequency is maintained for too long, large perturbations to the enthalpy field hinders the convergence rate. Similar features accompany the techniques of increasing the number of rays, and of moving to more accurate modelling of combustion environment properties as a solution proceeds. Presently, only general guidelines to these optimisation issues can be given. A detailed study would be necessary to develop an "intelligent solution controller" which could respond to all the nuances of convergence sensitivity.

A converged solution is not necessarily an accurate one. Therefore, it is also necessary to optimise accuracy, but without incurring excessive computational expense. Towards this end, optimisation of the distribution of rays was discussed above in relation to a strategy of launching the same number of rays from all boundary surfaces. Additionally, the same set of directions are applied relative to every surface. In some situations, the greatest improvement in accuracy will be attained by maximising the number of rays traversing each control volume. Such a coverage may be accomplished by adjustments to the CFD grid, or by varying the directions and numbers of rays launched from different locations. Alternatively, separate grids could be generated for the CFD and radiation algorithms,

and then, adapted as the solution proceeds. A further permutation would be to use the same grids, but to only launch rays from some boundary locations and interpolate the radiative flux between them. Optimising ray coverage by these various methods could, however, become significantly wasteful if detailed calculations were performed across regions of relative uniformity. Another enhancement to the overall procedure, which would also overcome this wastage, would be to "intelligently" adapt ray coverage. Then, fewer rays would traverse relatively uniform regions, and a greater density of rays could be directed towards regions of large fluxes and/or steep property gradients. Once again, ray adaptivity, possibly coupled to grid adaptivity, would require a detailed optimisation study.

It is expected that the development of so-called "intelligent" solution and ray coverage controllers would significantly enhance the discrete transfer radiation model maximising accuracy whilst minimising the demands of computational cost and storage.

3.3 RADIATIVE PROPERTIES OF THE PRODUCTS OF COMBUSTION

3.3.1 Introduction

The radiative properties of combustion systems are a complicated function of wavelength, temperature, pressure, composition and path length. Modelling of these dependencies demands three levels of delineation. First, a global model is required to describe the physics of radiation and how it links to the overall analysis of heat transfer and fluid dynamics. The discrete transfer radiation model is the basis of the present study. Within a particular model, solution of the radiative transfer equation can then be addressed in a number of ways. Finally, a method is required to represent the radiative properties of the participating media. The analysis is further complicated by the different representations of solid-gas and gas-gas

radiation. The discussion of the DTRM, thus far, has grossly oversimplified the solution of the RTE and the representation of radiative properties. Due to the intimate link between radiation and the formation of combustion products, especially soot, it is important to employ comparable levels of sophistication in the respective sub-models. Therefore, it is appropriate to here consider the principal radiative property models (and solution methods in section (3.4)) which can be used in the DTRM. Although the various approaches are described for application in the DTRM, they are also relevant to other radiation models.

Generally, radiation in combustion media is dominated by carbon-dioxide, water vapour and soot. Therefore, contributions from other components are neglected in the present context. The radiative properties of molecular gases are described first followed by those of soot and gas-soot mixtures.

3.3.2 Radiative Properties of Combustion Gases

The emission and absorption of radiation by molecular gases is strongly dependent on wavelength. Therefore, a hierarchy of gas property models can be described based upon the level of spectral resolution employed. At the highest end of this hierarchy are line-by-line models (cf. Taine, 1983) which use high-resolution spectroscopic data to generate integrated line intensities and spectral absorptivities. Despite their high accuracy, calculation times are prohibitive for engineering problems making line-by-line models unsuitable for the present study. However, the data generated by line-by-line models is used, together with experimental data, to calculate mean band parameters for narrow and wide band models. Of the various narrow band models, the Single Line Group (SLG) method due to Ludwig et al (1973) is used here as the basis for comparisons. Whereas narrow band models typically divide the spectrum into 25 cm^{-1} intervals, wide band models require over an order of magnitude fewer divisions (Edwards, 1976).

Many other gas property models do not explicitly treat the spectral variation of absorptivity since they employ curve-fitting strategies to experimentally measured or spectrally calculated total properties. Of these, the weighted sum of gray gases model (Hottel and Sarofim, 1967) is especially useful since it links the physical realism of Beer's law with the simplicity of the gray gas approximation. Other curve-fitting models - also known as total absorptivity-emissivity models - include those due to Modak (1979) and Leckner (1972). Curve-fits to mean absorption coefficient data have also been made by Hubbard and Tien (1978).

The single gray gas approximation, which assumes a constant absorption coefficient across an inhomogeneous path, is at the lowest end of the hierarchy.

3.3.2.1 Narrow band models

Narrow band models describe the spectral variation of radiative properties by assuming that the distribution of lines, their shape and their intensity can be represented mathematically. According to these representations, the mean transmissivity within a band can be calculated. The Goody statistical model assumes that lines within a band are randomly located. If line strengths and widths are assumed to be equal, the mean band transmissivity for the interval, $\Delta\nu$, is given by

$$\bar{\tau}_{\Delta\nu} = exp\left[-(S/d)X\left[1+(S/d)(X/BP_e)\right]^{-1/2}\right] \tag{3.24}$$

for a given partial-pressure path-length product, X; where (S/d) represents the mean line-intensity to spacing ratio, B is π times the mean line-width to spacing ratio, and BP_e denotes the line broadening pressure correction factor. The parameter (S/d) is the effective absorption-emission coefficient for small pressure-path-lengths, whilst BP_e describes the effects of line

saturation at larger pressure-path-lengths. Grosshandler (1980) adopted this formulation, along with data from Ludwig et al. (1973), and established good agreement with measurement for the principal emitting regions of CO_2 and H_2O. For a single homogeneous element, the band transmissivity is evaluated as the product of transmissivities for all species. Band transmissivities for non-uniform paths are calculated by using an equivalent homogeneous, isothermal path. This is achieved through the calculation of mean thermodynamic properties for the path, or by evaluating scaled band parameters using, for example, Curtis-Godson scaling which is discussed by Siegel and Howell (1992). The complete approach is contained in the computer code, RADCAL (cf. Grosshandler, 1980), which is widely used as a basis for comparing property models and solution algorithms. Indeed, a version of RADCAL is employed as the basis for comparisons below. Further details of narrow band solutions to the RTE are given in section (3.4.4). Other narrow band models are described by Soufiani et al. (1985).

Once all banded transmissivities are known, the total transmissivity can be obtained from

$$\tau^T = \int_0^\infty i_b(T,\nu)\bar{\tau}_{\Delta\nu}\,d\nu \Big/ \int_0^\infty i_b(T,\nu)\,d\nu \tag{3.25}$$

Leckner (1972) used narrow band data along with experimental information to generate total emissivity charts to which polynomial curve-fits were made in terms of temperature and pressure-path length products.

Narrow band gas property data has not been widely used in coupled flow heat transfer prediction due to the considerable computing time required to evaluate the transmissivities of hundreds of individual bands across numerous paths. Soufiani and Taine (1985) performed a fairly limited study of a laminar gas flow of H_2O-air mixtures between parallel

walls at fixed temperatures. In comparing narrow and wide band models, they only observed significant discrepancies at intermediate optical thickness'. The more detailed analysis of a turbulent flame in a cross-flow by Fairweather et al. (1992b) evaluated the radiative emission from the flame in a single post-processed calculation.

3.3.2.2 Wide band models

In contrast to narrow band models of gaseous emission, wide band models recognise the way in which individual lines tend to occur in groups. For example, CO_2 has large concentrations of lines approximately centred at 4.3 and 2.7 microns. The strongest grouping of lines for H_2O are found at about 2.7 microns. So, whereas narrow band models require representation of hundreds of bands, wide band models typically include only 11 bands for CO_2-H_2O mixtures (Edwards, 1976). The reduction in number of bands between the models represents a considerable time saving, especially in a DTRM calculation across non-uniform paths. However, wide band models should include corrections for overlapping bands.

Formulation of the radiative properties of individual wide bands is generally based upon an absorptance defined as

$$A_{i,j} = \int_{\Delta\nu} \left[1 - \tau_{\nu,i,j}\right] d\nu \tag{3.26}$$

for the j^{th} band of species i. It is necessary to incorporate an expression such as Eq. (3.24) for the transmissivity, and then to facilitate integration across the band by prescribing how the shapes of lines vary with wave number. The most popular wide band model is that due to Edwards and Menard (1964) - and extended by Edwards and Balakrishnan (1973). The exponential wide band model, as it is known, adopts the Goody statistical model, and assumes that the mean intensity-to-line-spacing ratio can be described by an exponential function of wave number which is dependent

upon the location of the band, and parameters describing the overall shape of the exponential function across the band.

Once band absorptances have been evaluated, either by approximate correlations, or by closed form expressions (cf. Tien and Lee, 1982), they can be used in a variety of ways. Apart from facilitating various solutions to the RTE as discussed in the next chapter, the exponential wide band model has been used by Felske and Tien (1973) to evaluate the total emissivity of luminous flames, by Buckius and Tien (1977) to assess the predictive capability across arrays of flames, by Modak (1979) to generate curve-fits to total emissivity data, and by Komornicki and Tomeczek (1992) who attempted to improve the evaluation of band absorptivities. Reported usage of wide band models in coupled flow heat transfer calculation is scarce, although Carvalho (1995) recommended the exponential wide band model for calculating total radiative properties on a cell by cell basis.

3.3.2.3 Weighted sum of gray gases models

Weighted sum of gray gases models comprise curve-fits - normally to total emissivity data - assuming the real gas to be composed of a number of gray gases with windows in the spectrum represented by a single clear gas. Total emissivity is defined by

$$\varepsilon^T = \sum_{j=0}^{J} a_j(T)\left[1-e^{-k_j pL}\right] \tag{3.27}$$

where the absorption coefficients, k_j, are assumed to be independent of temperature and the temperature dependence is carried by polynomial weighting factors, $a_j(T)$. Values have been generated for absorption and polynomial coefficients by many authors. The exponential wide band model has been the most popular method by which total data has been generated (cf. Taylor and Foster, 1974, Smith et al. 1982, Felske and

Charalampopolous, 1982, and Modest, 1991), although experimental data was originally used by Hottel and Sarofim (1967), and other authors have used narrow band data (cf. Truelove, 1975, and Soufiani and Djavdan, 1994). A new approach has recently been developed by Denison and Webb (1995) based on spectral line data in lieu of total emissivity data. They have derived mathematical correlations to so-called black body distribution functions for CO_2 and H_2O, from which the weights and absorption coefficients can be determined. Thus, although the method is more computationally expensive than others, it can be applied to any number of gray gas components.

Truelove's coefficients (1975) are adopted in the present analysis because they are derived from the narrow band Ludwig data, and since coefficients are included for gas-soot mixtures. They are tabulated for the following conditions :

$$\begin{aligned} 600 \le T \le 2400 \quad & K \\ 0.01 \le l \le 10.0 \quad & m \end{aligned} \tag{3.28}$$

The weighting coefficients, $a_j(T)$, are linear functions of temperature.

The weighted sum of gray gases model is really a sub-set of the group of models which employ curve-fits to total radiative property data. However, it is widely recognised as a distinct gas property model in its own right.

3.3.2.4 Total absorptivity-emissivity curve-fit models

Generally, total property models involve curve-fits to data derived experimentally or by spectrally resolved calculation. Historically, they have been designed to calculate radiative properties for homogeneous, isothermal media. However, they can be applied to non-uniform media using differential total property solutions or equivalent homogeneous path

approximations. The two principal curve-fitting strategies for mixtures of CO_2 and H_2O were derived by Leckner (1972) and Modak (1979). Both methods employ polynomial curve-fits in terms of temperature and pressure-path length products. Although Leckner's model involves fewer coefficients than Modak's, the latter is used in the comparisons presented below since it was established for gas-soot mixtures as well as gases alone, and because it was more thoroughly assessed, especially for mixtures of CO_2 and H_2O. Modak's model applied Chebyshev polynomial curve-fits to wide band total emissivity data, and was validated for the following range of gas parameters :

$$\begin{aligned} &300 \le T \le 2000\ K \\ &0.0011 \le p \le 1.0\ atm \\ &0.0011 \le pl \le 5.989\ atm\,m \end{aligned} \tag{3.29}$$

3.3.2.5 Mean absorption coefficients

An alternative method for evaluating total radiative properties is provided by defining a mean absorption coefficient, $\bar{k}$, from which the total transmissivity is given by $\tau^T = exp(-\bar{k}L)$. Mean absorption coefficients are then defined by

$$\bar{k} = \int_0^\infty F(\nu)\,k_\nu\,d\nu \Big/ \int_0^\infty F(\nu)\,d\nu \tag{3.30}$$

where $F(\nu)$ denotes a function of wave number such as the black body intensity, or a derivative of black body intensity with respect to temperature or transmissivity, or a product of transmissivity and black body intensity. More details concerning mean absorption coefficients are provided by Viskanta and Menguc (1987) and Traugott (1968). In practical terms of application to the repeated solution of the RTE, these mean coefficients

should be evaluated by narrow band data, making them computationally too expensive to calculate. However, Hubbard and Tien (1978) have generated curve-fits to Planck and Rosseland mean coefficients for mixtures of CO_2, H_2O and soot.

3.3.2.6 Empirically-based models

The final class of gas property models to be described here are those based upon empirically-based expressions for absorption coefficients or total radiative properties. Lefevre (1984) provides a lucid account of correlations for the total emissivity of luminous and non-luminous flames formulated to predict the output from flames in combustors. Such expressions possess considerable merit due to their simplicity, but are not intended for line of sight solutions to the RTE. More suitable in this respect is the correlation used by Fletcher et al. (1994) for a gas phase absorption coefficient,

$$k = 0.32 + 0.28\,exp\left(-T/1135\right) \tag{3.31}$$

derived by Gibb and Joyner (1978) using data from combustors.

3.3.3 Radiative Properties of Soot

In common with molecular gases, the attenuation of radiation by soot is known to obey Bouger's law (Siegel and Howell, 1992). The analysis presented here is simplified by neglecting scattering. This is justified from the Mie theory for many combustion environments in which the size parameter, $\pi D/\lambda$, where D is the particle diameter, is small. Despite this simplification, it is still necessary to model the absorption coefficient. Generally, the radiative properties of soot are represented in a comparatively simple manner. Many experimentally determined empirical relations reveal that the absorption coefficient of soot is directly proportional to soot volume fraction, Φ, and that an inverse relation exists

between the absorption coefficient and wavelength. These relationships are summarised by

$$k = c_0 \Phi \lambda^{-\alpha} \tag{3.32}$$

where, for a particular fuel, α is represented by a mean value, by a logarithmic function of wavelength, or by a polynomial function of wavelength. A detailed description of these dependencies is given by Siegel and Howell (1992). The dimensionless constant, c_0, is determined from the optical properties of soot,

$$c_0 = 36\pi nx \Big/ \left((n^2 - x^2 + 2)^2 + 4n^2 x^2 \right) \tag{3.33}$$

where n and x are the refractive index and extinction coefficient, respectively. For a given field of soot volume fraction, the solution of the RTE for soot is significantly simplified if α is assumed to be a constant value equal to unity so that

$$k = c_0 \Phi \nu \tag{3.34}$$

where the wave length has been replaced by the wave number. Further simplification is engendered if both the refractive index and the extinction coefficient are assumed to be weak functions of wavelength. (Typically, c_0 is assigned a constant value of *7.0* which lies in the middle of the reported range (cf. de Ris, 1979)). These assumptions are not unreasonable for soot particles that are small relative to the wavelength of radiation (cf. Grosshandler and Modak, 1981). Additionally, scattering can be neglected in media containing relatively small particles. Thus, unlike the line structure and consequent banded representation of gaseous radiative

properties, soot radiation is represented by a continuous spectrum throughout the visible and infrared. It is the visible radiation from soot particles which contribute to the luminosity of flames.

3.3.3.1 Exact total property model

The methods described above for evaluating the total properties of gases are all approximate. Of these, only the narrow band model and the weighted sum of gray gases model can be simply extended to include soot (cf. sub-section 3.3.4). For soot alone, it is possible to derive an exact expression within the limits associated with Eq. (3.34). When this equation, and the spectral black body intensity,

$$i_b(T,\nu) = \frac{2C_1\nu^5}{exp\left(C_2\nu/T\right)-1} \tag{3.35}$$

are substituted into

$$\tau^T = \int_0^\infty i_b(T,\nu)exp(-kL)d\nu \Big/ \int_0^\infty i_b(T,\nu)d\nu \tag{3.36}$$

the total transmissivity of soot across a path from s' to s is

$$\tau^T(s' \rightarrow s) = \frac{15}{\pi^4}\Psi^{(3)}\left(1+\frac{c_0T(s')}{C_2}\int_{s'}^{s}\Phi(s'')ds''\right) \tag{3.37}$$

The penta-gamma function, $\Psi^{(3)}$ is evaluated by the poly-gamma series expansion,

$$\Psi^n(z) \;=\; (-1)^{n+1} n! \sum_{k=0}^{\infty} (z+k)^{-n-1} \tag{3.38}$$

from Abramowitz and Stegun (1968).

Alternatively, if $exp\left(C_2 \nu / T\right) >> 1$ in Eq. (3.35), Wien's treatment of the black body intensity yields

$$\tau^T(s' \rightarrow s) \;=\; \left[1 + c_0 \overline{\Phi} L T(s') / C_2\right]^{-4} \tag{3.39}$$

as an approximation to Eq. (3.37). The mean value of soot volume fraction is evaluated from s' to s.

3.3.3.2 Mean absorption coefficients

Other authors have simplified the absorptivity further by assuming soot radiation to be gray (cf. Yuen and Tien, 1976). The dependence on temperature and soot distribution is then represented by an effective absorption coefficient such that

$$\tau^T(s' \rightarrow s) \;=\; exp\left[-C c_0 \overline{\Phi} L T(s') / C_2\right] \tag{3.40}$$

Suitable values for the constant C are obtained by substituting Eq. (3.34) into expressions for a mean absorption coefficient. The Rosseland mean in the optically thick limit yields a value of *3.6*. Yuen and Tien (1976) recommended this value in evaluating the total emissivity from a range of luminous flames. More recently, Kent and Honnery (1990) adopted the Planck mean absorption coefficient in the optically thin limit ($C = 3.827$) in the analysis of a laminar ethylene flame, but Fletcher et al. (1994) used a considerably lower value of *2.6*. Tien and Lee (1982) suggested that a mean

value of $C = 3.72$ best represented the entire range of optical thickness'.

3.3.4 Radiative Properties of Gas-Soot Mixtures

It is tempting to view radiation from gas-soot mixtures as a continuum due to soot onto which is superimposed a number of spikes due to the line/band structure of gaseous emission. However, for non-uniform gas-soot mixtures, it is not possible to simply add separate component emissivities, or to superimpose banded gas radiance onto the continuous spectrum due to soot. Grosshandler and Modak (1981) neatly demonstrated the way in which, for certain configurations of temperature and gas species and soot concentrations, increasing the soot loading reduced radiance from particular regions of the spectrum. Such features result from the presence of strongly absorbing gaseous bands at relatively low temperatures (i.e. the cool edges of the gas cloud act as a radiation shield, absorbing energy emitted by the soot). Thus, whereas the spectral radiance closely resembled the black body curve at high wave numbers, it contained significant inverted spikes in the regions of the strong gaseous bands.

Methods for evaluating the radiative properties of gas-soot mixtures have generally been developed as extensions to models originally devised for gases alone. Narrow band models simply incorporate soot as a separate component in the evaluation of banded transmissivities. The soot transmissivity is evaluated using Eq. (3.34) for the absorption coefficient at the centre of the band. Incorporation of soot into wide band models is less straightforward, since soot properties cannot be simply included in expressions for banded absorptances. It is necessary to follow a strategy described by Felske and Tien (1973) which requires a mean soot transmissivity for each band, and is further complicated by the need to account for the combined overlap of gaseous bands and soot. Application of this approach is considered further in the next chapter.

Weighted sum of gray gases models are more easily extended to gas-soot mixtures. The most straightforward representation, exemplified by

Truelove (1975), manipulates the coefficients for soot and gases alone into a single expression of the form

$$\varepsilon^T = \sum_{n,n'} a_{m,n,n'}(T)\left\{1-exp\left[-k_{g,n}\left[p_h+p_c\right]-k_{p,n'}\rho_p\Phi\right]L\right\} \tag{3.41}$$

which incorporates eight components. Values for these coefficients are tabulated in Table (3.2) for a partial pressure ratio of CO_2 to H_2O equal to 0.5. The subscripts n and n' signify individual soot and gaseous components, and the temperature polynomial coefficients are such that Eq. (3.41) reduces to the soot free and soot dominant limits. Henceforth, each pair of these values is represented by a single value, j, and the subscript m, denoting a mixture of soot and gas, is discarded. Other sets of coefficients have been generated by Felske and Charalampopoulos (1982) and by Modest (1991).

Finally, if mean absorption coefficients are required for gas-soot mixtures, they can be obtained by essentially summing up the individual contributions (cf. Tien and Lee, 1982).

Further consideration of the radiative properties of gas-soot mixtures is presented in the next chapter which analyses differential total property solutions to the radiative transfer equation. Before that, section (3.4) below provides an assessment of solutions to the RTE commonly used in the DTRM.

3.4 SOLUTIONS TO THE RADIATIVE TRANSFER EQUATION

3.4.1 Introduction

The main objective in this section is to establish the most suitable radiation algorithm which, constrained by current computing capabilities, is able to

yield acceptable accuracy without incurring excessive computational expense in a flow field calculation that continuously updates the radiative field. The question of accuracy acquires profound significance in the coupling between radiation and soot formation, and in other highly non-linear relationships. This is because a relatively small error in temperature predicted from local levels of radiative exchange, perhaps acceptable *de facto*, may generate considerable errors in soot yield and radiative flux. Thus, whereas, previously, it may have been appropriate to adopt simplified treatment of radiative properties in solution of the RTE, the sensitivity of other more sophisticated sub-models demands greater sophistication from the radiation algorithm. These considerations govern the emphasis of the analysis presented below, which culminates in a recommendation for a weighted sum of gray gases (WSGG) solution to the RTE incorporating a summation of separate solutions for each gray gas, primarily at the expense of the approach which solves a single RTE having evaluated absorption coefficients from local properties on a cell-by-cell basis.

A number of methods for solving the RTE, including various property models, have been reviewed by Tien and Lee (1982). They considered luminous and non-luminous radiation from both homogeneous and non-homogeneous paths. However, their treatment was primarily directed at the prediction of total flame emissivity with little consideration of coupled flow-radiation calculations. A more extensive review of radiation heat transfer was provided by Viskanta and Menguc (1987). They included a survey of global radiation models, and described some comparisons between them. Nonetheless, there are no references to detailed analyses of modelling techniques within a particular global model.

More recently, some comparisons have been made for the discrete ordinates radiation model. Kim et al. (1991) have shown that the computational time savings offered by gray-band solutions, relative to both narrow and wide band solutions, is accompanied by a considerable loss in accuracy in the internal fluxes and radiative source distributions across

inhomogeneous slabs between black walls. Song (1993) compared the wide band results from Kim et al. (1991) with an analytically based weighted sum of gray gases solution, and a gray gas solution. The WSGG solution was shown to accurately model the non-gray layers considered. Both of these studies only analysed layers between black walls. Liu and Tiwari (1994) also used the profiles from Kim et al. (1991) in a Monte Carlo calculation using a narrow band gas property model. Gray and black walls were considered, and the Monte Carlo method was found to be considerably faster than the discrete-ordinates model.

For the DTRM, Docherty and Fairweather (1988) compared solutions using exponential wide band and statistical narrow band data, but only for individual lines of sight. Generally, the DTRM has been applied in coupled CFD-heat transfer calculations by employing a total property solution typified by Lockwood and Malalasekera (1988) and Fletcher et al. (1994), and assessed below. Alternatively, data from flow field simulations have been post-processed as described by Fairweather et al. (1992b) and Soufiani and Djavdan (1994). The latter study is especially pertinent since the flow field solution obtained using a gray DTRM was then used to compare narrow band and weighted sum of gray gases model calculations of surface and volumetric flux. Good agreement was observed for the case of a hot medium surrounded by relatively cold walls.

3.4.2 Constant Absorption Coefficient (CAC) Solutions

The simplest solution to the RTE, and, therefore, the fastest computationally, is the constant absorption coefficient solution given by Eq. (3.6). Other than under uniform conditions, the use of a constant absorption coefficient throughout a domain can generate unacceptable errors particularly if the most appropriate value is not employed. Often, a reasoned "guess" has to be made. It is also possible to use a number of absorption coefficients on a zone basis as performed by Haidekker et al. (1994) in applying the DTRM to the prediction of wall heat fluxes in a

modelled aluminium remelting furnace. Values of 0.1 and 0.5 m^{-1}, respectively, were used in the bulk of the gas and in the combustion zones.

Paradoxically, as will be demonstrated below, it is possible to generate superior accuracy from the constant absorption coefficient (CAC) gray gas approximation relative to the total property solution now to be described.

3.4.3 Total Property (TP) Solutions

During the course of this analysis, a number of techniques have been investigated which assume a constant absorption coefficient can be applied across individual paths. One possibility is to replace every set of downstream cells by equivalent uniform paths such that emission from each cell in a path then traverses a single uniform layer. Alternatively, the intensity at the end of a line of sight can be approximated by emission from a single homogeneous layer, combined with the transmission of initial intensity across that path. Unfortunately, these techniques did not yield satisfactory accuracy.

Another approach, here entitled the total property (TP) solution to the RTE, applies Eq. (3.6) across all elements in a path. Consequently, the absorption coefficient (or transmissivity) has to evaluated for each element. Any of the radiative property models can be used to do this. For the purpose of the comparisons presented in sub-section 3.4.6, TP calculations are performed using both weighted sum of gray gases and narrow band models. The same property models are also used in weighted sum of gray gases (WSGG) and differential banded transmissivity (DBT) solutions to the RTE. The WSGG solution is ultimately recommended for application in the DTRM, and the DBT solution provides a benchmark for comparisons. Implementation into the DTRM of both methodologies is described in the following sub-sections.

3.4.4 The Weighted Sum of Gray Gases (WSGG) Solution

The weighted sum of gray gases property model was originally devised

to simply represent the total emissivity of combustion gases (cf. Hottel and Sarofim, 1967). However, the model can also be applied in a line of sight solution to the RTE if Eq. (3.6) is solved for each gray gas, with the black body intensity pre-multiplied by the corresponding weighting coefficients (cf. Modest, 1991). Thus, for the j^{th} gray gas

$$i_{j,n} = i_{0,j}\prod_{r=1}^{n}\tau_{j,r} + \sum_{r=1}^{n}\left[a_j i_{b,r}\varepsilon_{j,r}\prod_{r'=r+1}^{n}\tau_{j,r'}\right] \tag{3.42}$$

where transmissivities, $\tau_{j,r}$, emissivities, $\varepsilon_{j,r}$, and the black body intensity, $i_{b,r}$, are evaluated using mean properties across individual paths, assumed constant for each control volume. The total intensity, i_n, is then a summation of that contributed by each gray gas. For black boundaries, the emitted radiation, $i_{0,j}$, is given by the black body intensity multiplied by the a_j coefficient, both evaluated at the boundary temperature (cf. Modest, 1991). Johnson and Beer (1973) applied Eq. (3.42) to measured line of sight profiles of temperature, gas and soot concentrations in a furnace. Predictions from the WSGG solution closely matched the radiative intensity measured by a narrow-angle probe, progressively withdrawn through the flame, and sighted on a target having a known leaving intensity. Such line of sight calculations are useful for assessing the accuracy of different algorithms in preparation for their use in a global radiation model.

In the DTRM, with black boundaries, it is a fairly straightforward procedure to apply Eq. (3.42) along each ray. However, when boundaries are gray, separate expressions are required for the incident radiation of each gray gas, so that the reflected radiation in the individual transfer equations results solely from irradiation due to the same component. Therefore, at every surface, for each gray gas, the incident intensity must be

summed across all rays. Thus, the initial intensity of the j^{th} gray gas is

$$i_{0,j} = \left[a_j(T_0)\varepsilon_0\sigma T_0^4 + [1-\varepsilon_0]\sum_{m=1}^{M} w_m i_{m,j} \right] \Big/ \pi \tag{3.43}$$

where the summation represents the total incident flux for the j^{th} gas. From Eq. (3.8), the total irradiation of a surface element is now

$$q^- = \sum_{j=1}^{J}\sum_{m=1}^{M} w_m i_{m,j} \tag{3.44}$$

and the total radiosity from a surface is the same expression as for a single gray gas, since the a_j coefficients in Eq. (3.43) sum to unity.

When source term linearisation is employed, Eq. (3.14) applies with

$$L_1 = \sum_{all\ rays} w\Delta A \sum_{j=1}^{J}\left[1-e^{-k_j l}\right] i_{n-1} \tag{3.45a}$$

$$L_2 = \frac{\sigma}{\pi}\sum_{all\ rays} w\Delta A \sum_{j=1}^{J} a_j(T_{local})\left[1-e^{-k_j l}\right] \tag{3.45b}$$

3.4.5 The Differential Banded Transmissivity (DBT) solution

When Eq. (3.6) is written for a particular wave number, the spectrally correlated intensity across a band-width $\Delta\nu$ is

$$i_\nu^c = \frac{1}{\Delta\nu}\int_{\nu-\frac{\Delta\nu}{2}}^{\nu+\frac{\Delta\nu}{2}} \left\{ i_\nu(0)\prod_{r=1}^{n}\tau_{\nu,r} + \sum_{r=1}^{n}\left[i_{b,\nu,r}\varepsilon_{\nu,r}\prod_{r'=r+1}^{n}\tau_{\nu,r'} \right] \right\} d\nu \tag{3.46}$$

The correlation between emission and absorption is such that the history of every line emission must be traced. Downstream volumes in a path may or may not absorb energy from particular lines, and further emission may overlap other lines completely, partially or not at all. Clearly, the high resolution structure of the spectrum prohibits a complete representation of the correlation between intensity and absorptivity for engineering calculations. However, Taine (1983) demonstrated poor performance of a non-correlated solution

$$i_n = \sum_{j=1}^{J}\left[i_{0,j}\prod_{r=1}^{n}\bar{\tau}_{j,r} + \sum_{r=1}^{n}\left[\bar{i}_{b,j,r}\bar{\varepsilon}_{j,r}\prod_{r'=r+1}^{n}\bar{\tau}_{j,r'} \right]\Delta\nu \right] \tag{3.47}$$

where the strength, shape and distribution of individual lines was modelled by band descriptions of the spectrum, and mean values of intensity and transmissivity were used for each band.

The previous two algorithms focus on the recurrence interpretation of the RTE. If, however, the differential transmissivity in Eq. (3.4) is expanded, for each spectral band, as a finite difference at all upstream locations, the intensity becomes

$$i_n = \sum_{j=1}^{J}\left[i_{0,j}\bar{\tau}_{0\to n,j} + \sum_{r=1}^{n}\bar{i}_b\left(T_s,\nu_j\right)\left[\bar{\tau}_{r\to n,j} - \bar{\tau}_{r-1\to n,j}\right]\Delta\nu_j \right] \tag{3.48}$$

For combustion gases, it has been shown that division of the spectrum into 5-25 cm^{-1} wave number intervals can facilitate the use of narrow band data in banded solutions to the RTE (cf. Grosshandler, 1980). Thus, mean band transmissivities are evaluated from a narrow band gas property model. The transmissivity difference across an upstream cell is evaluated across paths from the leading and trailing edges of that cell. In Eq. (3.48),

and subsequently, $\phi_{a\to b}$ denotes the value of a property, ϕ, across a path where a and b signify the initial and final points in the path, respectively. The spectral black body intensity

$$\bar{i}_b\left(T_s,\nu_j\right) = \frac{2C_1\nu_j^5}{e^{C_2\nu_j/T_s}-1} \tag{3.49}$$

is evaluated at the centre of a band and midway between each path origin. C_1 and C_2 represent Planck's first and second constants, respectively.

Non-uniformities can be treated by either scaling the band parameters used to calculate the transmissivity, or by evaluating mean thermodynamic properties for an equivalent homogeneous, isothermal path. The transmissivity for bands comprising more than one species is calculated as the product of the individual species transmissivities. Henceforth, Eq. (3.48) and the accompanying description is entitled the differential banded transmissivity (DBT) solution to the RTE.

The initial intensity, $i_{0,j}$, is treated in a similar way to that for the WSGG solution. For the j^{th} band it is

$$i_{0,j} = \varepsilon_0\bar{i}_b\left(T_0,\nu_j\right)\Delta\nu_j + \frac{\left[1-\varepsilon_0\right]}{\pi}\sum_{m=1}^{M}w_m i_{m,j} \tag{3.50}$$

where the summation represents the total incident radiation within the band for all rays. Since solid wall radiation is treated as gray, account must be taken of the wings of the spectrum outside which the medium radiation is assumed to be negligible. This is accomplished by treating the wings as a separate band and applying Eq. (3.50) with the first term replaced by

$$\varepsilon_0\left[\frac{\sigma T_0^4}{\pi}-\sum_{j=1}^{J}\bar{i}_b\left(T_0,\nu_j\right)\Delta\nu_j\right] \tag{3.51}$$

The nature of the differential solution, does not permit the change in intensity across individual elements to be expressed in a manner which lends itself to source term linearisation. Therefore, for the DBT solution, and all other differential solutions, source terms are evaluated directly by Eq. (3.9).

3.4.6 Comparison of Solutions to the RTE

The following analysis principally compares the WSGG and TP solutions to the RTE. All comparisons are made relative to the differential banded solution employing the statistical narrow band model due to Ludwig et al. (1973) as implemented in RADCAL. Additional information is provided by appropriate constant absorption coefficient solutions. Initially, comparisons are made for single line of sight calculations across uniform and non-uniform mixtures. The more realistic combustion configurations are then analysed in a full DTRM calculation between solid walls.

3.4.6.1 Radiative intensity variation across uniform mixtures

The variation of radiative intensity across a selection of gas-soot mixtures is depicted in Fig. (3.10). In all cases,

$$T=1000\,K;\quad p_h=2\,p_c=0.16;\quad L=1.0\,m$$

and the soot volume fraction takes the values $0.0;\ 1.0e-7;\ 1.0e-6;\ 1.0e-5$.

Radiation calculations across uniform layers provide a useful means for assessing the correctness of different algorithms since the predictions should be independent of the number of elements in a path. The DBT and WSGG predictions shown in Fig. (3.10) for twenty elements are both

replicated by separate calculations across single paths for each corresponding distance. The CAC solutions are included to demonstrate the increasingly gray character of the DBT and WSGG solutions produced by raising the soot concentration. In the absence of soot, no absorption coefficient produces a satisfactory representation of gaseous radiation.

The TP solutions performed using weighted sum of gray gases and narrow band property models also agree very closely with each other. However, both of them produce increasing differences (with reduced soot loading) relative to the banded/component solutions.

Application of the TP solution to uniform paths generates equal cell-based absorption coefficients, and is therefore akin to a CAC solution, but with the absorption coefficient evaluated from local properties. Hence, radiation is treated as gray. The corresponding absorption coefficients for the TP solutions are approximately 1.4, 1.6, 3.2 and 15.7. However, molecular gases are non-gray, due to the distribution of absorption and emission lines of widely varying strengths and shapes which produce preferential self-absorption across the spectrum. Consequently, overall absorption across a path is likely to be under-estimated, as high absorptivity in particular regions of the spectrum is averaged across the whole spectrum. This characteristic can be demonstrated by considering the emitted intensity along a line of sight across a uniform path for two arbitrary bands (a and b) having different strengths (e_a, e_b), widths ($\Delta\nu_a$, $\Delta\nu_b$) and transmissivities (τ_a, τ_b). The intensity across two equal path lengths evaluated by separate treatment of each band is given by

$$i_{banded} = \left[e_a\left(1-\tau_a^2\right)+e_b\left(1-\tau_b^2\right)\right] \tag{3.52}$$

where e_a and e_b are the respective products of band strength and width. If, instead, a total transmissivity is defined as

$$\tau^T = (\tau_a e_a + \tau_b e_b)/(e_a + e_b) \tag{3.53}$$

the intensity becomes

$$i_{total} = (e_a + e_b)\left(1-\left(\tau^T\right)^2\right) \tag{3.54}$$

Simple algebraic manipulation then leads to

$$i_{total} - i_{banded} = e_a e_b (\tau_a - \tau_b)^2/(e_a + e_b) \tag{3.55}$$

such that $i_{total} \geq i_{banded}$. Thus, unless $\tau_a = \tau_b$, the use of total properties over-predicts intensity for the two bands emitting (and absorbing) across two identical path lengths. The same conclusion naturally follows for the entire spectrum since the same reasoning can be applied to an ensemble of band pairs. Despite this indictment of the total property solution, it has been commonly employed in the DTRM with total properties evaluated from the weighted sum of gray gases property model (cf. Lockwood and Malalasekera, 1988, and Carvalho and Coelho, 1989), or from curve fitting strategies such as those due to Modak (1979). Equally, any of the other property models reviewed above can be used to evaluate total properties.

Fig. (3.10) demonstrates the improvement in accuracy of the TP solution to gas-soot mixtures as the soot loading is increased. Markstein (1974) has demonstrated that the single gray gas approximation becomes an increasingly good approximation of soot radiation as soot concentration increases, thus validating the TP solution when gas radiation is dominated by that from soot.

The features just described are now investigated for non-uniform mixtures possessing property variations characteristic of flames. These configurations are summarised in Table (3.3).

3.4.6.2 Radiative intensity variation across non-uniform mixtures

In Fig. (3.11a), the variation of radiative intensity is shown across a 1m line of sight represented by configuration A :

$$\begin{aligned} T &= 800[5s[1.0-s]+1.0] \\ p_h &= 2p_c = [0.8s[1.0-s]+0.12] \end{aligned} \tag{3.56}$$

Negligible differences occur between the WSGG and DBT solutions, both increasing through a point of inflection to a maximum close to the end of the line of sight. The decrease in intensity results from an increase in absorption over emission in the cooler, less dense outer edges of the path. Absorption coefficients of 0.25 and 0.75 bracket these solutions, but no value in this range satisfactorily captures the shape of the profiles. The TP solutions, represented by an absorption coefficient just in excess of 1.0, exhibit the same overall profile variation, but over-predict intensity by over 100 % at locations beyond the mid-point of the line of sight.

The influence of soot is investigated by adding two concentration variations to configuration A. The first represents a relatively heavy loading given by configuration As :

$$\Phi = [40s[1.0-s]+6]\times 10^{-7} \tag{3.57}$$

Generally, when a high soot loading is imposed on a gas mixture, the overall radiative behaviour is dominated by the increasingly gray characteristics of soot. This is confirmed in Fig. (3.11b) in which the TP solution agrees very closely with the DBT solution. An absorption coefficient of 5.0 in the CAC solution closely represents all predictions. Interestingly, although the intensity increases through a point of inflection to a maximum, the profile is far more exaggerated than in the case of zero soot loading. Due to the high soot concentration at the centre of the path, the intensity increases rapidly

to a maximum which is almost five times greater than in Fig. (3.11a). Additionally, the turning point is located closer to the centre line. Subsequently, the cooler, less dense outer edges exhibit considerable absorption as the intensity decreases to almost half of its peak value.

Since the addition of a low soot loading to configuration A has a predictably minimal effect on the results (and associated conclusions) shown in Fig. (3.11a), the other soot concentration variation considered is representative of an intermediate range of soot loading. Under a variety of uniform conditions, Felske and Tien (1973) identified an appropriate range to be approximately centred at a value of $\Phi L = 10^{-7} m$. In order to encompass this range in the present analysis, a soot concentration variation is adopted given by configuration Bs :

$$\Phi = [40s[1.0-s]+6]\times 10^{-8} \tag{3.58}$$

The intensity variation across configuration A combined with this intermediate soot loading is shown in Fig. (3.11c). Relative to the intensity variation depicted in Fig. (3.11a), the gradient of the profile either side of the inflection point is increased, and the final value of radiance is approximately double that shown for the gas mixture without soot. Although the presence of soot reduces errors produced by the TP solutions relative to the case of zero soot loading, significant errors (greater than 30 %) are still evident. The TP solutions are represented by an absorption coefficient of 1.6, whilst a value of approximately 0.8 defines the DBT solution reasonably well.

The intensity variation across configuration B, represented by

$$\begin{aligned} T &= 200[20s[s-1.0]+9] \\ p_h &= 2p_c = [0.8s[s-1.0]+0.32] \end{aligned} \tag{3.59}$$

is shown in Fig. (3.12a). Now, the coolest temperature and lowest concentration are located at the centre of the path. Thus, in traversing the line of sight, the initial hot, high density region produces high emission, but a point is quickly reached whereby the cooler, less dense region absorbs more than it emits. Thereafter, absorption and emission are effectively balanced until increasing density and temperature at the far end of the path culminate in further augmentation of the radiative intensity. Figures (3.12b) and (3.12c) show the effect of adding heavy and intermediate soot loadings to the gas mixture. These are given by configurations Cs and Ds, respectively :

$$\Phi = [4s[s-1.0]+1.6]\times 10^{-6} \tag{3.60}$$

$$\Phi = [4s[s-1.0]+1.6]\times 10^{-7} \tag{3.61}$$

In Fig. (3.12b), the characteristic shape of Fig. (3.12a) is significantly accentuated by the rapid increases in emission at the edges of the line of sight, and by a clearly defined central region of net absorption. An intermediate soot loading has a less marked effect on the profile as shown in Fig. (3.12c).

For all three mixtures, the WSGG solution accurately predicts the DBT solution, and the TP solutions over-predict net emission in similar proportions to those observed for configuration A. Although each mixture appears to be defined by similar absorption coefficients to the ones used in the previous analysis, the heavy soot loading intensity variation could not be captured to the same level of accuracy. An absorption coefficient of 5.0 defines the initial maximum intensity, but then significantly under-predicts net absorption. In contrast, an absorption coefficient of approximately 2.5 greatly under-predicts intensity at the start of the path, but better predicts the minimum turning point.

Having demonstrated considerably different predictions by the WSGG and TP solutions applied to individual lines of sight, it is now necessary to assess their performance in a full DTRM calculation. For this purpose, the same mixtures are analysed bounded by infinite parallel walls. In all cases, the boundaries are isothermal at the same temperature as the extremities of the mixture. Heavy and intermediate soot loadings are combined with configurations A and B, in predictions of the volumetric radiative flux between both black and low emissivity ($\varepsilon = 0.25$) walls. The layer is divided into 20 elements, and 16 rays are launched from each wall. Differences of less than 1 % were produced by increasing the grid and/or the ray number resolution.

3.4.6.3 DTRM calculation between cold walls

For configuration A with walls at 800 K, the hot mixture is a net emitter of radiation. The relatively cool edges, however, absorb a proportion of this energy before it arrives at the walls. This energy exchange yields the radiative source variation shown in Figs. (3.13) and (3.14). When the walls have low emissivity, there is greater absorption by the mixture since a large fraction of radiation from the hot region is reflected at the walls. For $\varepsilon = 1.0$, all of the mixture radiance is absorbed by the walls. Consequently, higher wall reflectivity reduces the net emission from the mixture.

The radiative source variations between black boundaries are shown for heavy and intermediate soot loadings in Figs. (3.13a) and (3.13b), respectively. Relative to the intermediate soot loading given by Eq. (3.58), greater net emission from the high soot concentration represented by Eq. (3.57) produces increased net absorption at the edges. A similar effect is produced by the TP simulation shown in Fig. (3.13b), since the over-prediction of emission either side of the centre line leads to an over-prediction of net absorption in the cooler, less dense regions. Under heavy soot loading, this failing of the TP solution is almost indiscernible. The source term variation in Fig. (3.13a) is accurately modelled by the TP

solution. Close agreement is also produced for most of the layer by a CAC solution with an absorption coefficient equal to 5.0.

Similar characteristics apply to the prediction of source term variation between low emissivity walls as shown in Fig. (3.14). However, in addition to an overall increase in net absorption by all solutions as explained above, the TP solutions generate slightly larger errors than the calculations performed for black boundaries.

3.4.6.4 DTRM calculation between hot walls

When configuration B is applied between walls at 1800K the mixture becomes an overall absorber. The greatest net absorption occurs approximately one fifth of the distance from each wall, thus generating the M-shaped radiative source variation shown in Figs. (3.15) and (3.16). Since maximum net absorption does not occur in the coolest, least dense regions, this profile serves to emphasise the complex dependence of radiative behaviour on phenomena which compete to redistribute energy.

In the black wall case, only a narrow region of the mixture adjacent to the walls emits more radiation than it absorbs. This region expands for the mixture between gray walls, and the absolute value of this loss increases due to the low emissivity of the walls.

Heavy soot loadings (cf. Eq. (3.60)) shown in Figs. (3.15a) and (3.16a) produce greater net emission close to the boundaries than is produced by the intermediate loadings given by Eq. (3.61), and shown in Figs. (3.15b) and (3.16b). Therefore, a higher energy flux flows into the interior of the layer, which, being of a greater density, absorbs more strongly than when there is a lower concentration of soot.

As before, the total property solutions over-predict both emission (in hot dense regions), and absorption (in locations of relatively low concentration and temperature). For the intermediate soot loading, errors in excess of 100 % are produced at most locations, but significant errors are only evident for the heavy loading in the regions of net emission close to the

walls.

3.4 CONCLUDING REMARKS

Detailed numerical methods now are available to accurately model the radiative effects of combustion systems. However, the demands of computational expediency currently preclude the incorporation of such detail into CFD codes. Therefore, radiation models are required which can deliver acceptable accuracy at low cost. By virtue of its extensive use by many researchers, the discrete transfer radiation model (DTRM) would appear to provide a popular framework in which to satisfy these contrasting requirements. Indeed, its simple incorporation into general curvilinear CFD codes, and its suitability to modelling complex geometries, make it an attractive choice for predicting radiative energy transfer in a wide range of combustion environments.

In view of the expectation that the DTRM will maintain its popularity, a number of optimisation issues have been identified in this chapter which merit further investigation. Particular attention has been given to one of them; that is, concerning the distribution of ray directions relative to a surface, and the associated weighting set.

Alternative weighting sets have been derived which provide a better mapping of the "field of view" of a surface. Of these, the quasi-equal area weighting set represents a more uniform discretisation of the solid angle hemisphere. Additionally, it avoids the uncertainty accompanying selection of the distribution of rays in spherical polar co-ordinate space. The second alternative, designed for cylindrical polar geometries, constrains a ray to be launched perpendicular to a surface. Encouragingly, this weighting set also produces the best response to increasing numbers of rays in the rectangular geometries analysed above.

In the DTRM, and other radiation models, physical realism is often

sacrificed for speed of calculation by employing simplified representations of the radiative properties of combustion media. The fine resolution structure of radiation from the molecular gases, CO_2 and H_2O, generates highly complex, multi-dimensional radiative behaviour which cannot be adequately represented in a simple way. A hierarchy of gas property models has been discussed along with the more readily available strategies for incorporating them into solutions to the radiative transfer equation. Radiation from soot particles is generally modelled as a continuum; consequently, it presents a less challenging task. However, treatment of gas-soot mixtures introduces additional complexity since it is non-physical to superimpose the radiative effects of the separate components.

In order to compare the most widely used solutions to the RTE in the DTRM across non-uniform paths, a number of configurations have been analysed. Some of them are representative of the conditions prevailing in diffusion flames. The variation of radiative intensity across individual lines of sight, and of volumetric flux across layers bounded by solid walls, have been investigated. Both black and low emissivity walls ($\varepsilon = 0.25$) have been included. Special attention has been given to the effect of combining different soot concentrations with fixed distributions of CO_2 and H_2O.

A narrow band, differential banded transmissivity (DBT) solution to the RTE is commonly employed as the most sophisticated representation of radiative property variations. It has been used here as the benchmark for comparisons. The simplest solution to the RTE is afforded by assuming a constant absorption coefficient (CAC). The same algorithm is applied in the total property (TP) solution, but absorption coefficients of individual elements are evaluated from local properties. Although the TP solution attempts to realistically model the radiative behaviour of combustion media, it fails to do so due to the line structure of gaseous radiation. The weighted sum of gray gases property model fairly crudely represents this structure, but when it is incorporated into a weighted sum of gray gases solution to the RTE, it generates close agreement with the DBT solution.

Four further conclusions can be drawn from the preceding analysis of typical non-uniform property variations. First, both CAC and TP solutions are capable of generating good accuracy under conditions of high soot concentration. Second, when the radiative behaviour of gas-soot mixtures is not dominated by soot, large discrepancies are produced by the TP solution, whilst the CAC solution only tends to produce significant disagreement in certain regions. Third, large potential errors accompany the CAC solution since the most suitable value is not known in advance of calculation. Finally, the over-riding consequence of this analysis is that, for the range of conditions considered, the WSGG solution provides the most accurate method for fast, general prediction of radiative property variation.

The foregoing recommendation for the WSGG solution to the RTE does not necessarily extend to problems comprising a wider range of property variations, since the coefficients of the WSGG solution are evaluated for a particular set of conditions. Consequently, alternative solutions to the RTE are considered in the next chapter, which can better accomodate this failing of the WSGG solution.

number of rays, M	number of 'theta bands'
$M \leq 8$	2
$8 \leq M < 24$	3
$24 \leq M < 28$	5
$28 \leq M < 36$	6
$36 \leq M < 39$	8
$39 \leq M < 42$	9
$42 \leq M < 67$	10
$67 \leq M < 128$	12

Table 3.1 Preliminary recommendations for the number of 'theta bands' in the quasi-equal area discretisation of the solid angle hemisphere.

n	n'	b_1	$b_2 \times 10^3$	$k_{g,n}\left(m^{-1}atm^{-1}\right)$	$k_{p,n'}\left(m^{-4}kg^{-1}\right)$
1	1	0.588	-0.2401	0.0	541
1	2	-0.165	0.2834	0.0	2749
2	1	0.412	-0.1665	0.89	541
2	2	-0.127	0.2178	0.89	2749
3	1	0.2375	-0.0941	15.5	541
3	2	-0.0105	0.0265	15.5	2749
4	1	0.0585	-0.0243	239.0	541
4	2	0.0065	-0.0027	239.0	2749

Table 3.2 Absorption and weighting coefficients for the weighted sum of gray gases model due to Truelove (1975) - partial pressure ratio of CO_2 to H_2O equal to 0.5. In Eq. (3.41), $a_{m,n,n'}(T)=b_1+b_2T$.

Configuration	Temperature (K)	Partial pressure of CO_2 (atm)
A	$4000s(L-s)+800$	$0.4s(L-s)+0.06$
B	$4000s(s-L)+1800$	$0.4s(s-L)+0.16$

Table 3.3 Temperature-partial pressure configurations. L = 1.0 m.

Configuration	Soot volume fraction
A_s	$[40s(L-s)+6]\times10^{-7}$
B_s	$[40s(L-s)+6]\times10^{-8}$
C_s	$[4s(s-L)+1.6]\times10^{-6}$
D_s	$[4s(s-L)+1.6]\times10^{-7}$

Table 3.4 Soot volume fraction configurations. L = 1.0 m.

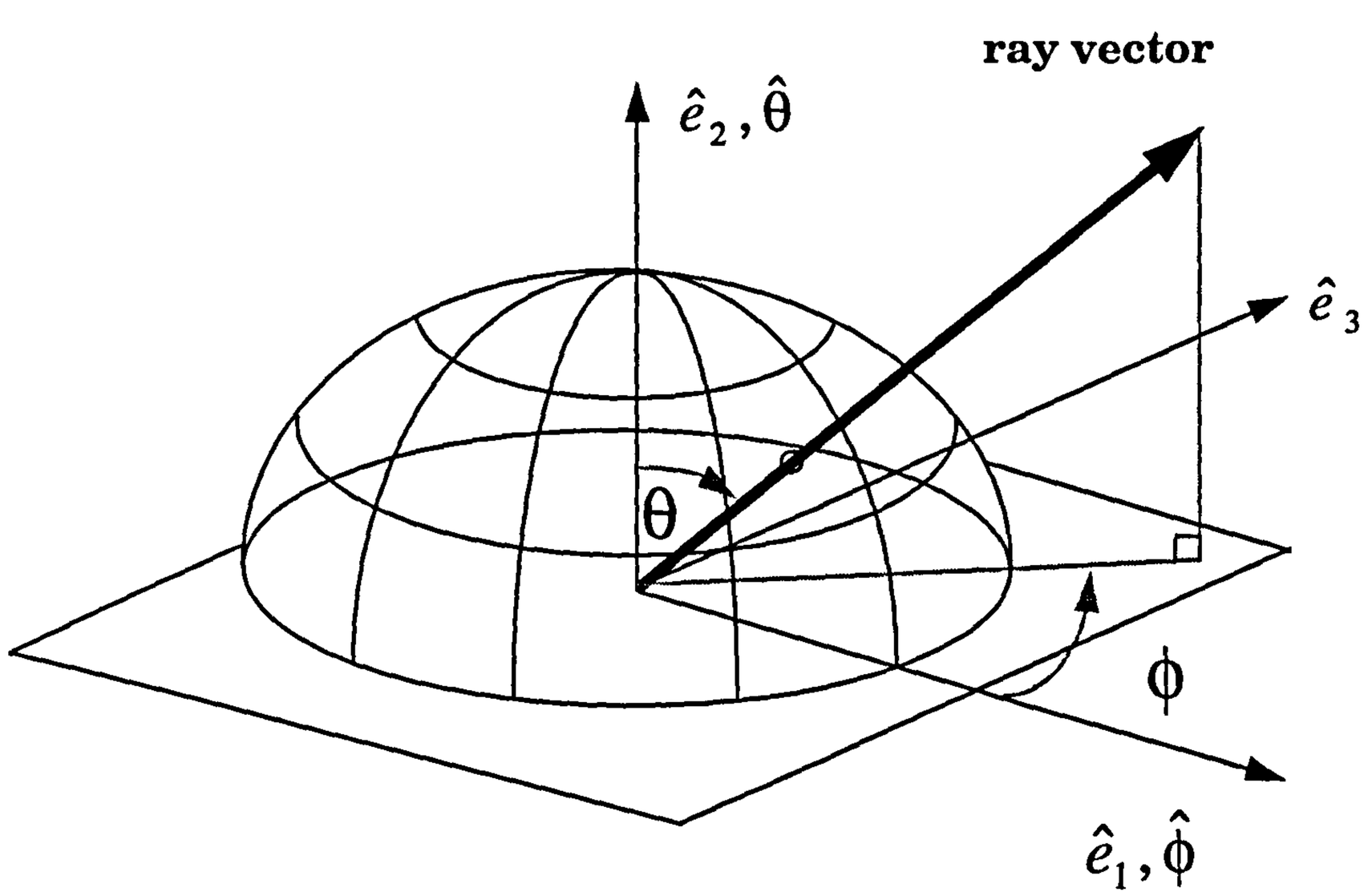

Fig. 3.1 Discretisation of the solid angle hemisphere using equal divisions of the polar and azimuthal angles.

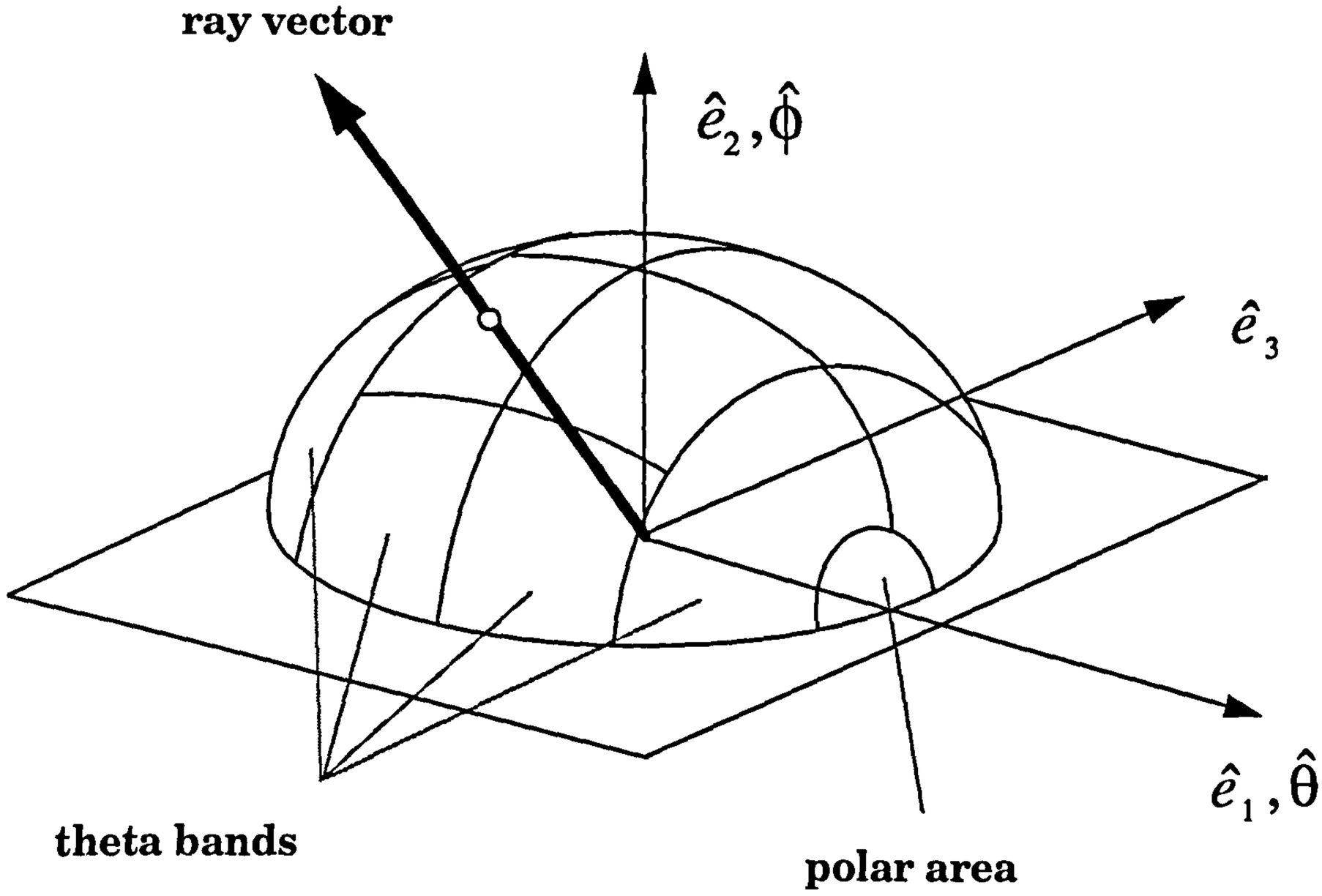

Fig. 3.2 Discretisation of the solid angle hemisphere using quasi-equal solid angles.

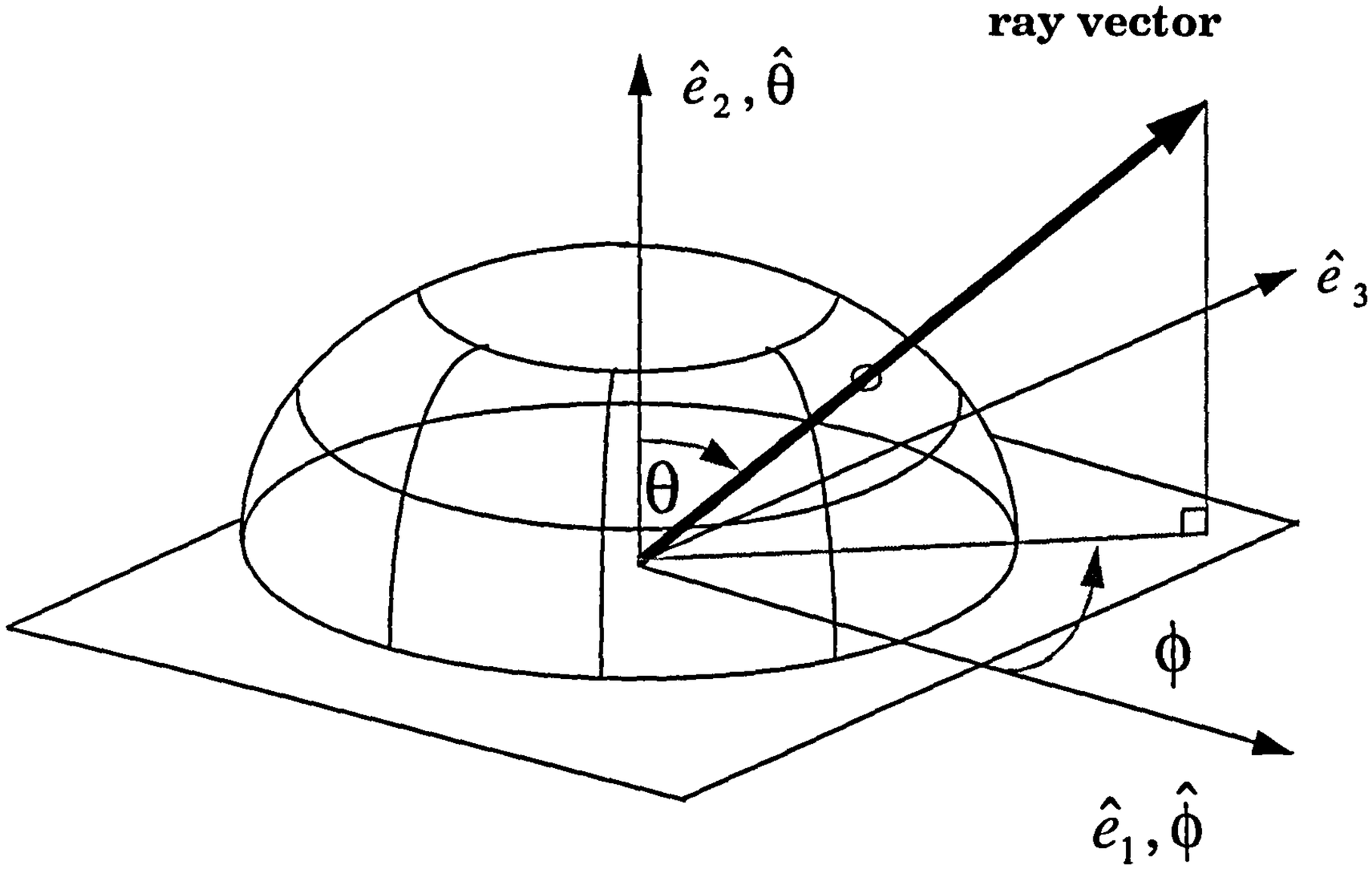

Fig. 3.3 Discretisation of the solid angle hemisphere such that a ray is launched perpendicular to a surface.

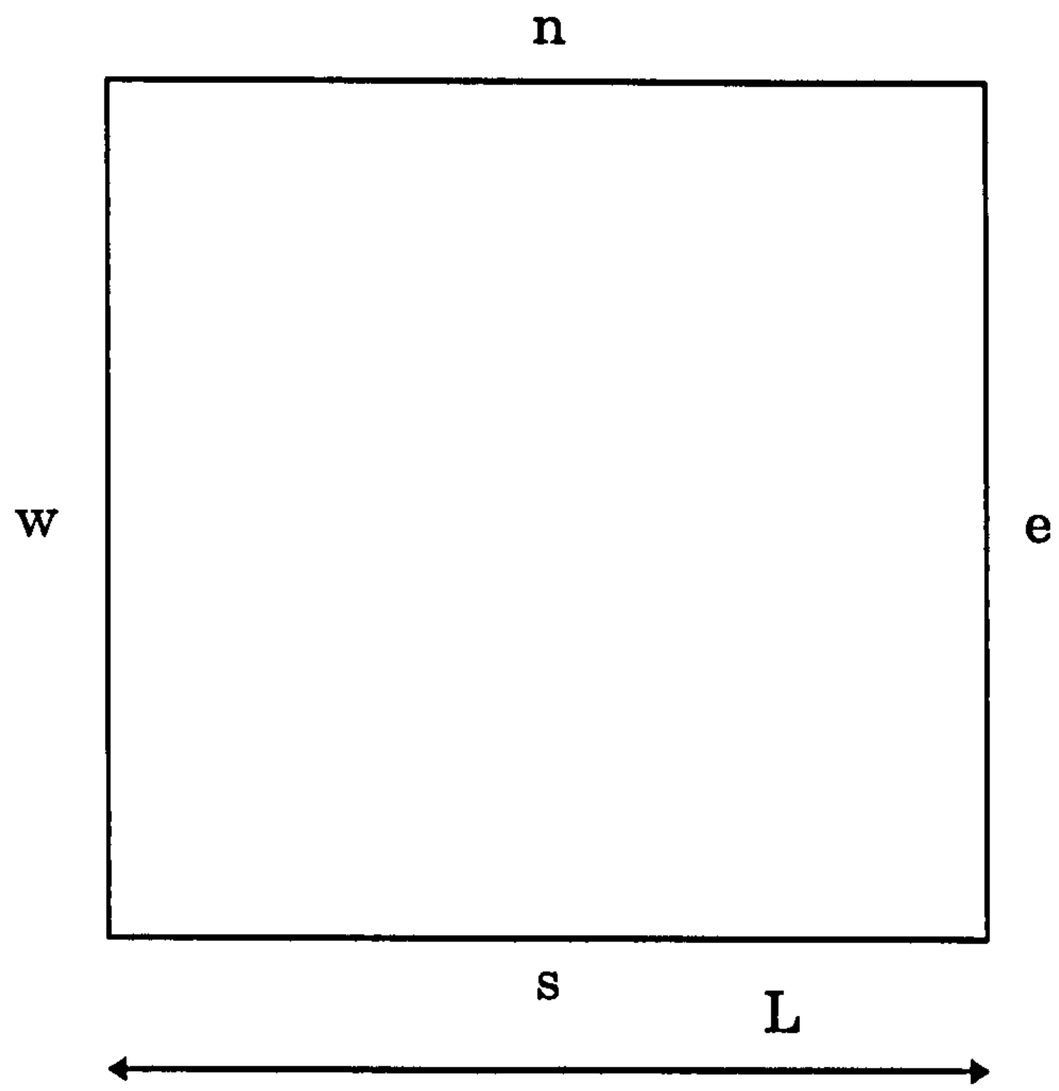

	Thynell and Lin (1989)	Crosbie and Schrenker (1984)
$L(m)$	*0.1*	*1.0*
ε	$\varepsilon_w = \varepsilon_e = 0.5$ $\varepsilon_s = \varepsilon_n = 0.99$	$\varepsilon_w = \varepsilon_e = \varepsilon_s = \varepsilon_n = 1.0$
$T_{wall}(K)$	$T_w = T_e = T_s = T_n = 0.0$	$T_w = T_e = T_n = 0.0$ $T_s = (\pi/\sigma)^{0.25}$
$T_{gas}(K)$	$(\pi/\sigma)^{0.25}$	$\left(\frac{\sum_{all\ rays} w\Delta A[1-exp(-kl)]i_{n-1}}{\frac{\sigma}{\pi}\sum_{all\ rays} w\Delta A[1-exp(-kl)]} \right)^{0.25}$
k	*1.0*	*0.25*

Fig. 3.4 Schematic of the infinitely long square cavity test problems.

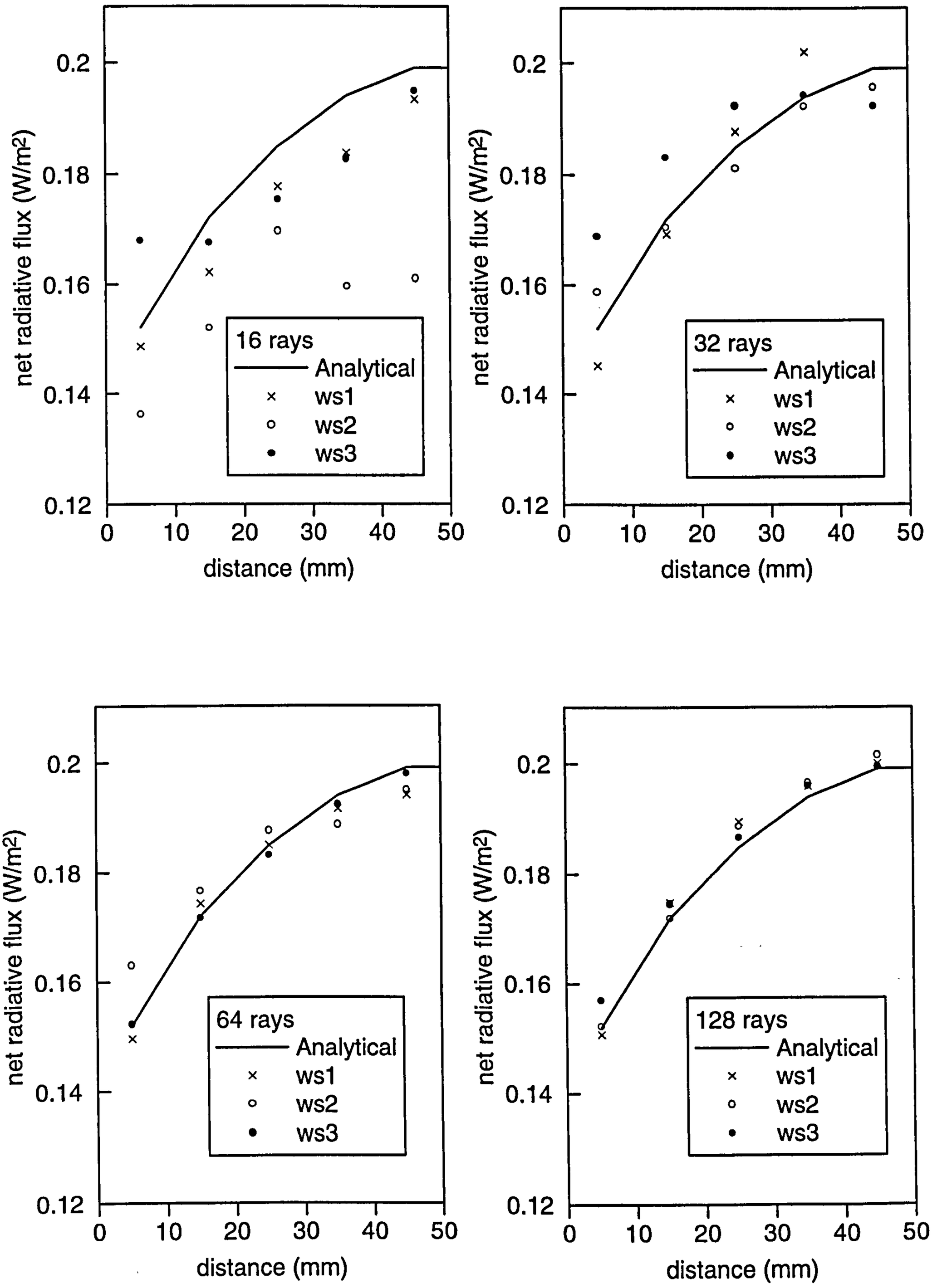

Fig. 3.5 Comparison of weighting sets for the prediction of the net radiative flux to a side wall in an infinite isothermal cavity.

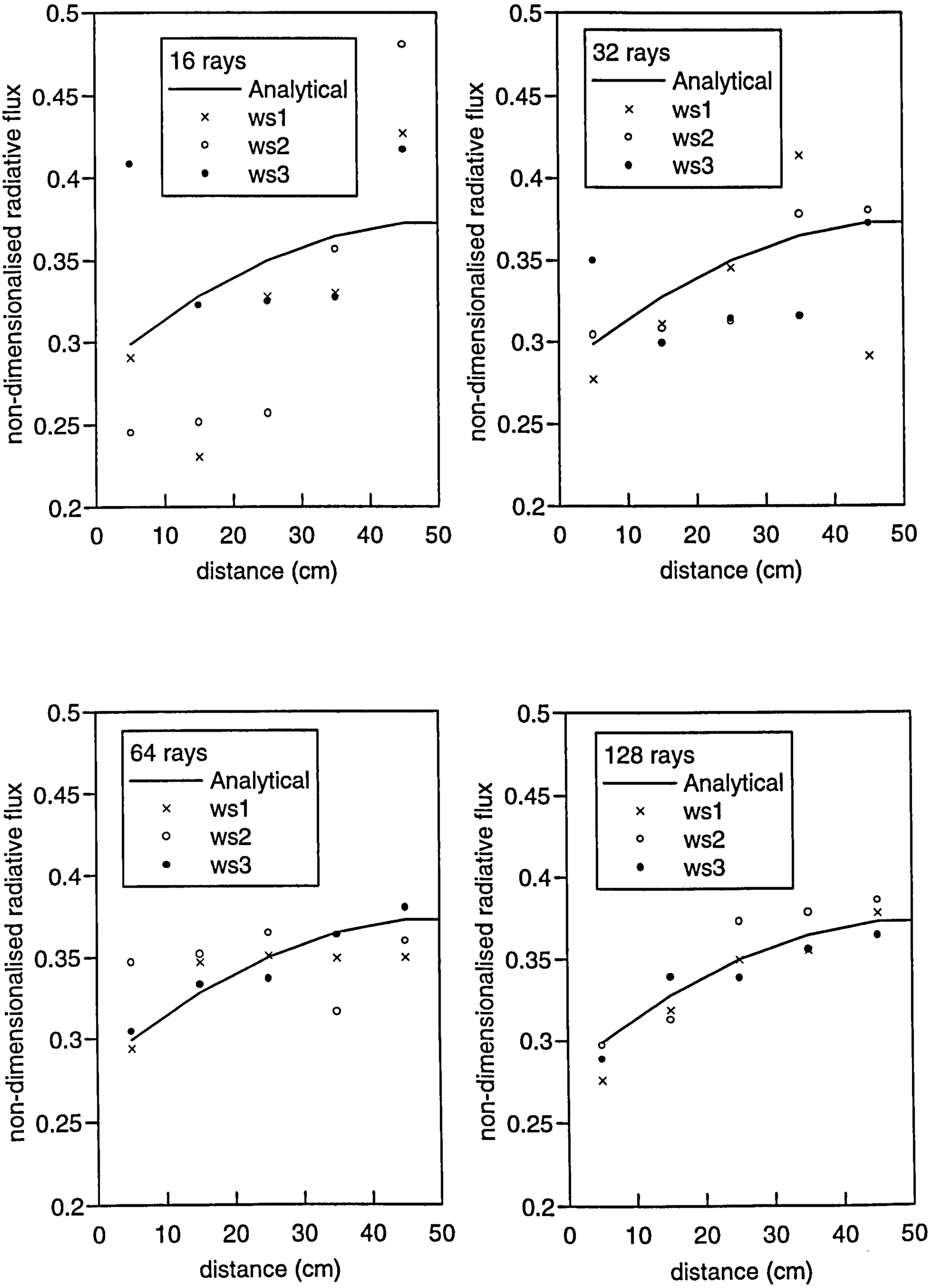

Fig. 3.6 Comparison of weighting sets for the prediction of the net radiative flux to a side wall in an infinite cavity in radiative equilibrium.

x = 0, x = 6, y = 0, y = 2, z = 2	T = 1090 K	ε = 0.70
z = 0	T = 320 K	ε = 0.86

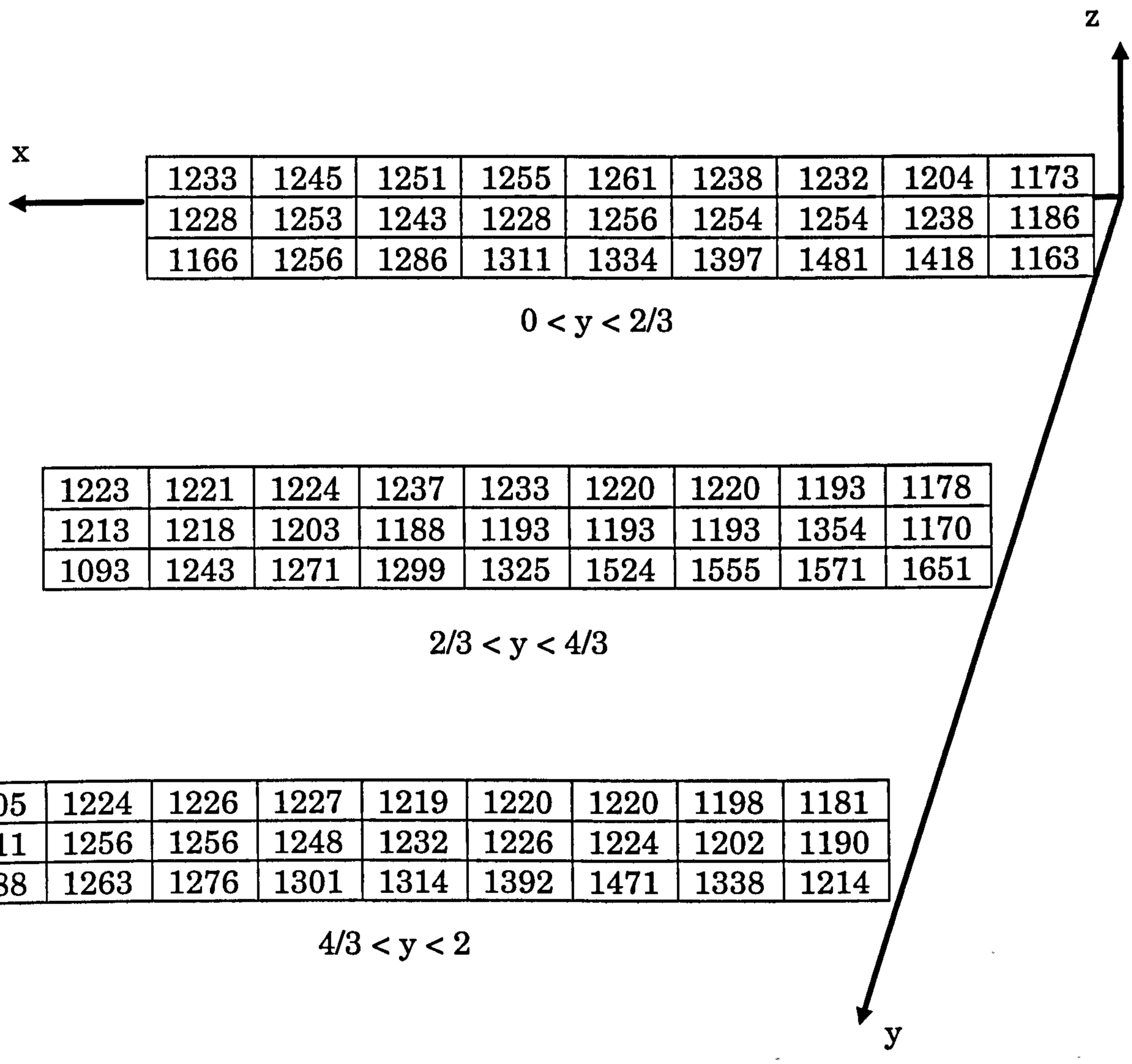

Fig. 3.7 Boundary conditions and temperature distribution from a modelled IFRF rectangular furnace. Total dimensions : 6 x 2 x 2 m. Gas absorption coefficient = 0.2 m^{-1}.

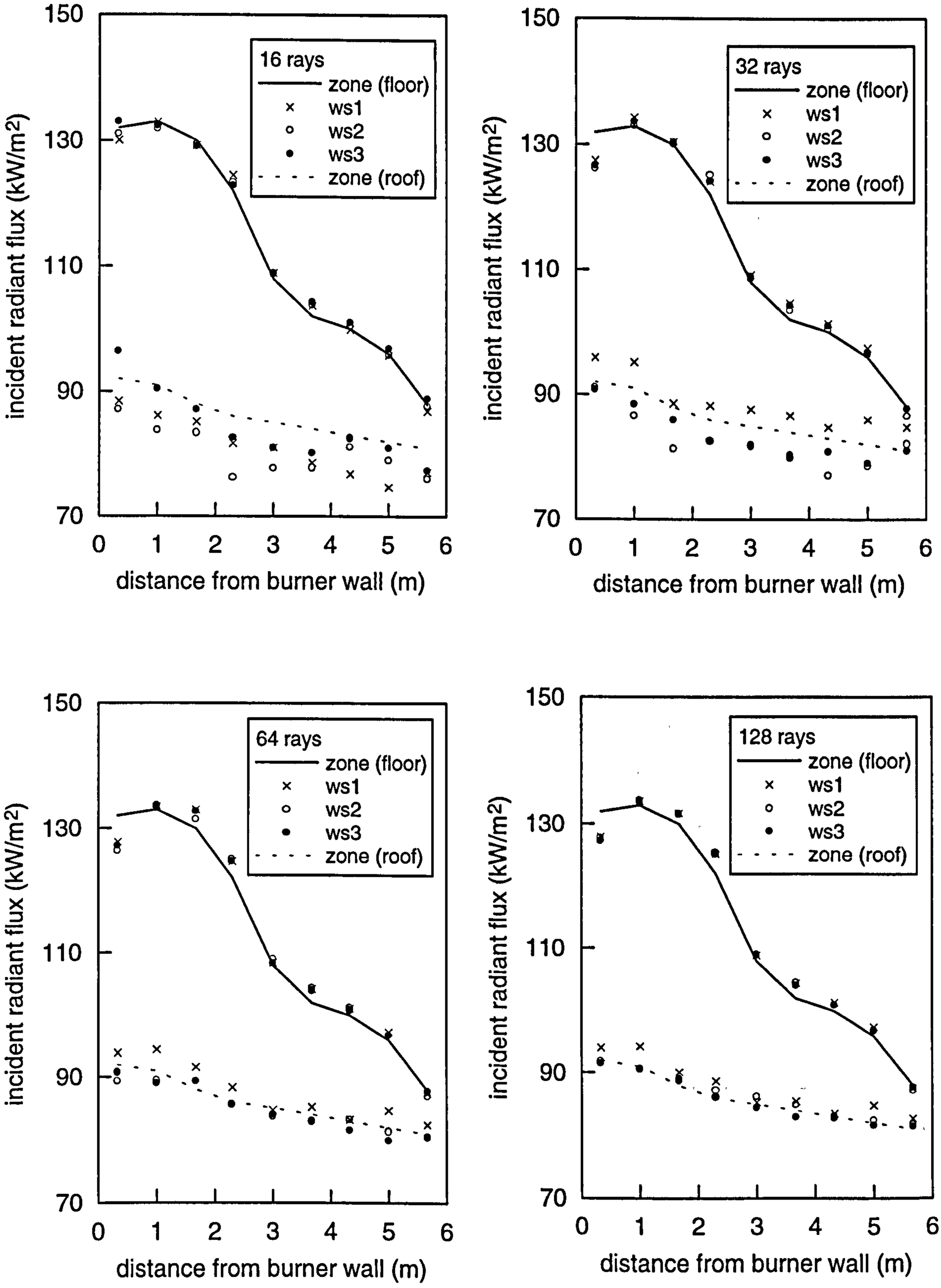

Fig. 3.8 Comparison of weighting sets for the prediction of the incident radiative flux to the roof and floor of an IFRF furnace.

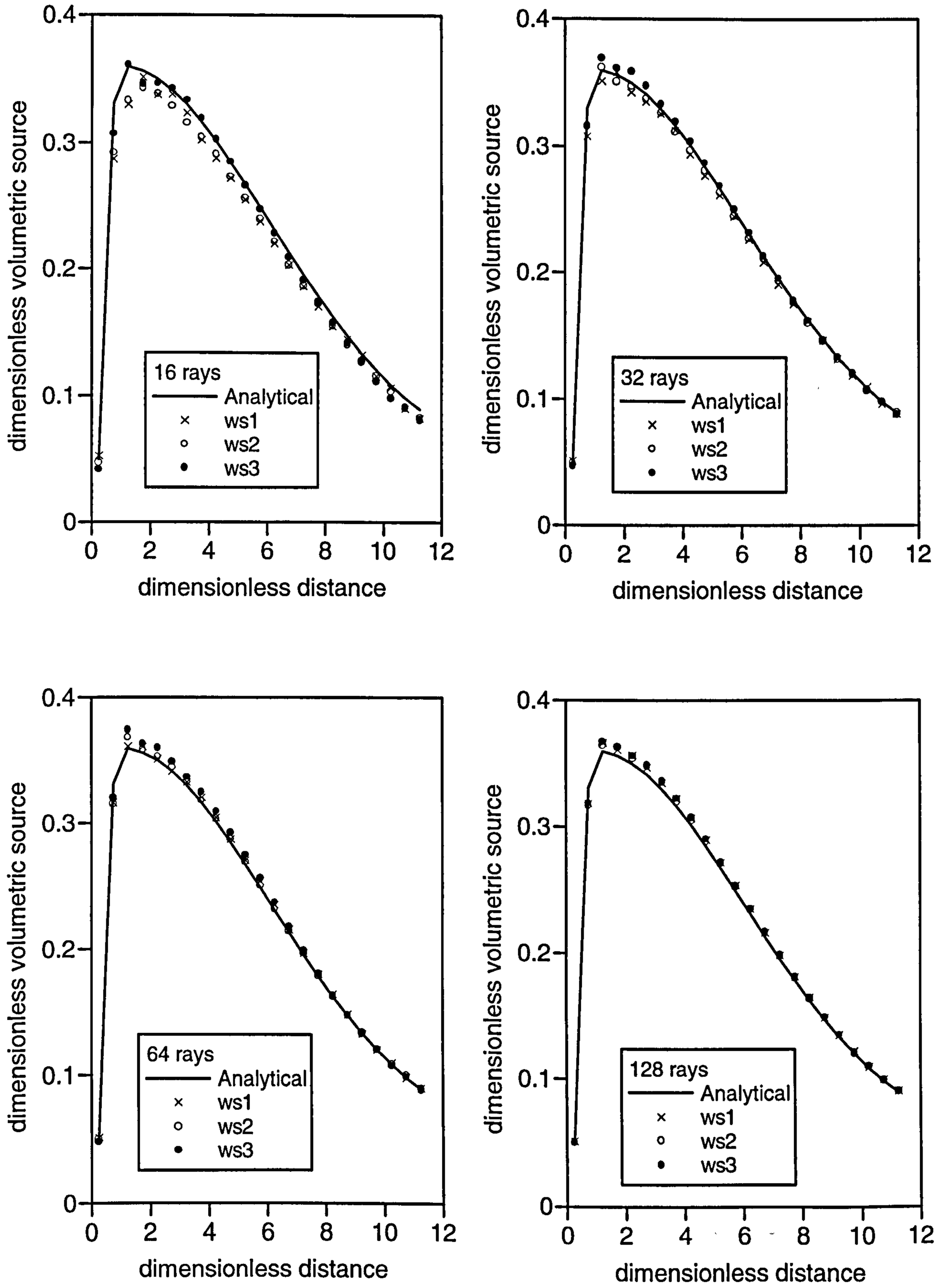

Fig. 3.9 Comparison of weighting sets for the prediction of the volumetric radiative source in an analytically solved tunnel furnace.

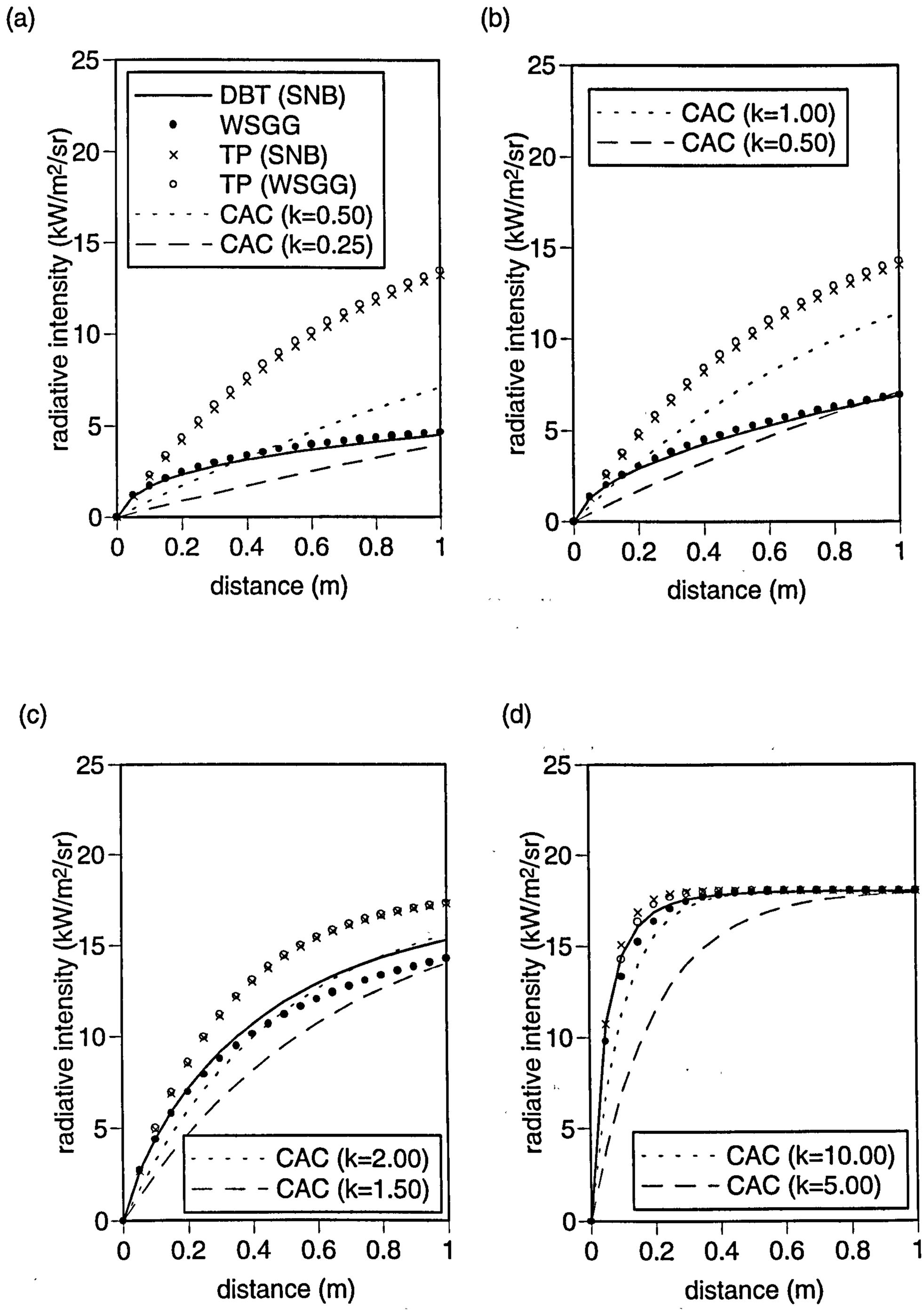

Fig. 3.10 Line of sight comparison between the WSGG and total property solutions to the RTE across a uniform CO_2-H_2O layer for various soot loadings : (a) $\Phi = 0.0$; (b) $\Phi = 1.0e-7$; (c) $1.0e-6$; (d) $1.0e-5$.

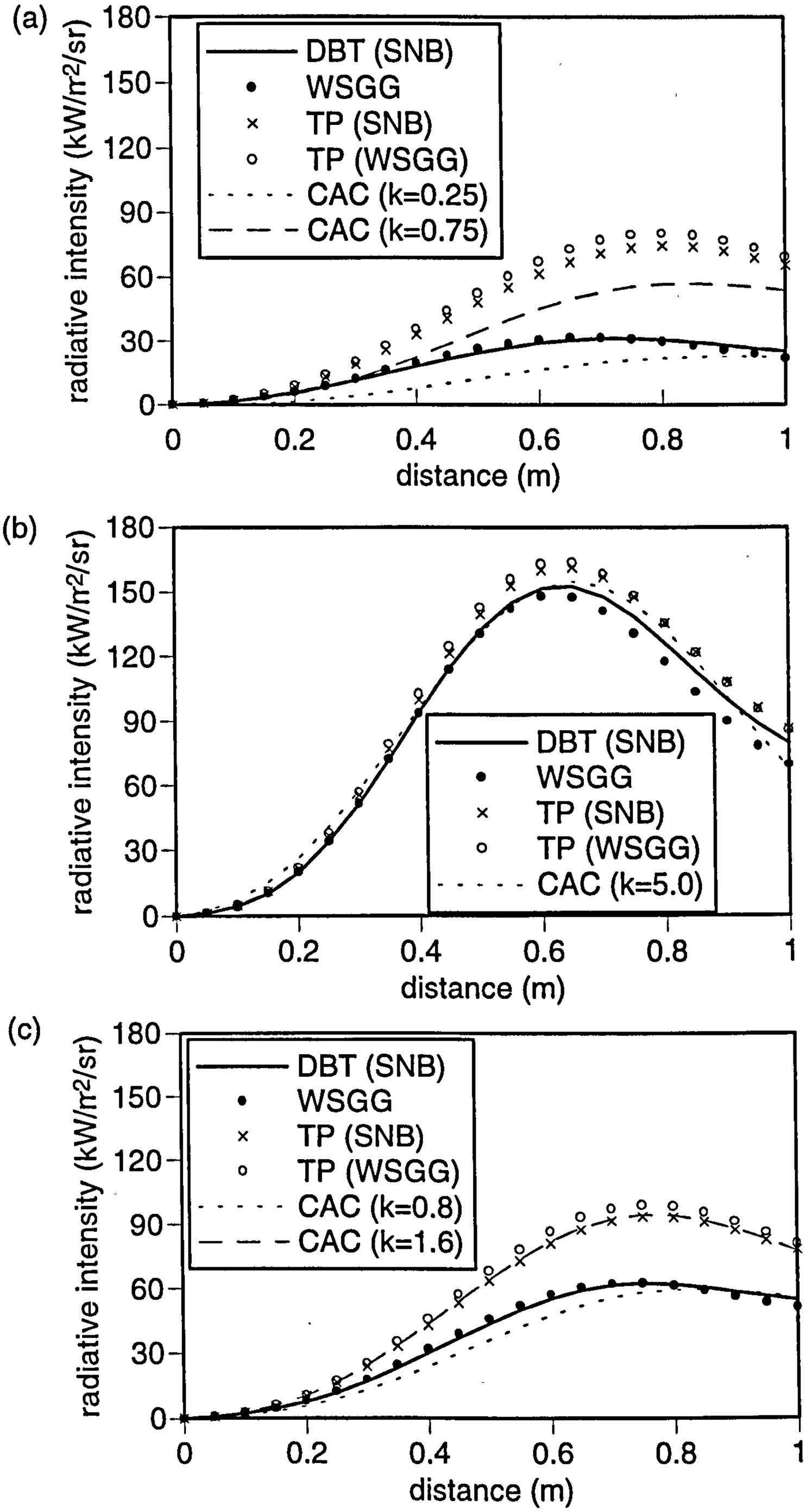

Fig. 3.11 Comparison between the WSGG and total property solutions to the RTE for configuration A across a CO_2-H_2O layer for various soot loadings : (a) no soot; (b) configuration A_s (high concentrations); (c) configuration B_s (intermediate concentrations).

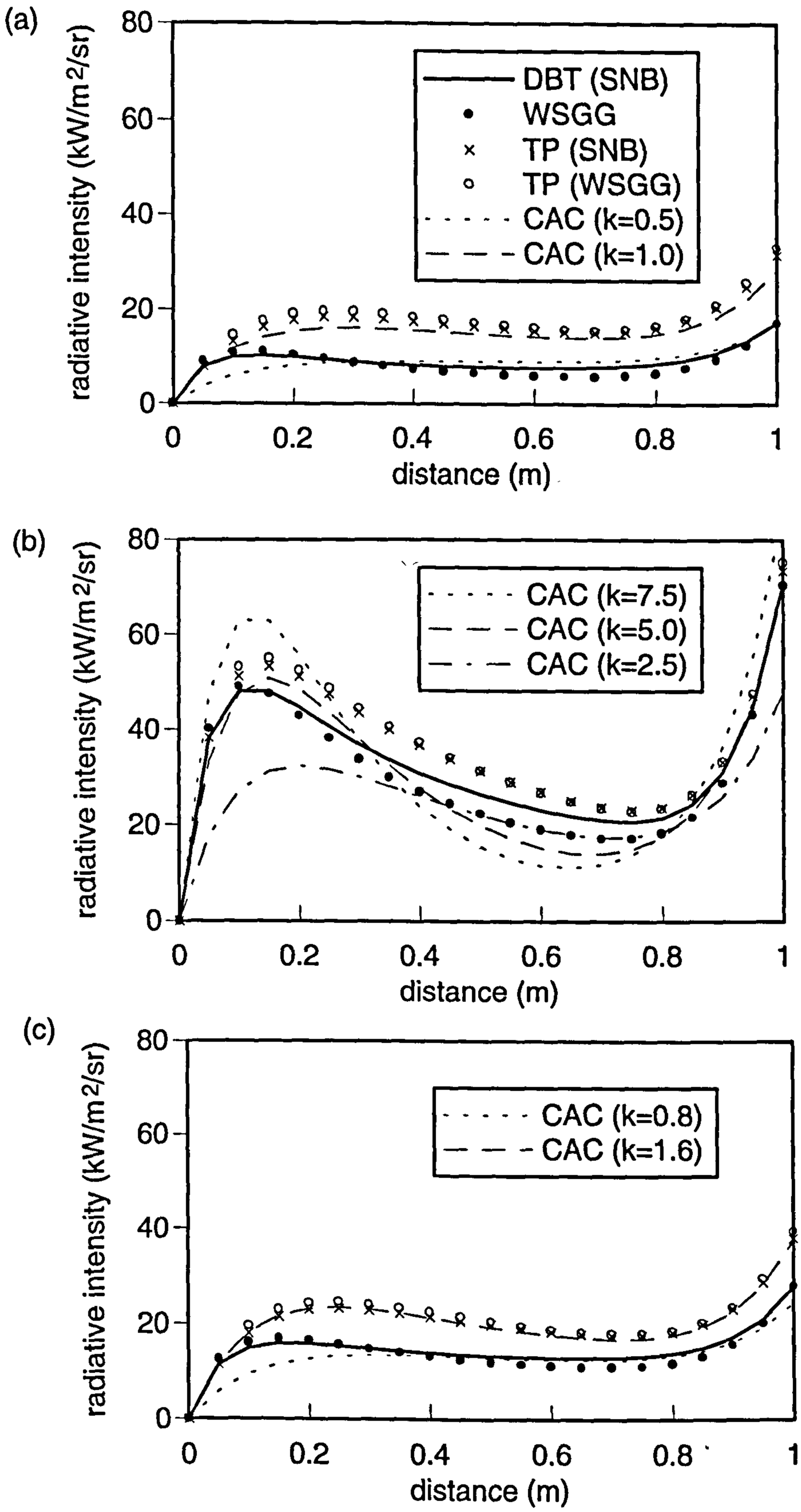

Fig. 3.12 Comparison between the WSGG and total property solutions to the RTE for configuration B across a CO_2-H_2O layer for various soot loadings : (a) no soot; (b) configuration C_s (high concentrations); (c) configuration D_s (intermediate concentrations).

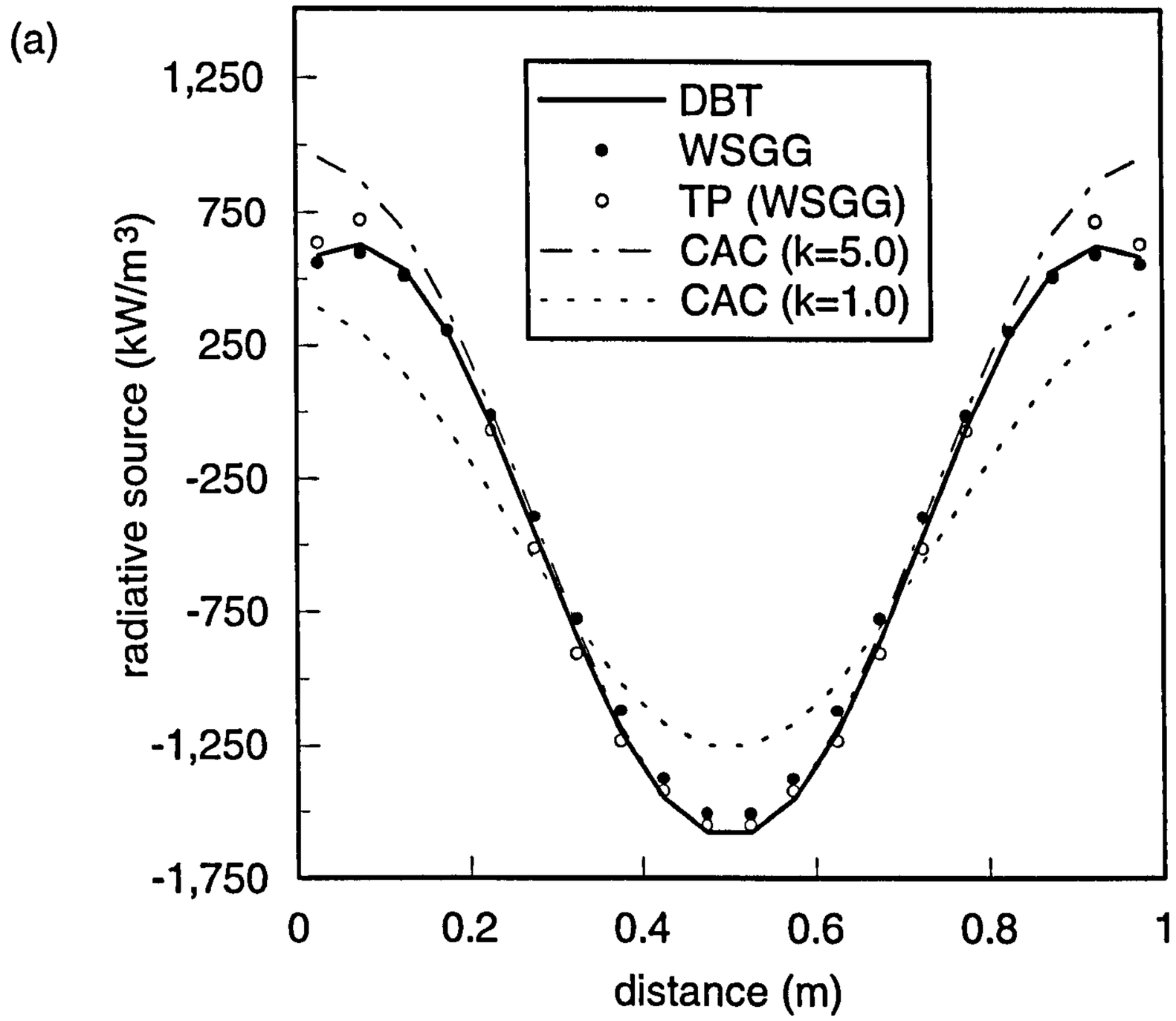

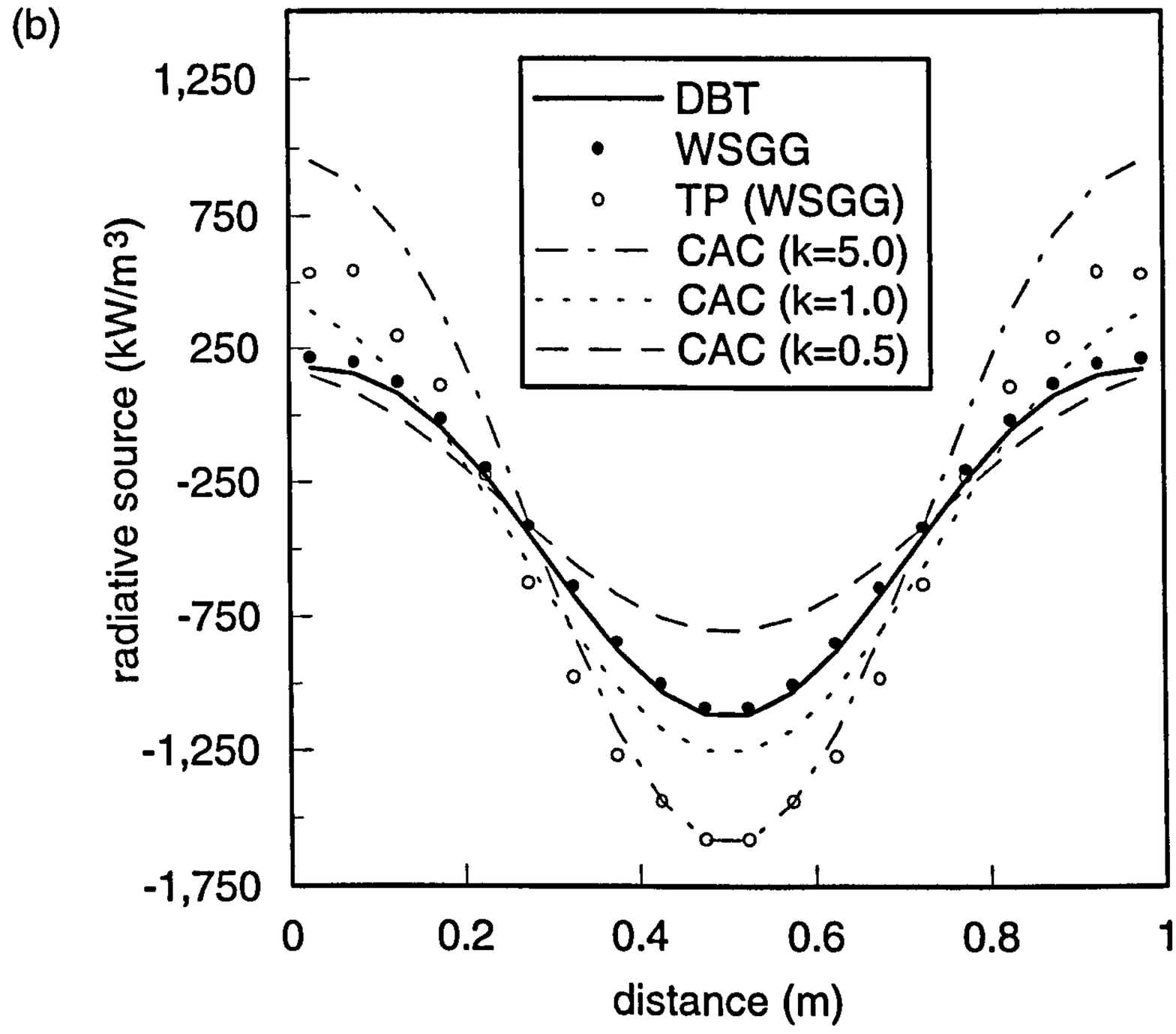

Fig. 3.13 Comparison of the WSGG and TP solutions for the prediction of volumetric flux variation across CO_2-H_2O-soot mixtures between cold black walls (configuration A) : (a) heavy soot loading (configuration A_s); (b) intermediate soot loading (configuration B_s).

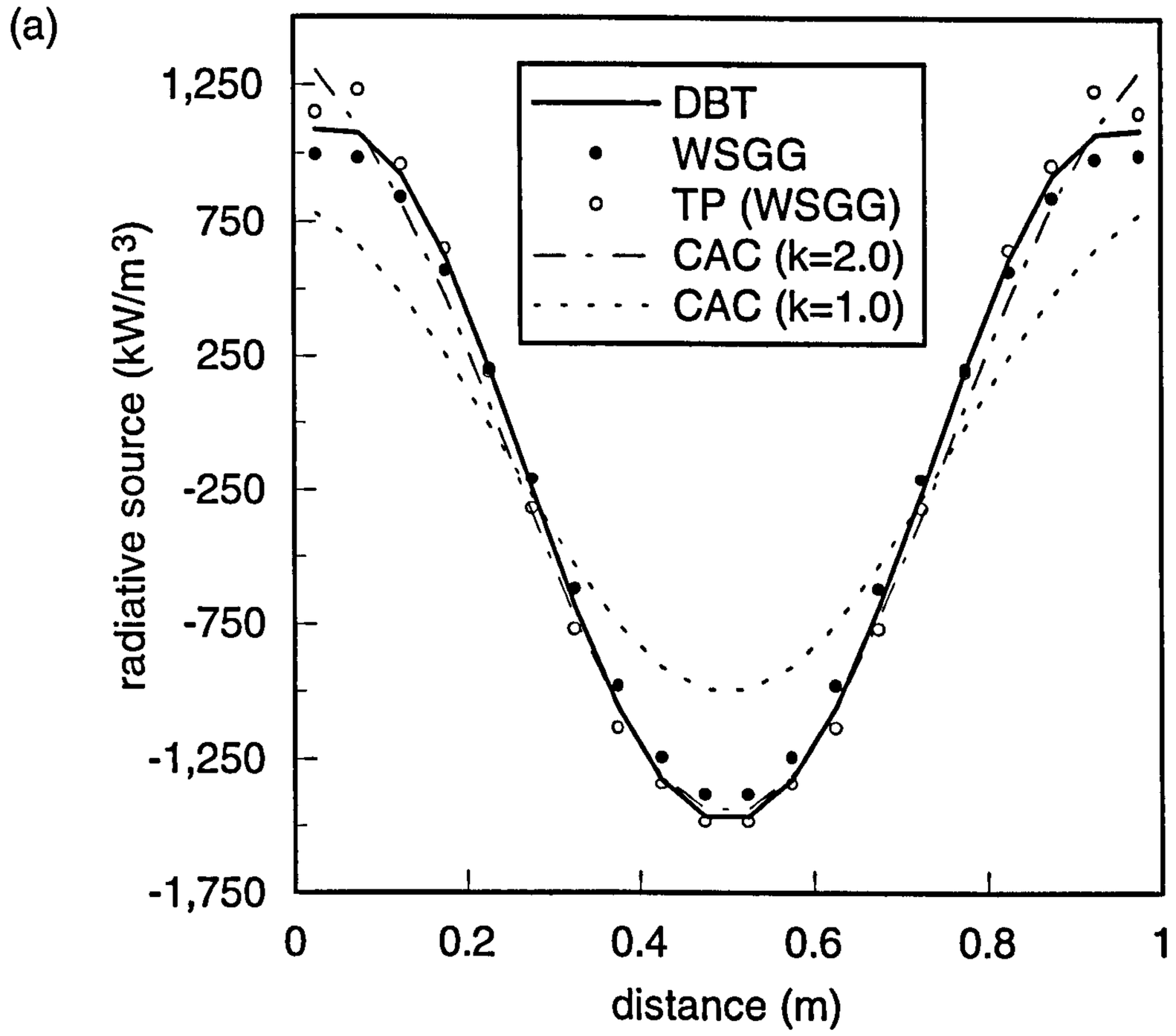

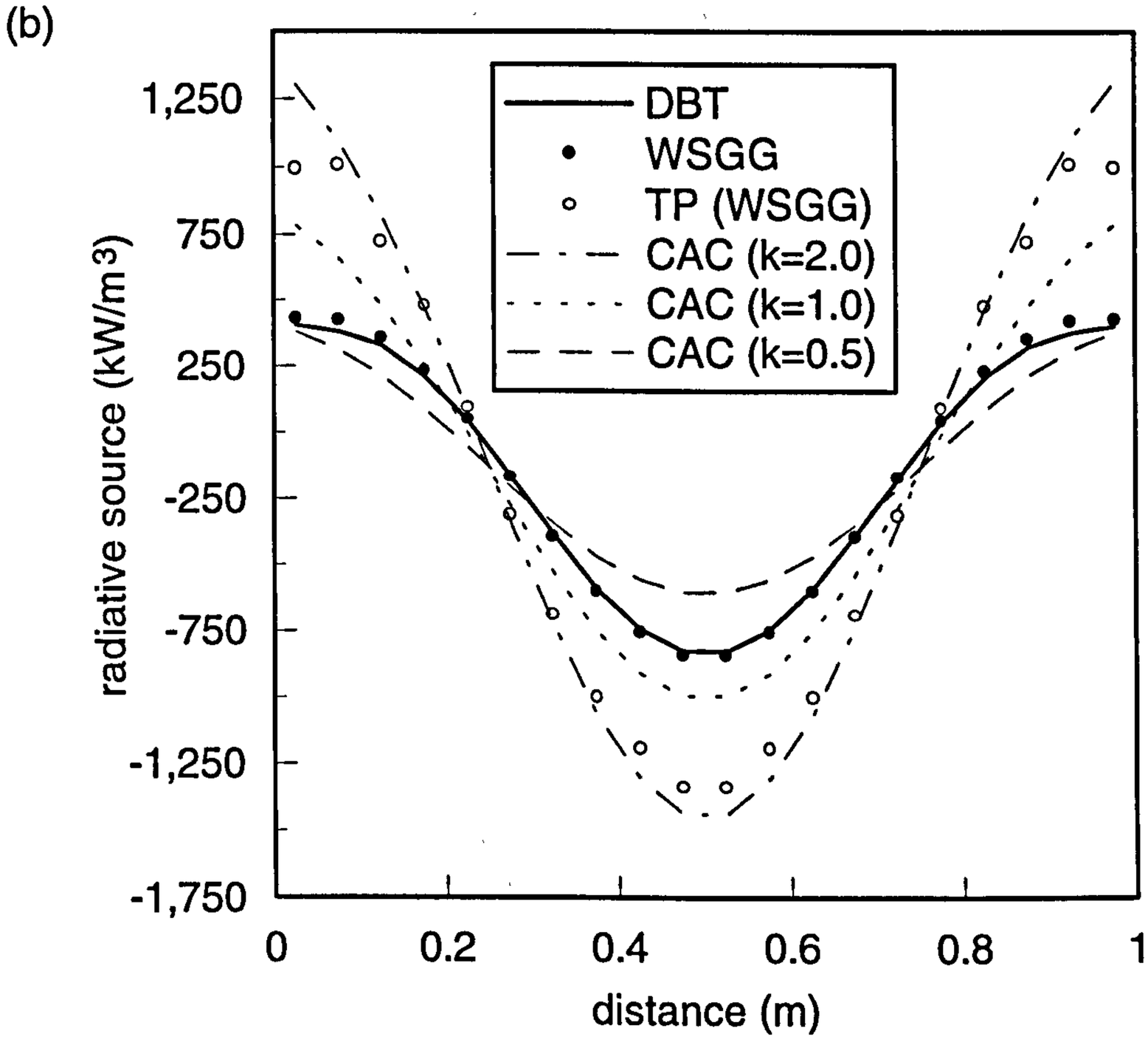

Fig. 3.14 Comparison of the WSGG and TP solutions for the prediction of volumetric flux variation across CO_2-H_2O-soot mixtures between cold low emissivity walls, $\varepsilon = 0.25$, (configuration A) : (a) heavy soot loading (configuration A_s); (b) intermediate soot loading (configuration B_s).

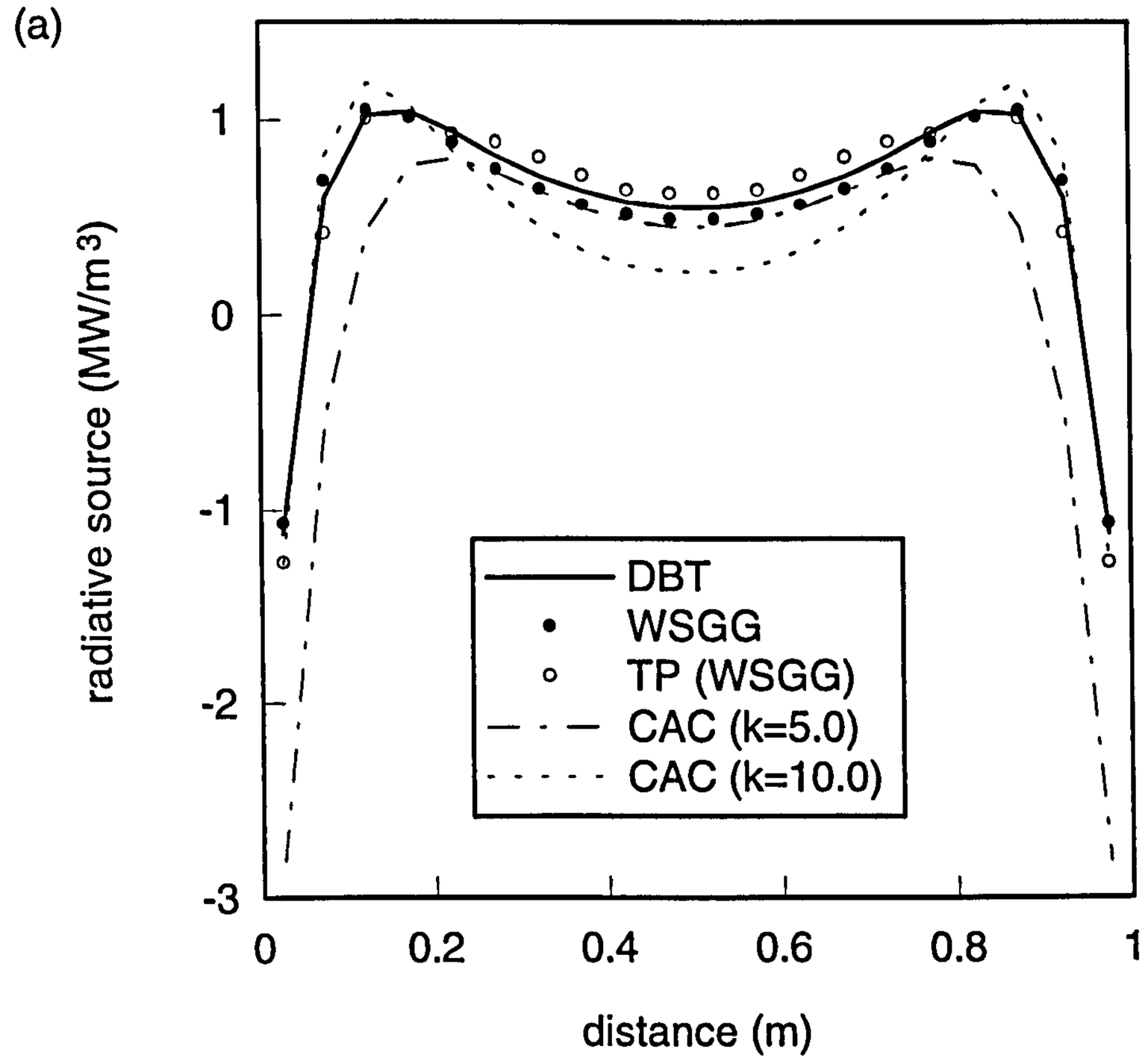

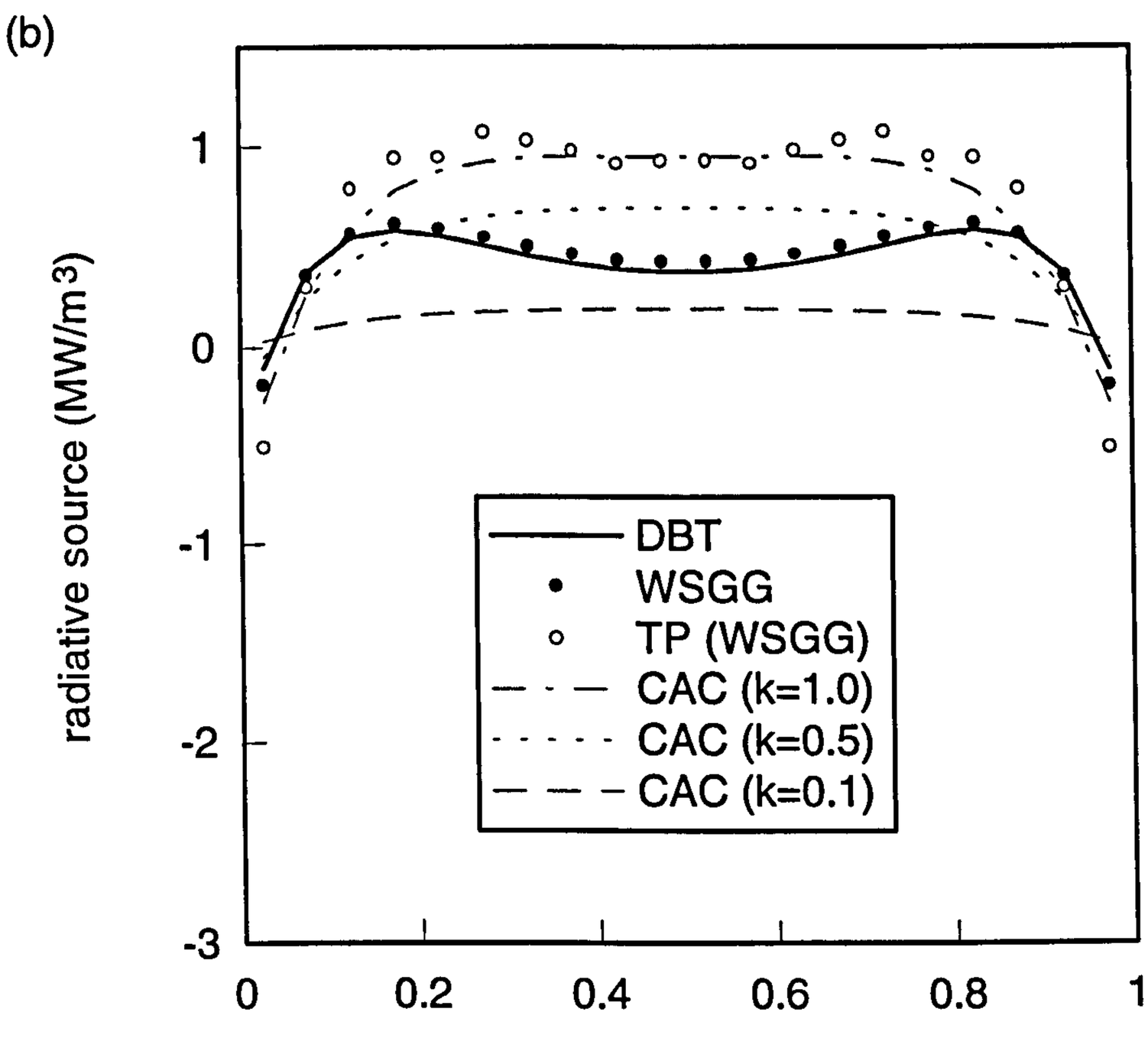

Fig. 3.15 Comparison of the WSGG and TP solutions for the prediction of volumetric flux variation across CO_2-H_2O-soot mixtures between hot black walls (configuration B) : (a) heavy soot loading (configuration C_s); (b) intermediate soot loading (configuration D_s).

(a)

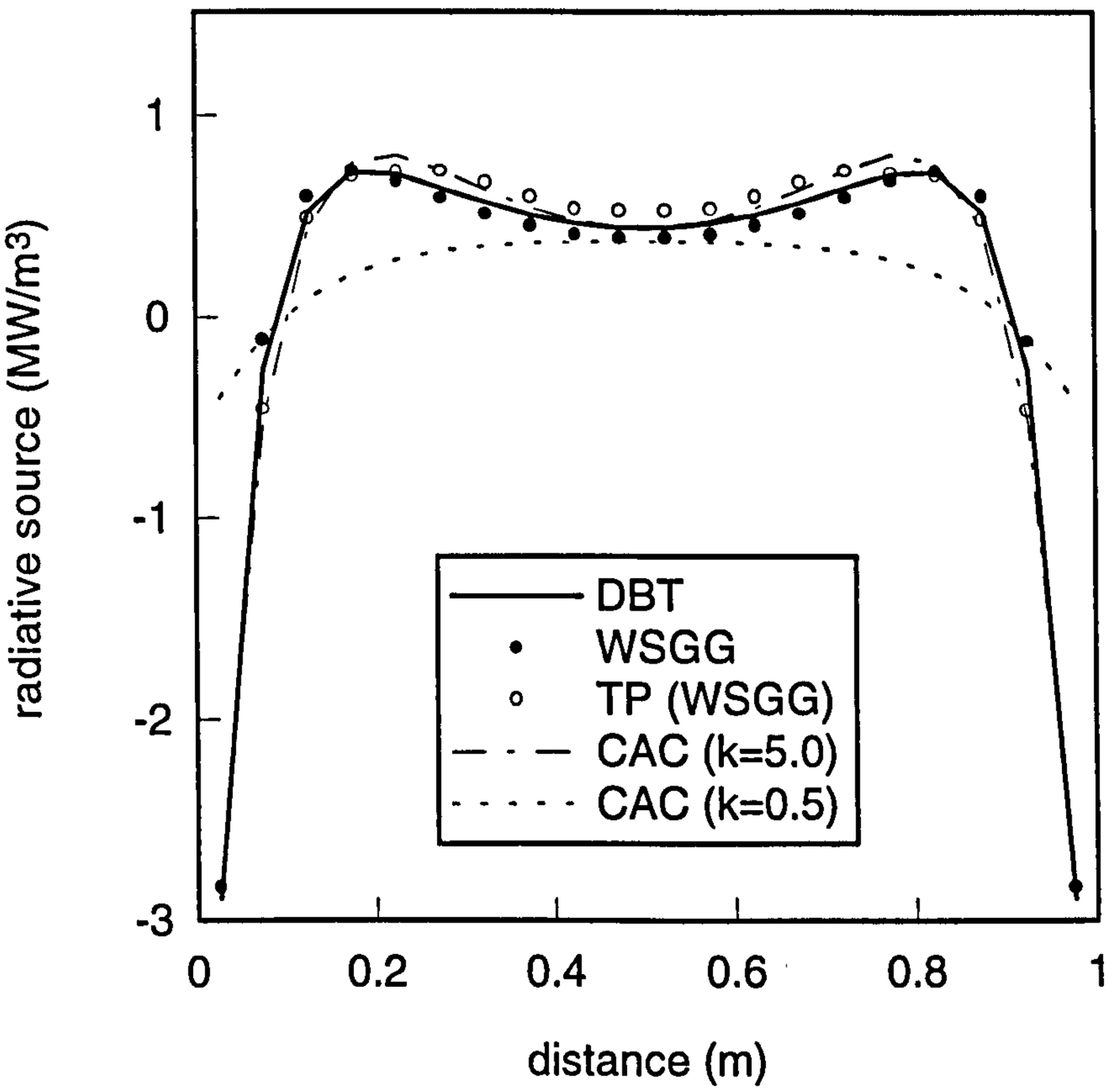

(b)

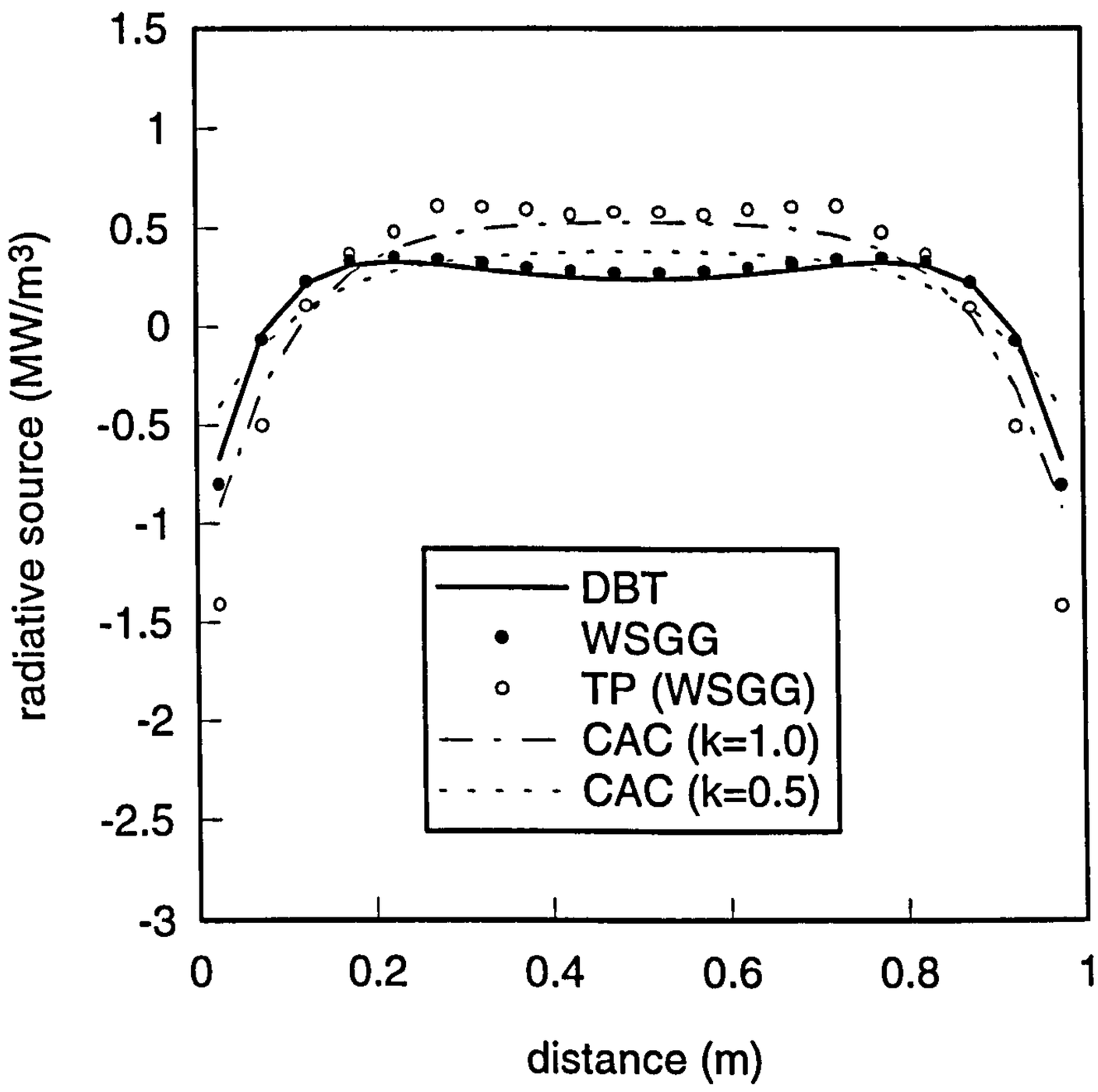

Fig. 3.16 Comparison of the WSGG and TP solutions for the prediction of volumetric flux variation across CO_2-H_2O-soot mixtures between hot low emissivity walls, $\varepsilon = 0.25$, (configuration B) : (a) heavy soot loading (configuration C_s); (b) intermediate soot loading (configuration D_s).

Chapter 4

A Differential Total Absorptivity Solution to the Radiative Transfer Equation

4.1 INTRODUCTION

The previous chapter has demonstrated the inappropriateness of disregarding correlations between intensity and absorption. Other than under conditions of high uniformity and/or high optical density, the total property solution generates unacceptably large errors. However, although the weighted sum of gray gases solution possesses good accuracy across the configurations analysed, it only models these correlations in a cursory fashion by solving separate equations for each gray gas component. The formulation of these equations is such that absorption does not depend upon the temperature of the originating source of radiation; indeed, all coefficients are solely dependent upon local values of temperature. Consequently, the validity of the WSGG solution becomes questionable when solving for radiation across paths possessing significant temperature differences, especially when the temperature gradient is large as well. Soufiani and Djavdan (1994) have investigated this failing of a WSGG solution across CO_2-H_2O mixtures between hot and cold walls. Parabolic temperature profiles were considered varying between 500 and 2500 K, and the gaseous partial pressures were assumed constant at 2/3 and 1/3 atm., respectively. The performance of the WSGG solution was compared against a narrow band solution for various overall path lengths and wall emissivities. Predictions of net wall fluxes differed by as much as 43 %, the largest differences occurring for the gas layer between hot walls. This

feature serves to emphasise the difficulty of accurately modelling absorption of radiation from a relatively hot source in the WSGG solution. Additionally, discrepancies were observed to increase as the medium became optically thin, and as wall emissivities decreased.

Of particular interest in the present study is the variation in accuracy of various solutions to the RTE, particularly the WSGG solution, as the temperature range is increased. Therefore, initially in this chapter, the response of the WSGG solution to increasingly larger temperature ranges is appraised. Then, some alternative algorithms are discussed, all of which posses greater sophistication than the WSGG solution, but, as a consequence, are more computationally expensive. A new algorithm is subsequently presented, entitled the differential total absorptivity solution, which has been developed in response to the weaknesses associated with the other algorithms.

4.1.1 Assessment of the WSGG Solution for High Temperature Radiation.

Figure (4.1) shows predictions of volumetric radiative flux by the WSGG and DBT solutions across a CO_2-H_2O mixture (in the ratio of 1 : 2) bounded by black walls. The partial pressure of CO_2 varies parabolically between 0.06 and 0.16. Comparisons are presented for three temperature ranges defined by symmetrical, parabolic profiles with minimum centre-line temperatures of 600 K, and maximum temperatures of 1600, 2000 and 2400 K. These configurations are summarised in Table (4.1). In all cases, the wall temperatures are fixed at the corresponding maximum values.

Net absorption is over-predicted by the WSGG solution across most of the path, but it over-predicts net emission close to the wall. Tabulated in Table (4.2) are mean absolute discrepancies in the volumetric source terms, given by

$$D_v = 100\left|\sum_{all\ cvs}\left[\left|\left[S_{DBT} - S_{WSGG}\right]\right| / S_{DBT}\right]\right| \qquad (4.1)$$

The increasingly poor agreement between the solutions with increasing temperature range is clearly demonstrated.

Smaller discrepancies are evident for a gas layer between cold walls with parabolic maximum temperature and partial pressure profiles defined by configurations F, G and H (cf. Table (4.1)). As shown in Fig. (4.2), the WSGG solution now over-predicts net absorption in the near wall region, and net emission in the hot, high density core. Mean absolute discrepancies again increase with temperature difference, but all values are lower than the corresponding hot boundary cases.

The variation in performance of different solution algorithms relative to the level of soot loading imposed upon a particular gas mixture is also of special interest in the present study. An assessment of the WSGG solution applied to gas-soot mixtures across the same property variations as used above is presented in Figs. (4.3) and (4.4) under intermediate and heavy soot loadings, respectively. The intermediate soot loading generates approximately four times higher emission and absorption than that observed for the gas mixture in the absence of soot, whilst the heavy loadings produce about twice as much again. In both cases, the presence of soot reduces relative differences, and mean absolute discrepancies, between the WSGG and DBT solutions (cf. Table (4.2)).

Encouragingly, these results suggest that the WSGG solution should yield good accuracy when applied to confined flames at temperatures lower than 2000 K, especially in regions where radiative properties are dominated by the presence of soot. The methane jet flame at an elevated total pressure of 3 atm (analysed in chapter 5) can be categorised in this way. However, the performance of the WSGG solution is likely to deteriorate across regions where radiation from gaseous components becomes more significant. Since

such conditions prevail in the methane flame at atmospheric pressure (also simulated in chapter 5), this raises the question of whether the improvement in accuracy of employing more sophisticated algorithms can be justified in terms of the additional computational expense they incur.

4.2 DIFFERENTIAL SOLUTIONS TO THE RTE

4.2.1 Introduction

The WSGG solution to the RTE is particularly economical since it circumvents the need to discretise spectrally resolved transmissivity differentials as well as avoiding spectral integration - cf. Eq. (3.4). In contrast, numerical integration of the differential in the DBT solution becomes prohibitively expensive when performed across numerous lines of sight. A compromise would appear to be appropriate, which provides greater sophistication (and accuracy) than the WSGG solution, but which does not demand the excessive computational expense of the DBT solution. Two approaches have been available for some time. The first, here entitled the differential banded absorptance (DBA) solution, is based upon a wide band description of gaseous radiative properties, and the second employs total radiative properties in a differential total transmissivity (DTT) solution. Both of these solutions are described as they apply to the molecular gases. Then, their extension to gas-soot mixtures are considered.

4.2.2 The Differential Banded Absorptance (DBA) Solution

In the differential banded transmissivity solution, there exists a certain degree of flexibility concerning the minimum acceptable resolution of each band. The majority of bands in the DBT calculations performed here have a width of 25 cm^{-1}. If wide band property models were employed in the same algorithm, band widths of over an order of magnitude greater would be introduced. Notwithstanding the attraction of reducing the

number of modelled bands, evaluation of wide band transmissivities involves uncertainty relating to the most suitable transmissivity for a band, and further approximations are required due to the different widths of corresponding bands across adjacent paths. However, an alternative approach is facilitated by the definition of absorptance given by Eq. (3.26), whereby, integration of the differential transmissivity in Eq. (3.4) can be manipulated into a differential absorptance. Then, the radiative intensity along a path becomes

$$i_{g,n} = \sum_{i=1}^{I}\sum_{j=1}^{J}\left[i_{0,j}\bar{\tau}_{0\to n,j} + \sum_{r=1}^{n}\bar{i}_b\left(T_s,\nu_j\right)\left[F_{r-1\to n,j} - F_{r\to n,j}\right]\right] - C \qquad (4.2)$$

where $F_{r\to n,j}$ represent black body fractions evaluated from band absorptances, and C incorporates all corrections for band overlap when more than one species is considered. Kim et al. (1991) applied Eq. (4.2) in a form modified for the discrete ordinates radiation model, and obtained good agreement with an equivalently modified differential banded transmissivity solution. Notwithstanding the attraction of the DBA solution in terms of the substantially reduced number of bands relative to the DBT solution, the algorithm still incurs considerable computational expense due to the relatively complex expressions required to evaluate band absorptances. Additionally, the corrections for band overlap have to be evaluated.

4.2.3 The Differential Total Transmissivity (DTT) Solution

An entirely different approach to narrow and wide band solutions to the RTE is engendered by reversing the order of integration in Eq. (3.4). Then, the summation of spectrally resolved transmissivity differences is replaced by a difference of total transmissivities, leading to

$$i_{g,n} = i_0 \tau^T_{0\to n}\left(\overline{T}_{0\to n}, \overline{p}_{c,0\to n}, \overline{p}_{h,0\to n}, l_{0\to n}\right) + \sum_{r=1}^{n} i_b\left(T_{r-\frac{1}{2}}\right)\left[\tau^T_{r\to n}\left(\overline{T}_{r\to n}, \overline{p}_{c,r\to n}, \overline{p}_{h,r\to n}, l_{r\to n}\right) - \tau^T_{r-1\to n}\left(\overline{T}_{r-1\to n}, \overline{p}_{c,r-1\to n}, \overline{p}_{h,r-1\to n}, l_{r-1\to n}\right)\right] \quad (4.3)$$

Eq. (4.3) represents the differential total transmissivity (DTT) solution. In contrast to the complexity of the DBA solution, all that is required is a method to evaluate total transmissivities defined by

$$\tau^T_{r\to n}\left(\overline{T}, \overline{p}_c, \overline{p}_h, l\right) = \int_0^\infty i_b(T_s,\nu)\tau_{r\to n}\left(\overline{T}, \overline{p}_c, \overline{p}_h, l, \nu\right)d\nu \Big/ \int_0^\infty i_b(T_s,\nu)d\nu \quad (4.4)$$

The DTT solution was employed by Grosshandler (1980) in the total transmittance non-homogeneous (TTNH) model. To calculate radiative properties for non-homogeneous non-isothermal paths, Grosshandler (1980) recommended concentration weighted temperatures and partial pressures given by

$$\overline{T}_{s'\to s} = \int_{s'}^{s}\left[p_w(s'') + p_c(s'')\right]ds'' \Big/ \int_{s'}^{s}\left\{\left[p_w(s'') + p_c(s'')\right] / T(s'')\right\}ds'' \quad (4.5)$$

$$\overline{p}_{i,s'\to s} = \int_{s'}^{s}\left[p_i(s'')\right]^2 / T(s'')ds'' \Big/ \int_{s'}^{s}\left\{\left[p_i(s'')\right] / T(s'')\right\}ds'' \quad (4.6)$$

Using the total emissivity curve-fits due to Modak (1979), Grosshandler demonstrated good accuracy of the DTT solution applied to lines of sight through a range of flame configurations. However, correction to the transmissivities were required in order to account for the different

temperature dependence in Eq. (4.4) of the black body intensity and the total transmissivity. This shortcoming of the TTNH method led to the development of the differential total absorptivity solution by Bressloff et al. (1996a), which is described in section 4.3.

4.2.4 Gas-soot Mixtures

When using narrow band data in the differential banded transmissivity solution, transmissivities are simply evaluated as the product of all contributing components, where the soot transmissivity from the leading edge of a cell to the end of a path is

$$\tau_{p,r\to n,j} = e^{-c_0 \Phi \nu L} \tag{4.7}$$

ν denotes the wave number at the centre of a band and L represents the distance from r to n. For inhomogeneous paths a mean value of soot volume fraction is required. Treatment of gas-soot mixtures is less straightforward in the DBA and DTT solutions, since the approximations made in their formulation do not permit simple combination of the contributions to the total intensity from individual components. Expansion of the spectral absorptivity of a gas-soot mixture leads to

$$\alpha_{\nu,g+p} = \alpha_{\nu,g} + \alpha_{\nu,p} - \alpha_{\nu,g}\alpha_{\nu,p} \tag{4.8}$$

Substituting this equation into the integrated radiative transfer equation then yields the total intensity as the sum of the intensities solved separately for the solid and gaseous states together with a correction. Therefore, a method is required to solve the RTE for soot.

Due to the continuous nature of soot radiation, fewer solution techniques have been developed for soot than for the treatment of gases.

However, under the assumptions described in section (3.3.3), it is possible to derive an exact expression for the variation of intensity through a medium containing only soot.

When Eq. (3.34) and the Planck function, Eq. (3.35), are substituted into Eq. (3.4), integration by parts yields, for cold black boundaries,

$$i_p = -\frac{c_0 C_1}{\pi C_2{}^5} \int_0^s T(s')^5 \Phi(s') \Psi^{(4)} \left(1 + \frac{c_0 T(s')}{C_2} \int_{s'}^s \Phi(s'') ds'' \right) ds' \tag{4.9}$$

Representing Eq. (4.9) numerically across n elements yields a direct solution to the RTE for soot

$$i_{p,n} = -\frac{c_0 C_1}{\pi C_2{}^5} \sum_{r=1}^{n} I \left(T_r^5 \Phi_r \Psi^{(4)} \left(1 + \frac{c_0 T_n}{C_2} \sum_{r'=r}^{n} I\left(\Phi_{r'}, \Delta s_{r'}\right) \right), \Delta s_r \right) \tag{4.10}$$

where $I(a,b)$ represent individual terms in the numerical integration, and the hexa-gamma function, Ψ^4, is evaluated from Eq. (3.38).

Eq. (4.8) has been applied by Grosshandler and Modak (1981) using the TTNH model for gaseous radiation, Eq. (4.10) for particulate radiation and an iterated temperature term for the correction. Grosshandler and Modak (1981) identified weaknesses of this method for certain paths. They suggested that for some configurations the correction should be incorporated into a term representing soot radiance that is transmitted by the gas. This would then be added to the gas radiance. A further alternative is to write the combined absorptivity from Eq. (4.8) as

$$\alpha_{\nu,g+p} = \alpha_{\nu,p} + \alpha_{\nu,g} \tau_{\nu,p} \tag{4.11}$$

such that gas radiance transmitted by the soot is added to the radiance due to soot alone.

Eq. (4.11) has been employed by Buckius and Tien (1977) in solutions to the RTE based upon the exponential wide band gas property model. The differential banded absorptance solution was manipulated to incorporate soot by assuming constant particulate transmissivity across a band. Thus,

$$i_n = i_{p,n} + \sum_{i=1}^{I}\sum_{j=1}^{J}\left[i_{0,j}\bar{\tau}_{0\to n,j} + \sum_{r=1}^{n}\bar{i}_b\left(T_s,\nu_j\right)\left[\bar{\tau}_{p,r-1\to n}F_{r-1\to n,j} - \bar{\tau}_{p,r\to n}F_{r\to n,j}\right] - C\right] \tag{4.12}$$

where $i_{p,n}$ is evaluated by Eq. (4.10). The correction, C, and the transmissivity of boundary radiation, $\bar{\tau}_{0\to n,j}$, both now account for the presence of soot (cf. Felske and Tien, 1973). The mean transmissivity of soot in a band is approximated by

$$\bar{\tau}_{p,r\to n} = \frac{1}{2}\left\{exp-\left[c_0\bar{\Phi}L\nu_l\right] + exp-\left[c_0\bar{\Phi}L\nu_u\right]\right\} \tag{4.13}$$

which represents the mean of the values evaluated at the lower, ν_l, and upper, ν_u, wave numbers of the band. The complexity associated with the DBA solution for gases alone is clearly exacerbated when extended to mixtures of gases and soot.

Although both the DBA and DTT solutions possess intrinsically attractive formulations, both are weakened by their associated assumptions, and by the cumbersome extension to gas-soot mixtures. A new algorithm has been developed, the differential total absorptivity solution, which avoids these shortcomings.

4.3 THE DIFFERENTIAL TOTAL ABSORPTIVITY (DTA) SOLUTION

4.3.1 Introduction

Current computing capabilities suggest that both the WSGG and DTT solutions satisfy the broad compromise between accuracy and cost. The weighted sum of gray gases method is relatively fast but is inhibited by the aspiration for general applicability of a set of coefficients evaluated for a limited range of conditions. Grosshandler's TTNH model, which applies the DTT solution, is slower than the WSGG method, and is weakened by the need for corrections as explained above. These corrections can be avoided if the differential transmissivity of the DTT solution is treated as a differential absorptivity. This then permits explicit modelling of the source temperature dependence of absorption.

The differential total absorptivity solution was originally devised for combustion gases by Bressloff et al. (1996a). Its derivation is based upon re-writing Eq. (3.4) in terms of absorptivities :

$$i(s) = \int_0^\infty i_\nu(0)\left[1-\alpha_\nu(0\rightarrow s)\right]d\nu - \int_0^\infty\int_0^s i_{b,\nu}(s')\frac{\delta\alpha_\nu(s'\rightarrow s)}{\delta s'}ds'd\nu \qquad (4.14)$$

Then, if a total absorptivity is defined as

$$\alpha^T_{r\rightarrow n}\left(T_s,\overline{T},\overline{p}_c,\overline{p}_h,l\right) = \int_0^\infty i_b\left(T_s,\nu\right)\alpha_{r\rightarrow n}\left(T_s,\overline{T},\overline{p}_c,\overline{p}_h,l,\nu\right)d\nu \Big/ \int_0^\infty i_b\left(T_s,\nu\right)d\nu \qquad (4.15)$$

the DTA solution is given by

$$
\begin{aligned}
i_n &= i_0\left[1-\alpha^T_{0\to n}\left(T_0,\overline{T}_{0\to n},\overline{p}_{c,0\to n},\overline{p}_{h,0\to n},l_{0\to n}\right)\right] \\
&+ \sum_{r=1}^{n} i_b\left(T_{r-\frac{1}{2}}\right)\left[\alpha^T_{r-1\to n}\left(T_{r-\frac{1}{2}},\overline{T}_{r-1\to n},\overline{p}_{c,r-1\to n},\overline{p}_{h,r-1\to n},l_{r-1\to n}\right)\right. \\
&\qquad \left. - \alpha^T_{r\to n}\left(T_{r-\frac{1}{2}},\overline{T}_{r\to n},\overline{p}_{c,r\to n},\overline{p}_{h,r\to n},l_{r\to n}\right)\right]
\end{aligned}
\tag{4.16}
$$

where mean temperatures and partial pressures are evaluated by Eqs. (4.5) and (4.6). The source temperature dependence of absorption requires that absorptivities are evaluated from both the trailing and leading edges of each element as a function of the source temperature, $T_{r-1/2}$, and the mean thermodynamic properties for the corresponding paths. The subscripts in Eq. (4.16) are such that each element is signified by $r-1/2$ with properties from the trailing and leading edges to the end of the line of sight denoted by $r-1\to n$ and $r\to n$, respectively.

In contrast, transmissivities in the DTT solution are evaluated from the trailing edge of each element along a path as a function of the mean temperature for that path. These transmissivities are then also used in the finite difference calculation for the leading edge of the adjacent element.

All that is required by the DTA solution is an accurate and efficient means for evaluating total absorptivities. Most of the gas property models are formulated to generate emissivities, and relatively simple expressions are available to convert them into absorptivities. A commonly used example suggested by Hottel and Egbert (1942) is

$$
\alpha^T = \varepsilon^T\left[\overline{T}/T_s\right]^{\left[0.65-\frac{0.2\,p_h}{p_h-p_c}\right]} \tag{4.17}
$$

Alternatively, weighted sum of gray gases curve-fits to total absorptivity data can be used. Smith et al. (1982) generated such data from the exponential wide band model. The total absorptivity is defined by

$$\alpha^T = \sum_{j=0}^{J} a_j(T,T_s)\left[1-e^{-k_j pL}\right] \tag{4.18}$$

where

$$a_j(T,T_s) = \sum_{k=1}^{K}\left[\left[\sum_{l=1}^{L} c_{j,k,l}T_s^{k-1}\right]T^{j-1}\right] \tag{4.19}$$

The coefficients, $c_{j,k,l}$, are tabulated in Table (4.3).

In the assessment of the DTA solution presented below, the DBT solution is again used as a benchmark for the prediction of radiative intensity across single lines of sight, and of the volumetric radiative flux across layers bounded by solid walls. Comparisons are made between the WSGG solution, the DTT solution, and two DTA solutions, the first using Modak's data and Eq. (4.17), and the second employing the weighted sum of gray gases total absorptivity expression given by Eq. (4.18). The differential banded absorptance solution (employing wide band property data) is not included in the analysis since the method does not satisfactorily satisfy the compromise between accuracy and cost relative to the DBT solution.

The same parabolic temperature and partial pressure configurations as described above are used for both the individual line of sight calculations, and in the full DTRM calculations. Since Modak's curve-fits were validated up to a maximum temperature of 2000 K, performance of the DTA and DTT solutions which employ this data is expected to lose reliability across the largest temperature range analysed here. Both sets of weighted sum of gray gases data were validated up to a temperature of 2400 K.

4.3.2 Assessment of the DTA Solution Applied to CO_2-H_2O Mixtures

Figs. (4.5) and (4.6) show the variation of radiative intensity across the parabolic minimum and maximum profiles, respectively. The characteristic shapes were described in sub-section (3.4.6.2), and they remain unchanged as the temperature range is increased.

In Fig. (4.5), the differential total property solutions capture the initial turning point of intensity after which absorption exceeds further emission. However, subsequently, all methods over-predict absorption relative to the DBT solution, and these differences increase with the widening temperature range. In accordance with features observed in section (4.1), the WSGG solution over-predicts emission at the start of the path and absorption thereafter.

Values of the mean absolute discrepancy for radiative intensity (relative to the DBT solution) are evaluated by

$$D_i = 100\left|\sum_{all\ cvs}\left[\left|\left[i_{DBT}-i\right]\right|/i_{DBT}\right]\right| \tag{4.20}$$

They are tabulated in Table (4.4). Somewhat surprisingly, D_i is effectively constant for the WSGG solution, whereas there is a trend of increasing differences with temperature range in the differential total property solutions. Lowest values of D_i are associated with the DTA solution using weighted sum of gray gases absorptivities due to Smith et al. (1982).

Significantly better performance is produced by all solutions when applied to the parabolic maximum temperature and partial pressure profiles. The intensity variation is shown in Fig. (4.6) and the associated discrepancies are given in Table (4.4). Now, as the temperature range is increased, the discrepancy of the WSGG solution increases, whilst that for the second DTA solution decreases. This latter trend is a consequence of large relative errors at the start of the path produced for the lower

temperature profiles.

Line of sight calculations provide relatively limited insight into the performance of an algorithm since only a small number of path length configurations are encountered. Evaluation of radiative fluxes across a layer bounded by solid walls presents a sterner test of an algorithms ability to predict radiative property variations. Figs. (4.7) and (4.8) compare predictions of the volumetric radiative flux by the DTRM using the same algorithms, and across identical temperature and partial pressure configurations as above. The boundaries are assumed to be black and isothermal with temperatures given by the end-point values of the functional variations imposed on the layer.

The characteristic M- and U-shaped profiles of volumetric flux described in chapter 3 are repeated for hot and cold boundary temperatures, respectively, for all temperature ranges. Both net emission and net absorption increase with temperature range.

With reference to Table (4.5), the second DTA solution using total absorptivity data produces significantly superior performance across configurations E and H representing the largest temperature ranges. The method is particularly accurate in the interior of the layers, where mean absolute discrepancies are reduced to below 15 %; that is, if relative differences at elements adjacent to the boundaries are excluded from the calculation.

4.3.3 Assessment of the DTA Solution Applied to Soot

The DTA solution can be applied to soot, in which case Eq. (4.16) becomes

$$
\begin{aligned}
i_{p,n} \;=\; & i_0\left[1-\alpha^T_{0\to n}\left(T_0,\overline{\Phi}_{0\to n},l_{0\to n}\right)\right] \\
& + \sum_{r=1}^{n} i_b\left(T_{r-\frac{1}{2}}\right)\Big[\alpha^T_{r-1\to n}\left(T_{r-\frac{1}{2}},\overline{\Phi}_{r-1\to n},l_{r-1\to n}\right) \\
& \qquad - \alpha^T_{r\to n}\left(T_{r-\frac{1}{2}},\overline{\Phi}_{r\to n},l_{r\to n}\right)\Big]
\end{aligned}
\tag{4.21}
$$

where the absorptivities are functions of the source temperature and the distribution of soot. It is to be recalled, that in contrast to the curve-fitting methods adopted for CO_2 and H_2O, accurate and relatively simple analytical expressions are available for the total absorptivity of soot (cf. Eqs. (3.37), (3.39) and (3.40)).

The radiative intensity variation across configurations C to E are shown in Fig. (4.9) for the intermediate soot loading configuration, D_s. The DTA solution employing Eq. (3.37) is compared against the path integral given by Eq. (4.10), the WSGG solution and the DBT solution for soot in the absence of any gases. The same comparisons are made for configurations F to H with an intermediate soot loading configuration, B_s (cf. Fig. (4.10)). Mean absolute discrepancies are shown in Table (4.6).

Extremely good agreement is produced between the DBT solution, the path solution represented by Eq. (4.10) and the DTA solution. The WSGG solution produces larger differences which become more significant with an increasing temperature range.

An assessment of the DTA solution applied to soot in a complete DTRM calculation is effectively provided in the next section (which appraises the method when extended to gas-soot mixtures) since the radiative contribution from soot dominates the overall behaviour of a gas-soot mixture when soot concentrations are high.

4.3.4 The DTA Solution Applied to Mixtures of CO_2, H_2O and Soot

Extension of the DTA solution to mixtures of CO_2-H_2O and soot is

established by defining a transmissivity product

$$\tau_g^T \tau_p^T = \int_0^\infty i_b(T_s,\nu)\tau_{\nu,g}\tau_{\nu,p}d\nu \Big/ \int_0^\infty i_b(T_s,\nu)d\nu \tag{4.22}$$

such that the spectral transmissivity product implicit in Eq. (3.4) can be re-expressed as the product of total transmissivities. The DTA solution for gas-soot mixtures is then given by

$$\begin{aligned} i_n &= i_0 \tau^T_{g,0\to n}\tau^T_{p,0\to n} \\ &+ \sum_{r=1}^{n} i_b\left(T_{r-\frac{1}{2}}\right)\left[\tau^T_{g,r\to n}\tau^T_{p,r\to n} - \tau^T_{g,r\to n-1}\tau^T_{p,r\to n-1}\right] \end{aligned} \tag{4.23}$$

where the transmissivities are evaluated from source temperature dependent absorptivities. The complete set of dependencies for gases and soot are the same as those expressed in Eqs. (4.16) and (4.21), respectively. Solid wall radiation is multiplied by a total transmissivity calculated for the whole path from the wall to the end of the line of sight. If the soot transmissivity is extracted from the product of spectral transmissivities, the transmission of solid wall radiation is then represented by the product of total transmissivities given by the first term in Eq. (4.23).

In order to incorporate the path solution represented by Eq. (4.10) into the following comparisons for gas-soot mixtures, an approach is followed which avoids the need for corrections of any description.

From the definition,

$$\alpha_g^T \tau_p^T = \int_0^\infty i_b(T_s,\nu)\alpha_{\nu,g}\tau_{\nu,p}d\nu \Big/ \int_0^\infty i_b(T_s,\nu)d\nu \tag{4.24}$$

substitution of Eq. (4.11) into the integrated form of the RTE yields the radiative intensity,

$$i_n = i_0\tau^T_{g,0\to n}\tau^T_{p,0\to n} + i_{p,n} + \sum_{r=1}^{n} i_b\left(T_{r-\frac{1}{2}}\right)\left[\alpha^T_{g,r\to n-1}\tau^T_{p,r\to n-1} - \alpha^T_{g,r\to n}\tau^T_{p,r\to n}\right] \quad (4.25)$$

where $i_{p,n}$ is given by Eq. (4.10). This representation is preferred to those requiring corrections, since the transmissivity of soot is then based upon the source temperature of each differential path. Additionally, it avoids the need to evaluate an equivalent temperature for the correction term as proposed by Grosshandler and Modak (1981). The gaseous total absorptivities, and the total soot transmissivities, can be calculated by the methods previously discussed.

Comparisons are now made between the solution based upon Eq. (4.25), the WSGG solution, the DTA algorithm given by Eq. (4.23), and the DBT solution. Appendix A summarises the various algorithms. First, volumetric flux predictions between black boundaries are compared across configurations C to E with intermediate and heavy soot loading configurations, D_s and C_s, respectively. The results are shown in Figs. (4.11) and (4.12), and mean absolute discrepancies are tabulated in Table (4.7). In all cases, the DTA solution agrees to within 5 % of the DBT solution, with particularly close agreement for the heavy soot loading. The WSGG solution and Eq. (4.25) generate significantly larger differences, but demonstrate considerably better concurrence than for the corresponding solutions generated by the same gas mixtures in the absence of soot. Second, the parabolic maximum configurations, F to H, are combined with intermediate and heavy soot loadings, B_s and A_s, respectively. Volumetric

flux predictions between black walls are depicted in Figs. (4.13) and (4.14), and the corresponding mean absolute discrepancies are shown in Table (4.8). Differences are generally greater than those produced by the mixtures between hot walls, but still, in nearly every case, the DTA solution agrees most closely with the DBT solution.

4.3.5 Assessment of the DTA Solution between Gray Boundaries

In the differential total property solutions, a problem has been encountered regarding the transmission of radiation from gray boundaries, especially in cases where high reflectivity cool walls bound a hot gas. It would seem that when a relatively low wall temperature is used to evaluate the absorption of radiation, part of which originates at a higher temperature, this produces an under-estimation of overall absorption. In order to compensate for this discrepancy, an effective wall temperature can be defined as

$$T_w' = \left[\frac{\pi}{\varepsilon\sigma}\left[\frac{\varepsilon\sigma T_w^4}{\pi} + [1-\varepsilon]q^-\right]\right]^{0.25} \tag{4.26}$$

T_w' is then treated as the source temperature in the calculation of total absorptivities such that the wall is assumed to be radiating as a black body at this temperature.

Figs. (4.15) and (4.16) depict the same analyses as those represented in Figs. (4.11) and (4.13), respectively, but for low emissivity walls ($\varepsilon = 0.25$). Now that reflection has to be accounted for, the DBT and WSGG solutions become more complex. As explained in the previous chapter, reflected radiation must be treated separately for each band/component. In contrast, the total property solutions simply require an initial intensity which comprises the sum of emitted and reflected contributions.

Most notable amongst the results shown in Table. (4.8), is the excellent

agreement between the DTA and DBT solutions for the mixture bounded by cold walls. Discrepancies are less than 5 %. Larger differences are produced in the other case, with considerable relative differences at the second node from the wall.

4.3.6 Comparison of Computational Expense

The cpu times reported in this sub-section were recorded on a DEC Alpha 200 4/100 workstation for one iteration of the discrete transfer radiation model performed for the one-dimensional layers analysed above. Thus, the quoted times represent the cost accrued by each algorithm when applied across 20 control volumes of a gas-soot mixture bounded by solid boundaries (with reflection at four symmetry planes). 16 rays were employed from two launch sites. In order to extrapolate this information to other problems, it would be necessary to know the number of individual path elements actually comprised in such a specification. Nonetheless, it is not the intention to do that here, since the relative cost of each algorithm is of greater concern.

The DBT solution required almost a second for each of its 566 bands. Therefore, a considerable time saving accompanied the differential total property solutions, which required approximately 3 seconds per iteration. However, the DTA and DTT solutions were over an order of magnitude slower than the WSGG solution. These significantly different costs represent the fulcrum upon which a balance has to be struck between accuracy and computational expense. There would appear to be a strong case for employing the WSGG solution to combustion media possessing relatively low maximum temperatures across individual paths, and in which radiative behaviour is dominated by soot. This issue is further discussed in chapter 5.

4.4 CONCLUSIONS

Motivated by failure of the weighted sum of gray gases (WSGG) solution to adequately represent the source temperature dependence of absorption, this chapter has sought to investigate the viability of modelling the radiative transfer equation by differential solutions. The WSGG solution is particularly inaccurate when predicting absorption of high temperature radiation in mixtures comprising significant concentrations of gases. Better performance is produced when radiation is dominated by soot.

Although the second term in Eq. (3.4) is modelled directly by the more sophisticated differential banded absorptance (DBA) solution and the differential total transmissivity (DTT) solution, both algorithms become fairly cumbersome when applied to mixtures of gases and soot. Consequently, they incur considerable computational expense relative to the WSGG solution. Since the DBA solution is particularly expensive, it has not been included in the comparisons presented above. The DTT solution as used in the TTNH model by Grosshandler (1980) is less costly, but requires corrections to differential transmissivity terms to account for the dependence of absorption on the source temperature of radiation.

In response to the various weaknesses of the WSGG, DBA and DTT solutions, a new algorithm has been developed entitled the differential total absorptivity (DTA) solution. Most notably, the DTA solution treats the source temperature dependence of absorption explicitly, and it can be simply applied to mixtures of gases and soot.

For gases, two methodologies are available for evaluating total absorptivities. Since most total radiative property data is provided in terms of emissivities, empirically based modifications have been formulated to obtain absorptivities from emissivities. However, the direct evaluation of absorptivities is to be preferred. Indeed, in this chapter, a weighted sum of gray gases model of total absorptivities for CO_2-H_2O mixtures due to Smith et al. (1982) has been successfully combined with a numerical integration of

soot absorptivity, in the DTA prediction of volumetric radiative flux across a range of configurations. Relative to the other algorithms considered, closest agreement with a narrow band differential banded transmissivity solution has been produced by the DTA algorithm.

The performance of differential total property solutions to the RTE is constrained by the quality of total property data. Thus, since the range of validity of a particular set of data is unlikely to completely satisfy the conditions prevailing in practical combustion media, a broader data base is required than that currently available. Another problem is associated with the treatment of solid wall radiation. For example, although the present formulation of the DTA solution incorporates the boundary temperature in the evaluation of absorption from solid wall radiation, it is only possible to use a single mean temperature to represent the absorbing path. Such an approach cannot be expected to adequately capture the radiative behaviour across non-uniform paths. An alternative must be sought.

The preceding analysis has demonstrated that greater concurrence exists between various algorithms when modelling soot radiation as opposed to the radiative behaviour of molecular gases. (Better agreement is also obtained for lower temperature ranges.) Therefore, significant quantities of soot in gas-soot mixtures mitigates against the application of more complex (and costly) algorithms for the computational prediction of radiative exchange in practical combustion problems. Consequently, the WSGG solution should yield acceptable accuracy when applied to the turbulent diffusion flames modelled in the following chapter. These are characterised by intermediate to high soot concentrations, and relatively low overall temperature ranges. Under such conditions, the moderate improvement in accuracy likely to be afforded by the differential total absorptivity solution cannot justify the greater cpu expense. The reverse may be true in environments possessing low soot concentrations and/or high temperature ranges.

Configuration	Temperatrue (K)	Partial pressure of CO_2 (atm)
C	$7200s(s-L)+2400$	$0.4s(s-L)+0.16$
D	$5600s(s-L)+2000$	$0.4s(s-L)+0.16$
E	$4000s(s-L)+1600$	$0.4s(s-L)+0.16$
F	$7200s(L-s)+600$	$0.4s(L-s)+0.06$
G	$5600s(L-s)+600$	$0.4s(L-s)+0.06$
H	$4000s(L-s)+600$	$0.4s(L-s)+0.06$

Table 4.1 Temperature-partial pressure configurations. L = 1.0 m.

Configuration	Mean Absolute Discrepancy (%)
C	43.2 (39.5) *
D	60.5 (50.3) *
E	86.6 (63.4) *
F	30.9
G	32.9
H	42.0
C, D_s	16.6 (8.3) *
D, D_s	28.2 (9.2) *
E, D_s	53.2 (12.0) *
F, B_s	14.4 (14.4) #
G, B_s	26.8 (11.8) #
H, B_s	18.5 (11.7) #
C, C_s	7.7
D, C_s	8.2
E, C_s	10.1
F, A_s	8.6
G, A_s	10.1
H, A_s	17.8

Table 4.2 Mean absolute discrpancies for the volumetric flux of the WSGG solution relative to the DBT solution across various gas and gas-soot mixtures between black walls. (Bracketed values denote discrepancies : excluding 4th node from wall #; excluding 1st node from wall *).

j	k	l = 1	l = 2	l = 3	l = 4
1	1	0.59324e-00	-0.61741e-03	0.29248e-06	-0.45823e-10
2	1	-0.35644e-01	0.21502e-03	-0.13648e-06	0.24284e-10
3	1	0.12951e-00	0.54520e-04	-0.80049e-07	0.17813e-10
1	2	0.5739e-03	0.22122e-06	-0.26380e-09	0.45951e-13
2	2	0.51605e-03	-0.70037e-06	0.38680e-09	-0.70429e-13
3	2	0.15210e-03	-0.37750e-06	0.21019e-09	-0.36011e-13
1	3	-0.71313e-06	0.46181e-09	-0.70858e-13	0.38038e-17
2	3	0.12245e-06	0.99434e-10	-0.15598e-12	0.37664e-16
3	3	-0.13165e-06	0.20719e-09	-0.96720e-13	0.14087e-16
1	4	0.17806e-09	-0.11654e-12	0.19939e-16	-0.13486re20
2	4	-0.57563e-10	-0.10109e-12	0.19939e-16	-0.13486e-20
3	4	0.26872e-10	-0.34803e-13	0.14336e-16	-0.19754e-20

Table 4.3 Coefficients, $c_{j,k,l}$, for the absorptivity of a CO_2-H_2O mixture at a total pressure of 1atm (cf. Eq. 4.19). p_c/p_h=*0.5*. (cf. Smith et al, 1982).

Configuration	WSGG	DTT	DTA(Modak)	DTA(wsgg)
C	17.8	12.5	15.9	9.9
D	18.2	16.5	19.0	13.6
E	17.5	20.2	17.4	16.0
F	5.5	5.4	5.0	8.6
G	7.0	5.5	4.2	7.7
H	11.0	9.7	14.2	5.7

Table 4.4 Mean absolute discrepancies of radiative intensity relative to the DBT solution for lines of sight across CO_2-H_2O mixtures.

Configuration	WSGG	DTT	DTA(Modak)	DTA(wsgg)
C	43.2 (39.5) *	32.2 (31.6) *	34.1 (34.1) *	30.1 (23.7) *
D	60.5 (50.3) *	43.6 (42.1) *	46.0 (43.6) *	33.0 (18.0) *
E	86.6 (63.4) *	68.8 (71.5) *	68.7 (71.4) *	49.1 (14.0) *
F	30.9	13.4	31.7	33.4
G	32.9	30.8	24.2	32.5
H	42.0	50.1	56.1	28.4

Table 4.5 Mean absolute discrepancies of volumetric radiative flux relative to the DBT solution for a DTRM calculation across CO_2-H_2O mixtures between black walls. (Bracketed values denote discrepancies excluding 1st node from wall *).

Configuration	WSGG	Eq. (4.10)	DTA - Eq. (4.21)
C, D_s	1.5	0.01	0.02
D, D_s	3.9	0.09	0.10
E, D_s	7.3	0.46	0.47
F, B_s	2.0	0.02	0.02
G, B_s	4.5	0.13	0.14
H, B_s	7.5	0.63	0.64

Table 4.6 Mean absolute discrepancies of radiative intensity relative to the DBT solution for lines of sight across intermediate soot concentrations.

Configuration	WSGG	Eq. (4.25)	DTA - Eq. (4.23)
C, D_s	16.6 (8.3) *	19.9 (9.1) *	11.2 (4.6) *
D, D_s	28.2 (9.2) *	27.7 (6.9) *	17.0 (3.2) *
E, D_s	53.2 (12.0) *	113.7 (6.3) *	35.8 (3.1) *
C, C_s	7.7 (7.7) *	14.6 (12.1) *	1.4 (1.2) *
D, C_s	8.2 (8.8) *	10.7 (9.5) *	1.5 (1.2) *
E, C_s	10.1 (11.0) *	16.7 (11.5) *	1.5 (1.2) *
F, B_s	69.9 (14.4) #	34.1 (6.6) #	42.1 (9.5) #
G, B_s	26.8 (11.8) #	17.9 (8.0) #	13.9 (6.9) #
H, B_s	18.5 (11.7) #	16.2 (11.8) #	8.4 (5.9) #
F, A_s	8.6	1.8	2.0
G, A_s	10.1	0.9	1.3
H, A_s	17.8	3.6	1.3

Table 4.7 Mean absolute discrepancies of volumetric radiative flux relative to the DBT solution for a DTRM calculation across CO_2-H_2O-soot mixtures between black walls. (Bracketed values denote discrepancies : excluding 4th node from wall #; excluding 1st node from wall *).

Configuration	WSGG	Eq. (4.25)	DTA - Eq. (4.23)
C, D_s	25.2 (9.4) *	41.9 (8.5) *	41.5 (15.3) *
D, D_s	21.5 (11.0) *	38.8 (11.4) *	24.6 (11.4) *
E, D_s	23.8 (12.7) *	23.8 (13.6) *	16.4 (9.9) *
F, B_s	6.1	13.5	4.5
G, B_s	8.3	11.5	3.5
H, B_s	10.5	10.7	3.5

Table 4.8 Mean absolute discrepancies of volumetric radiative flux relative to the DBT solution for a DTRM calculation across CO_2-H_2O-soot mixtures between low emissivity walls (ε = 0.25). (Bracketed values denote discrepancies excluding 2nd node from wall *).

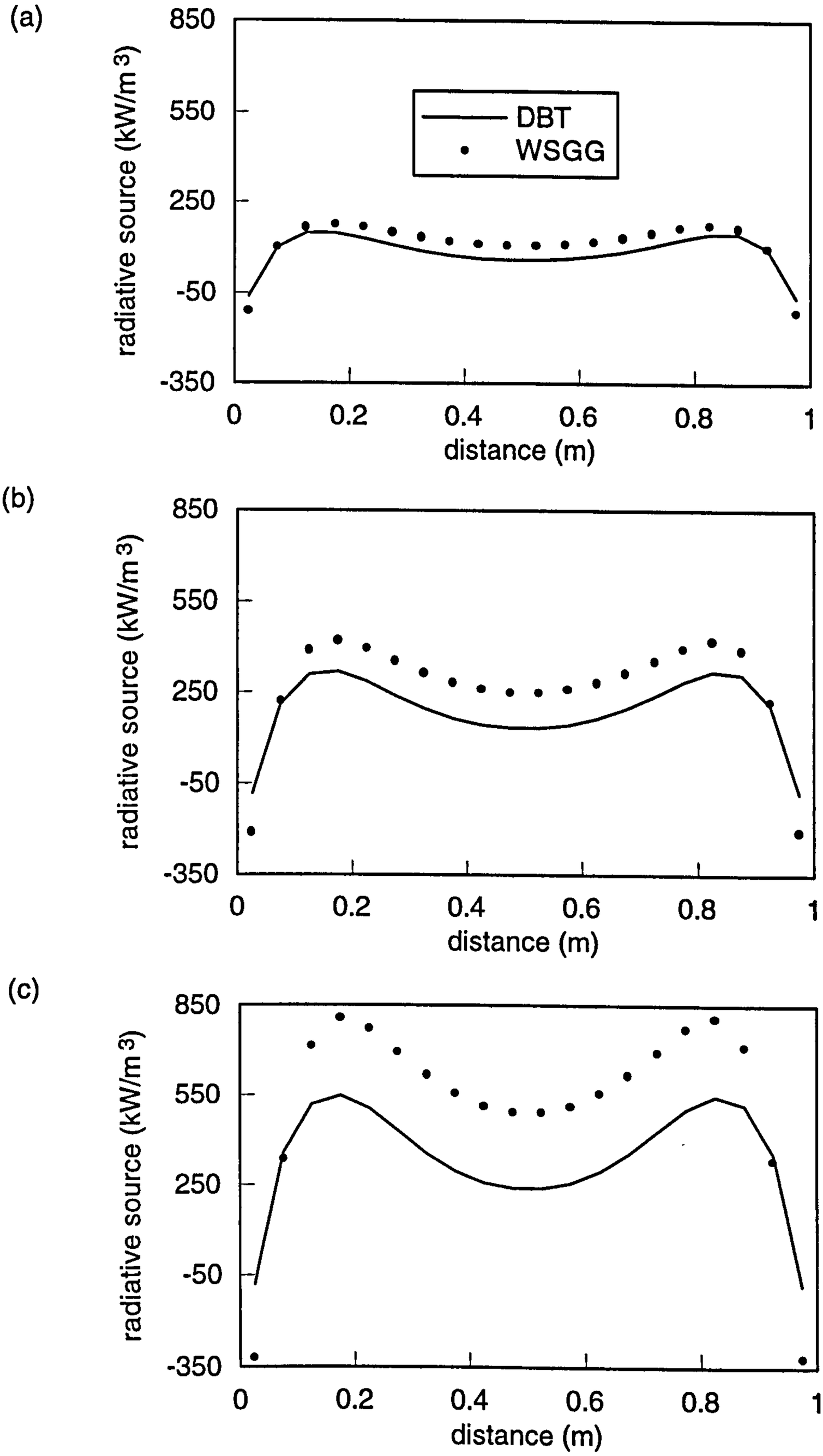

Fig. 4.1 Comparison of the WSGG and DBT solutions for a CO_2-H_2O mixture between hot black walls : (a) configuration C (T_w = 1600 K); (b) configuration D (T_w = 2000 K); (c) configuration E (T_w = 2400 K). (T_{cl} = 600 K).

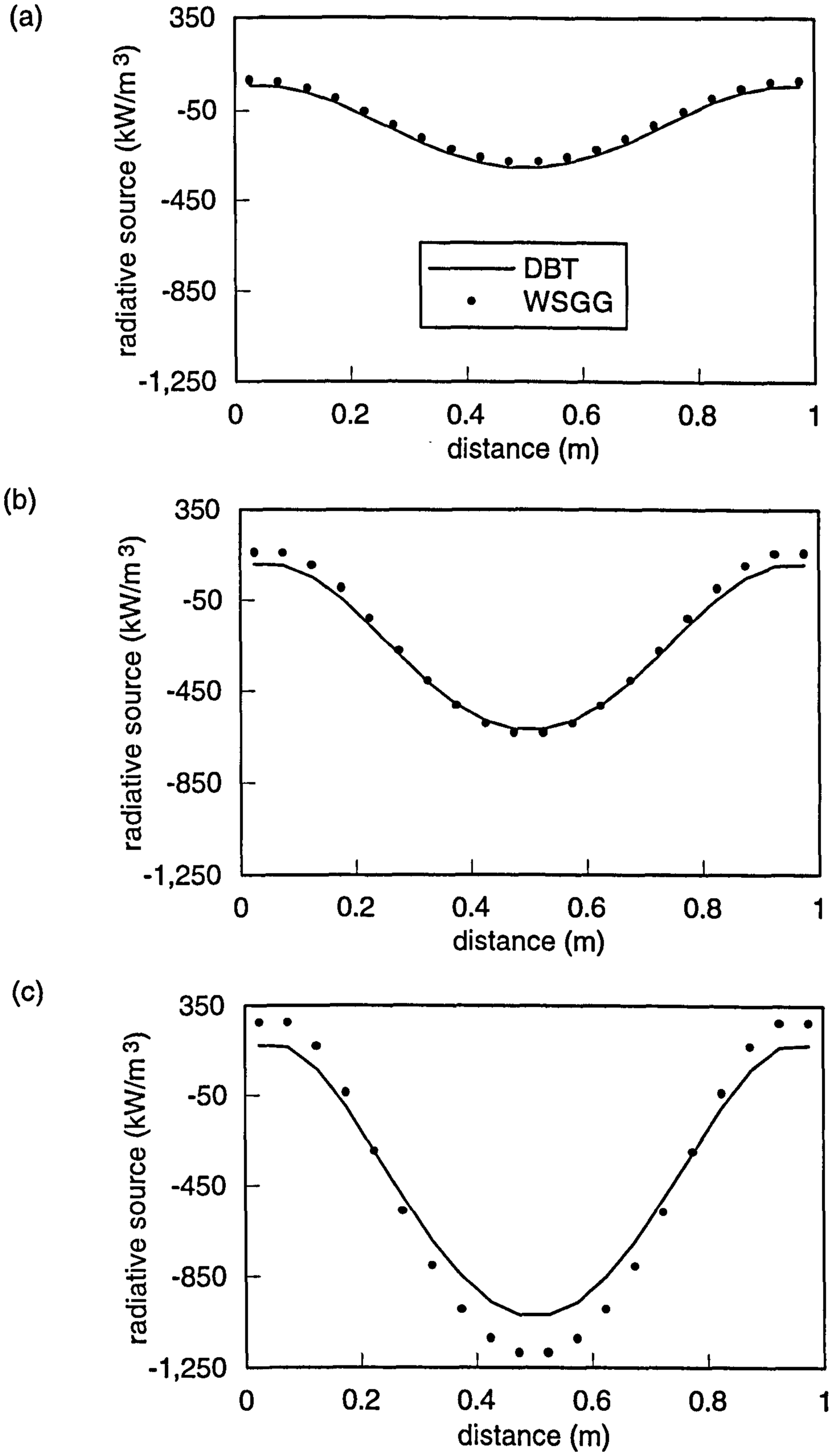

Fig. 4.2 Comparison of the WSGG and DBT solutions for a CO_2-H_2O mixture between cold black walls : (a) configuration F (T_{cl} = 1600 K); (b) configuration G (T_{cl} = 2000 K); (c) configuration H (T_{cl} = 2400 K). (T_w = 600 K).

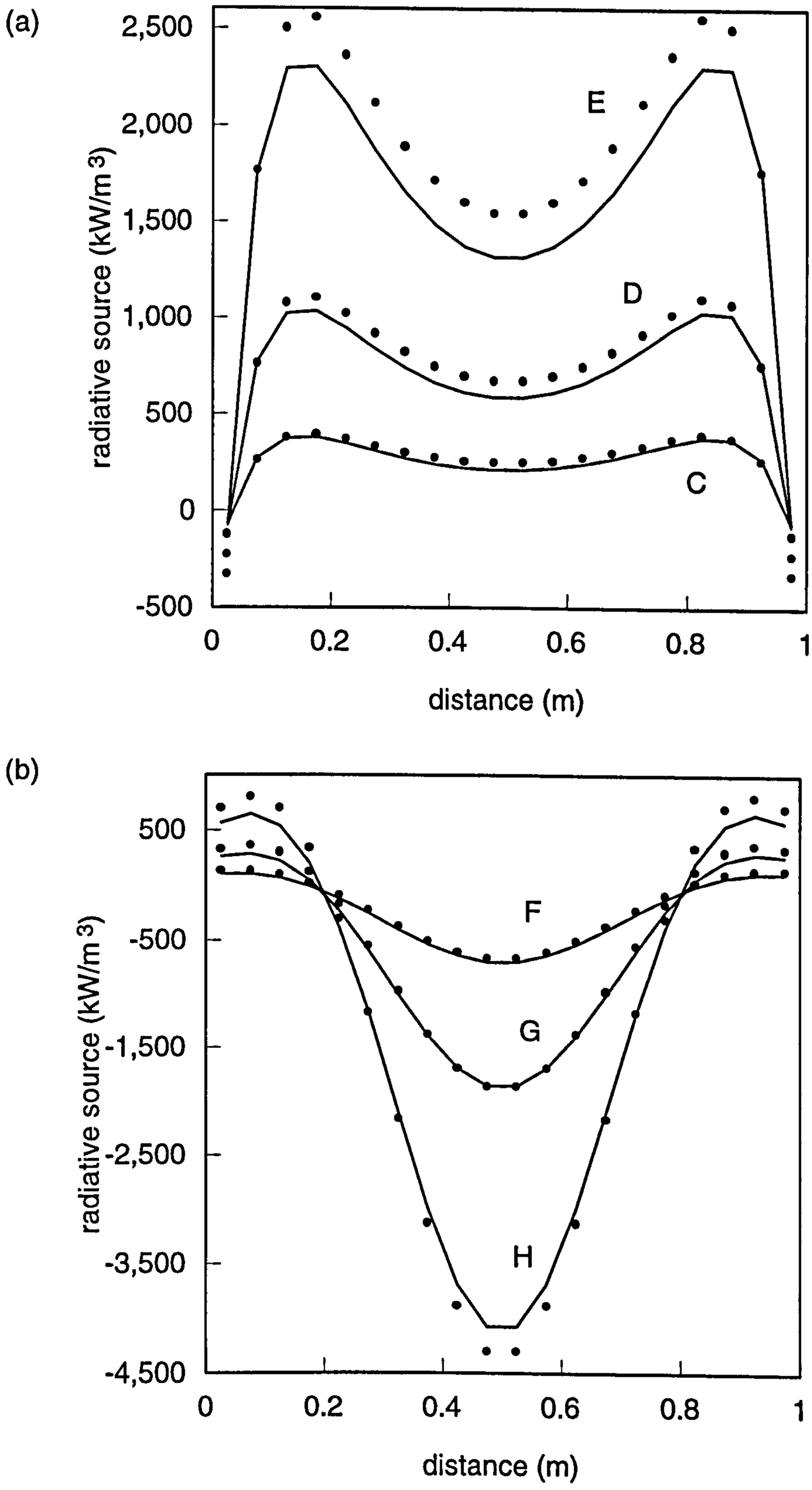

Fig. 4.3 Comparison of the WSGG and DBT solutions across gas-soot layers for configurations C to H combined with intermediate soot loadings : (a) between hot black walls (soot configuration D_s; T_{cl} = 600 K); (b) between cold black walls (soot configuration B_s; T_w = 600 K).

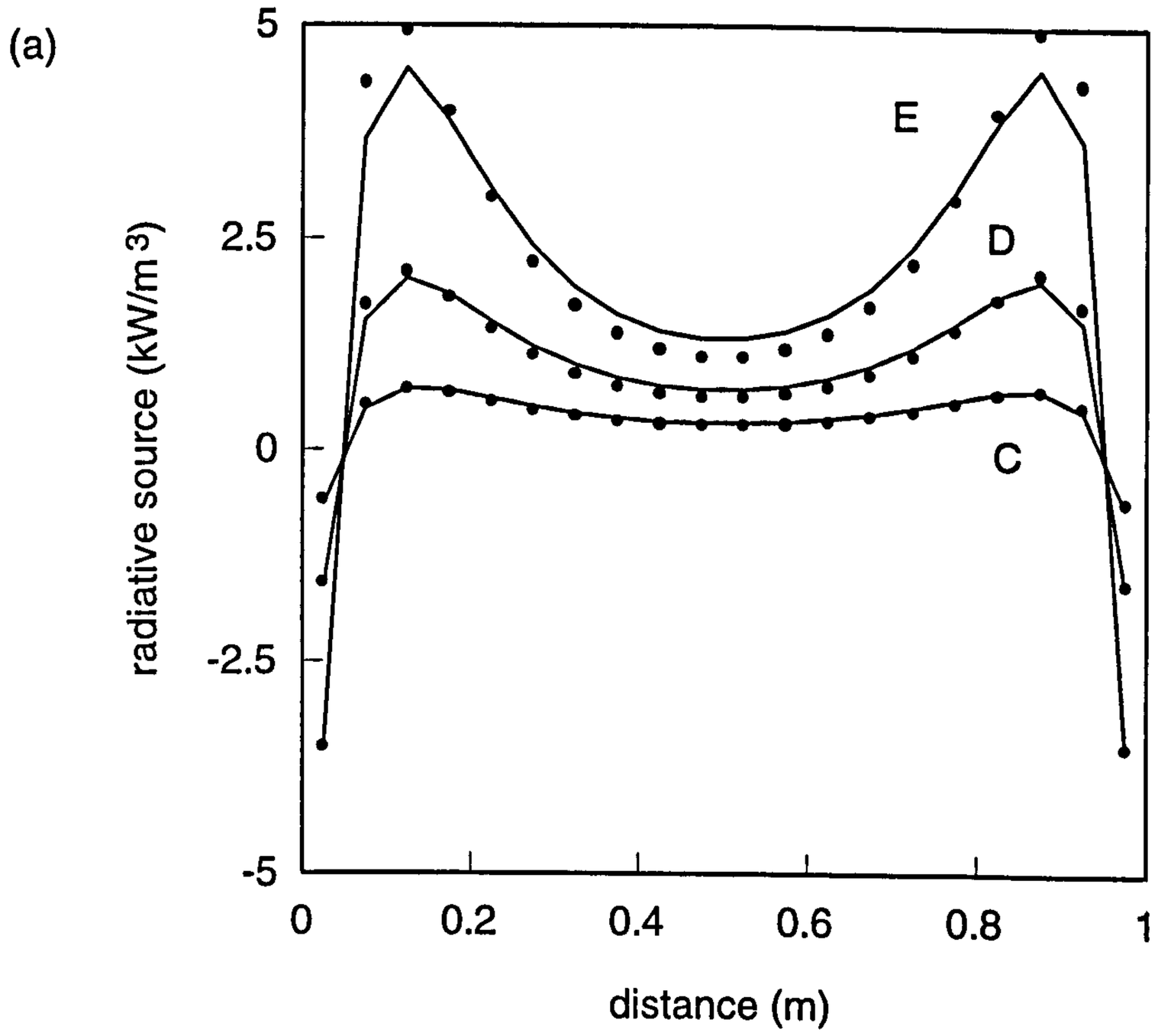

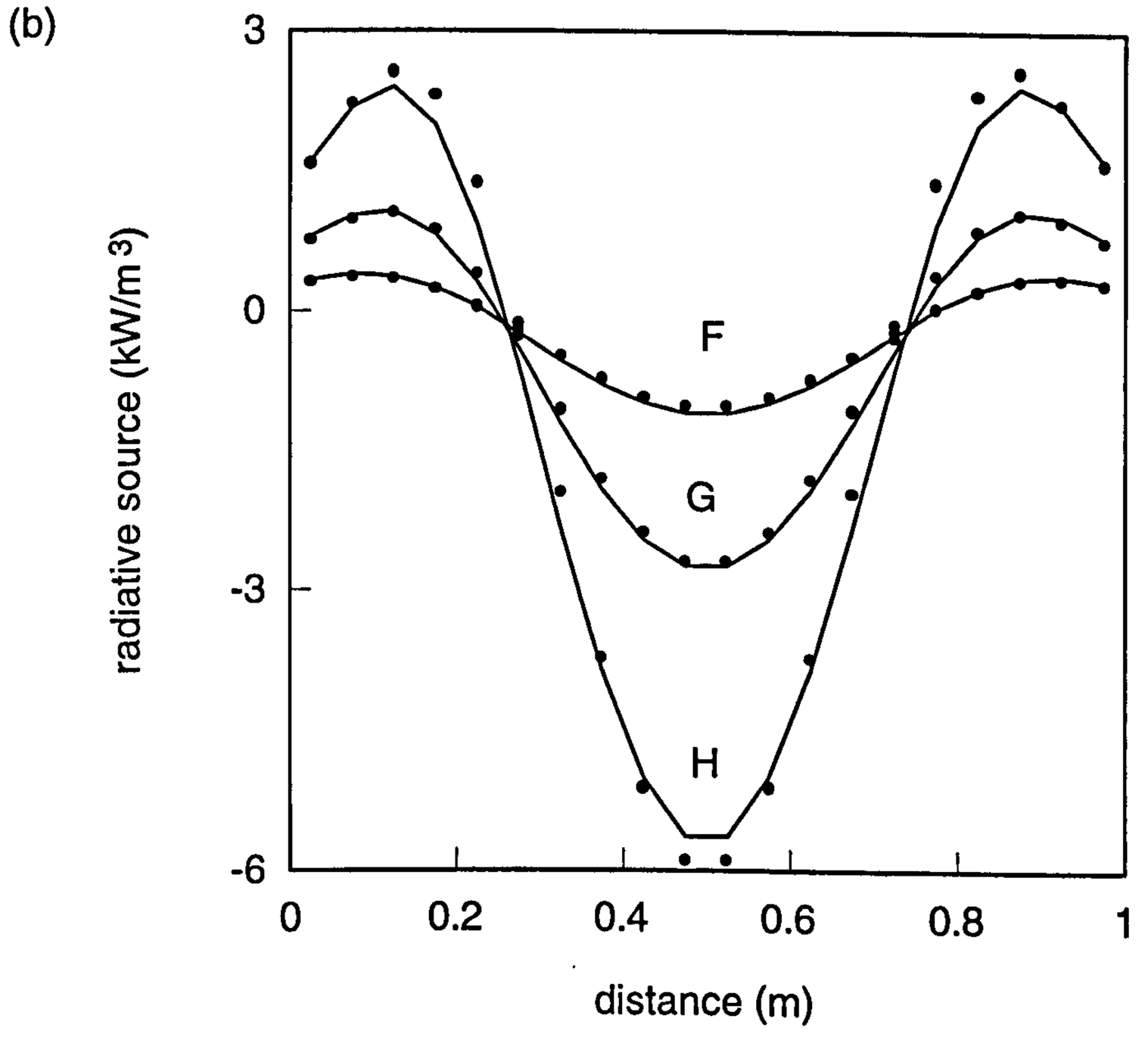

Fig. 4.4 Comparison of the WSGG and DBT solutions across gas-soot layers for configurations C to H combined with heavy soot loadings : (a) between hot black walls (soot configuration C_s; T_{cl} = 600 K); (b) between cold black walls (soot configuration A_s; T_w = 600 K).

(a)

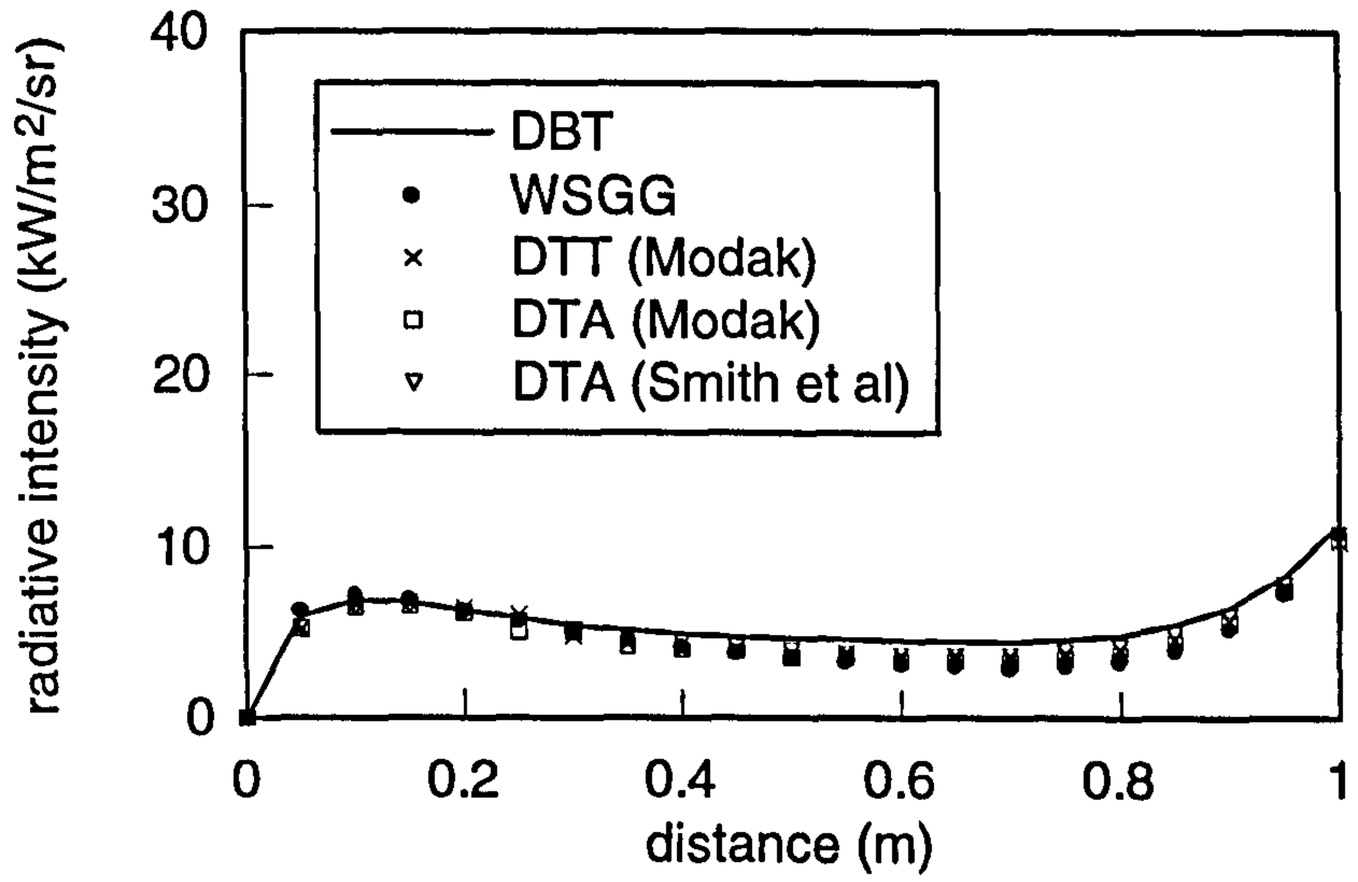

(b)

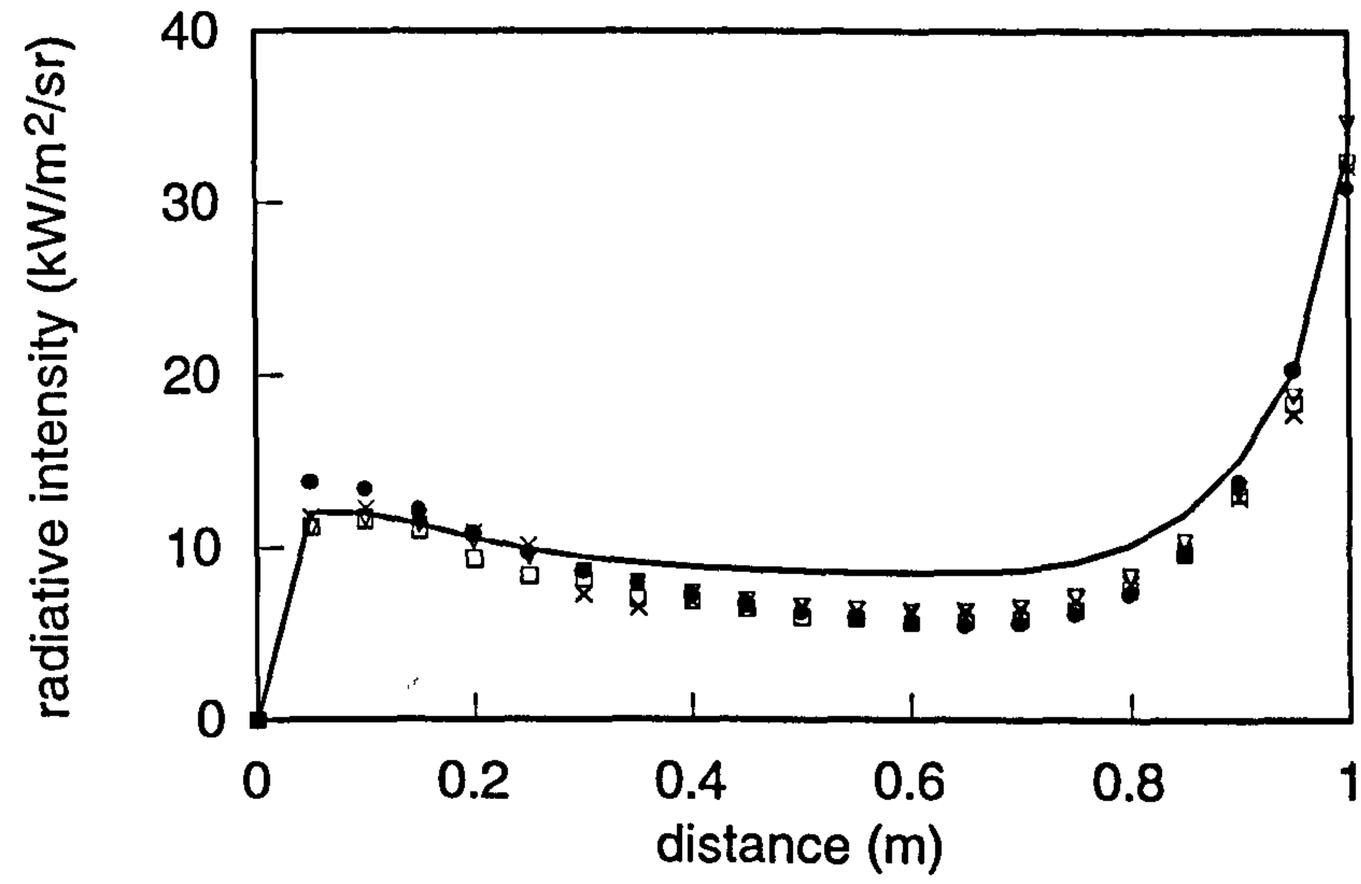

(c)

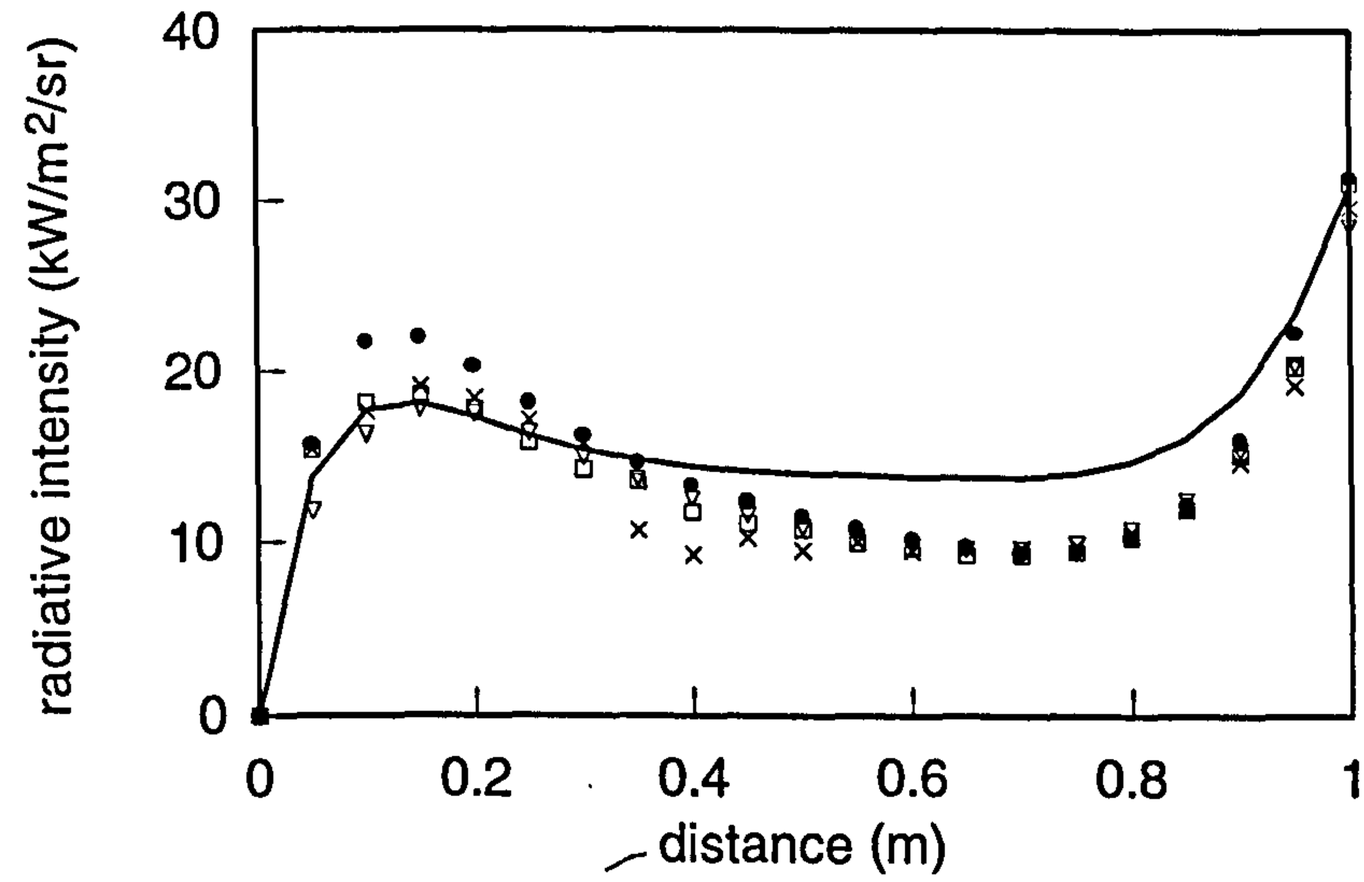

Fig. 4.5 Line of sight assessment of the DTA solution across a CO_2-H_2O mixture : (a) configuration C (T_0 = 1600 K); (b) configuration D (T_0 = 2000 K); (c) configuration E (T_0 = 2400 K). (T_{cl} = 600 K).

(a)

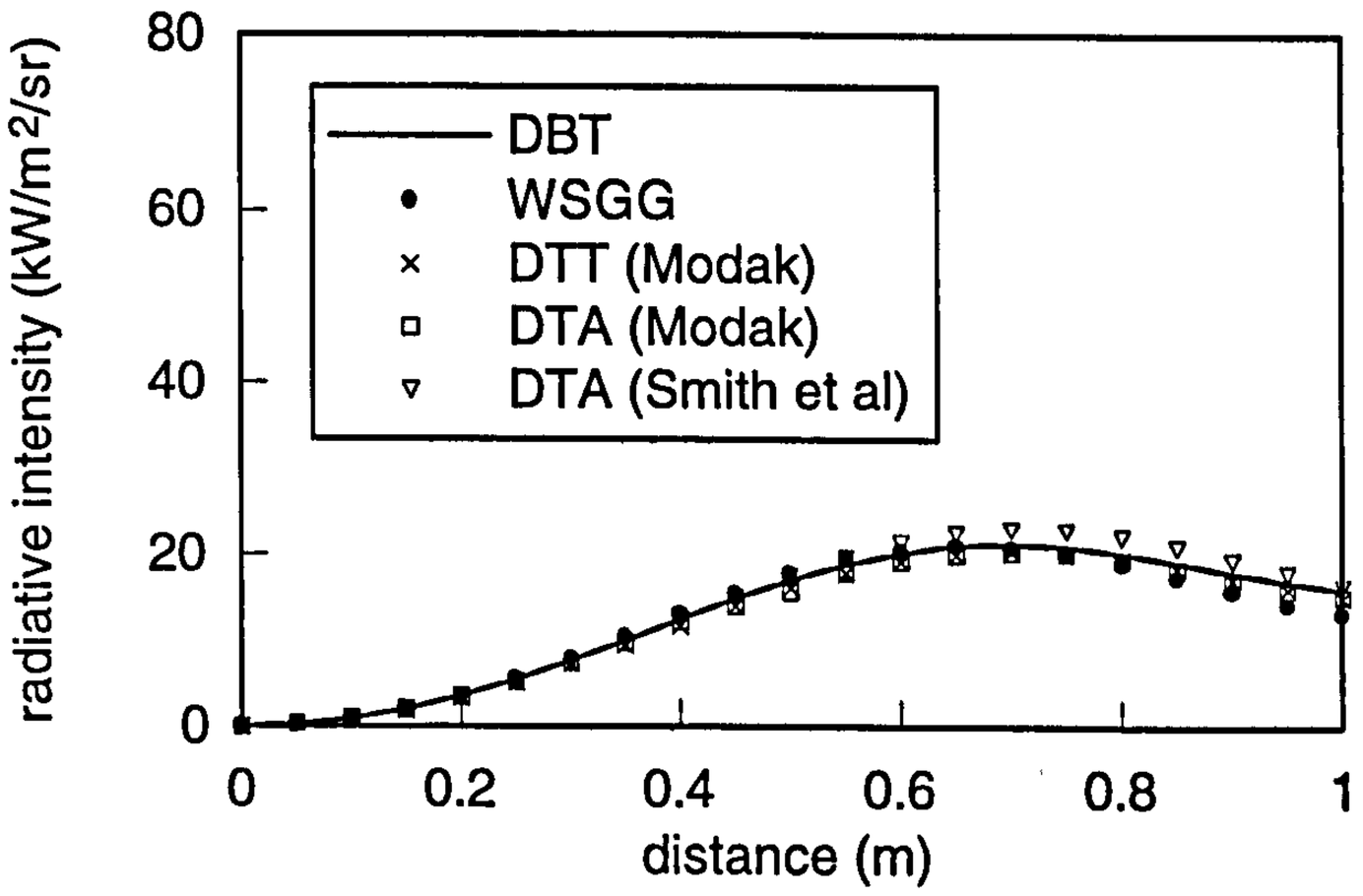

(b)

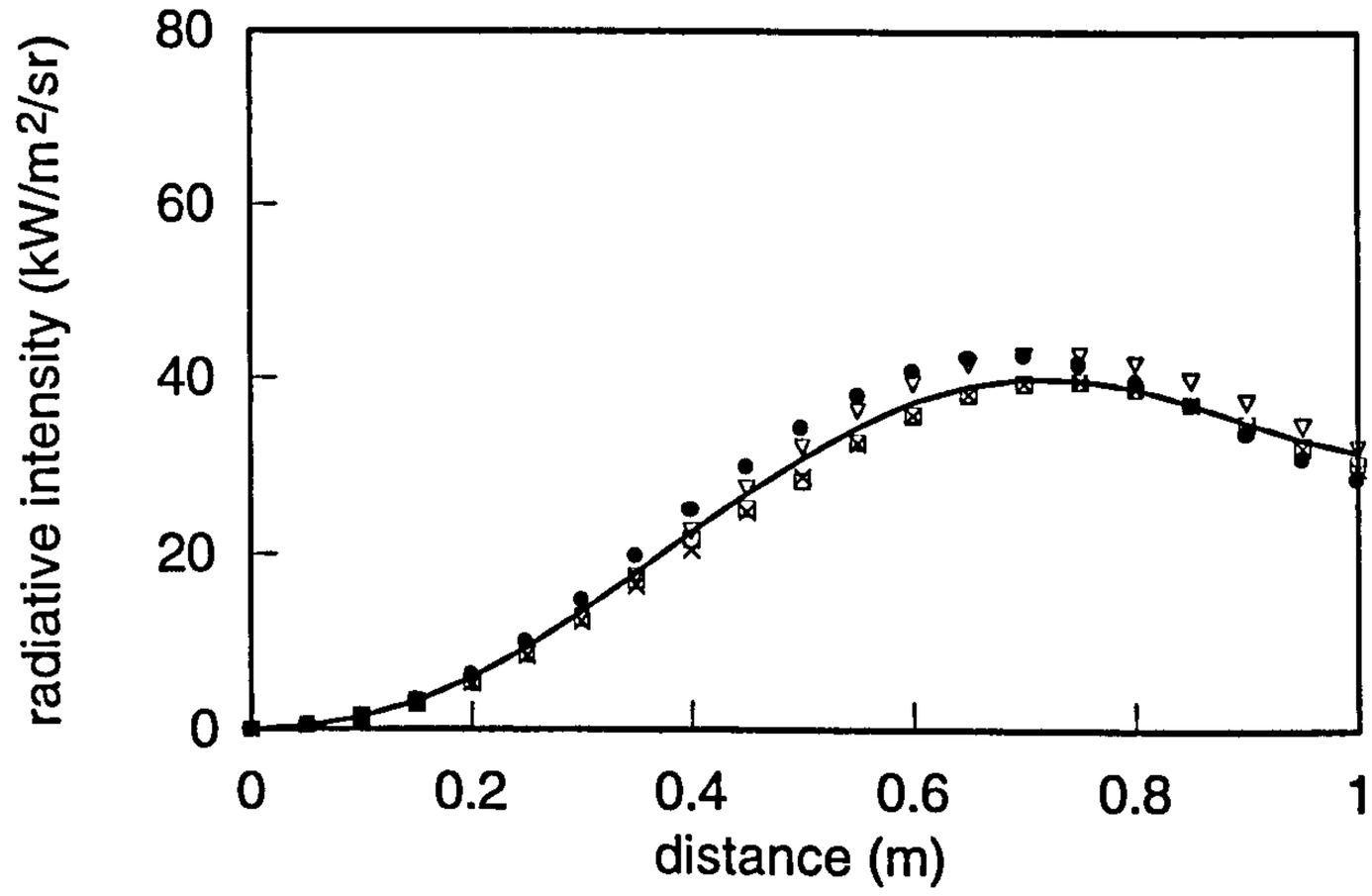

(c)

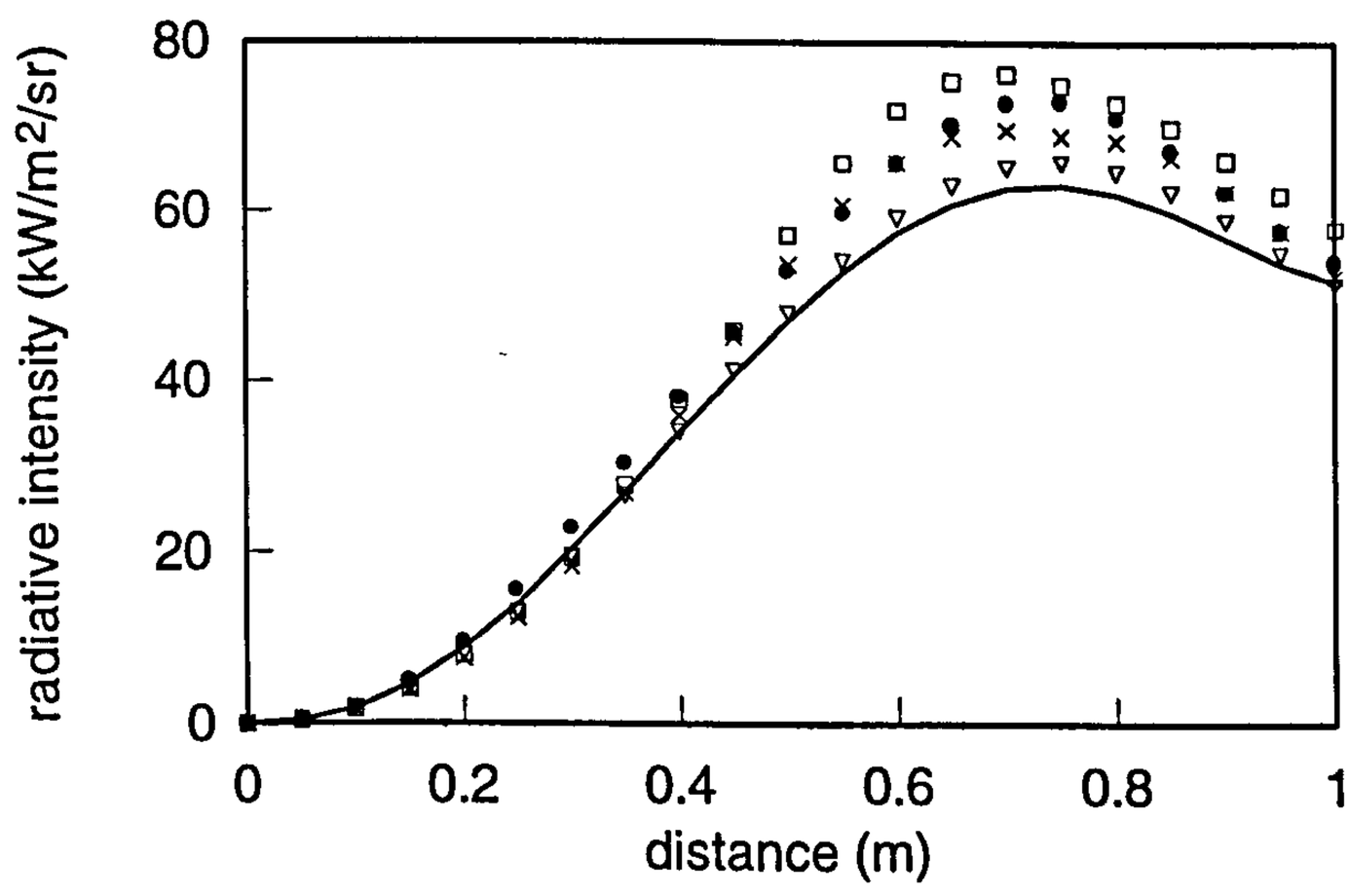

Fig. 4.6 Line of sight assessment of the DTA solution across a CO_2-H_2O mixture : (a) configuration F (T_{cl} = 1600 K); (b) configuration G (T_{cl} = 2000 K); (c) configuration H (T_{cl} = 2400 K). (T_0 = 600 K).

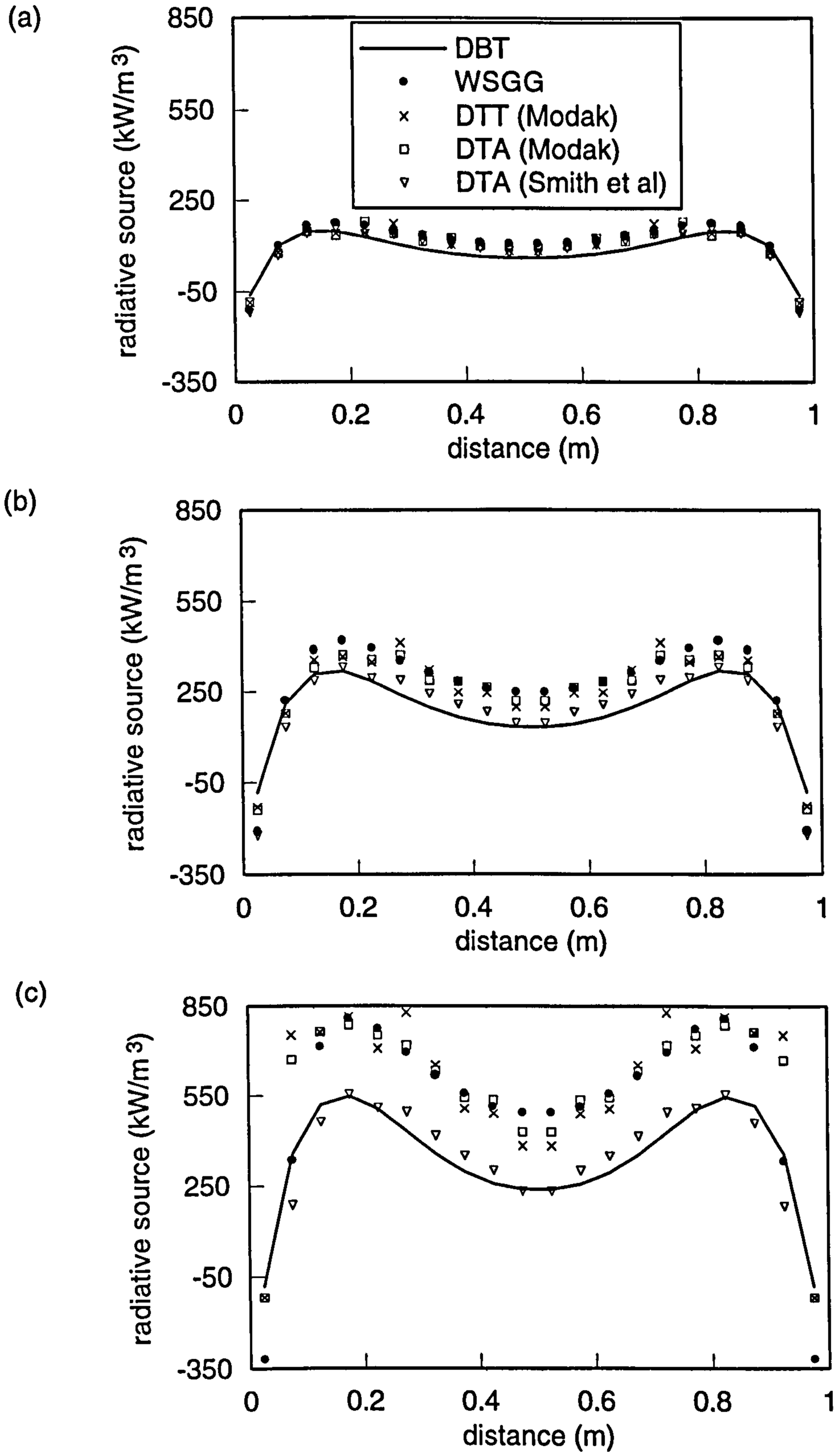

Fig. 4.7 Assessment of the DTA solution across CO_2-H_2O mixtures between hot black walls : (a) configuration C (T_w = 1600 K); (b) configuration D (T_w = 2000 K); (c) configuration E (T_w = 2400 K). (T_{cl} = 600 K).

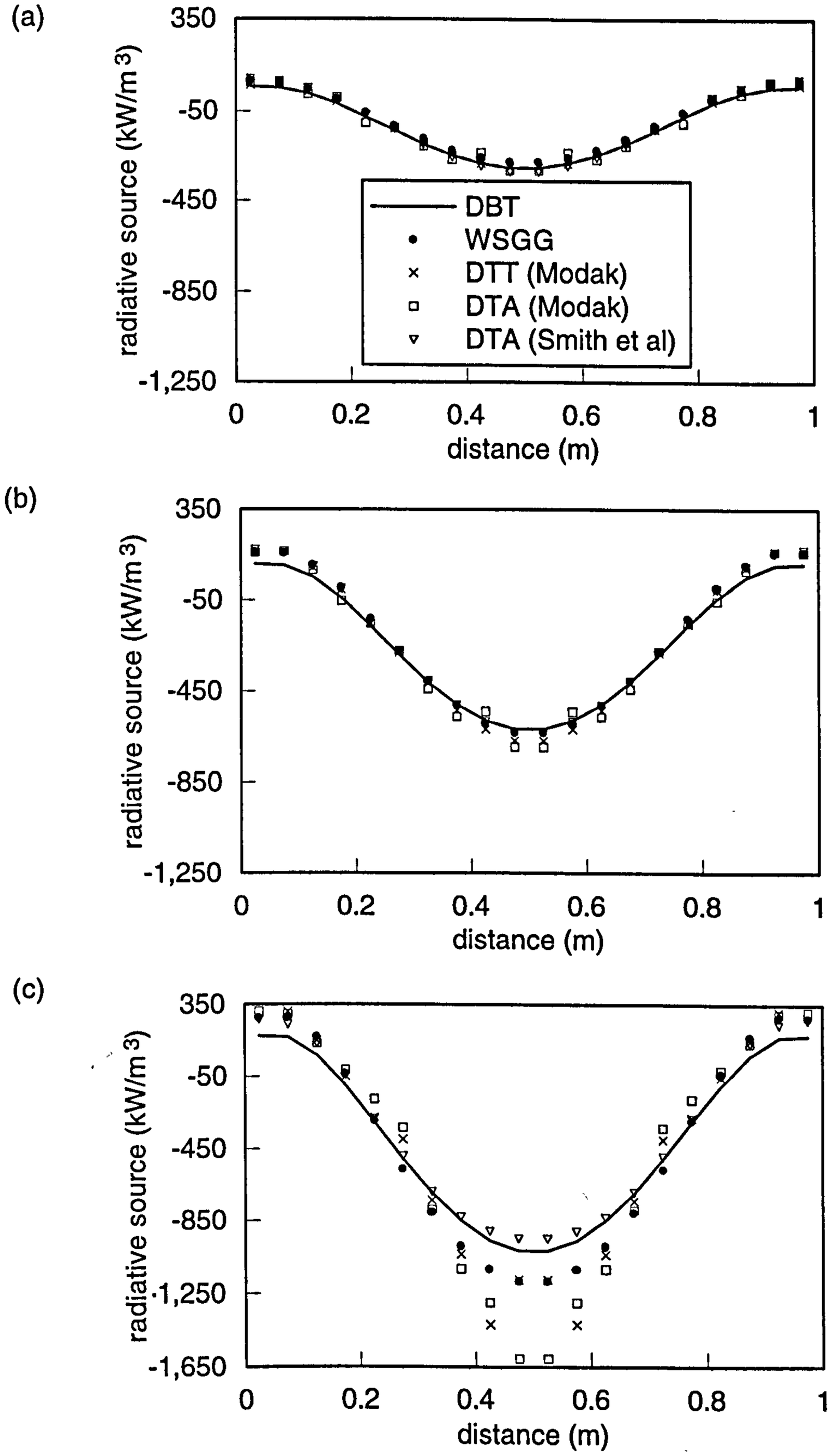

Fig. 4.8 Assessment of the DTA solution across CO_2-H_2O mixtures between cold black walls : (a) configuration F (T_{cl} = 1600 K); (b) configuration G (T_{cl} = 2000 K); (c) configuration H (T_{cl} = 2400 K). (T_w = 600 K).

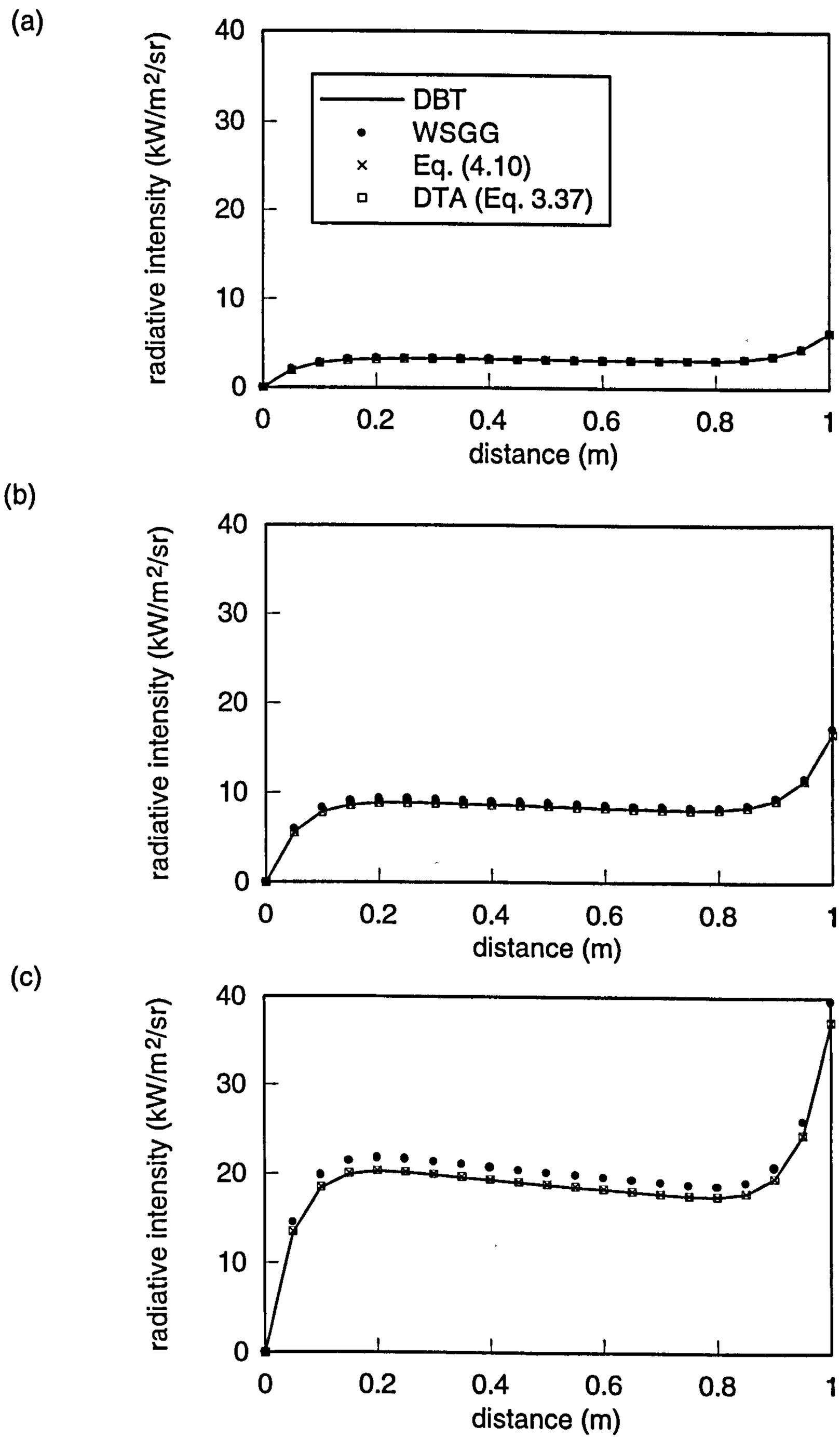

Fig. 4.9 Line of sight assessment of the DTA solution across a soot layer (configuration D_s) : (a) configuration C (T_0 = 1600 K); (b) configuration D (T_0 = 2000 K); (c) configuration E (T_0 = 2400 K).. (T_{cl} = 600 K).

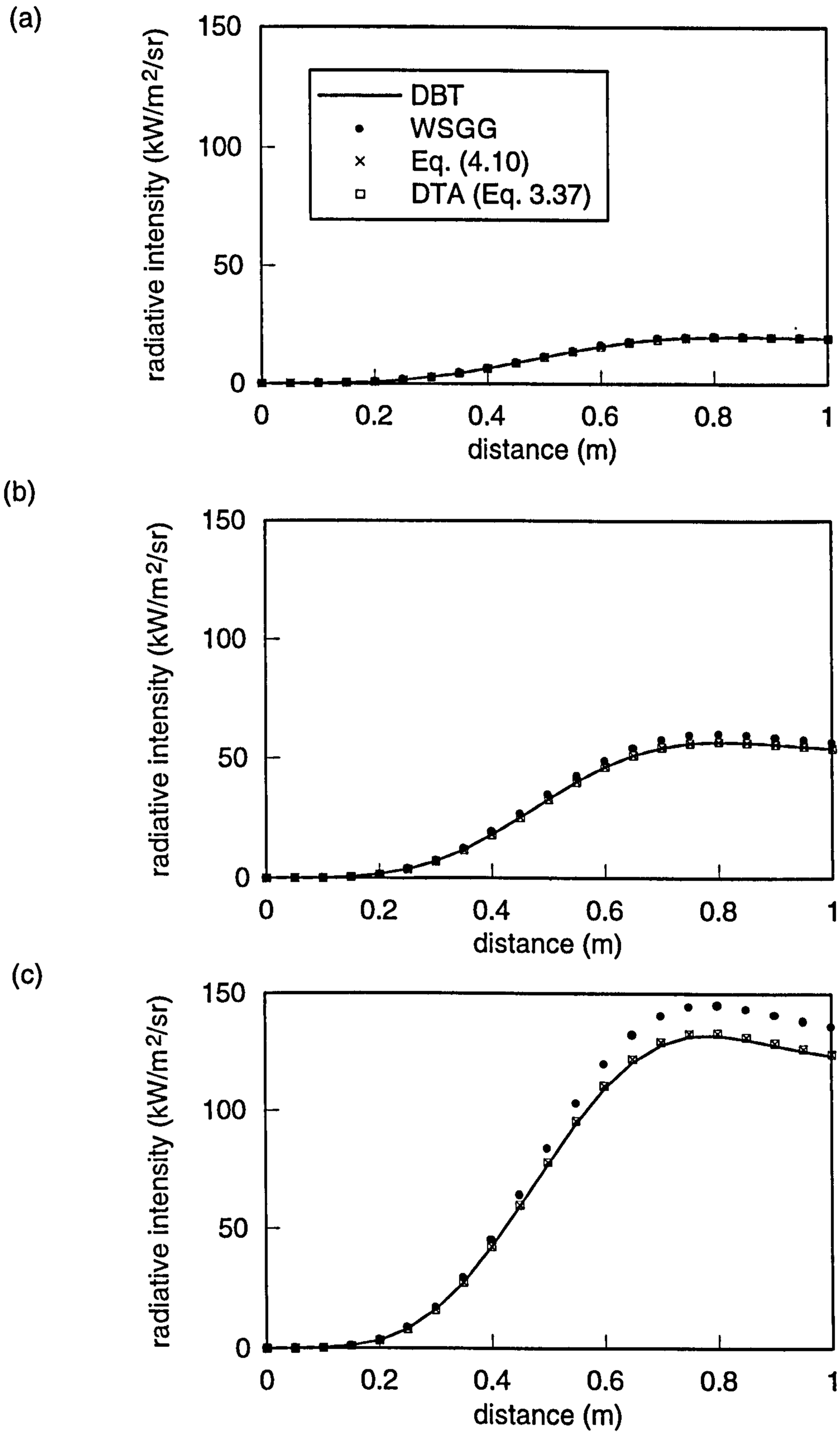

Fig. 4.10 Line of sight assessment of the DTA solution across a soot layer (configuration B_s) : (a) configuration F (T_{cl} = 1600 K); (b) configuration G (T_{cl} = 2000 K); (c) configuration H (T_{cl} = 2400 K). (T_0 = 600 K).

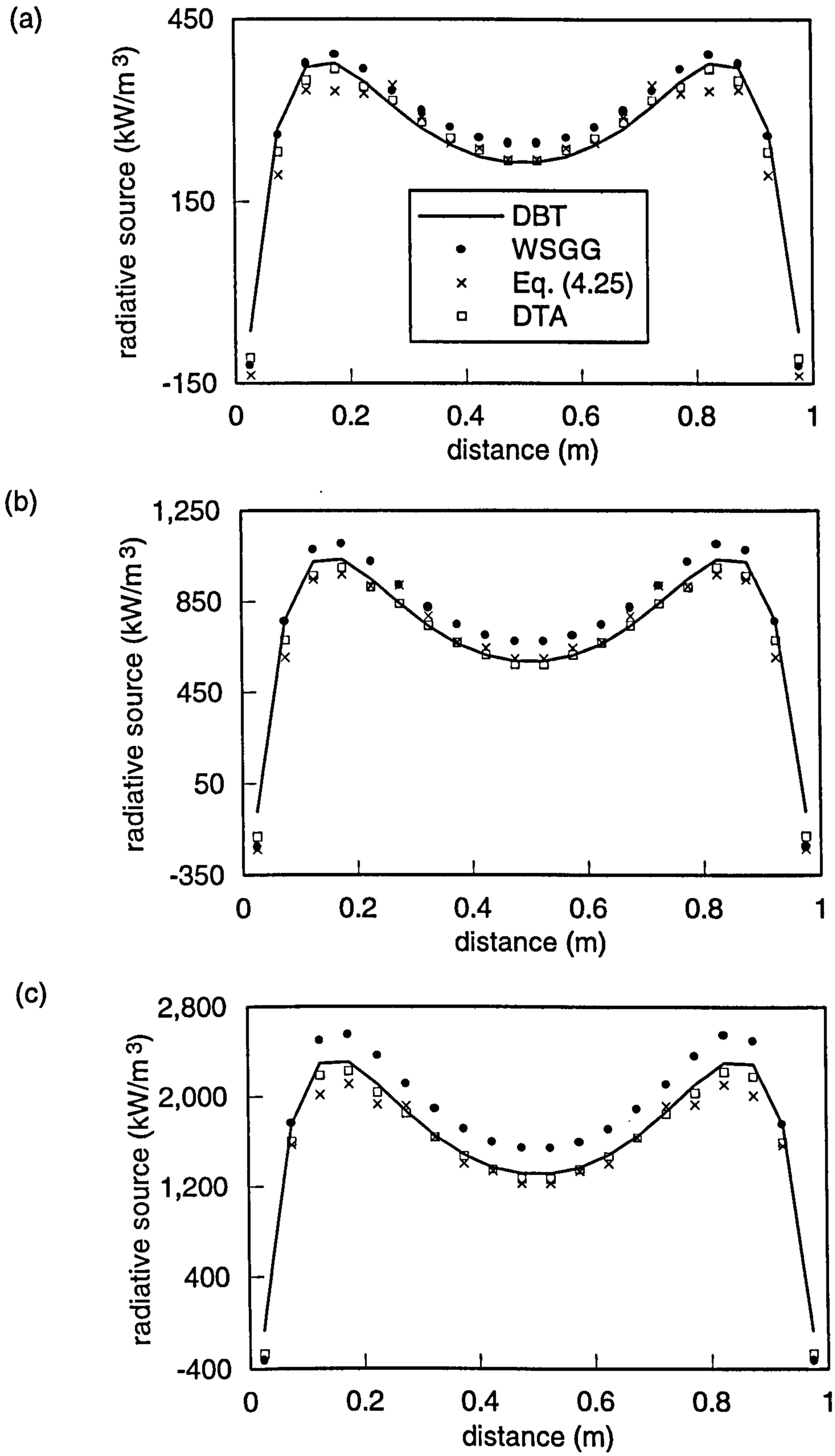

Fig. 4.11 Assessment of the DTA solution across CO_2-H_2O-soot mixtures between hot black walls : (a) configuration C (T_w = 1600 K); (b) configuration D (T_w = 2000 K); (c) configuration E (T_w = 2400 K). (T_{cl} = 600 K). Intermediate soot loading (configuration D_S).

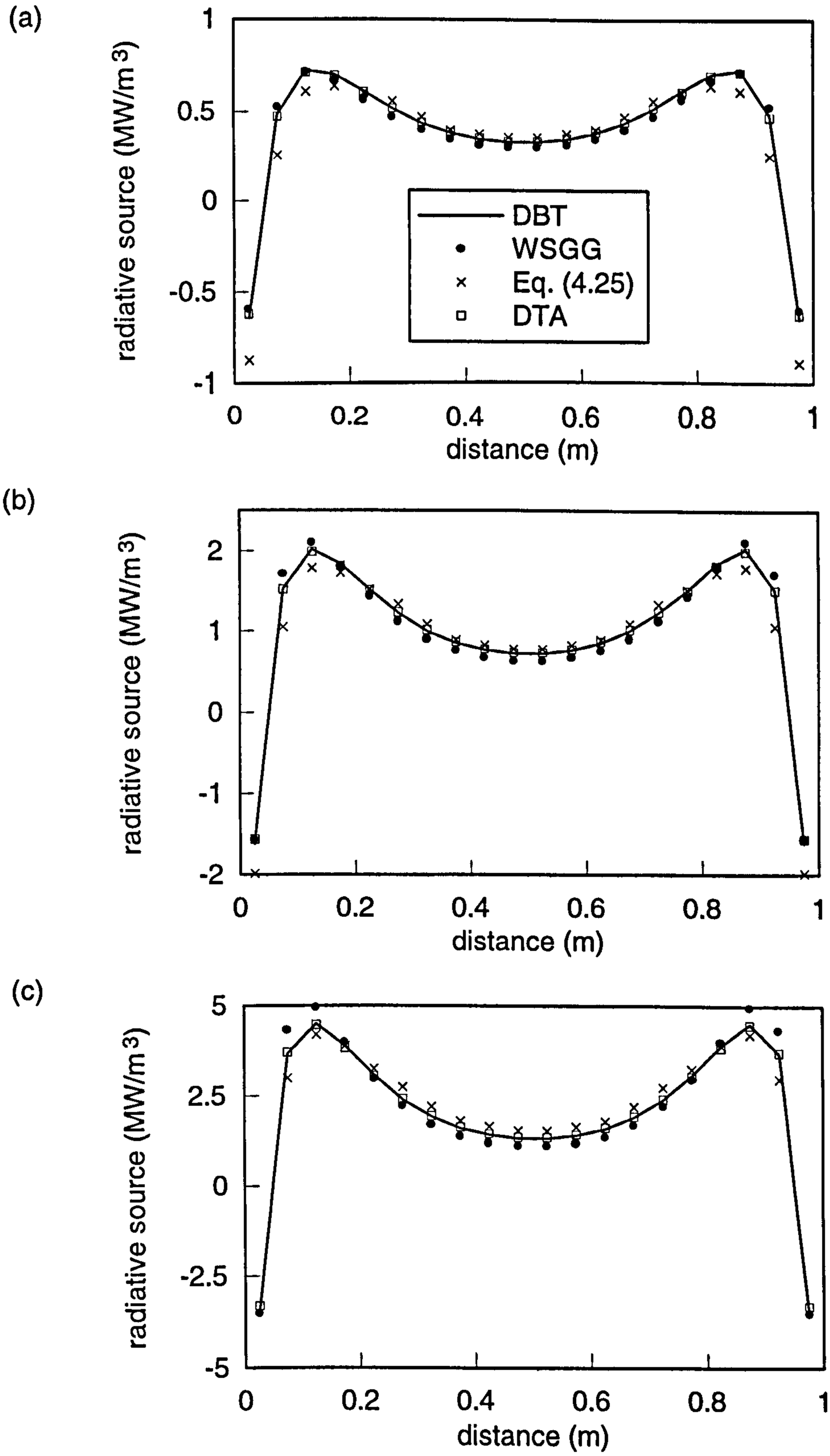

Fig. 4.12 Assessment of the DTA solution across CO_2-H_2O-soot mixtures between hot black walls : (a) configuration C (T_w = 1600 K); (b) configuration D (T_w = 2000 K); (c) configuration E (T_w = 2400 K). (T_{cl} = 600 K). Heavy soot loading (configuration C_s).

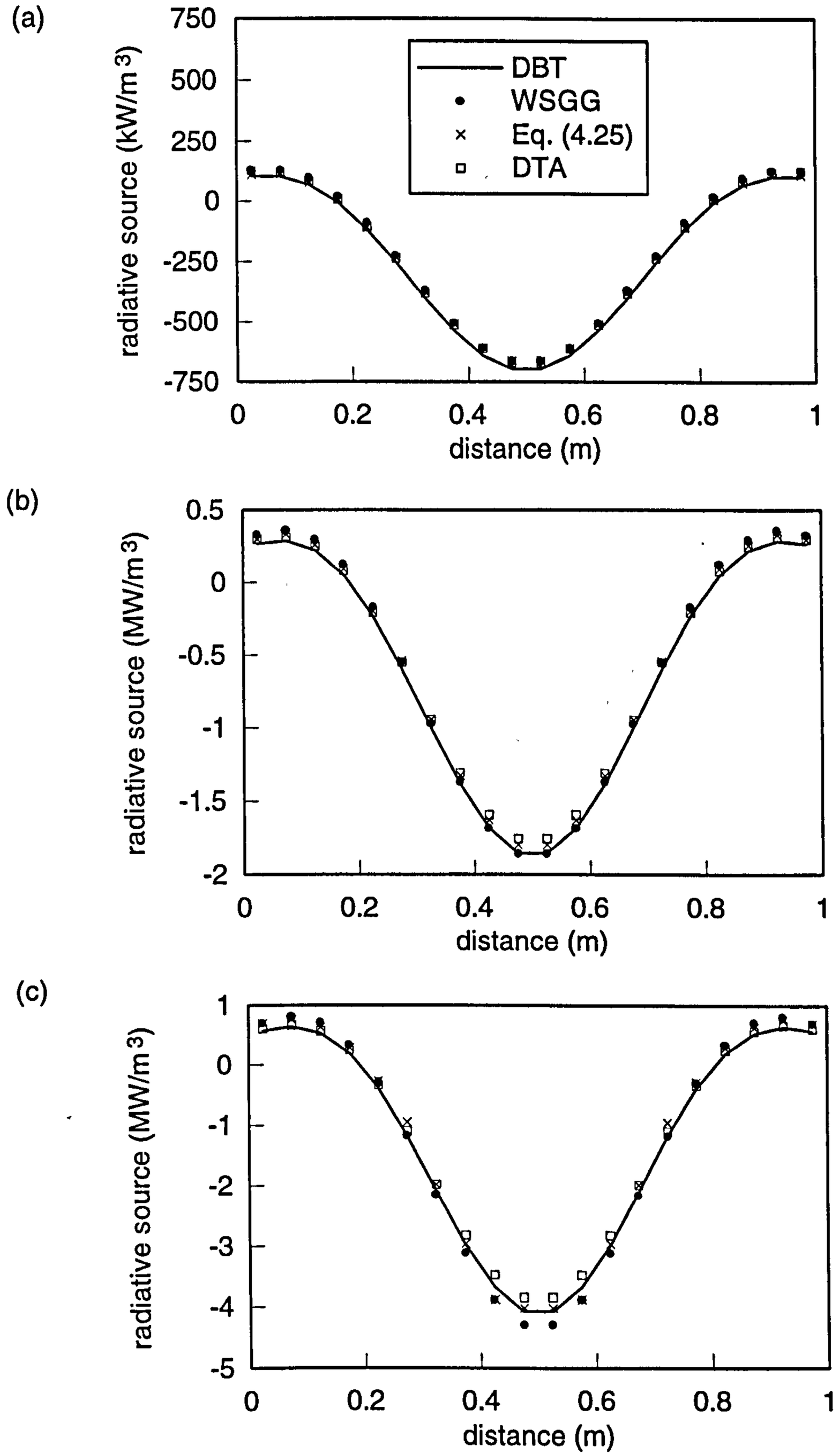

Fig. 4.13 Assessment of the DTA solution across CO_2-H_2O-soot mixtures between cold black walls : (a) configuration F (T_{cl} = 1600 K); (b) configuration G (T_{cl} = 2000 K); (c) configuration H (T_{cl} = 2400 K). (T_w = 600 K). Intermediate soot loading (configuration B_S).

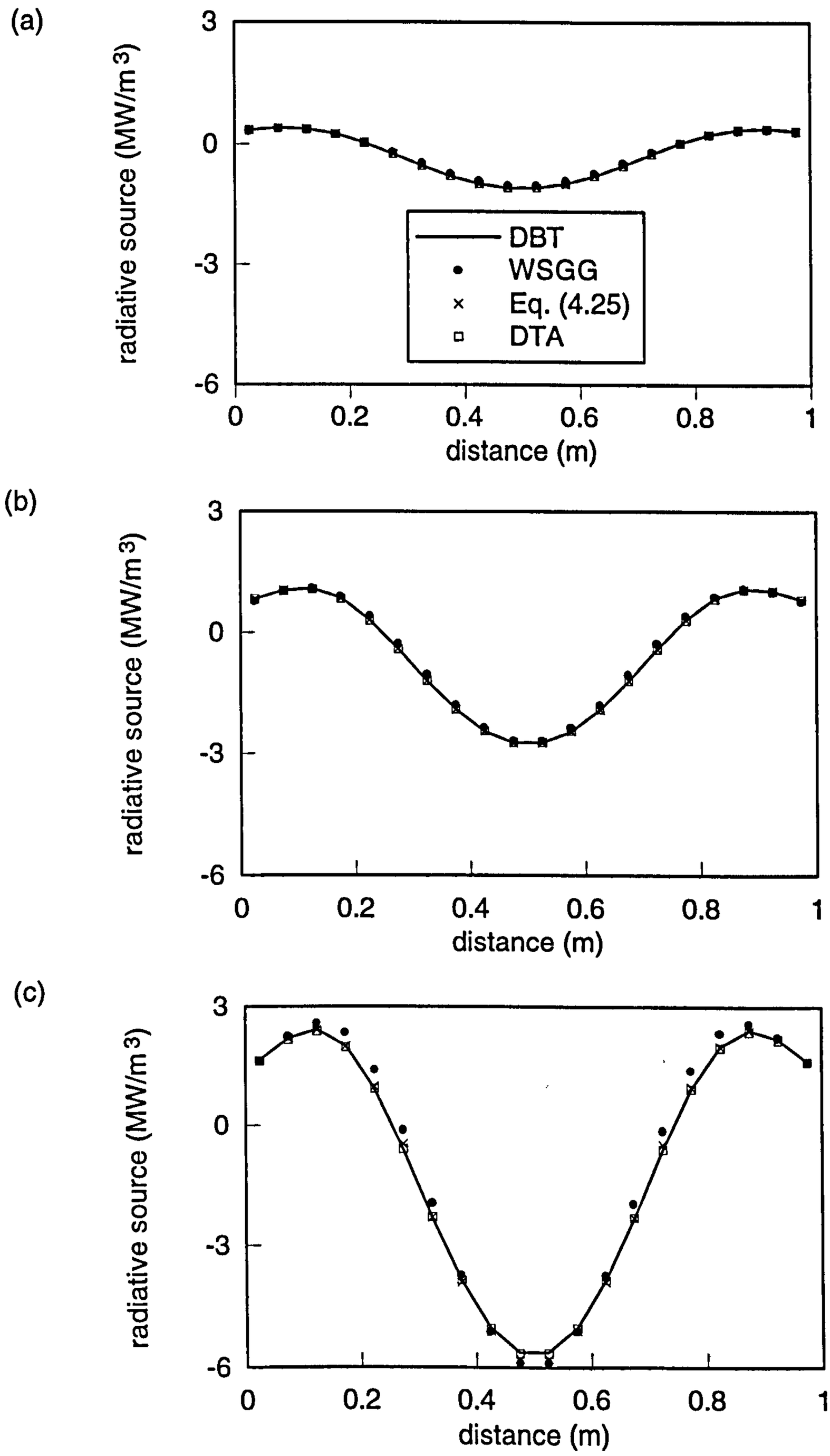

Fig. 4.14 Assessment of the DTA solution across CO_2-H_2O-soot mixtures between cold black walls : (a) configuration F (T_{cl} = 1600 K); (b) configuration G (T_{cl} = 2000 K); (c) configuration H (T_{cl} = 2400 K). (T_w = 600 K). Heavy soot loading (configuration A_S).

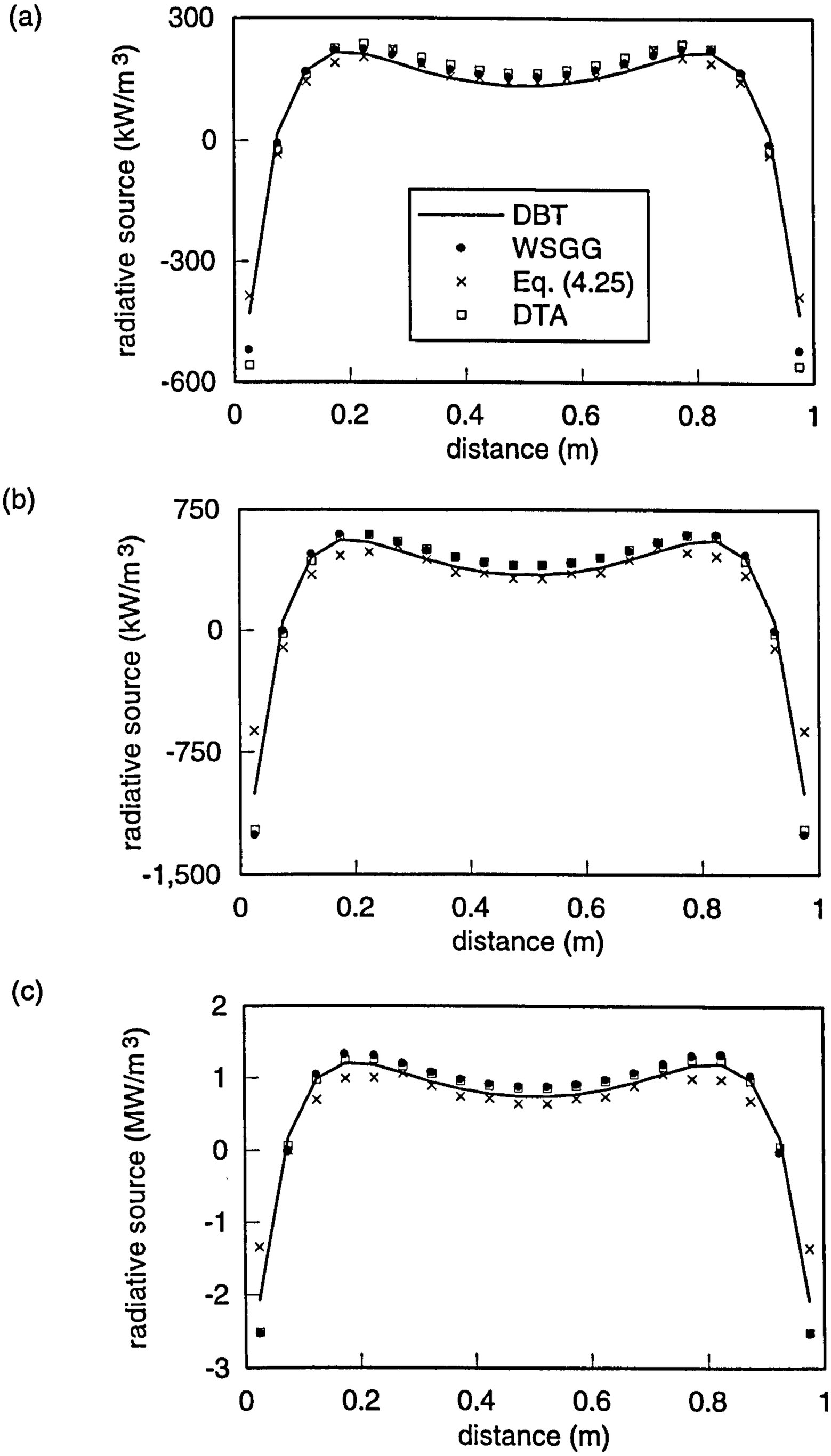

Fig. 4.15 Assessment of the DTA solution across CO_2-H_2O-soot mixtures between hot low emissivity walls ($\varepsilon = 0.25$) : (a) configuration C ($T_w = 1600$ K); (b) configuration D ($T_w = 2000$ K); (c) configuration E ($T_w = 2400$ K). ($T_{cl} = 600$ K). Intermediate soot loading (configuration D_s).

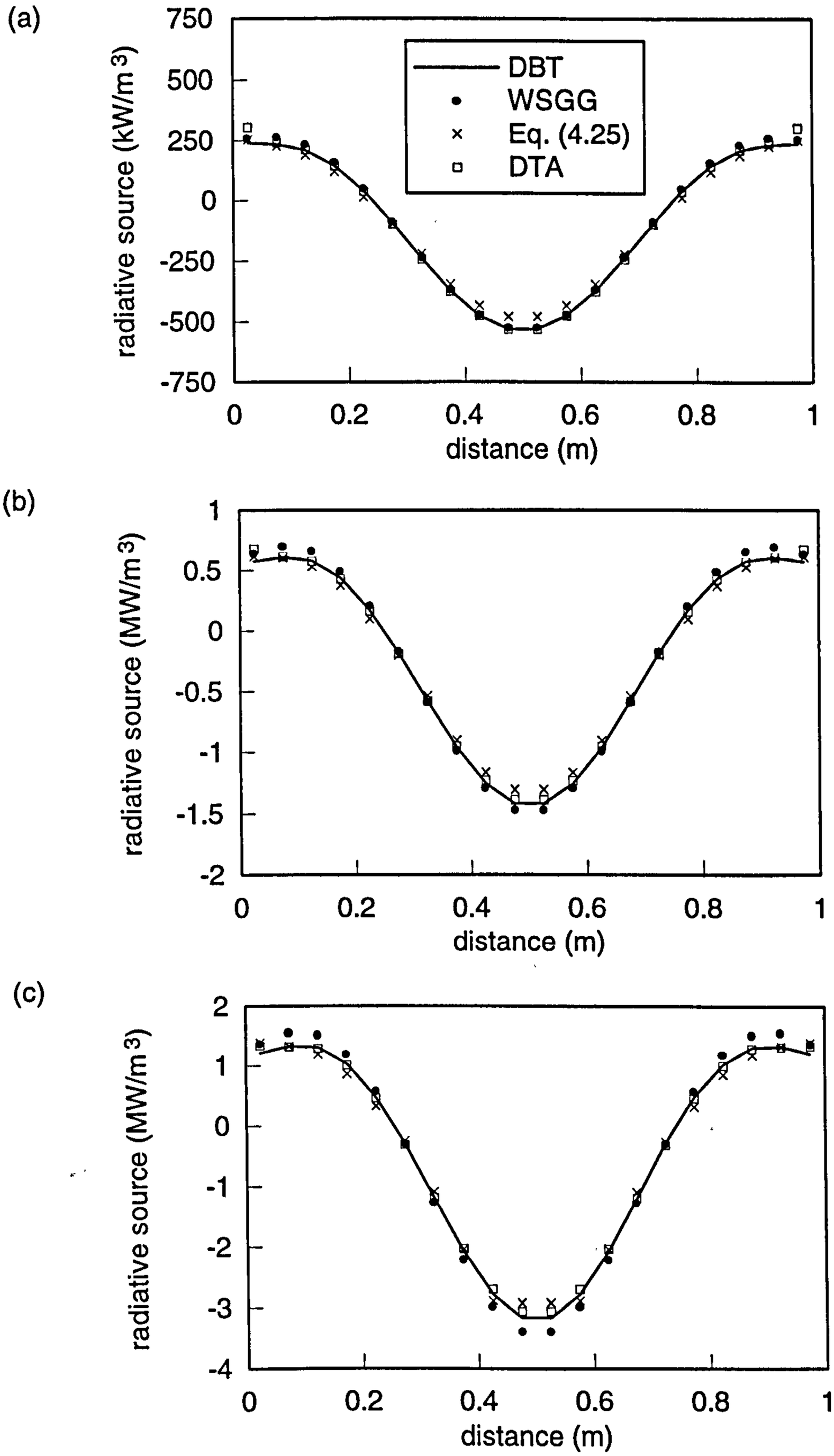

Fig. 4.16 Assessment of the DTA solution across CO_2-H_2O-soot mixtures between cold low emissivity walls ($\varepsilon = 0.25$) : (a) configuration F ($T_{cl} = 1600$ K); (b) configuration G ($T_{cl} = 2000$ K); (c) configuration H ($T_{cl} = 2400$ K). ($T_w = 600$ K). Intermediate soot loading (configuration B_s).

Chapter 5

Coupled Soot Formation and Thermal Radiation in Confined Turbulent Jet Diffusion Flames Burning Methane in Air

5.1 INTRODUCTION

Computational fluid dynamics modelling of combustion systems is still some considerable distance from being able to provide fast accurate solutions to practical problems. It is constrained by the complexity of the physical phenomena involved and the level of computing power available. Advancement in the accuracy of particular predictive techniques is often restricted by their coupling to parallel sub-models which do not possess the same degree of sophistication. Ideally, all components would have comparable accuracy. Nonetheless, overall progress cannot be dependent upon a requirement to neglect certain details of a complete model since simplifying assumptions are adopted elsewhere. The methodology investigated in the present work possesses a number of weak links, including the neglect of turbulent fluctuations in the evaluation of temperature and the simplified representation of boundary conditions. However, it provides some useful insight into the coupling between thermal radiation and soot formation, and it successfully demonstrates a strategy for incorporating interaction of the combustion environment with its boundaries.

Accurate prediction of heat transfer to the walls of gas turbine combustors is essential for extending the limits of operating performance, largely constrained by the properties of casing materials. In enclosure fires,

breakage of window glass due to thermal stresses imposed by exposure to high interior heat transfer, can have dramatic consequences on the subsequent development of the fire. Consequently, there is considerable attraction in being able to link models of combustion product formation, heat release, radiative energy exchange, and heat transfer at boundaries, all within the CFD framework.

Although an experimental jet flame is considerably different to the uncontrolled, unwanted fires commonly occurring in enclosures, the laboratory flame provides a far more convenient testing ground for the development of computational models. Once validated, they can then be applied to practical problems. The following discussion employs data from experimentally analysed confined turbulent jet diffusion flames to investigate the sensitivity of soot formation prediction to variation in a range of model parameters, including the representation of radiative energy exchange applied in the discrete transfer radiation model. Central to the complete methodology is the prediction of temperature, which demands a compromise between the accurate representation of the turbulent chemistry and the heat transfer across solid-fluid boundaries.

Conjugate heat transfer at the interface of solid and fluid is accommodated by solution to an energy equation, thus facilitating the determination of temperature from enthalpy. Such an approach requires a model of combustion heat release within the fluid. The eddy break-up concept is used here as it provides a computationally efficient means for modelling single step reactions. However, in addition to such a simplified representation of chemical reaction, this approach is weakened by the neglect of turbulent fluctuations in the evaluation of temperature. Therefore, although the laminar flamelet model does not recognise heat transfer at boundaries, the inclusion of turbulent fluctuations in its formulation for calculating fluid temperature provides important information relevant to the appraisal of the former approach.

In the next section, a general description of the CFD simulations is

provided. Following that, details of the calculations are discussed with special emphasis on the method of temperature prediction. The coupling between thermal radiation and soot formation is investigated in sections (5.3) and (5.4) in relation to flames burning at 1 and 3 atm., respectively. The chapter finishes with some concluding remarks.

5.2 NUMERICAL SIMULATION

5.2.1 Introduction

The numerical simulations described below have been performed on an experimentally investigated vertical, co-flowing turbulent jet diffusion flame burning methane in air, confined within a cylindrical liner. Methane issued from a cylindrical tube, 4.07 mm in diameter, at a flow rate of 10.3 g/min. The jet flame was rim stabilised by an annular premixed pilot flame. A co-flowing air stream occupied the remainder of the inlet contained within a pyrex cylindrical liner of 155 mm internal diameter. The overall equivalence ratio was 0.25. Brookes (1996) has reported detailed scalar measurements for this confined flame configuration at total pressures of 1 and 3 atmosphere. Radial profiles of time-averaged mixture fraction were measured by microprobe sampling and mass spectrometric analysis, temperature by exposed bead, fine wire thermocouple and soot volume fraction by integrated laser absorption and tomographic inversion. Further details are provided by Brookes (1996).

Fig. (5.1) shows a schematic of the computational geometry. Previous computational simulations of axisymmetric flames have generally employed a parabolic solution strategy, thus facilitating a fast, fine resolution modelling approach. Polar co-ordinate systems are normally used as well. From this perspective, it may seem inappropriate to investigate the present flame configuration by a three-dimensional curvi-linear procedure conducted in Cartesian co-ordinates. However, most combustion geometries

are three-dimensional in nature, and the detailed measurements attainable in experimental flames provide a useful data base against which it is possible to validate various physical models before applying them to practical combustion systems. Clearly, the present strategy possesses value both in terms of theoretical interest and practical relevance.

In common with previous studies of axisymmetric jet flames, a top-hat inlet profile is assumed. Since each control volume is represented by a trapezoidal prism, the modelled fuel stream inflow area requires an inlet fuel velocity of 20.16 ms^{-1} to produce a flow rate of 10.3 g/min. The corresponding air flow velocity is 0.61 ms^{-1}. The mixture fraction and mass fraction of fuel are both assumed to be unity in the fuel stream and zero in the air stream. Thus, the total enthalpy is evaluated for the non-premixed reactant streams from the enthalpy of formation of each constituent at the uniform inflow temperature of 290.0 K. The only other variables assigned inflow values different from zero are the turbulence quantities, k and ε. Although various relationships have been adopted to generate suitable values for k and ε, the present analysis is effectively insensitive to differences between them due to the large turbulence generation which occurs downstream of the inlet. Nonetheless, values of k and ε were initiated from the expressions :

$$k = 0.003\tilde{u}^2 \tag{5.1}$$

$$\varepsilon = k^{1.5}/r \tag{5.2}$$

used previously by Syed (1990) and Young (1993).

Although the flame is confined within a pyrex casing, which is itself contained inside a pressure vessel, only the inner flow field is modelled. However, the interface between the flow and the pyrex casing is treated as a conjugate heat transfer boundary, and the pressure vessel is assumed to contain quiescent air at a uniform temperature of 500.0 K. The outflow is

treated as a zero gradient boundary. The other boundaries are represented by the centre-line and the two longitudinal faces, all of which are treated as symmetry planes. The centre-line presents a problem in the generation of hexahedral control volumes since it is important not to lose information by neglecting a significant cross-section of the flow field, whilst convergence difficulties arise when generating order of size volume differences between control volumes along the radius.

The boundary conditions for the DTRM are as follows. Rays are launched from cell faces on the solid pyrex boundary and both flowing boundaries. They are reflected at the planes of mirror symmetry and then terminated on impact at a launch face. The pyrex is assumed to be emitting as a gray surface with an emissivity of 0.8. This value is broadly representative of pyrex for infra-red radiation. A more detailed - and costly - representation of the transmission properties of the material are not considered appropriate in the present study. Flowing boundaries are assumed to radiate as black bodies at the temperature of the adjacent gas.

5.2.2 Solved Variables

For the purposes of the following discussion, solved variables are defined as those for which a separate balance equation is solved. Other variables required to close the set of equations are defined as derived variables, and these are discussed in the subsequent sub-sections. In all simulations, the flow field is determined by solving for two momentum components, u and v, the pressure correction, dp, and the turbulence quantities, k and ε. The third momentum component is zero due to the alignment of the co-ordinate axes. Additionally, the soot model requires equations for the total enthalpy, H, the mean and variance of mixture fraction, ξ and ξ''^2, respectively, and the soot number density, n, and volume fraction, f_v. All solved variables are described by the generic equation,

$$\frac{\partial(\bar{\rho}\tilde{\phi})}{\partial t} + \frac{\partial(\bar{\rho}\tilde{u}_j\tilde{\phi})}{\partial x_j} = \frac{\partial}{\partial x_j}\left(\Gamma_\phi \frac{\partial \tilde{\phi}}{\partial x_j}\right) + \bar{S}_\phi \qquad (5.3)$$

where the unsteady term is zero in the steady state calculations performed here. The corresponding source terms and diffusion coefficients are tabulated in Table (5.1).

In its standard form, the $k-\varepsilon$ model fails to adequately model both free and confined round jets, generally overestimating the spreading rate by between 30 and 40 %. Therefore, modifications to the model constants have been established to better represent these type of flows. Effectively, all proposals have sought to reduce eddy viscosity by increasing the turbulence dissipation rate. Pope (1978) proposed a complex modification to the dissipation equation based on the scale reduction associated with the positive strain imposed on vortex tubes. A more straightforward approach has attempted to instigate larger eddy viscosity by applying corrections to C_μ and/or $C_{\varepsilon 1}$ and $C_{\varepsilon 2}$, related to centre line deceleration. In accordance with earlier work on confined turbulent jet diffusion flames by Young (1993), the empirical corrections due to Rodi (1972) are employed here :

$$\begin{aligned} C_\mu &= 0.09 - 0.04 F_{cl} \\ C_{\varepsilon_2} &= 1.92 - 0.0667 F_{cl} \end{aligned} \qquad (5.4)$$

where

$$F_{cl} = \frac{\delta}{u_{cl}}\left[\left|\frac{d\tilde{u}}{dx}\right|\right]_{cl}^{0.2} \qquad (5.5)$$

and δ denotes the half width of the jet. Other researchers have simply modified the model constants by a fixed amount. For example, Benim (1989) reduced C_μ and $C_{\varepsilon 2}$ to 0.075 and 1.89, respectively.

It is to be recalled that the eddy viscosity concept represents turbulence as an adjustment to fluid viscosity. Therefore, modifications to the $k-\varepsilon$ model constants are manifested in the combined effect this has on the diffusion of all solved variables. Consequently, the general definition of a diffusion coefficient, Γ_ϕ, as the ratio of the effective viscosity and the Prandtl-Schmidt number, σ_ϕ, suggests that variation of σ_ϕ may also have a significant effect on the flow field.

There is considerable uncertainty concerning the most realistic value to adopt for σ_ϕ in the balance equations for the mean and variance of mixture fraction, enthalpy and mass fraction of fuel. A value of 0.7 has been most widely adopted (cf. Jeng and Faeth, (1984a), Benim (1989), Syed (1990) and Bai and Fuchs (1993)). However, values of 1.0 and 0.9 have been favoured by Young (1993) and Elkaim et al. (1993), respectively. The analysis presented below suggests that the lowest value, representative of the Prandtl number for real gases, produces a better simulation of the present flames.

5.2.3 Derived Variables

The principal derived variables are the thermodynamic properties of pressure, temperature and density. Pressure is determined directly from the pressure correction with under-relaxation of 0.5. Various methodologies can be compiled for deriving temperature and density, and these largely depend upon the type of combustion model employed. Therefore, the approaches adopted are discussed in the next sub-section. Other derived variables include conductivity, specific heat capacity, fluid viscosity and heat of formation, and mass (or molar) fractions of fluid species. Once again, the overall approach determines which of these variables is calculated.

5.2.4 Combustion Models and Temperature Prediction

5.2.4.1 Eddy break-up model

As described in chapter 2, the eddy break-up concept assumes that the consumption of fuel can be related to a time-scale derived from the $k-\varepsilon$ turbulence model. Thus, if combustion is described by a single-step reaction in which fuel and oxidant react to form a mixture of simple products, the CFD procedure requires an extra balance equation for the mass fraction of fuel, and a method for determining the mass fractions of oxidant, O_2, products, CO_2 and H_2O, and the diluent, N_2. The source term for the mass fraction of fuel is shown in Table (5.1).

The empirically derived eddy break-up constant has been shown to lack generality (cf. Brizuela and Bilger, 1996). For example, in a recent parametric study applied to the turbulent combustion of propane by Bai and Fuchs (1993), considerable differences were observed in the prediction of temperature for values ranging between 2 and 6. Selection of the most suitable value for the present analysis is presented in sub-section 5.3.1.

Once the mass fraction of fuel is known, the definition of mixture fraction is manipulated to determine the mass fractions of other species :

$$\begin{aligned} Y_o &= s\left(Y_{fu}-\xi\right)+Y_{o_{in}}\left(1-\xi\right) \\ Y_n &= \left(1-Y_{o_{in}}\right)\left(1-\xi\right) \\ Y_p &= 1-Y_{fu}-Y_o-Y_n \end{aligned} \tag{5.6}$$

The distribution of species is required in order to evaluate temperature from enthalpy. Solution of the energy conservation equation yields the distribution of total enthalpy, H, defined by Eq. (2.7). If a polynomial representation of molecular specific heats is employed given by

$$c_{p_i} = \sum_{n=0}^{N} a_{n_i} T^n \tag{5.7}$$

for N species, the definition of sensible enthalpy then permits the implicit evaluation of temperature from

$$\overline{T} = \left[H - \sum_{i=1}^{N} \tilde{Y}_i \left(h_{f,i}^{0} - \overline{T}_0 c_{p_i}{}^{*}(\overline{T}_0) \right) \right] / \, c_{p_i}{}^{*}(\overline{T}) \tag{5.8}$$

$\overline{T} c_{p_i}{}^{*}(\overline{T})$ represents the integrated form of the individual molecular specific heats for CH_4, CO_2, H_2O, O_2 and N_2 (tabulated in McBride et al. (1993)) at a mean temperature, $\overline{T}$. Radiative loss is manifested as a sink of energy, and thus reduces the energy available to increase sensible enthalpy (and temperature). The equation of state for real gases is used to evaluate density :

$$\rho = p \left(R_0 T \sum_{i=1}^{N} \frac{Y_i}{W_i} \right)^{-1} \tag{5.9}$$

A key element of this methodology concerns the capability to incorporate conjugate heat transfer at the interface between a fluid-solid boundary. However, the full potential of such an approach has not been realised in the present simulations due to the complexity, and associated computational expense, demanded by a detailed representation of solid boundary properties - including the radiative properties of pyrex. Thus, the pyrex casing has been modelled as a single layer of cells, possessing gray surfaces and constant thermal properties shown in Fig. (5.1). This crude level of detail provides some justification for approximating the pyrex casing as an isothermal boundary. Indeed, this approximation has little effect on the overall flow field as discussed in the next section, and it is employed in conjunction with the laminar flamelet combustion model which does not admit calculation of solid material temperature.

5.2.4.2 Laminar flamelet concept

In the CFD community, the eddy break-up concept still provides an efficient means of approximating the chemistry of combustion and its associated heat release. This is exemplified in the present work by its role in facilitating the investigation of coupled soot formation and thermal radiation. However, it is not easy to assess the overall impact on the present methodology of the simplified representation of chemical reaction. For example, as demonstrated in the next section, the evaluation of temperature from Eq. (5.9) employing a laminar flamelet description of the chemistry, agrees very closely with eddy break-up based predictions with the eddy break-up constant set to unity. A more significant weakness is identified as the neglect of turbulent fluctuations in the evaluation of temperature.

The multiple flamelet approach described in chapter 2 is used in all predictions of soot formation regardless of the accompanying combustion model. The same strategy can be employed to determine temperature and density, thus replacing the eddy break-up approach incorporating Eqs. (5.8) and (5.9). Instead, temperature and density are evaluated by interpolating between the mean values obtained from integration across a beta function pdf of their respective flamelet families according to the level of radiative loss. Thus, Reynolds mean temperature is given by

$$\overline{T} = \overline{T}_l + x\left(\overline{T}_u - \overline{T}_l\right) \tag{5.10}$$

where $\overline{T}_u$ and $\overline{T}_l$ are determined from

$$\overline{T_u} = \int_0^1 \frac{\overline{\rho}}{\rho_u(\xi)} T_u(\xi) \tilde{P}(\xi) d\xi$$
$$\overline{T_l} = \int_0^1 \frac{\overline{\rho}}{\rho_l(\xi)} T_l(\xi) \tilde{P}(\xi) d\xi \qquad (5.11)$$

The interpolation fraction, x, derives from a comparison of the family of enthalpy flamelets with the value obtained from solution of its balance equation. Mean density is evaluated by a similar expression to Eq. (5.10) with each integrated value calculated from

$$\overline{\rho} = \left(\int_0^1 \frac{1}{\rho} \tilde{P}(\xi) d\xi \right)^{-1} \qquad (5.12)$$

All flamelets were derived from the stagnation streamline predictions of a counterflow burner using the code due to Warnatz (1981). Flamelets for the molar fractions of chemical species were assumed invariant with radiative loss, this being justified by the determination of nearly universal state relationships for the concentrations of major gas species (cf. Gore and Faeth, 1988). Further details are available in Brookes (1996).

5.3 FLAME AT ATMOSPHERIC PRESSURE

5.3.1 Introduction

In the analysis to follow, base calculations for either the eddy break-up approach or the laminar flamelet concept are assumed to comprise the structures described above. Both models couple to the soot formation model detailed in chapter 2 (without oxidation), and to the discrete transfer radiation model employing the WSGG solution to the radiative transfer

equation. 129 rays are launched from each boundary face. Within the constraints imposed by computational memory and speed, this number of rays was deemed to be appropriate for the current problem. Additionally, the base calculations employ identical CFD conditions (summarised in chapter 2) on a 3600 fluid node grid. Less than 1 % differences were observed in velocity, temperature and mixture fraction profiles at a number of distinct heights on grids of a finer resolution. All subsequent simulations are assumed to entail these base calculations unless stated otherwise.

One of the main conclusions to be drawn from this analysis concerns the sensitivity of soot concentration prediction to solution parameters whose variation yields less than significant differences in every other respect. Thus, to assess the quality of a particular sub-model, it is important that the simulated flow field possesses sufficient accuracy. Since only scalar measurements have been made for the flames under consideration, mixture fraction profiles provide the most effective means by which to do this, having established that the solution is independent of the underlying grid.

Uncertainty concerning the most realistic value to use for the Prandtl-Schmidt number in the balance equations for enthalpy, mass fraction of fuel and the first two moments of mixture fraction was discussed above. Thus, an assessment of mixture fraction predictions should include a consideration of this important parameter. Radial profiles of mixture fraction at heights of 150, 300 and 425 mm are shown in Fig. (5.2). The experimental measurements are compared against predictions from the eddy break-up model for values of the Prandtl-Schmidt number equal to 0.7 and 1.0. Closest agreement with experiment is demonstrated for a value of 0.7, and this is adopted in subsequent calculations. Further analysis of the mixture fraction predictions is presented below.

5.3.2 Flow Field Prediction using the Eddy Break-up Combustion Model

It has already been noted that large differences in temperature

prediction may accompany considerably smaller discrepancies in mixture fraction. Therefore, whereas satisfactory agreement between experiment and simulation for mixture fraction may confirm the plausibility of a particular CFD methodology, weaknesses may prevail in the calculation of temperature. These observations are reinforced in Figs. (5.3) and (5.4), which depict the radial variation of Reynolds mean temperature and Favre mean mixture fraction at three distinct heights for various values of the eddy break-up constant, A. Whilst significant differences in predicted mean temperature occur, particularly in the region of maximum temperature, for values of A equal to 1, 2 and 4, numerical predictions of mean mixture fraction demonstrate little variation.

Since the eddy break-up constant effectively scales the rate at which fuel is consumed, an increase in A generates faster consumption and produces higher mean temperatures. These differences are heightened at the stoichiometric mixture fraction. Either side of this, the profiles tend to converge as the reaction rate becomes dominated by the lack of oxidant close to the centre line, or by the scarcity of fuel at larger radii. Whilst selection of the most appropriate value of A has some bearing on the inner profile shape, no single value is able to capture the spreading rate; this being manifested as a significant under-prediction of temperature in the lean region at a height of 425 mm. Additionally, an adiabatic flame calculation of temperature for $A=4.0$ similarly under-predicts temperature. Since negligible net radiative absorption occurs in low soot (CO_2 and H_2O) concentration and temperature regions of the flame, the adiabatic profiles should envelope the measured values. Reasons for the failure of the overall methodology are addressed following an appraisal of soot concentration predictions, and the selection of the most suitable value of A.

Radial variations of Favre mean soot volume fraction are shown in Fig. (5.5) for the same values of A. Due to the weakly sooting nature of methane-air flames at atmospheric pressure, combined with the difficulty of accurately recording low levels of soot concentration, measurements of soot

volume fraction were only performed at heights of 300, 350 and 425 mm above the inlet. The numerical predictions are expected to be somewhat greater than the measured values due to the exclusion of oxidation from the soot model. However, when $A=4.0$ the reverse is true, and significant allowance for oxidation is only accommodated by a value of 1.0. Nonetheless, the key trends in the evolution with downstream distance are captured by all the computed profiles. Even in the absence of oxidation, the rate of increase of centre line soot concentration is reduced as the mixture fraction (and fuel concentration) falls. The axial variation of soot volume fraction and temperature are depicted in Fig. (5.6).

With respect to selecting a value for A which best represents the rate of heat release in the present flame, the previous soot predictions would appear to favour a value in the range $1.0 < A < 2.0$. Additionally, the inclusion of oxidation, which would yield lower levels of soot, would also reduce radiative loss, and hence increase temperature. It is to be recalled from Fig. (5.3) that the solution for $A=1.0$ under-predicted temperature in the region of the maximum. An alternative viewpoint, which focuses upon the neglect of turbulent fluctuations, might recommend a higher value of A since the incorporation of fluctuations is most likely to reduce temperature in hot regions close to the centre-line, and increase it in lean regions where the present methodology significantly under-predicts temperature. (Further insight into this phenomenon is provided by the laminar flamelet methodologies presented in the next sub-section.) However, in Fig. (5.7), very close agreement is achieved for temperature predictions incorporating an eddy break-up calculation of species with $A=1.0$, and a laminar flamelet calculation employing the species CH_4, O_2, N_2, CO, CO_2 and H_2O. Thus, $A=1.0$ is adopted in all subsequent eddy break-up simulations.

5.3.3 Flow Field Prediction using the Laminar Flamelet Concept

The effect of neglecting turbulent fluctuations in the eddy break-up model is investigated here by comparison against two laminar flamelet

based solutions. The first, comprises the base calculation described above. The second, directly interpolates on the temperature and density flamelets; that is, it sets the variance to zero. Inaccuracies in the prediction of temperature due to the $k-\varepsilon$ turbulence model cannot be assessed in a similar fashion since the model is common to the three solutions.

Radial variations of mean temperature are compared in Fig. (5.8). Relative to the calculation of temperature from mean total enthalpy, the conventional laminar flamelet approach significantly reduces discrepancies between prediction and experiment in rich regions low in the flame, and in lean regions where the former approach poorly reproduces the spreading rate.

At all heights, the zero variance flamelet calculation produces a more pronounced peak than that observed experimentally, and converges to the eddy break-up profiles on the negative gradient. Clearly, the inclusion of fluctuations flattens the peak temperature by mixing with cooler regions on either side, and enhances the spreading rate across the negative gradient due to the higher temperatures closer to the centre line.

The discontinuities in gradient of the laminar flamelet profiles result from the difficulty of producing a smooth transition at low values of mixture fraction from integration of the beta-function pdf to a delta function. A finer grid would resolve this problem. A less easily surmountable weakness of the laminar flamelet approach concerns the inability to incorporate interaction with solid boundaries. These weaknesses thus favour the determination of temperature from enthalpy.

Although the laminar flamelet calculation of temperature demonstrates superior performance to that obtained from mean enthalpy, temperature is still under-predicted at a height of 425 mm. Further evidence for the comparatively poor prediction of mixing was provided in Fig. (5.4) where computed profiles of mixture fraction were shown to lie below the measured values in lean regions of the flame. Despite the uncertainty relating to mixture fraction measurements by probe sampling

in leaner regions at the edges of sooting flames (due to carbon retained in the sampling lines), the under-prediction of temperature indicates a significant weakness in the overall methodology presented here. Possible explanations for this require further investigation. They largely concern the applicability of the high Reynolds number $k-\varepsilon$ turbulence model to regions in the flame where both buoyancy and low Reynolds number effects are becoming significant. Based on the fuel inlet diameter, the Reynolds number is approximately 2800, and by 425 mm the maximum velocity is less than 6 ms^{-1}.

5.3.4 The Influence of Different Radiation Solutions and Radiative Property Models on the Distribution of Soot

All of the foregoing predictions employed the weighted sum of grey gases (WSGG) solution to the radiative transfer equation. The theoretical investigation in earlier chapters indicated that this methodology provides the best compromise between accuracy and cost for the flame configuration analysed here. However, it is not clear to what extent different predictions of radiative exchange have on flame structure, particularly temperature and the distribution of soot. Thus, to ascertain some understanding of this potentially important interaction, comparisons of temperature and soot volume fraction are depicted in Figs. (5.9) and (5.10), respectively, at a height of 425 mm, for different radiation algorithms coupled to the eddy break-up model with $A=1.0$. In order to accomodate the relatively expensive differential total absorptivity (DTA) solution, calculations were performed on a 400 node grid, and the number of rays per surface were reduced to 64.

In addition to the WSGG and DTA solutions, predictions are shown for a total property (TP) solution using the Truelove (1975) weighted sum of grey gases data, and three constant absorption coefficient (CAC) solutions. The DTA solution employed the weighted sum of grey gases total absorptivity data due to Smith et al. (1982).

In Fig. (5.9), particularly close agreement is demonstrated between the DTA and WSGG solutions, and the TP solution differs from them by less than 100 K. An absorption coefficient of approximately *2.0* appears to model the prediction of radiative loss very closely, whereas values of *1.0* and *4.0*, respectively, significantly under- and over-predict net emission.

The radial variation of soot volume fraction shown in Fig. (5.10) demonstrates the sensitivity of soot prediction to the calculation of radiative exchange. Whilst temperatures in the TP solution agreed to within 7 % of those in the more accurate solutions, the soot distributions differ by over 30 %. Also, somewhat paradoxically, the CAC solution predictions of soot volume fraction do not completely mirror the levels of radiative loss manifested in the associated temperature profiles. The relative positions of the CAC solution soot concentration profiles concur with the temperature profiles; that is, in terms of a higher absorption coefficient producing greater radiative loss, and culminating in a lower level of soot formation. However, whilst an absorption coefficient close to unity would appear to generate soot levels in good agreement with the DTA and WSGG solutions, a value closer to *2.0* better predicts the temperature variation. The reasons for this are unclear, but most likely relate to the relatively weak coupling between soot formation and the CAC solution to the radiative transfer equation.

Another interesting feature depicted in Fig. (5.9) concerns the higher temperatures produced by the CAC solutions with increasing absorption coefficient near to the outer boundary. Although this phenomenon is unrealistic for the present flame, the overall net absorption that it characterises does become significant in the 3 atm. flame analysed below.

Ultimately, CFD simulation of combustion is required to yield accurate prediction of the output from a flame or a fire, both in terms of pollutant emissions and energy. Clearly, soot formation is particularly sensitive to radiative loss, largely as a result of the exponential dependence of the governing kinetic mechanisms on temperature. Whilst the radiative output

from a combustion source may also possess a high level of sensitivity, due to a fourth order dependence on temperature, the consequent effect on boundary temperature is less dramatic. This phenomenon is reflected in Fig. (5.11), which depicts the incident radiative flux to the pyrex casing, and the accompanying face temperature evaluated from a flux balance across the conjugate boundary. Whereas, the TP solution over-predicts incident radiative flux relative to the DTA and WSGG solutions by over 20 %, the face temperature predictions agree to within 5 %.

For the present flame configuration, the interaction between radiative loss and soot formation is only weakly dependent upon the boundary conditions employed to represent the pyrex casing. Notwithstanding the complex radiative properties of the material, accurate modelling of these properties would not appear to be justified in the present analysis. For example, halving the emissivity to 0.4 produces insignificant differences in temperature, even for the adjacent gas. The flow field is more sensitive to the temperature of the external pressure vessel. When this is reduced from 500 to 300 K, the internal face temperature decreases by up to 100 K, the adjacent gas by approximately 40 K, but centre-line temperatures differ by less than 1 K. The overall implication of this description is that radiation is dominated by that from the flame, with boundary radiation having little impact on the flow field.

5.3.5 Coupled Thermal Radiation, Soot Formation and Oxidation

Considerable uncertainty still surrounds the prediction of soot formation. Although the foregoing analysis, and other related work demonstrate the capability of producing reasonably accurate predictions of the distribution of soot in turbulent non-premixed flames, the underlying assumptions, and the complexity of the mechanisms they seek to describe, currently preclude the attainment of an accuracy commensurate with that obtainable for the concentrations of the major gas species. The problem is exacerbated by the even greater uncertainty concerning soot destruction (or

oxidation). Although a certain amount of progress has been made in ascertaining the important contributors to soot destruction, and how the oxidation rate depends on properties of the flow, a universal description is not available. Nonetheless, it is generally accepted that the OH radical dominates oxidation in the interior of flames, whilst O_2 has a greater influence at the periphery, largely governed by the degree of turbulent mixing.

Soot oxidation is here modelled by an OH mechanism based upon the expression proposed by Fenimore and Jones (1967) and discussed by Brookes (1996). The flamelet family thus generated is integrated across the pdf of mixture fraction according to the level of radiative loss, and subtracted from the source of soot concentration. Unfortunately, this type of oxidation rate expression fails to reproduce experimentally observed levels of soot volume fraction. Substantial scaling is required to reduce the rate of soot oxidation, as originally acknowledged by Syed (1990). For the present analysis, a constant scaling factor of 0.05 was adopted. The effect of oxidation is investigated in Figs. (5.12) to (5.18).

Initially, predictions of soot volume fraction are presented for the DTA, WSGG and TP solutions obtained on the coarse grid. Radial profiles at a height of 425 mm, shown in Fig. (5.12a), demonstrate the capability of generating good agreement at a particular height. As before, the TP solution significantly under-predicts the concentration of soot relative to the DTA and WSGG solutions.

Unfortunately, the single oxidising mechanism used in the present format is unable to yield a common level of accuracy throughout the flow field. Whereas the DTA solution closely predicts the centre line soot concentration at 425 mm, it differs from the experimental measurement by almost a factor of three at 300 mm. Although the WSGG solution generates a better mean representation of the measurements, in common with the other solutions it too fails to capture the centre line trend of increasing concentration.

Fig. (5.13) shows the effect of oxidation on the radiative flux received by the pyrex casing, and the consequent change in face temperature. As expected, lower levels of soot reduce the incident flux leading to temperature reductions of up to 50 K. Very close agreement is again obtained between predictions from the DTA and WSGG solutions.

Figs. (5.14) and (5.15) depict the radial variations of temperature and soot volume fraction obtained for the WSGG solution obtained on the fine grid. Marginal differences in temperature are produced by the inclusion of oxidation, whilst soot concentration is reduced by approximately a factor of two on the centre line, and by considerably more radially. As expected, a lower soot yield reduces the radiative loss, and thus raises temperature. However, the net temperature increase is constrained due to the joint dependence of emission on soot concentration and temperature.

The small amount of experimental soot concentration data demands caution in the comparisons between measurement and prediction. Nonetheless, the data points plotted in Fig. (5.6b) imply that the maximum soot volume fraction has not been reached on the centre line by a height of 425 mm. Likewise, the peak temperature occurs downstream of the available data. The contour plot of soot volume fraction shown in Fig. (5.17b) reveals that, relative to the coarse grid solution, the peak value occurs further downstream, but its occurrence at a height close to 425 mm is lower than that observed experimentally. When oxidation is excluded from the prediction of soot concentration, the peak value occurs just below 450 mm (cf. Fig. (5.16b)). Thus, the location of the predicted maximum is not expected to vary significantly with adjustment to the oxidation rate.

The set of contour maps for mean temperature, soot volume fraction and CO_2 molar fraction shown in Figs. (5.16) and (5.17) also confirm that, for this lightly sooting flame, the inclusion of oxidation in the soot model only has a significant effect on soot yield. Whilst considerable shrinkage of high soot concentration regions is produced by oxidation, the distributions of temperature and CO_2 molar fraction are broadly maintained.

The coupling between thermal radiation and soot formation in the present configuration can only be expected to demonstrate discernible interaction in regions where there are significant levels of soot. Even there, the presence of relatively high concentrations of CO_2 and H_2O may dominate the radiative effects of the gas-soot mixture. This phenomenon is demonstrated in Fig. (5.18) which depicts the variation of volumetric radiative flux with height, at three distinct radii, for the previous WSGG solutions with and without oxidation, and for WSGG solutions in which either the gaseous or the particulate contributions have been ignored.

Although it is physically unrealistic to view net radiative exchange as a linear combination of that due to individual components, the adjustment for overlap is relatively small. Additionally, different overall solutions are produced when neglecting one of the radiating components. Nonetheless, interpretation of Fig. (5.18a) reveals that, close to the centre line, the volumetric flux of the mixture is dominated by gaseous radiation for approximately 25 cm before the soot contribution rapidly increases, and finally dominates the net emission either side of its maximum at a height of 40 cm. Away from the axis, a very different interaction occurs. For example, in Fig. (5.18b), the volumetric flux variation with height at a radius of 20.6 mm maximises lower in the flame at a location where gaseous radiation exceeds that due to soot. Then, at a radius of 40.1 mm a positive volumetric flux is produced since absorption exceeds emission, cf. Fig. (5.18c). Primarily, this is due to the presence of a significant concentration of relatively cool gases. Notwithstanding the considerable variation in radiative exchange which occurs at different locations, the overall distribution of volumetric flux is dominated by emission from the hot, high concentration core of the flame.

5.3.6 Turbulence-radiation Interaction

Since radiative emission has a fourth order dependence on temperature, the neglect of turbulent fluctuations is believed to be largely

responsible for the poor performance of many spectrally based radiation predictions (cf. Syed et al., 1990). However, when employing approximate algorithms to calculate radiative exchange (such as the WSGG solution), the significance of turbulence-radiation interaction is less clear. Unfortunately, it is not presently feasible to incorporate stochastic methods into the repeated solution of the radiative transfer equation as conducted here. Nonetheless, fluctuations in temperature can be included in the DTRM algorithm by applying a laminar flamelet integration to the fourth order black body intensity which underpins radiative exchange. Thus, from Eq. (3.42),

$$i_{j,n} = i_{0,j}\prod_{r=1}^{n}\tau_{j,r} + \frac{\sigma}{\pi}\sum_{r=1}^{n}\left[a_j\,\overline{T^4}\,\varepsilon_{j,r}\prod_{r'=r+1}^{n}\tau_{j,r'}\right] \tag{5.13}$$

where $\overline{T^4}$ is evaluated according to the methodology described in sub-section (5.2.4.2), the set of T^4 flamelets having been generated from the corresponding temperature flamelets. Likewise, radiative loss is given by

$$\overline{S}_R = L_1 - L_2\overline{T^4} \tag{5.14}$$

with L_1 and L_2 given by Eqs. (3.45a) and (3.45b), respectively. In this approach, all other terms in Eqs. (5.13) and (5.14) are evaluated as before from conventional mean values. Therefore, it is possible to assess the impact of calculating $\overline{T^4}$ instead of $\overline{T}^4$. For the WSGG solution coupled to the soot model with oxidation, the effect on radial soot volume fraction profiles is small as depicted in Fig. (5.19). Consequently, the temperature field is only marginally affected. This finding concurs with recent work by Adams and Smith (1995) who included the effect of turbulent fluctuations on the absorption coefficient, as well as on the emissive power. Such results

mitigate against incorporation of turbulence-radiation interaction into CFD simulation of weakly sooting practical combustion systems. However, higher soot concentrations often occur, and both total property (cf. Adams and Smith, 1995) and spectrally resolved calculations (cf. Gore and Faeth, 1988) have demonstrated the increased importance of turbulence-radiation interaction for more heavily sooting environments. The following section, which presents an investigation of the same methane flame as above, but burning at a total pressure of 3 atm., includes a similar analysis of turbulent fluctuations.

5.4 FLAME AT TOTAL PRESSURE OF 3 ATM.

5.4.1 Introduction

In addition to the experimental analysis of the methane diffusion flame at atmospheric pressure, Brookes (1996) also performed measurements on the same rig at a total pressure of 3 atm. The mass flow rate of fuel, and overall equivalence ratio were unaltered from the 1 atm. flame. Thus, for the computational simulation, inlet velocities were accordingly reduced to 6.72 and 0.17 m/s for the fuel and air streams, respectively. Apart from the accompanying adjustments to the turbulence intensity and dissipation rates, all other boundary conditions were unchanged.

Since the higher pressure flame generates soot concentrations approximately an order of magnitude greater than the 1 atm. flame, the increased level of radiative emission requires a wider range of radiative loss to be accommodated in the multiple flamelet approach. Thus, flamelet families were generated which incorporated losses up to 35 %.

When performing radiation prediction in non-atmospheric pressure environments, the WSGG solution is weakened by the lack of curve-fits to total radiative property data at different total pressures. Primarily, properties vary due to the pressure broadening effect on the radiative line

structure of the molecular gases. Originally, Hottel and Sarofim (1967) provided a set of pressure correction curves to generate such data. Leckner's (1972) total property curve-fits also incorporated a correction for non-atmospheric pressure. These approaches cannot be used in a general way for the WSGG solution without generating a new set of coefficients. An alternative methodology is provided by the scaling rules for total properties developed by Edwards and Matavosian (1984). Effectively, they recommended a scaling of path length for a range of temperatures, total pressures and partial pressure-path-length products. However, since the scaling exponent tends to zero for short pressure-path-length products, the effect of pressure broadening is neglected in the present flame configuration, and the weighted sum of grey gases coefficients for atmospheric pressure total properties are employed unadjusted.

5.4.2 Flow Field Prediction

Figures (5.20) and (5.21) show contour maps of temperature, soot volume fraction and CO_2 molar fraction for simulations of the 3 atm. flame with the exclusion and inclusion of oxidation, respectively. Both calculations were performed on the fine grid employing 128 rays per boundary face, and the WSGG solution. The eddy break-up constant was unity. Peak values of temperature, soot volume fraction and gaseous partial pressure all occur lower than in the 1 atm. flame.

Without oxidation, excessively high soot volume fractions are produced ($> 4.0 \times 10^{-5}$). This is believed to result from a model dependence of soot surface growth on pressure squared. Brookes (1996) is expected to report a better representation of this relationship following a parametric study of the growth rate, in which he attempts to optimise the joint dependence on density and surface area per unit volume. In its present form, predicted soot concentrations are brought into line with measured values by a scaling factor of 0.1 applied to the oxidation rate.

Compared to the contour maps for the 1 atm. flame, the inclusion of

oxidation now has a significant effect on temperature. This results from a large over-prediction of radiative loss accompanying the excessively high levels of soot concentration generated by the soot formation model. The distribution of CO_2 is little affected by these differences.

Centre line variation of temperature and soot volume fraction are depicted in Fig. (5.22). In contrast to the equivalent profiles for the 1 atm. flame, close agreement is obtained for temperature, and, although peak soot levels are over-predicted, the location of the maximum is well reproduced. Profiles are also shown for a solution in which turbulence-radiation interaction was included in the evaluation of black body intensity (cf. Eqs. (5.13) and (5.14)). In this case, the evolution of soot volume fraction with downstream distance is significantly improved. Although the reproduction of these variations is encouraging, it must be recalled that *ad hoc* scaling of the oxidation rate was required to reduce soot concentrations to a suitable level.

Radial temperature measurements were made by Brookes (1996) only up to a height of 250 mm. Numerical predictions are compared against experimental data at heights of 50, 150 and 250 mm in Fig. (5.23). At the lowest height, the steep gradients are poorly reproduced. An attempt was made to capture this profile by applying grid expansion in the axial direction, but convergence difficulties could not be overcome. The possibility of obtaining an improvement in accuracy by employing a finer grid was not investigated, since the current emphasis did not warrant the severe computational penalty. One of the primary objectives here concerns the extension of the overall methodology to enclosure fires, such that very fine grid resolution is unlikely to be appropriate even when embedded grids, and/or local grid refinement are employed. Additionally, the imposition of increasingly shorter path lengths in radiative property calculations further weakens the applicability of the available data. At heights of 150 and 250 mm generally good agreement is achieved between experiment and prediction, particularly in terms of peak temperature and the negative

gradient.

Predictions of soot volume fraction are compared against experiment in Fig. (5.24) at heights of 150, 250 and 350 mm. The radial profiles are generally well reproduced, although predictions of the magnitude close to the centre line exceed measured values, for the specified scaling of the oxidation rate.

Once again, profiles generated by the inclusion of turbulent fluctuations into the evaluation of radiative emission are also shown in Figs. (5.23) and (5.24). Although only small differences in temperature are generated, they are more significant than observed for the 1 atm. flame. Additionally, soot concentration is more dramatically affected. At all heights shown in Fig. (5.24), reduction by over a factor of two is produced. This most likely results from multiplication of the black body intensity by a larger value of emissivity generated by the greater soot loading.

5.4.3 Analysis of Radiative Exchange

In chapter 3, it was demonstrated that solution of the radiative transfer equation employing total radiative properties calculated on a cell-by-cell basis produced closer agreement with the WSGG solution as the soot loading was increased. Therefore, it is not surprising that differences in temperature and soot concentration produced by these different solutions are less pronounced in the more heavily sooting flame. Temperature and soot volume fraction predictions are compared in Figs. (5.25) and (5.26) for these solutions applied on the coarse grid. Also shown are predictions obtained employing the CAC solution with absorption coefficients of *5.0*,*10.0*, and *15.0*. A representative value appears to lie in the range : $5.0 < k < 10.0$; although all values over-estimate absorption in the outermost regions of the flame.

The numerical analysis of volumetric radiative flux conducted for the 1 atm. flame revealed a complex interaction between the gaseous and particulate contributions to the total flux. Fig. (5.27) depicts a similar

comparison for the 3 atm. flame. Close to the centre line, emission is dominated by soot throughout the height, apart from an initial region of gaseous absorption. This is in marked contrast to the lower sooting flame in which the gaseous contribution is significant at all heights. Additionally, the peak flux is approximately four times greater in the high pressure flame, and it occurs at a lower height corresponding to the location of maximum soot concentration. Differences between the flames for the relative contributions to radiative flux are less marked away from the axis. For both flames, net radiative emission is dominated by the gaseous components at radii of 20.6 and 40.1 mm. Also, at the larger radius absorption exceeds emission.

Since volumetric flux represents a balance between emission and absorption, a higher level of radiative loss from the high temperature, high concentration core of a particular flame may produce lower net emission in other cooler, less dense regions - due to greater absorption - relative to a flame which emits less powerfully from its core. This phenomenon is captured by comparison of Figs. (5.27b) and (5.18b), since lower net emission is produced by the heavier sooting flame at this radius.

Finally, in this section, some important consequences for the evaluation of incident radiative flux to the boundaries are considered.

The crude representation of the pyrex casing has already been addressed, and assumptions also have to be made concerning the radiative boundary conditions most appropriate for flowing boundaries. The foregoing analysis assumed that the outgoing flux comprised the black body intensity evaluated at the temperature of the adjacent gas. At the outlet, this produces a considerable over-estimate of the radiative intensity, since rays starting from this boundary actually originate from a relatively cool surface external to the computational domain. Also, emission across a path would be a fraction of the black body value. However, these effects are offset by the relative areas involved; that is, very small areas occur on control volume faces close to the centre line, and these expand radially to

the relatively large faces on the circumference. The most significant effect of this boundary condition concerns the incident flux to the pyrex boundary. If the initial intensity at the outflow is represented by

$$i_0 = \frac{\alpha\sigma}{\pi} T_0^4 \tag{5.15}$$

variation of α between zero and unity produces the flux profile shown in Fig. (5.28a) for the 3 atm. flame. In all cases, a peak is produced corresponding to the high concentration, high temperature core of the flame. Further downstream, a second peak is observed for values of α equal to 0.5 and 1.0, whilst the flux continuously decreases when radiation from the outflow boundary is completely neglected. The associated surface temperature profiles are depicted in Fig. (5.28b), for which the differences are far less severe. At most, the extreme cases differ by 100 K. It is not surprising, therefore, that flow field predictions are effectively insensitive to the radiation boundary condition imposed at the outflow. Nonetheless, greater accuracy in surface flux predictions are often required in other problems. Consequently, further investigation into the radiation treatment of hot flowing boundaries is required.

Closer scrutiny of the incident radiative flux for $\alpha = 0.0$ reveals a point of inflection at a height of approximately 400 mm. In fact, a second peak downstream of the first may occur due to the increasing contribution from gaseous emission. Such a possibility is evident in Fig. (5.28a) which compares the incident radiative flux predicted for the gas-soot mixture with those that neglect one or the other components. (Attention is focused away from selection of the most appropriate value of α by only showing the flux variation up to a height of 350 mm. It is after this point that the profiles significantly diverge). Following the soot dominated peak at approximately 250 mm, the incident flux due to the gases alone continues to increase, and is maximised at a location downstream of this. The predicted location

depends on the value of α in Eq. (5.15), but, whatever its value, there exists the possibility that the rate of increase of incident flux due to the combustion gases may, even for a short distance, exceed the rate of decrease due to soot.

A somewhat different variation of incident flux is predicted for the less heavily sooting 1 atm. flame, as depicted in Fig. (5.29b). In this case, the flux distribution is initially dominated by gaseous radiation. The contribution from soot becomes increasingly significant with increasing height. Unlike the 3 atm. flame, both components contrive to produce a single peak flux just downstream of the 400 mm height. Variation of the radiation boundary condition at the outflow only affects the intensity of the peak without changing its overall shape. This is not shown here in order to focus on the relatively invariant portions of the profiles.

In Fig. (5.30), surface temperatures are shown which accompany the incident fluxes depicted in the previous figure. Although slightly higher temperatures are predicted for the 3 atm. flame adjacent to the peak emission zone of high soot concentration, differences are generally small. In the absence of experimental measurements of surface temperature, and without a more detailed simulation of the radiative (and other) heat transfer properties of the material, it is difficult to postulate how much these temperature predictions would vary due to the different response of pyrex to emission from gaseous and particulate components.

5.5 CONCLUSIONS

This chapter has sought to investigate a general methodology for coupling the prediction of thermal radiation and soot formation (and oxidation) within the framework of a three-dimensional, elliptic simulation of turbulent combustion. Whilst it is hoped that the overall approach will prove suitable for modelling practical problems, particularly enclosure fires,

it has been initially tested for two, relatively small, enclosed laboratory flames for which a reasonable set of scalar data was available. Despite having to confront many difficulties, largely associated with modelling a cylindrical polar geometry in Cartesian co-ordinates, the methodology has been shown to work effectively, and a number of important issues have been successfully appraised.

Initially, the effects of varying the Prandtl-Schmidt number, σ_ϕ, and the eddy break-up constant, A, were investigated. Consistent with most other researchers, $\sigma_\phi = 0.7$ was shown to yield the best representation of mixture fraction evolution with downstream distance. Less certainty could be ascribed to the selection of A, but a value of unity was deemed to be appropriate. Having established values for these parameters, the sensitivity of temperature and soot volume fraction predictions was assessed, relative to different algorithms for solving the radiative transfer equation, to the inclusion of oxidation in the soot model, and to incorporation of turbulent fluctuations in the evaluation of black body intensity. Generally, temperature predictions were only weakly correlated to these various changes, whilst in some instances, soot concentration predictions varied significantly. For example, with the inclusion of oxidation, the total property solution to the radiative transfer equation yielded half as much soot at a height of 425 mm compared to the weighted sum of gray gases solution. Meanwhile, the corresponding temperature profiles differed by less than 50 K.

Although generally good agreement was obtained between experimental and numerical temperature profiles low in the flame, a significant under-prediction of the spreading rate was produced higher up. The neglect of turbulent fluctuations in the evaluation of temperature from mean total enthalpy was believed to be largely responsible.

Results from earlier chapters had led to a recommendation for the weighted sum of gray gases (WSGG) solution to be used in the coupled

calculations performed in this chapter. Encouragingly, very close agreement was obtained between the WSGG solution and the differential total absorptivity solution applied on a relatively coarse grid. Furthermore, the total property (TP) solution significantly differed from these more accurate methods. In chapter 3, it was shown that discrepancies between the TP solution and the WSGG solution diminished with increasing soot loading. The 1 atm. flame produced relatively low levels of soot. Therefore, a flame burning at a higher pressure of 3 atm. provided a useful data set against which to further assess this hypothesis, as well as to extend the analysis of coupled thermal radiation and soot formation in a more heavily sooting environment. As expected, considerably closer agreement was obtained between the TP and WSGG solutions in the 3 atm. flame.

Radial temperature predictions in the higher pressure flame were poor at a height of 50 mm, primarily due to the difficulty of capturing steep temperature gradients. Closer agreement with experiment was obtained at intermediate heights in the flame, but a lack of experimental data prevented further assessment of the spreading rate beyond 250 mm. However, the centre line variation of temperature was better reproduced than in the 1 atm. flame, as was the evolution of soot volume fraction with downstream distance. However, these results must be viewed with cautious optimism due to uncertainties in the soot model.

As expected, predicted radiative emission from the higher pressure flame was dominated by that from soot. Less predictable, however, was the significant interaction of the gaseous components away from the high soot concentration core, particularly with respect to net absorption. This confirms the need to model both gaseous and particulate radiative energy exchange. Larger soot concentrations were also believed to be responsible for the greater effect produced by the inclusion of turbulence-radiation interaction in the evaluation of black body intensity.

Another interesting comparison concerned the small differences in predicted surface temperatures. Although the 3 atm. flame generated over

an order of magnitude higher levels of soot, the incident flux to the boundary at the height of maximum soot concentration was less than double that for the 1 atm. flame at the same height. The consequent surface temperature difference was even less significant. Since radiative loss increases with soot volume fraction, the net effect on emission is weakened due to the lower temperature which results. Also, higher net absorption is produced by cooler, adjacent regions which strongly absorb the more powerfully emitted radiation.

This chapter has presented a general strategy for the prediction of turbulent non-premixed hydrocarbon combustion which combines modelling of finite rate soot formation (and oxidation), sensitive to the influence of turbulent scalar fluctuations, with a relatively detailed solution of the accompanying coupled equation of radiative exchange, all within an elliptic representation of the governing equations. The analysis has successfully demonstrated the suitability of the overall methodology for simulation of non-premixed fuel sources commonly occurring in practical combustion problems.

ϕ	Γ_ϕ	Volumetric source term, $\overline{S}_\phi$
u_i	μ_e	$-\frac{\partial \overline{p}}{\partial x_i} + g_i\left(\overline{\rho} - \rho_{ref}\right) + \frac{\partial}{\partial x_j}\left(\mu_e \frac{\partial \tilde{u}_j}{\partial x_i}\right)$
k	μ_e/σ_k	$\mu_e\left(\frac{\partial \tilde{u}_i}{\partial x_j}\left(\frac{\partial \tilde{u}_i}{\partial x_j} + \frac{\partial \tilde{u}_j}{\partial x_i}\right) + \frac{\lvert g_x \rvert}{\sigma_H} \frac{1}{\overline{\rho}} \frac{\partial \overline{\rho}}{\partial x} - \overline{\rho}\varepsilon\right)$
ε	μ_e/σ_ε	$\mu_e \frac{\varepsilon}{k}\left\{C_{\varepsilon 1}\left(\frac{\partial \tilde{u}_i}{\partial x_j}\left(\frac{\partial \tilde{u}_i}{\partial x_j} + \frac{\partial \tilde{u}_j}{\partial x_i}\right) + \frac{\lvert g_x \rvert}{\sigma_H} \frac{1}{\overline{\rho}} \frac{\partial \overline{\rho}}{\partial x}\right) - C_{\varepsilon 2}\overline{\rho}\varepsilon\right\}$
H	μ_e/σ_H	$\sum_{all\ rays} w \Delta A \sum_{j=1}^{J}\left[1 - e^{-k_j l}\right]\left[i_{n-1} - a_j i_b\right]$
ξ	μ_e/σ_ξ	0
ξ''^2	μ_e/σ_g	$C_{g1}\mu_T\left(\frac{\partial \tilde{\xi}}{\partial x_i}\right)^2 - C_{g2}\frac{\varepsilon}{k}\widetilde{\xi''^2}$
ϕ_f	μ_e	$\overline{\delta} + \overline{\rho}\,\overline{\gamma}\,\tilde{\phi}_n^{1/3}\tilde{\phi}_f^{2/3} - \overline{\rho}\,\overline{\omega}\,\tilde{\phi}_n^{1/3}\tilde{\phi}_f^{2/3}$
ϕ_n	μ_e	$\overline{\alpha} - \overline{\rho}^2\,\overline{\beta}\,\tilde{\phi}_n^{7/3}\tilde{\phi}_f^{-1/3}$
Y_{fu}	μ_e/σ_{fu}	$-A\overline{\rho}\frac{\varepsilon}{k} min\left(\tilde{Y}_{fu}, \frac{\tilde{Y}_o}{s}, B\frac{\tilde{Y}_p}{1+s}\right)$

Table 5.1 Volumetric source terms and diffusion coefficients for all solved balance equations. ($\sigma_k = 1.0, \sigma_\varepsilon = 1.3, \sigma_H = 0.7, \sigma_\xi = 0.7, \sigma_g = 0.7, \sigma_{fu} = 0.7$).

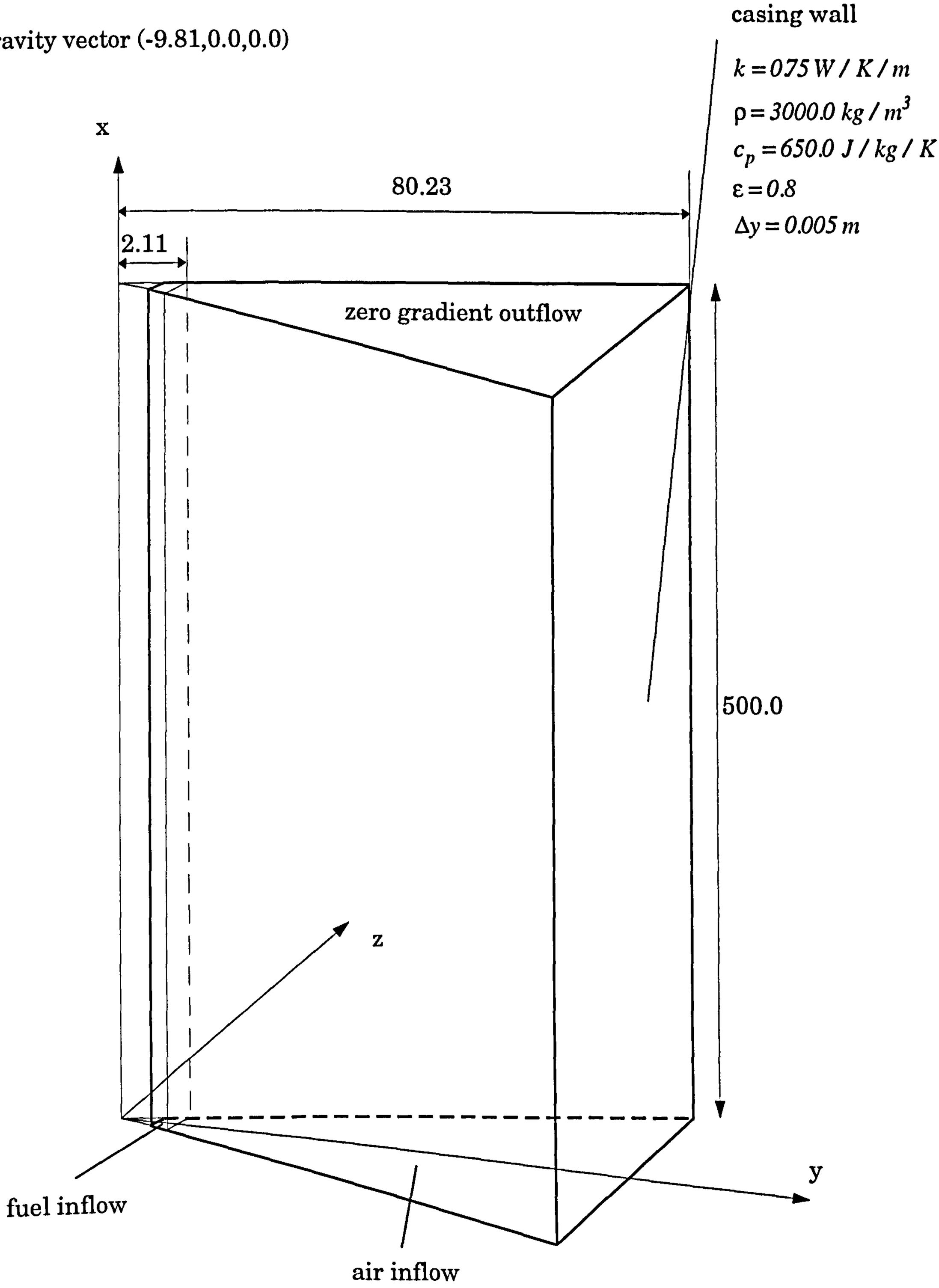

Fig. 5.1 Computational geometry (measurements in mm).

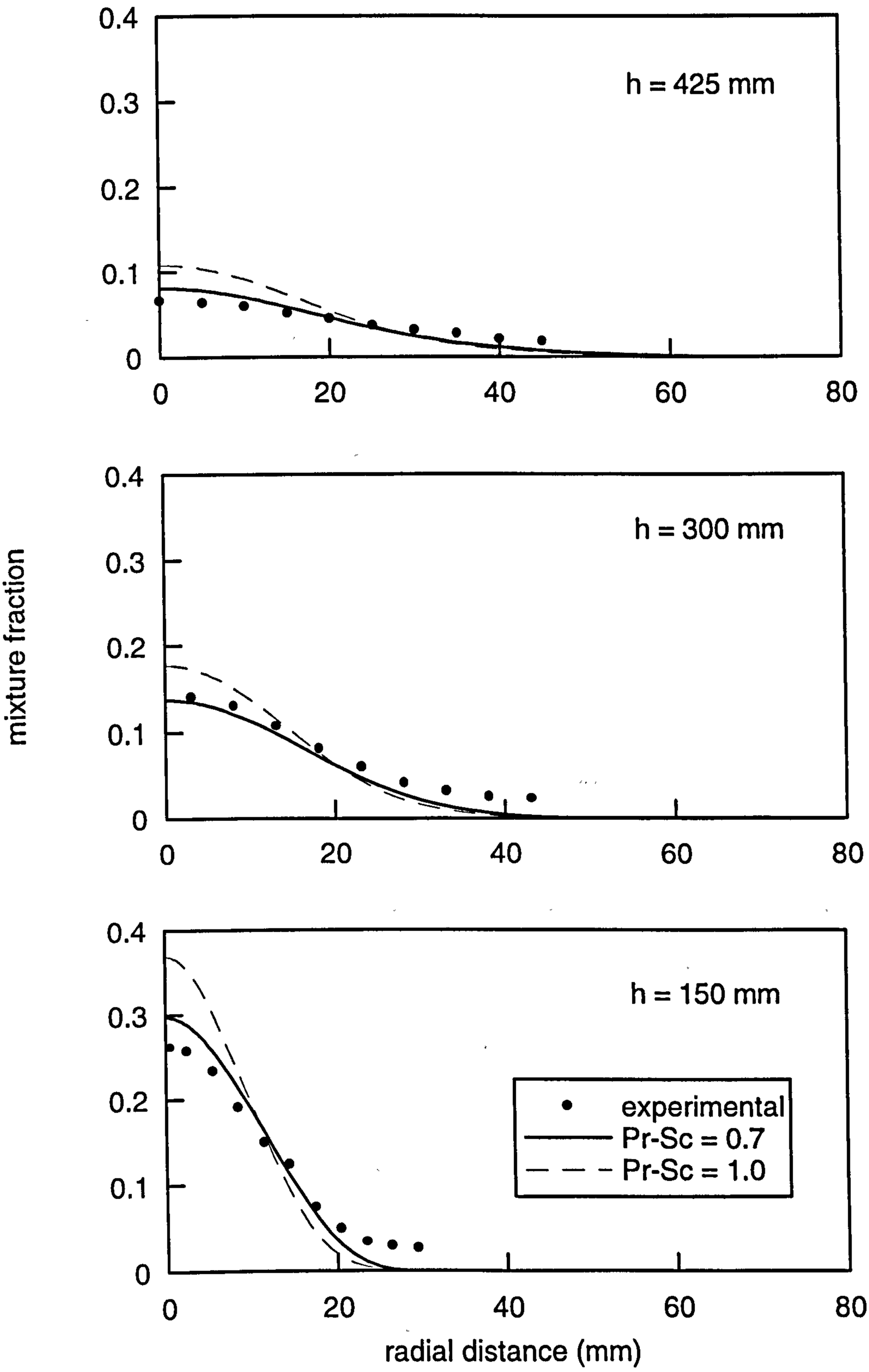

Fig. 5.2 Comparison of radial mean mixture fraction variation at three heights for different values of the Prandtl-Schmidt number.

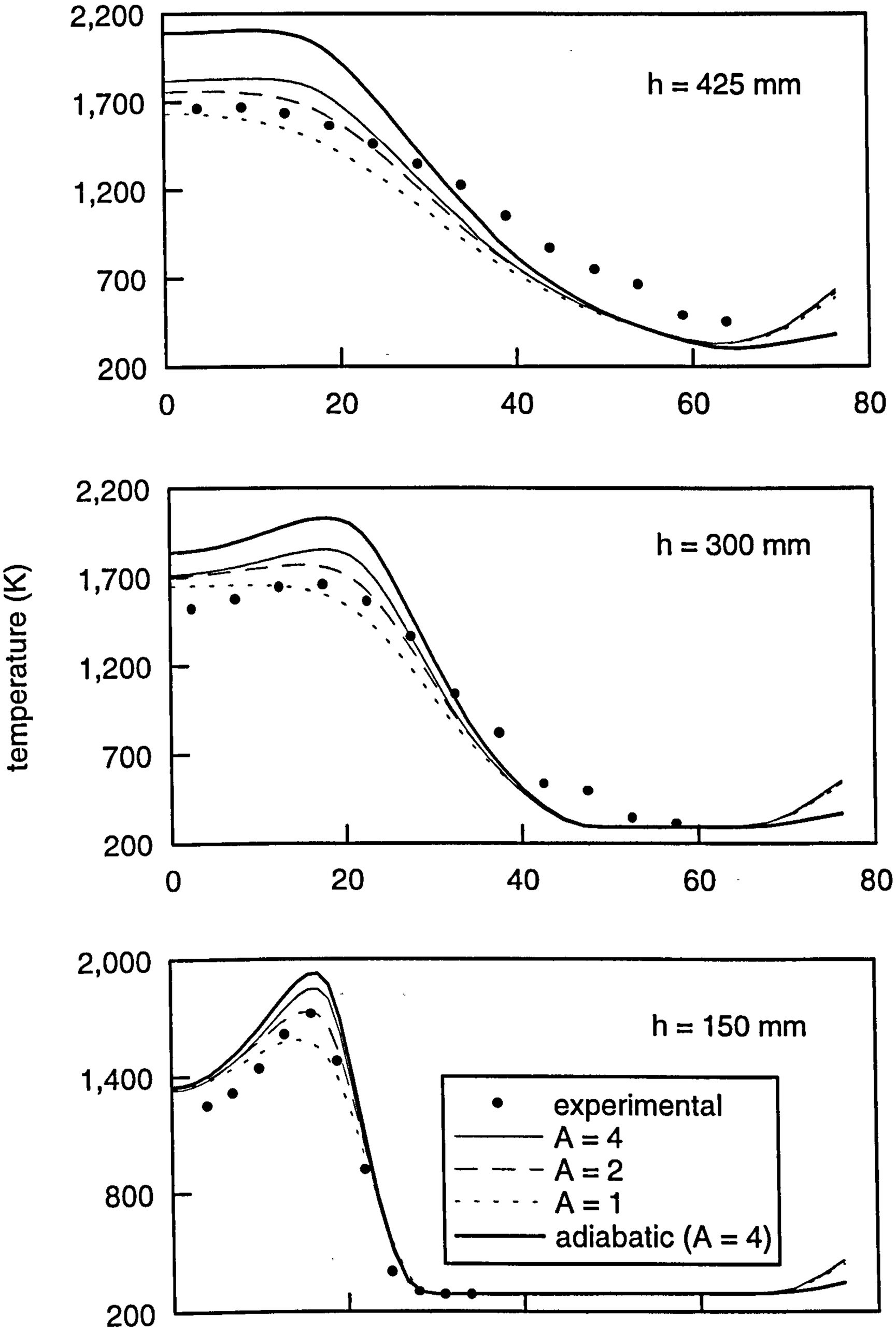

Fig. 5.3 Comparison of radial mean temperature variation at three heights for various values of the eddy break-up constant, A.

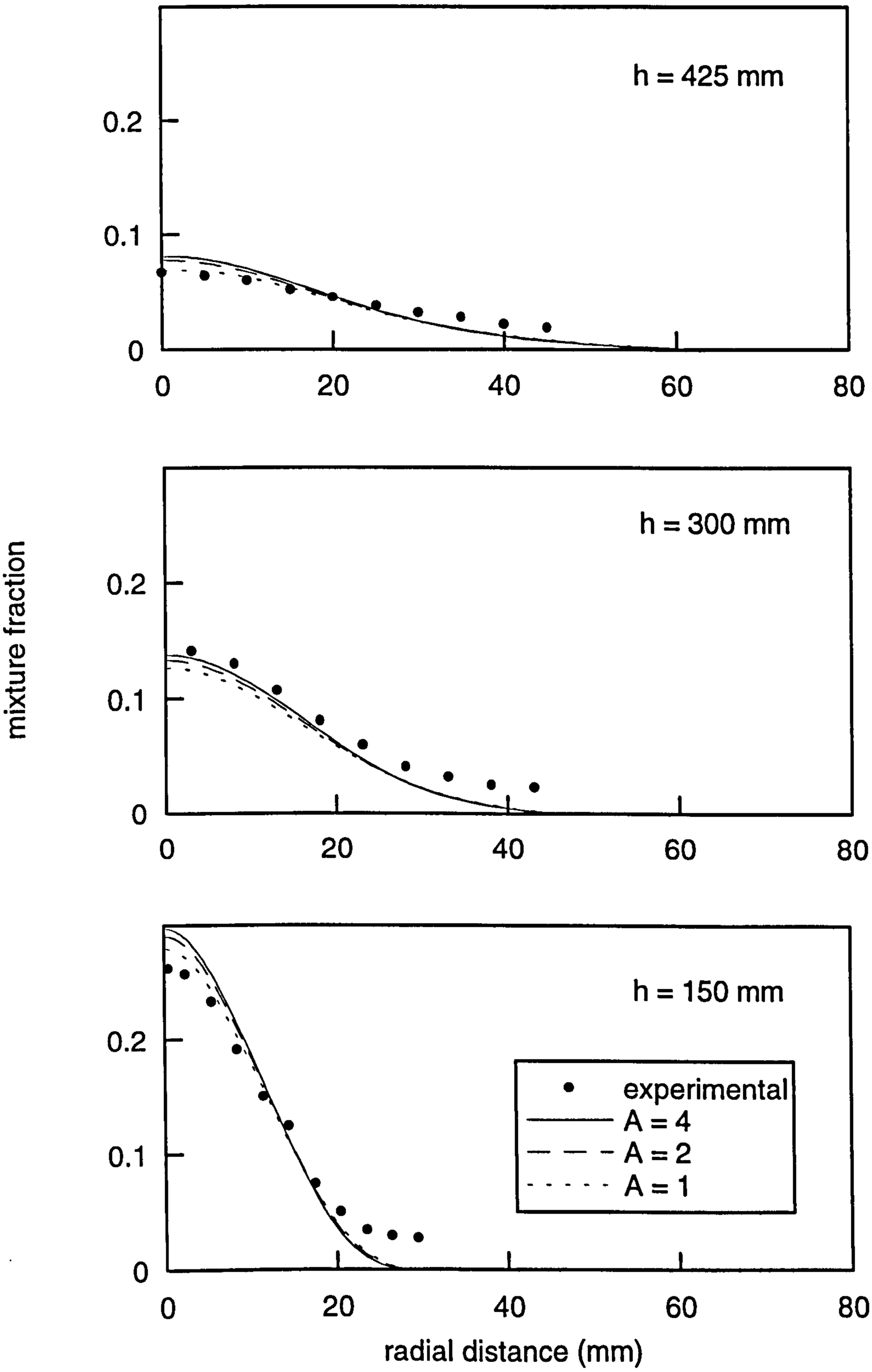

Fig. 5.4 Comparison of radial mean mixture fraction variation at three heights for various values of the eddy break-up constant, A.

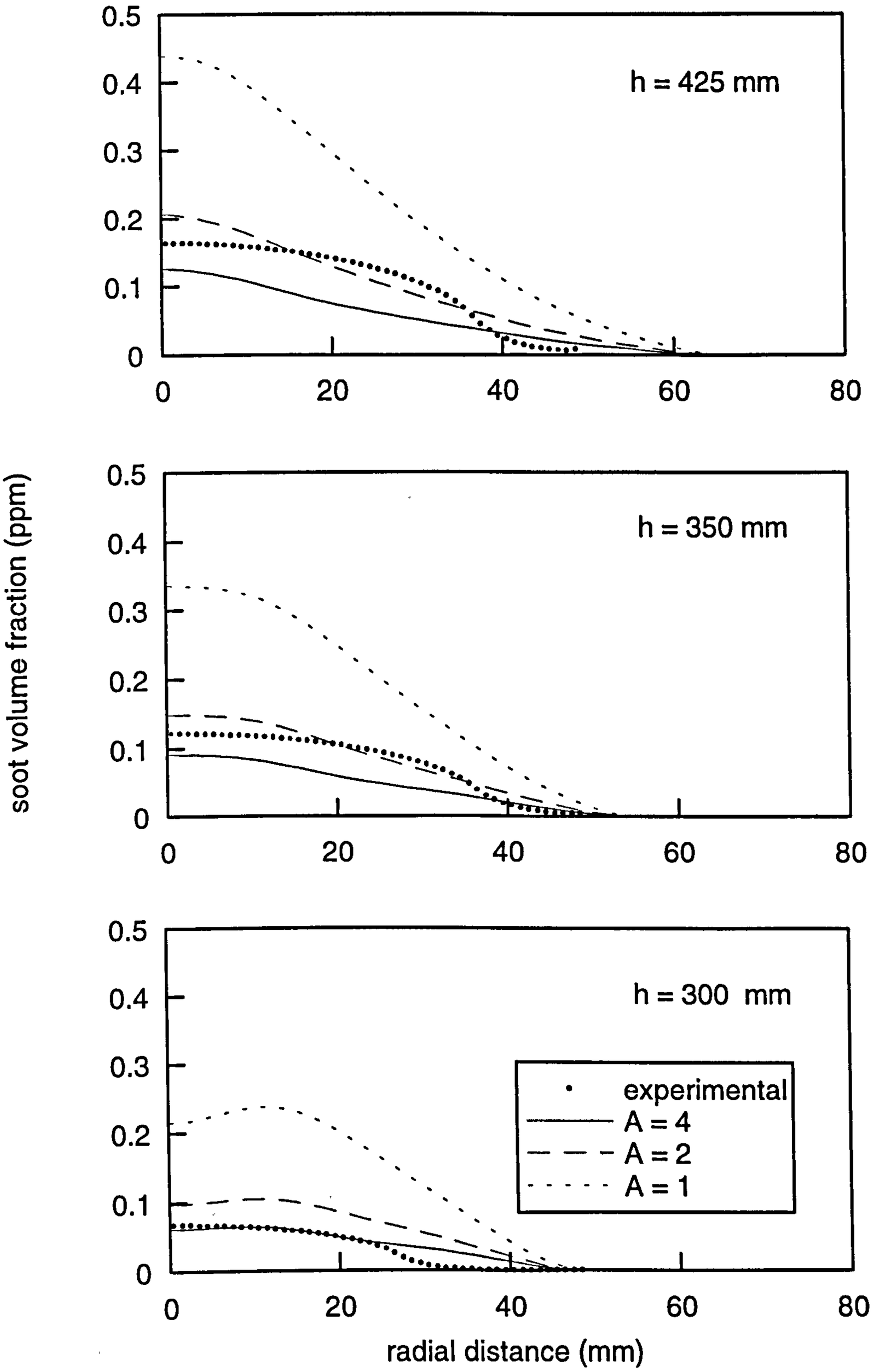

Fig. 5.5 Comparison of radial mean soot volume fraction variation at three heights for various values of the eddy break-up constant, A.

(a)

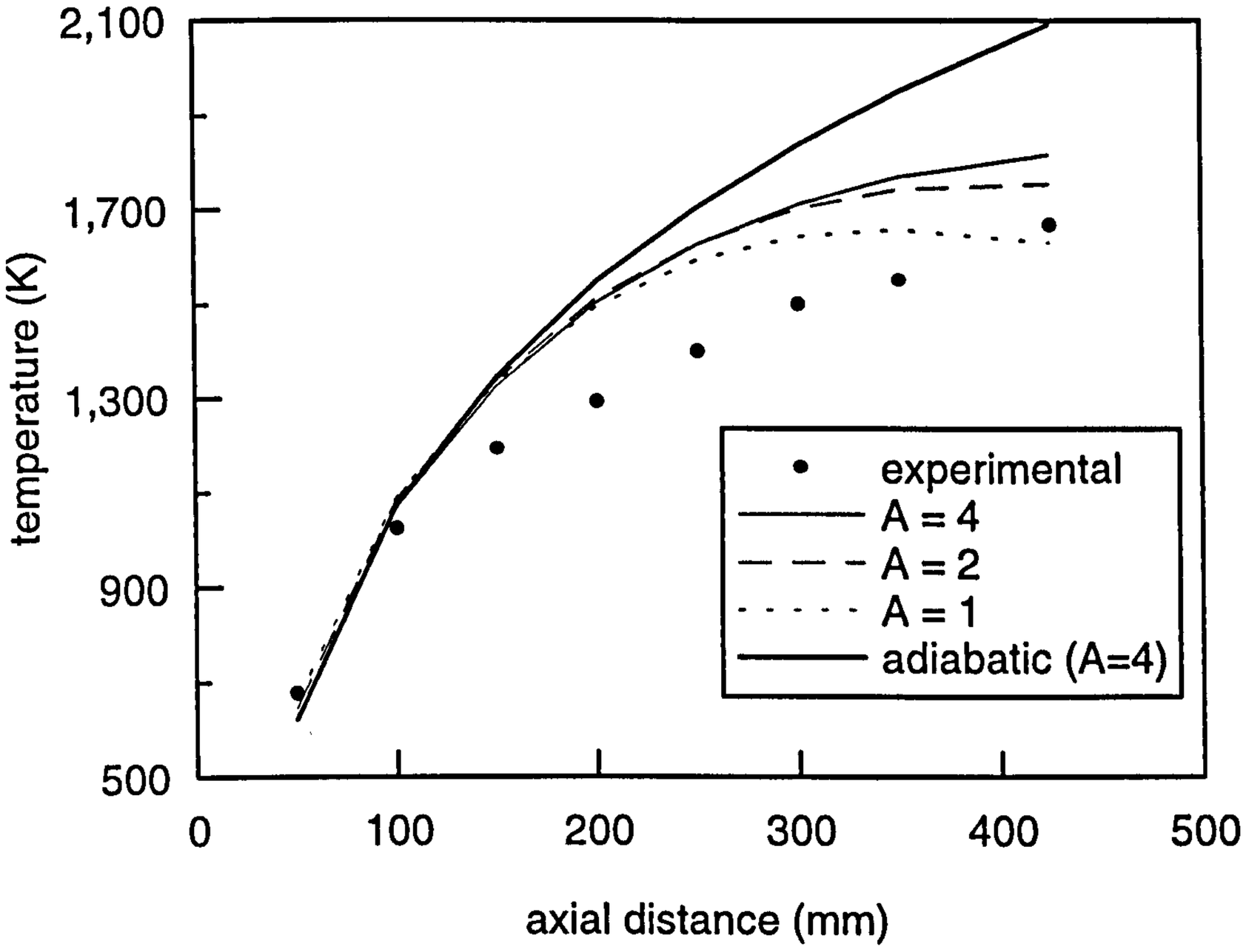

(b)

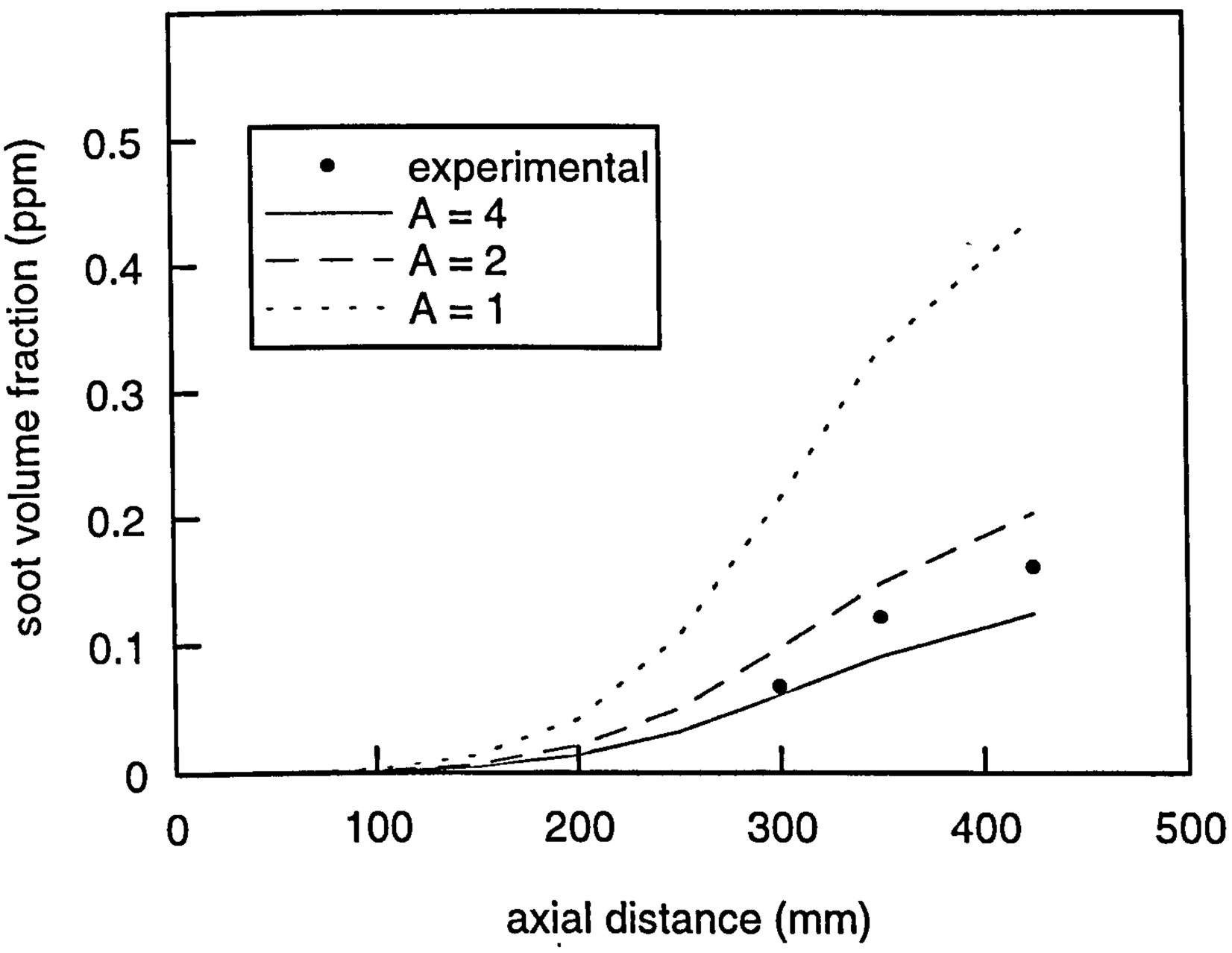

Fig. 5.6 (a) Axial variation of mean temperature for various values of the eddy break-up constant, A. (b) Axial variation of mean soot volume fraction for various values of the eddy break-up constant, A.

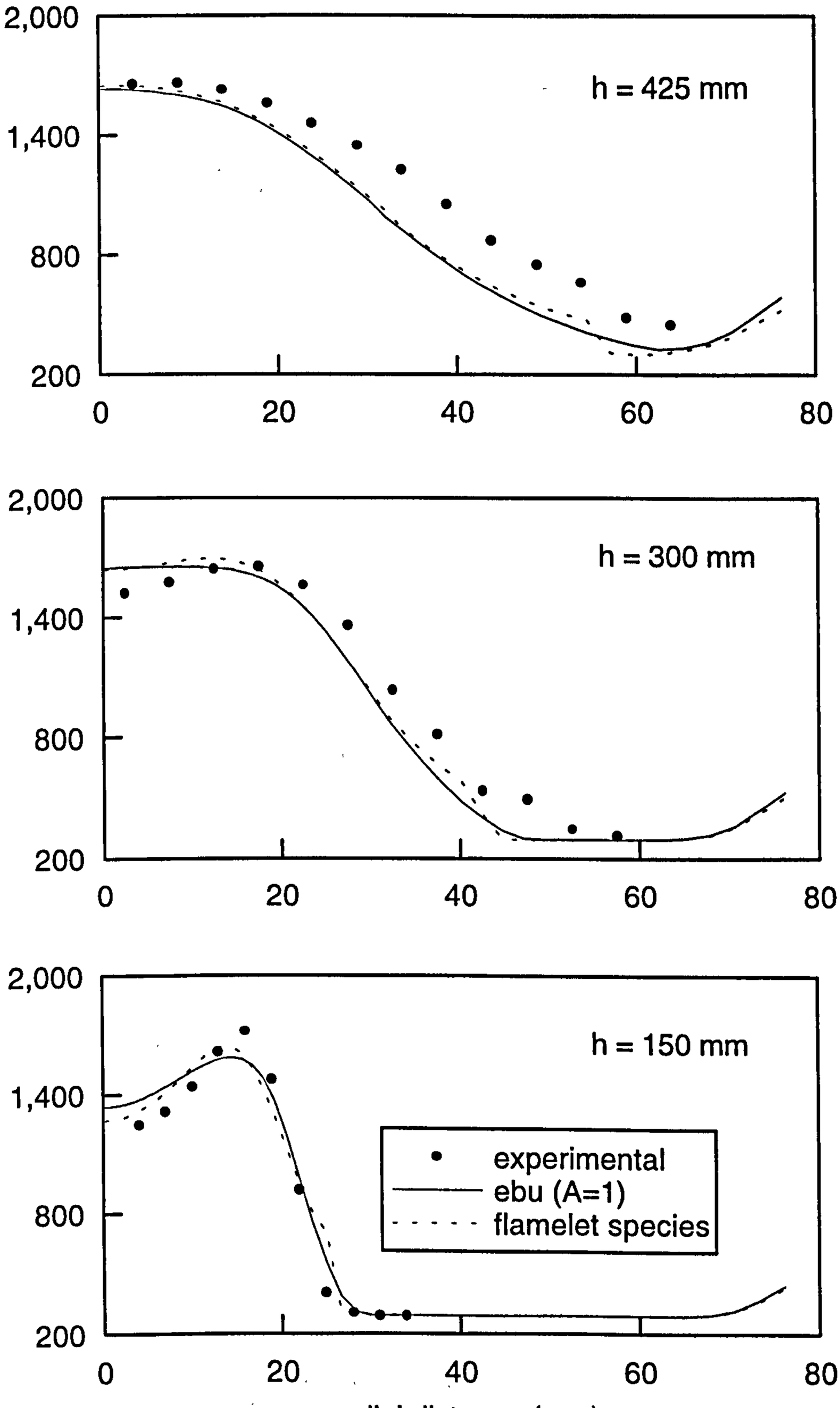

Fig. 5.7 Radial predictions of mean temperature at three distinct heights. Comparison of eddy break-up and flamelet methods for calculation of species concentrations.

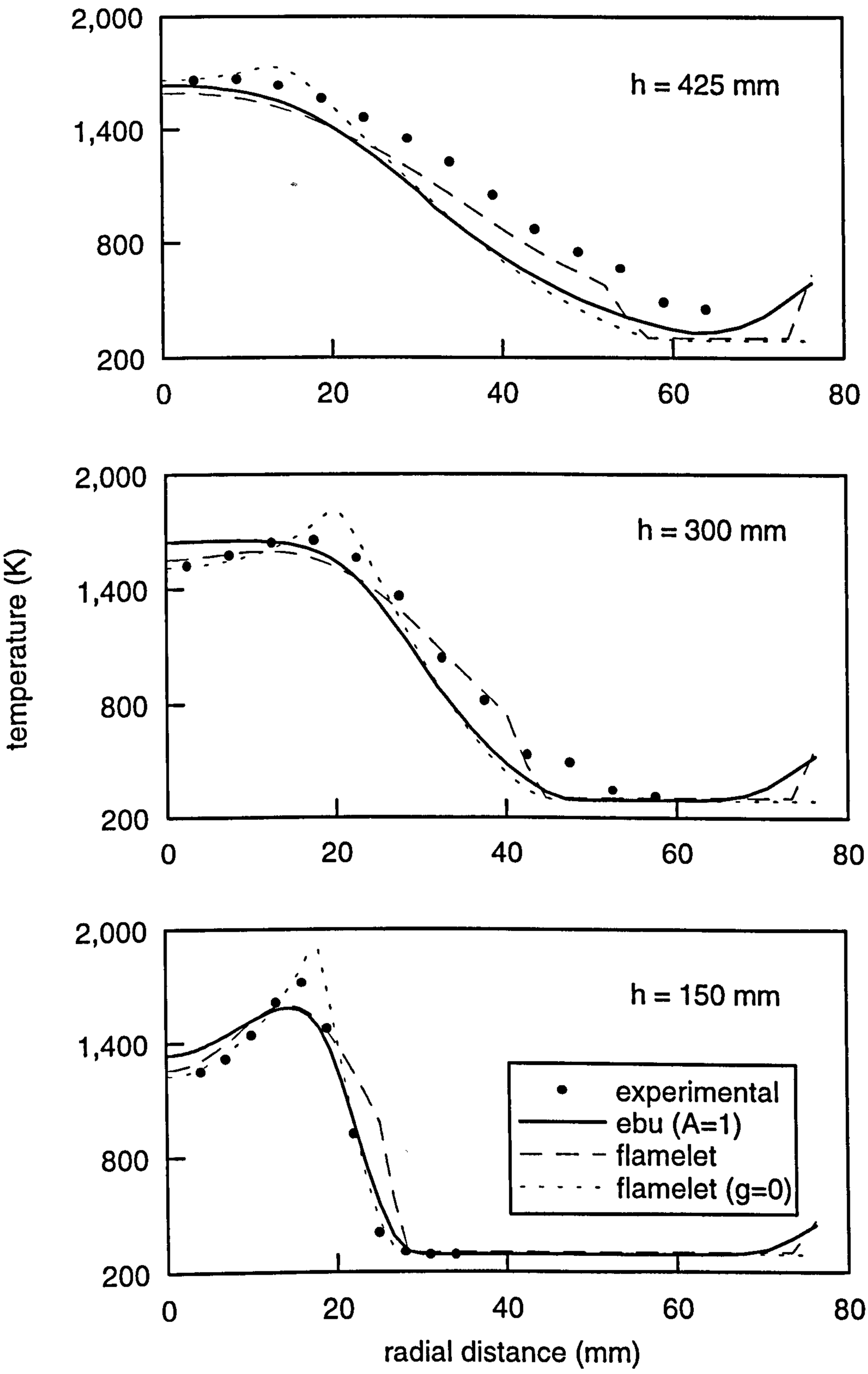

Fig. 5.8 Radial predictions of mean temperature at three distinct heights. Comparison of total enthalpy and flamelet methods for calculation of temperature.

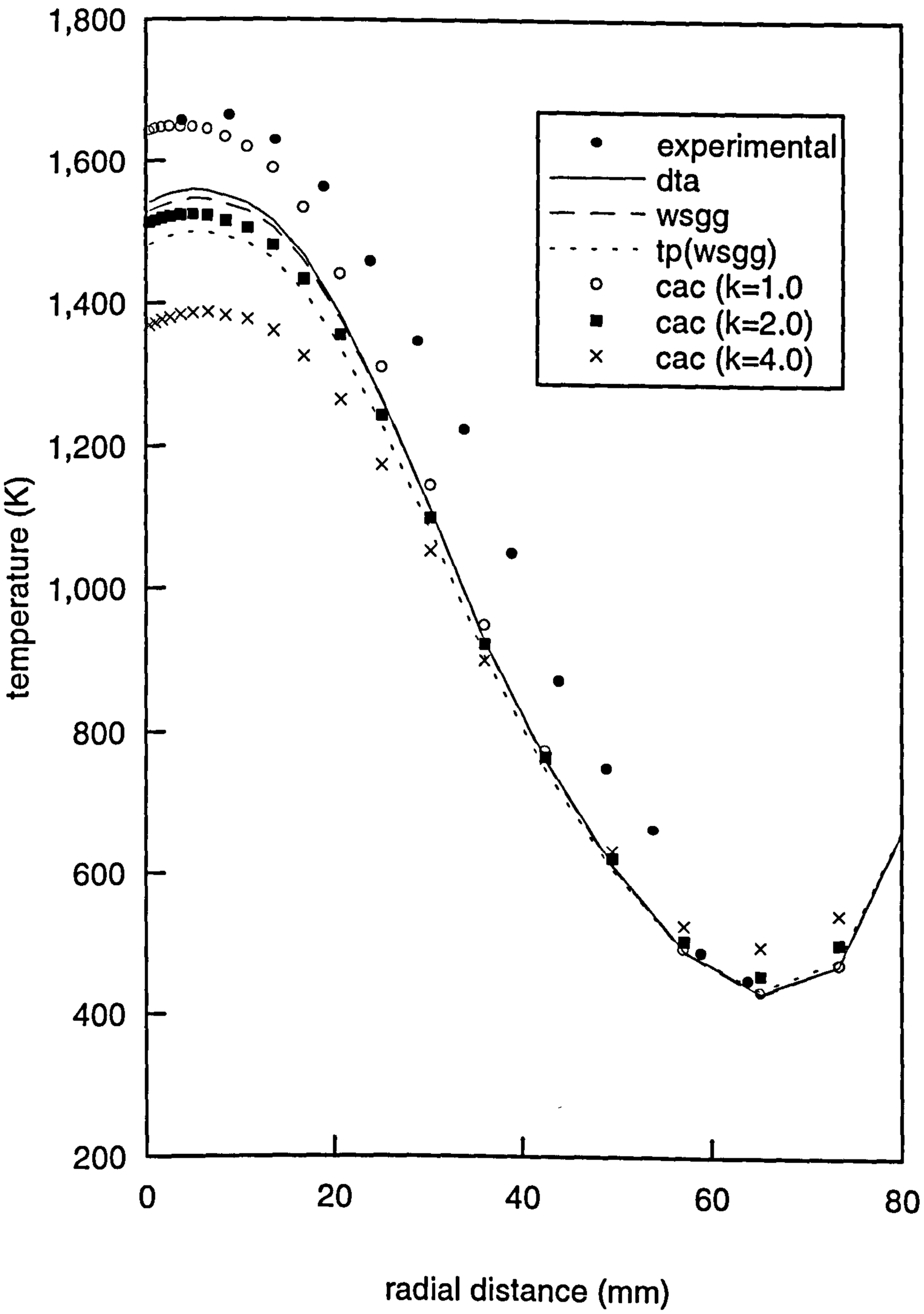

Fig. 5.9 Influence of different solutions to the RTE on the radial mean temperature variation at a height of 425 mm.

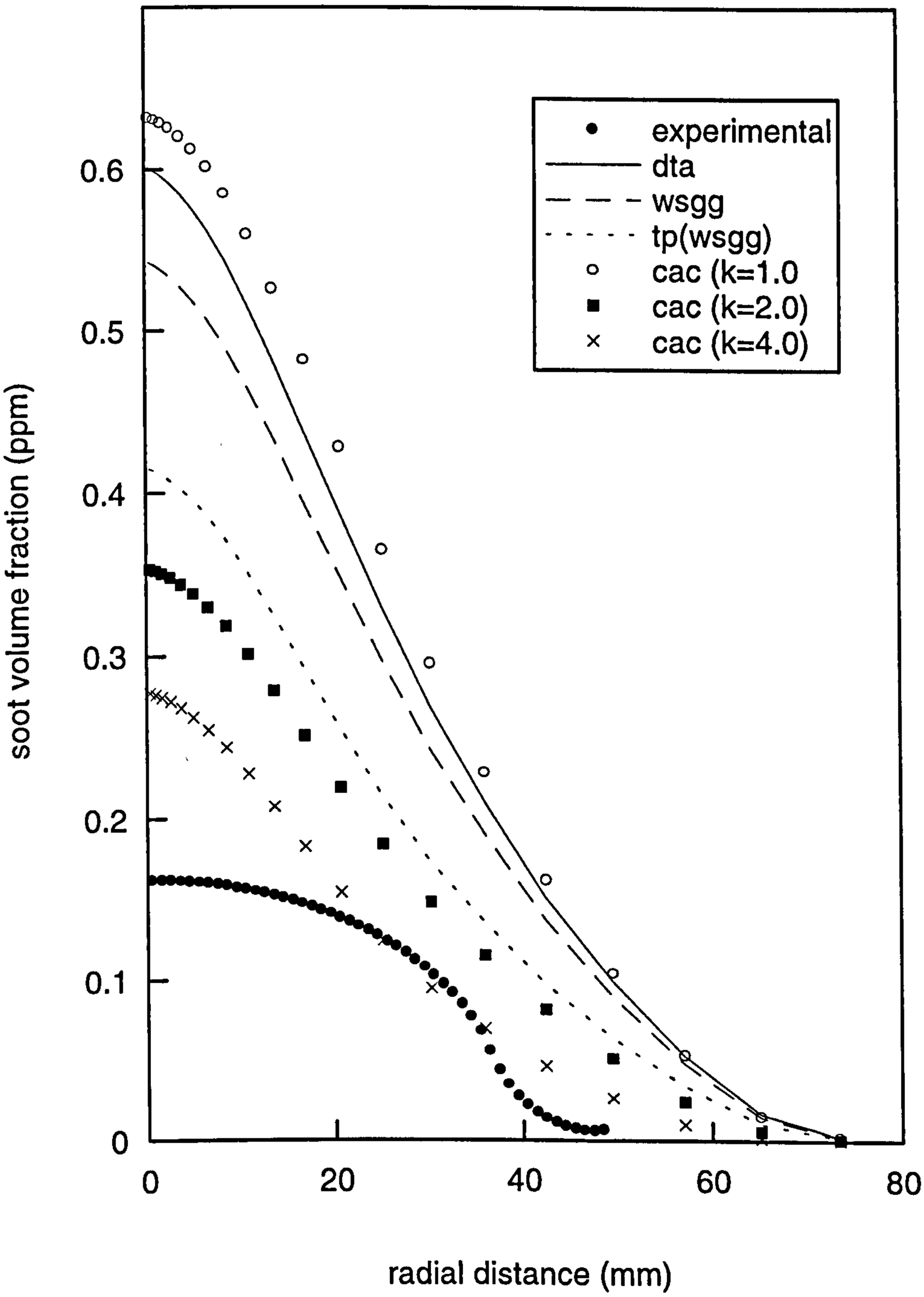

Fig. 5.10 Influence of different solutions to the RTE on the radial soot volume fraction variation at a height of 425 mm.

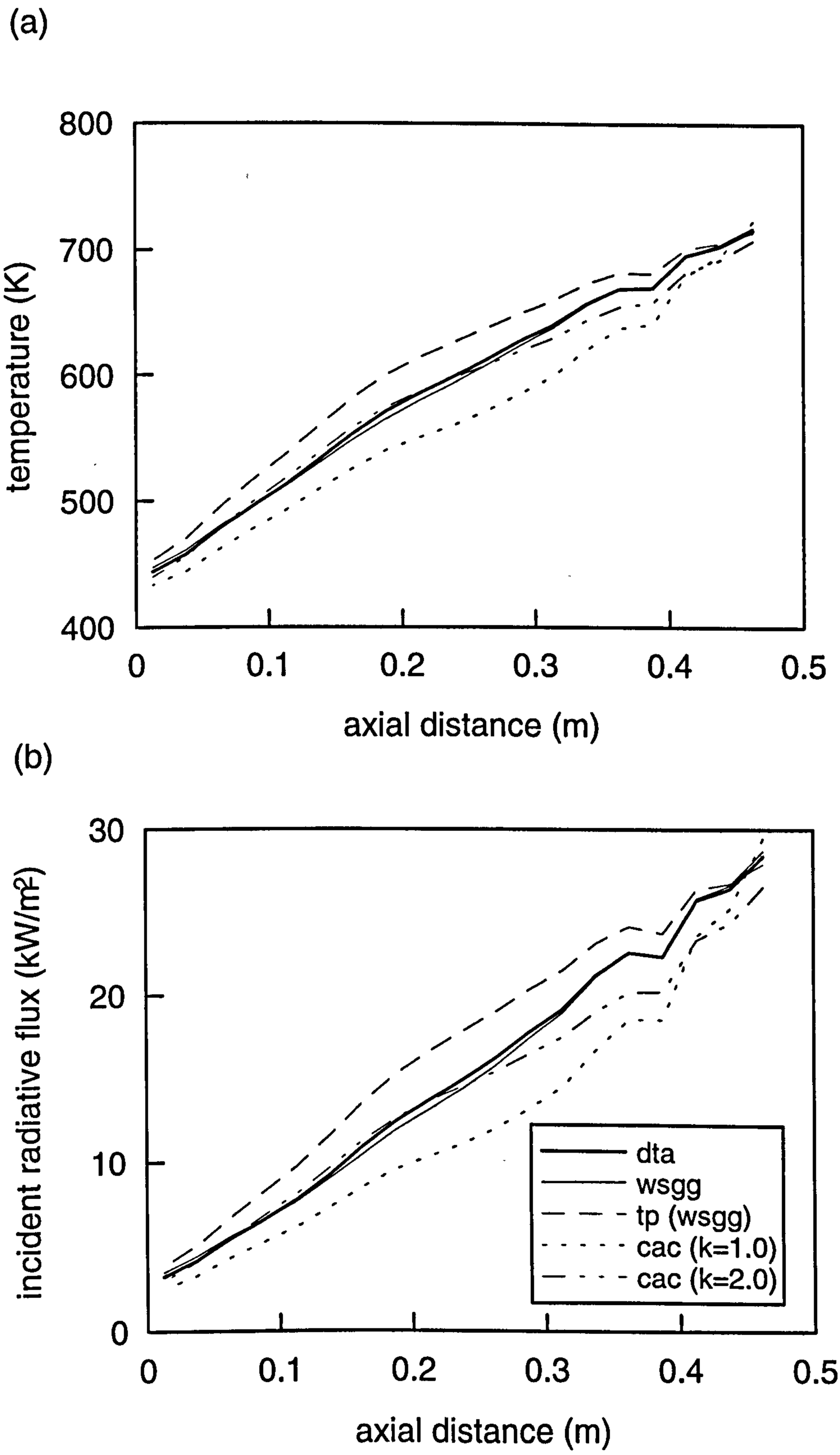

Fig. 5.11 Influence of different solutions to the RTE on (a) temperature, and (b) incident radiative flux, at the pyrex casing boundary.

(a)

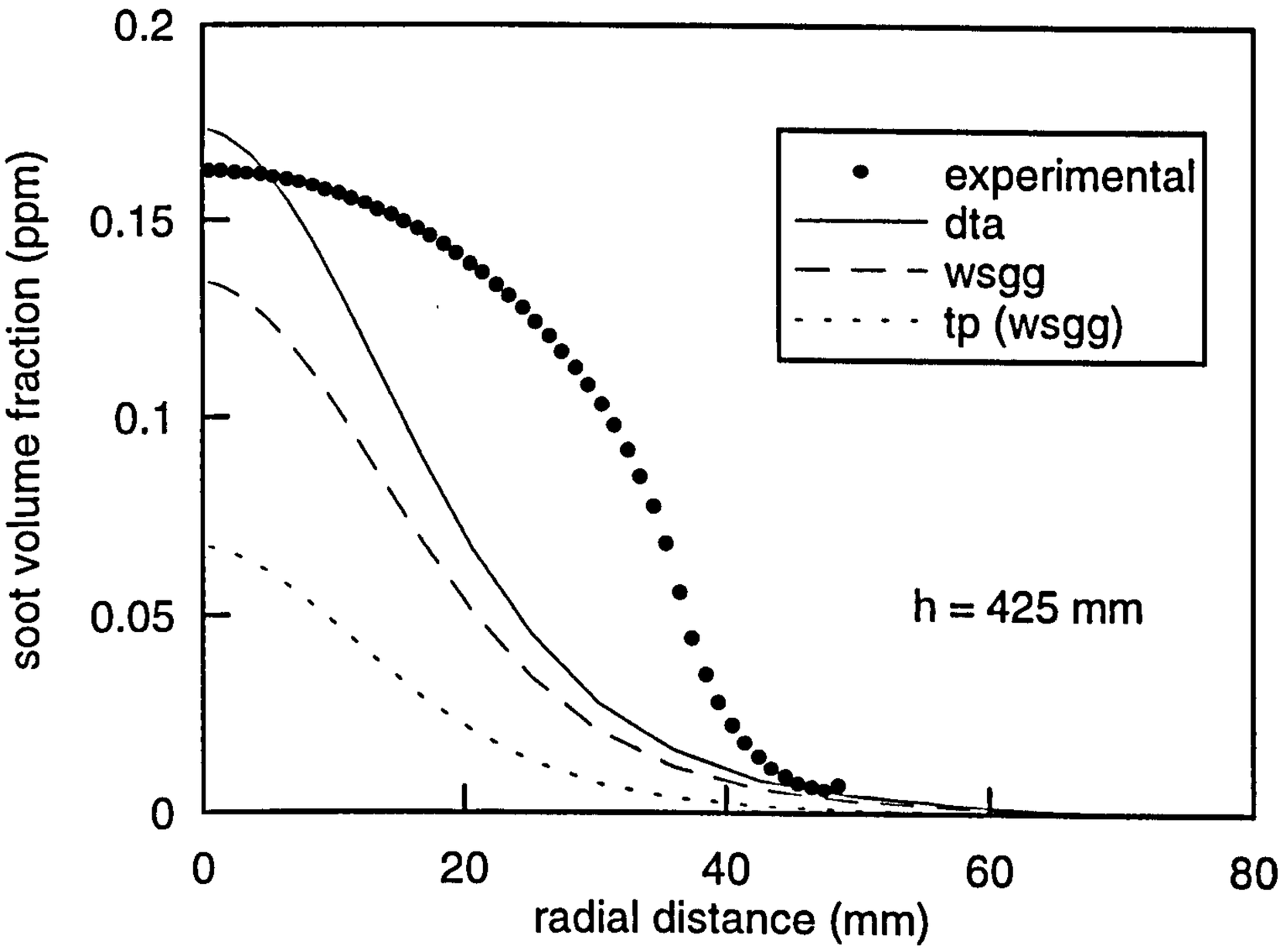

(b)

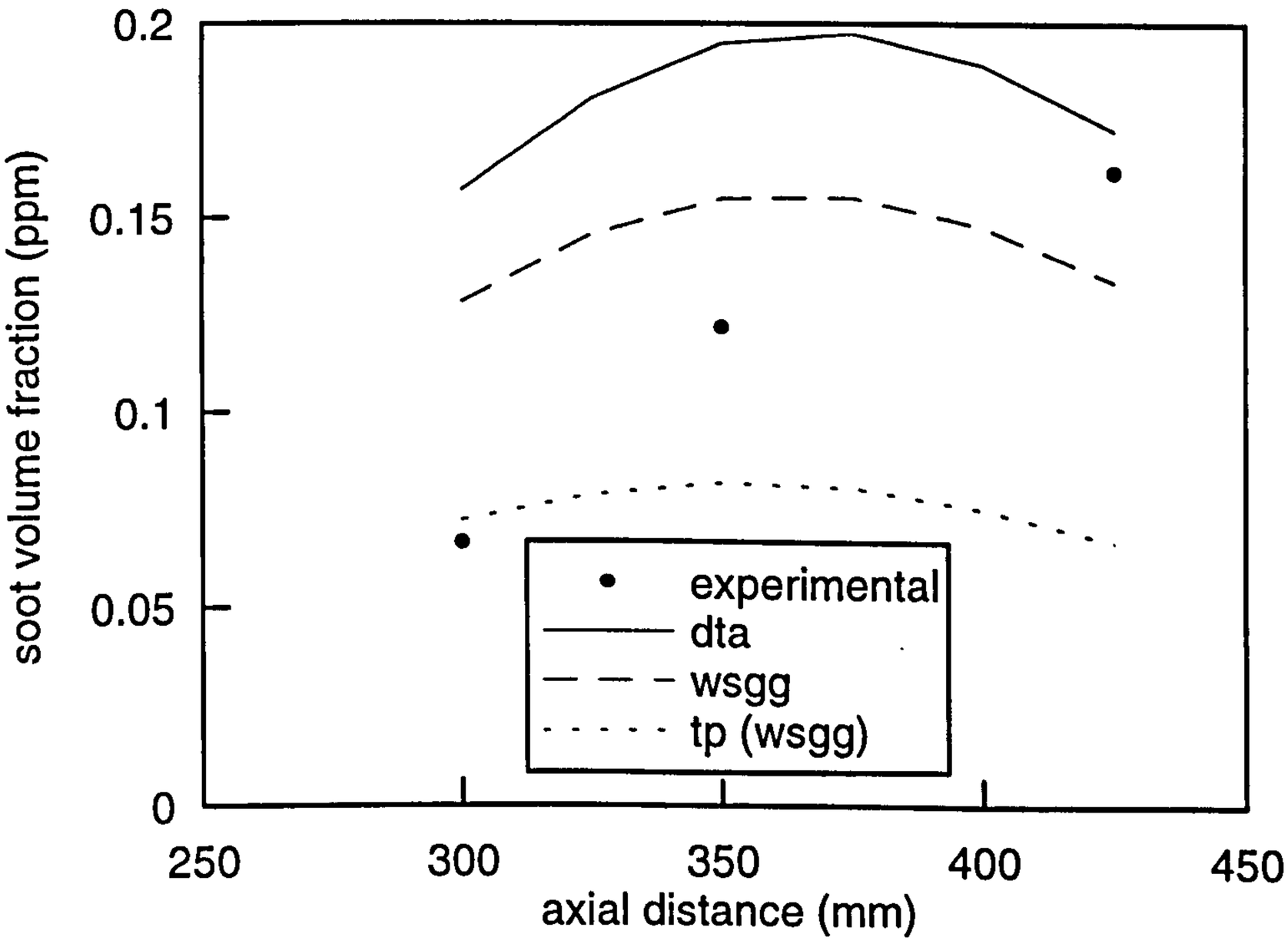

Fig. 5.12 Soot volume fraction prediction by different solutions to the RTE : (a) radial variation at a height of 425 mm, (b) axial variation.

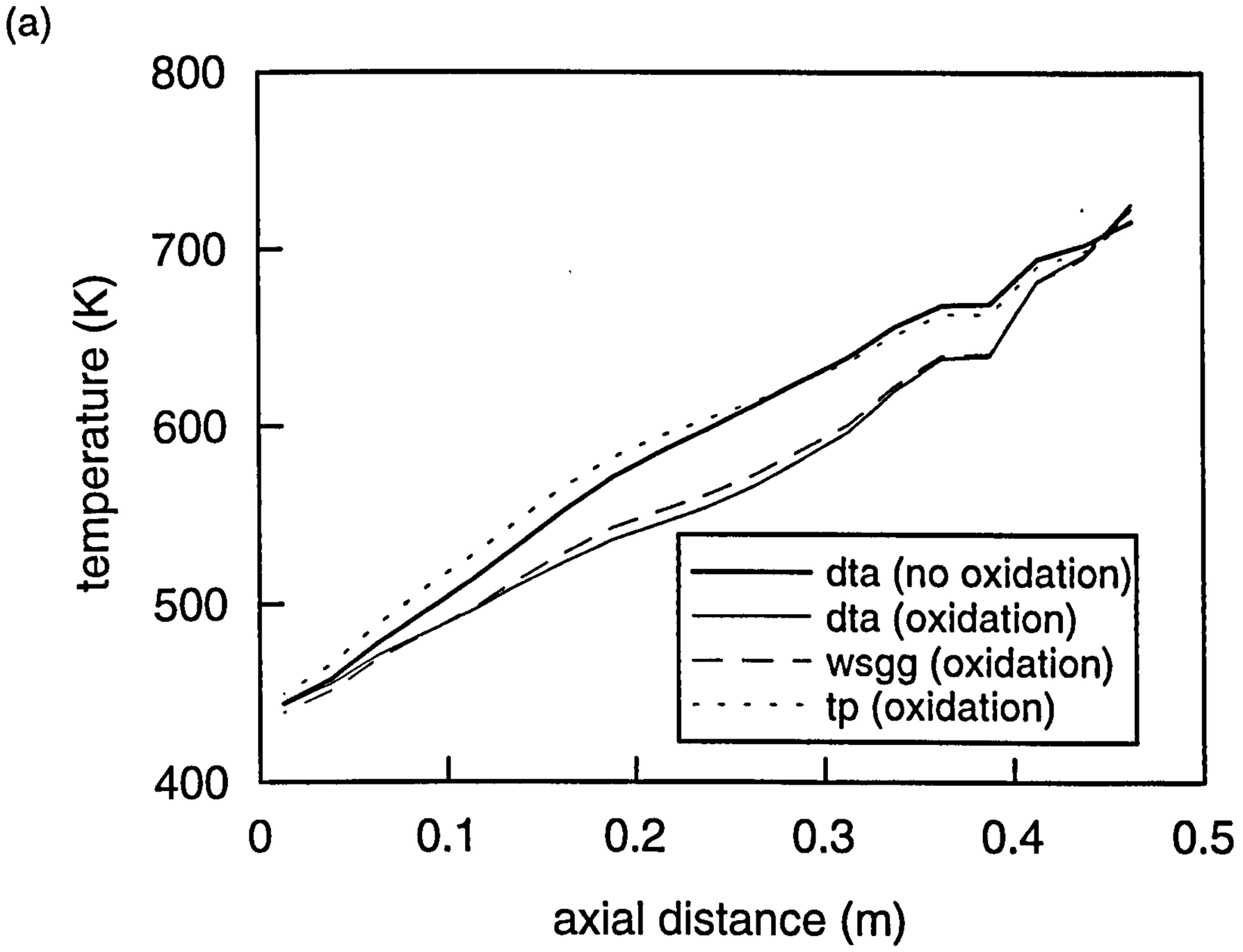

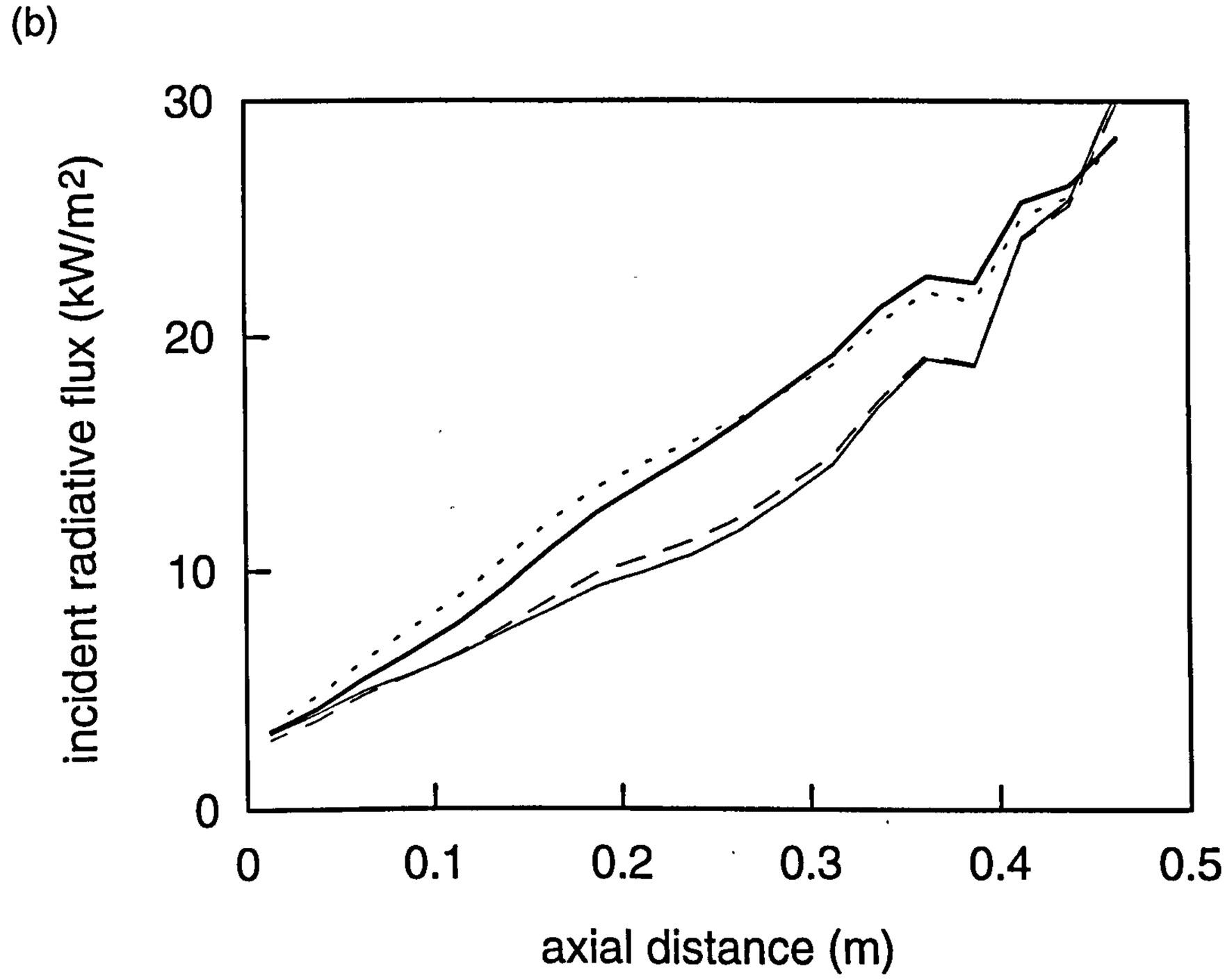

Fig. 5.13 Influence of different solutions to the RTE with oxidation included in the soot model on (a) temperature, and (b) incident radiative flux, at the pyrex casing boundary.

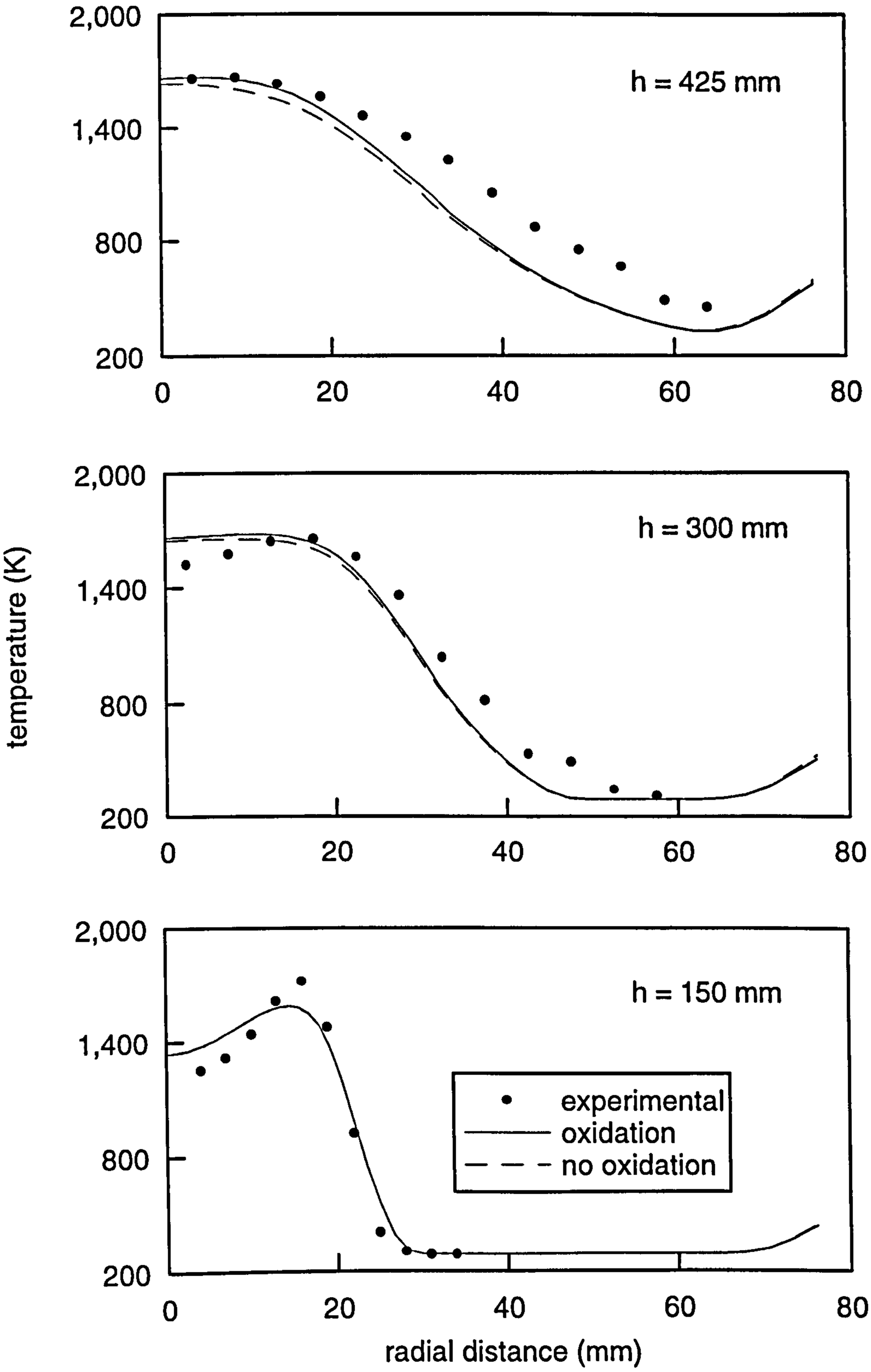

Fig. 5.14 Radial temperature variation at three distinct heights for the WSGG solution with and without oxidation included in the soot model.

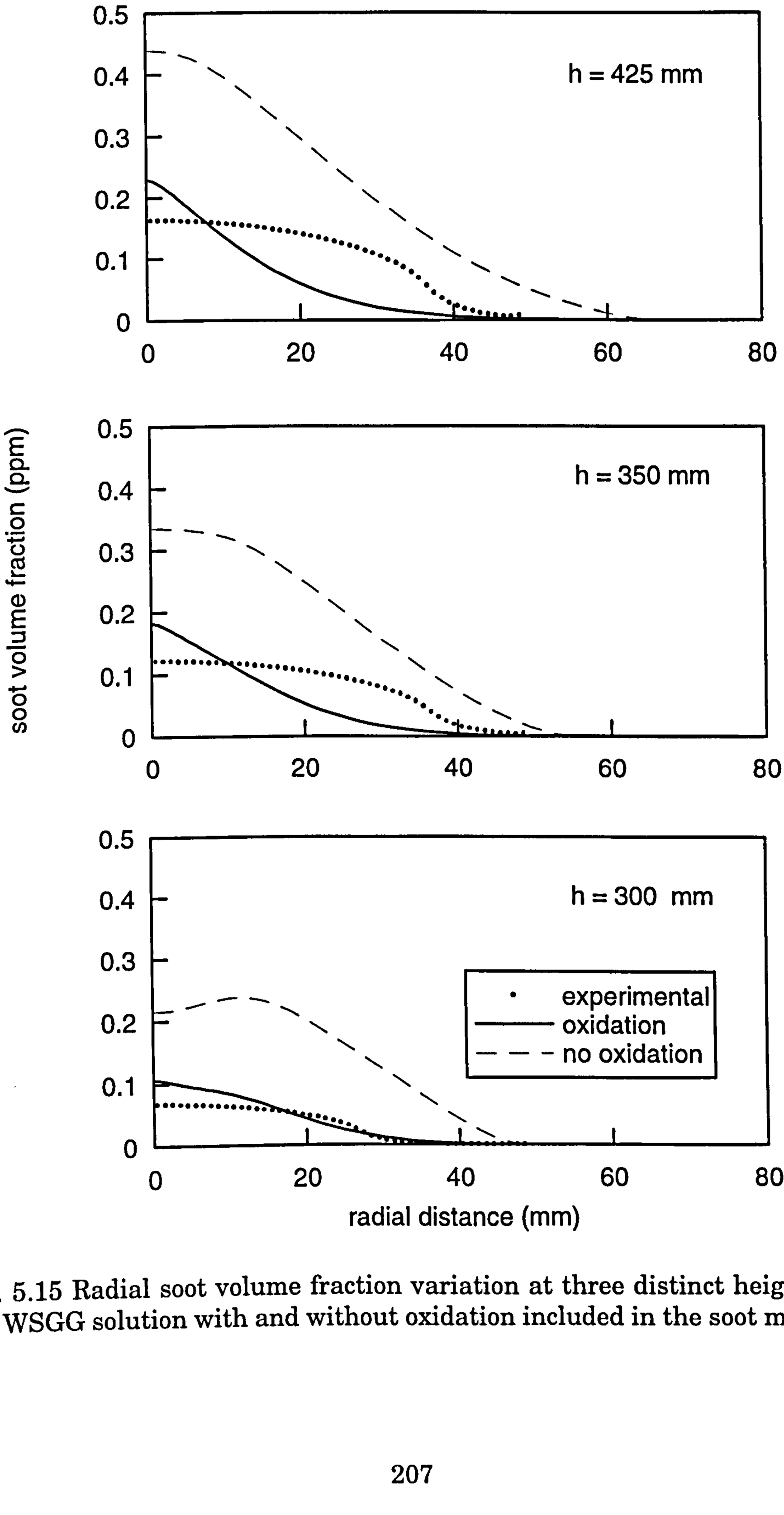

Fig. 5.15 Radial soot volume fraction variation at three distinct heights for the WSGG solution with and without oxidation included in the soot model.

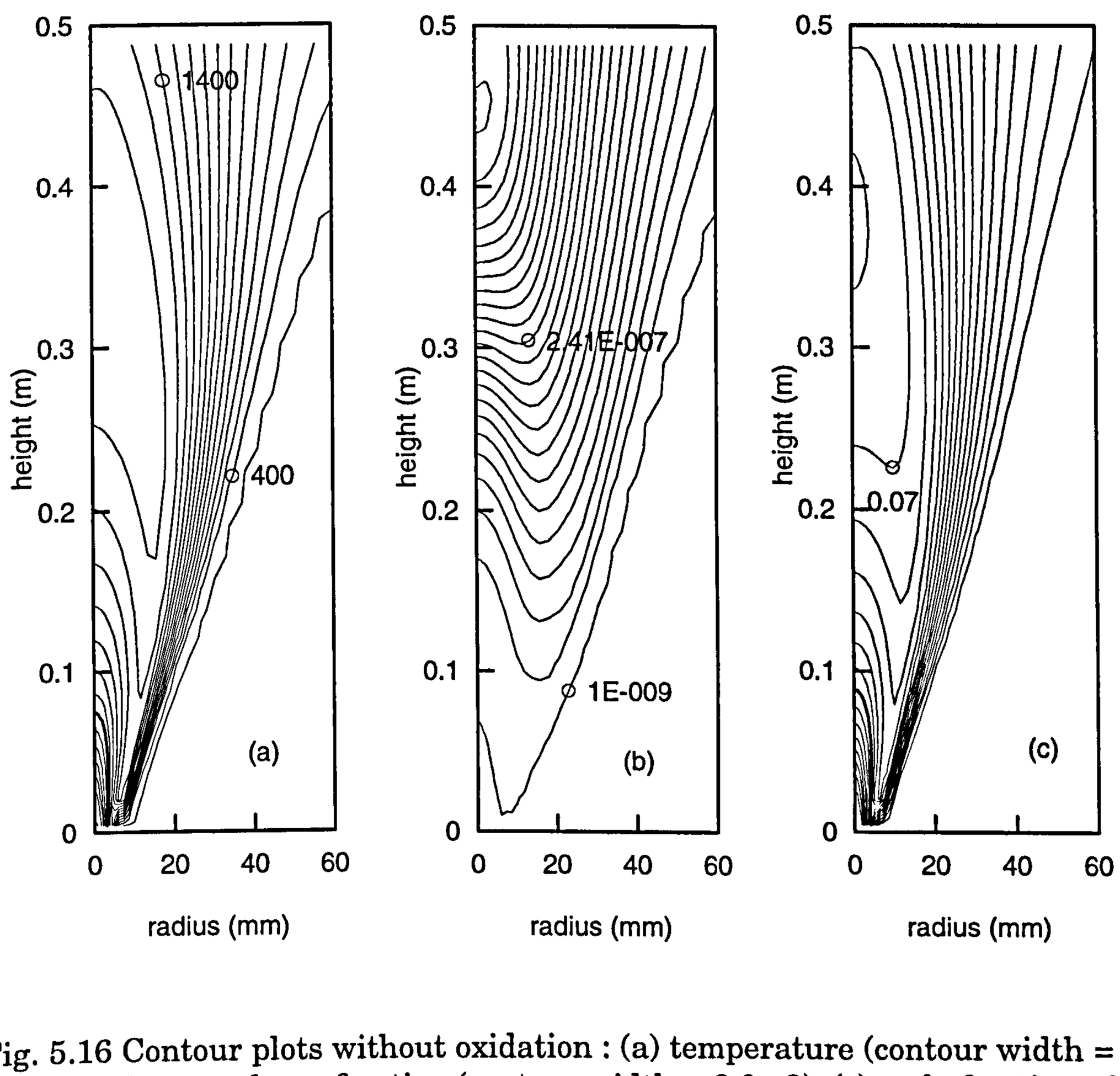

Fig. 5.16 Contour plots without oxidation : (a) temperature (contour width = 100 K), (b) soot volume fraction (contour width = 2.0e-8), (c) mole fraction of CO_2 (contour width = 0.005).

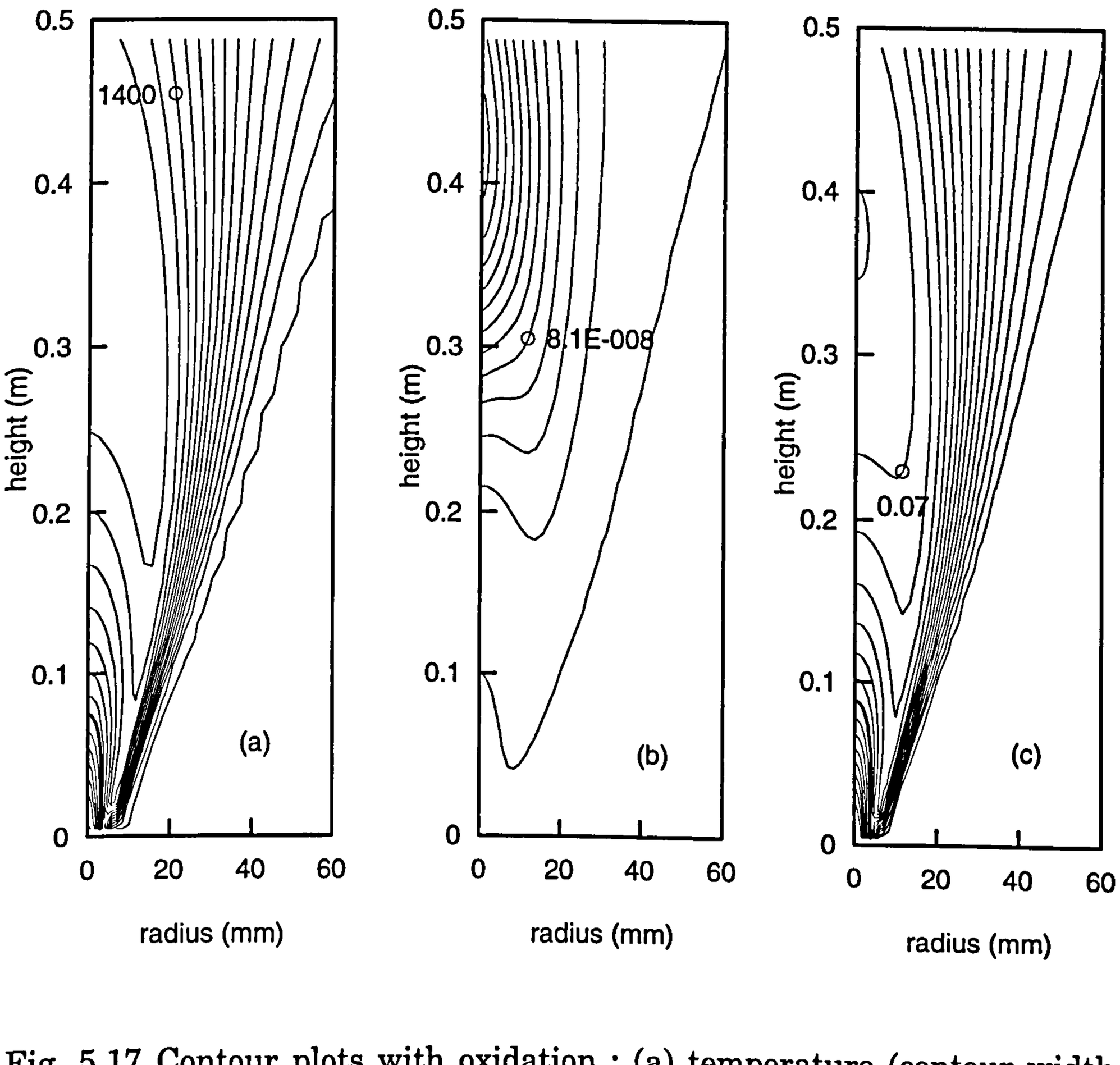

Fig. 5.17 Contour plots with oxidation : (a) temperature (contour width = 100 K), (b) soot volume fraction (contour width = 2.0e-8), (c) mole fraction of CO_2 (contour width = 0.005).

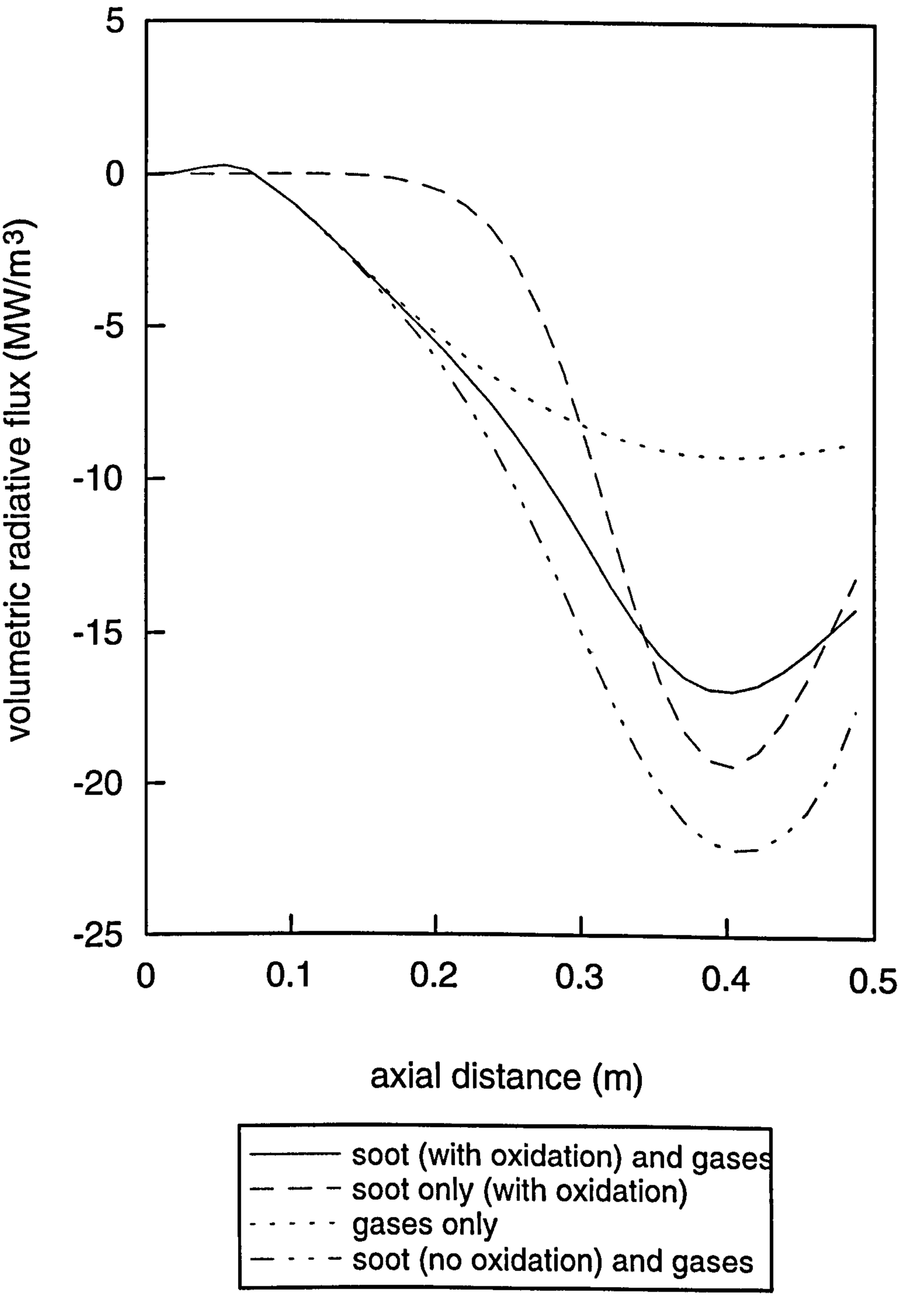

Fig. 5.18a Centre line variation of volumetric radiative flux.

(b)

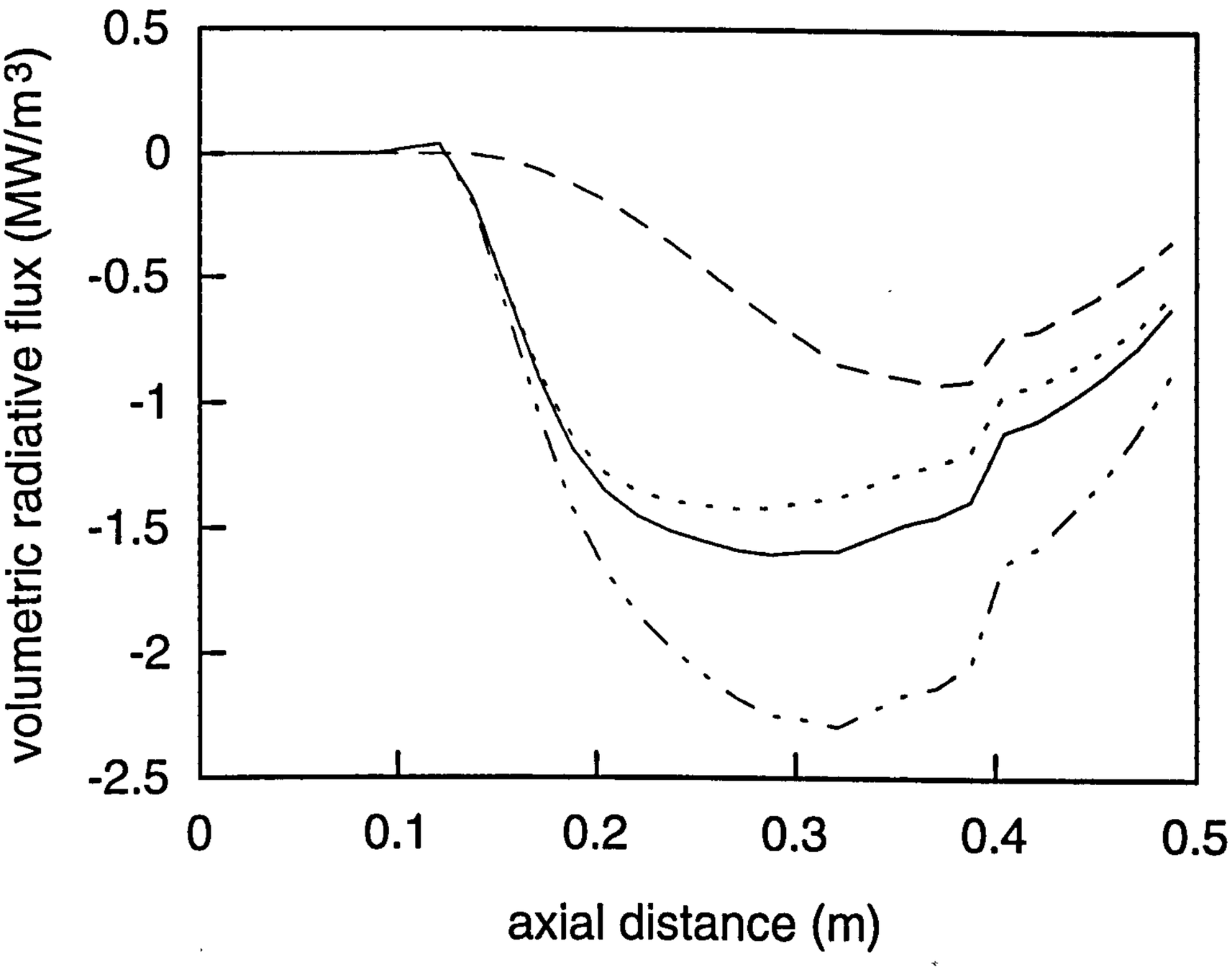

(c)

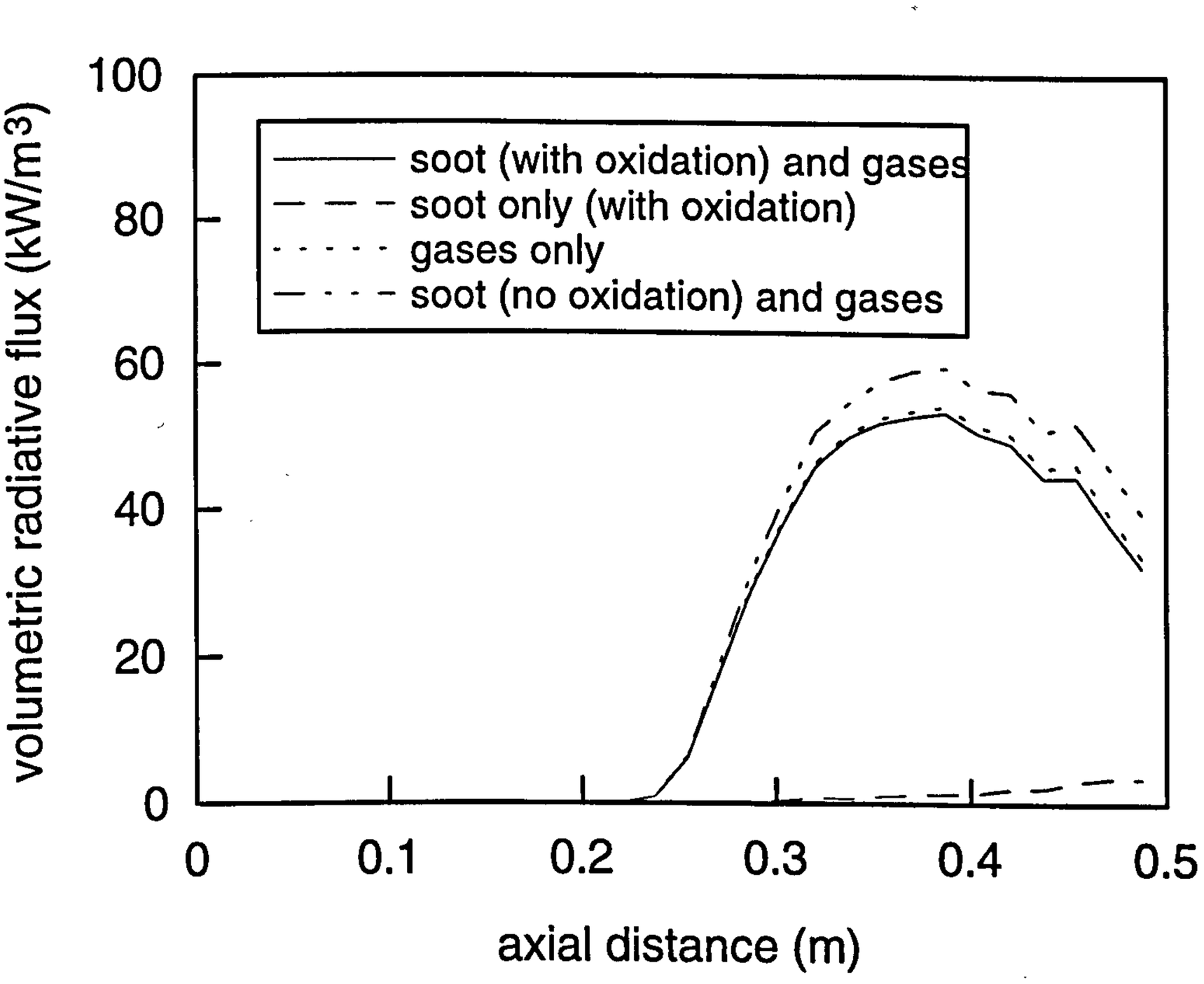

Fig. 5.18 Axial variation of volumetric radiative flux at radii of : (b) 20.6mm, and (c) 40.2 mm.

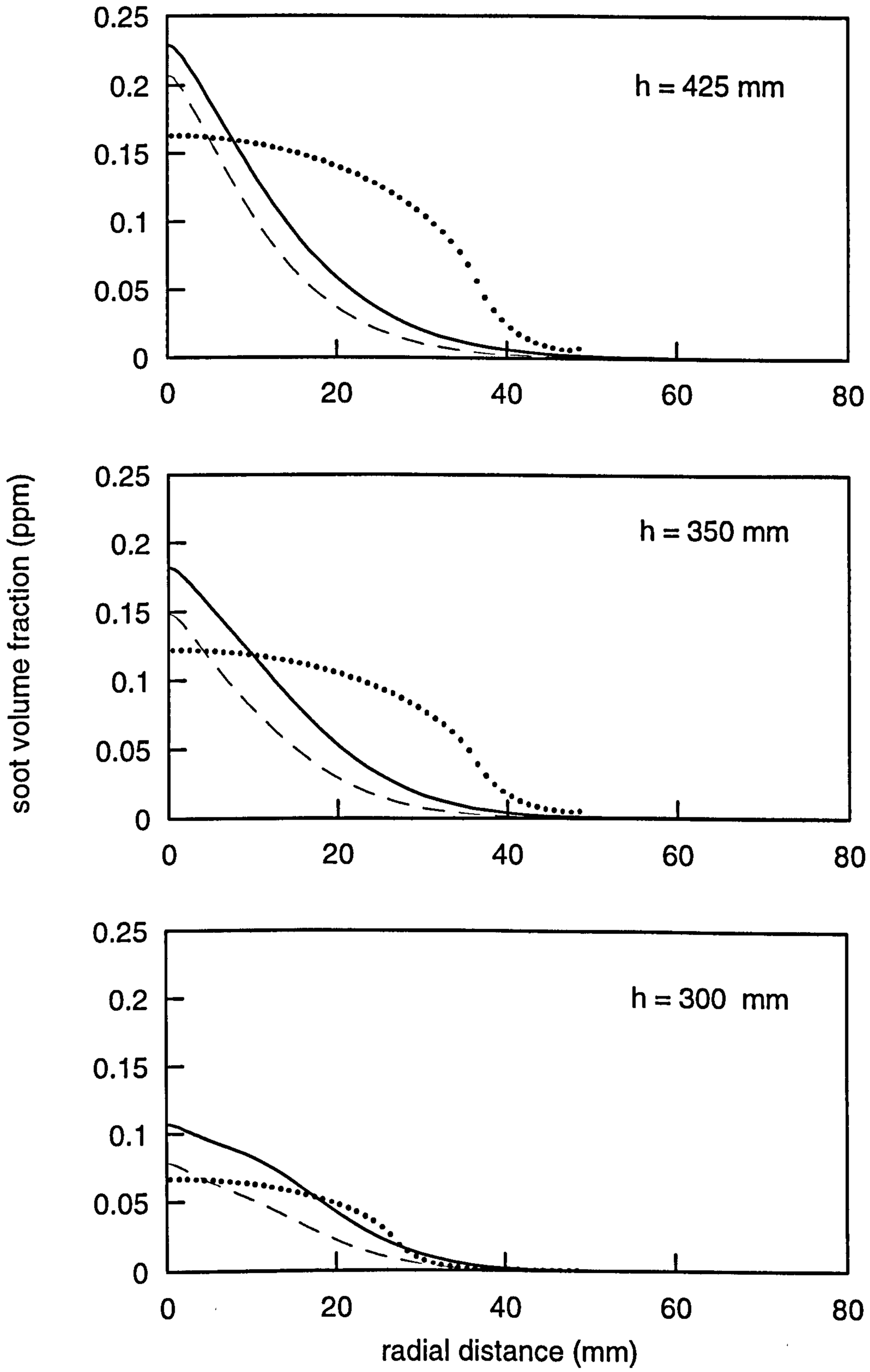

Fig. 5.19 Influence of including turbulence-radiation interaction on radial soot volume fraction profiles. Experimental data shown as dot symbols; solid lines exclude turbulence-radiation interaction; dashed lines incorporate turbulent fluctuations into evaluation of black body intensity.

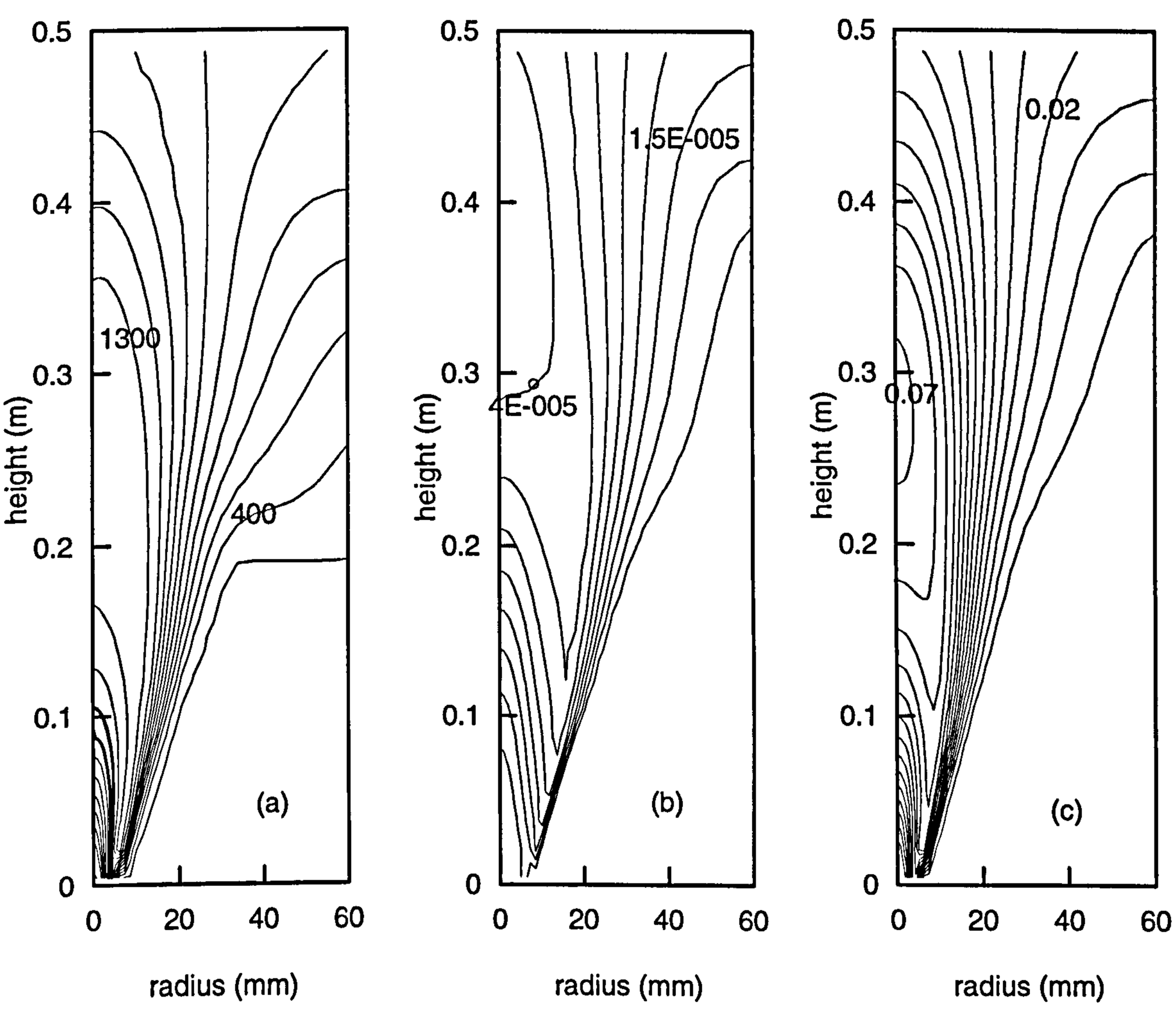

Fig. 5.20 Contour plots for 3 atm. flame without oxidation : (a) mean temperature (contour width = 100 K), (b) mean soot volume fraction (contour width = 0.5e-5), (c) mean mole fraction of CO_2 (contour width = 0.005).

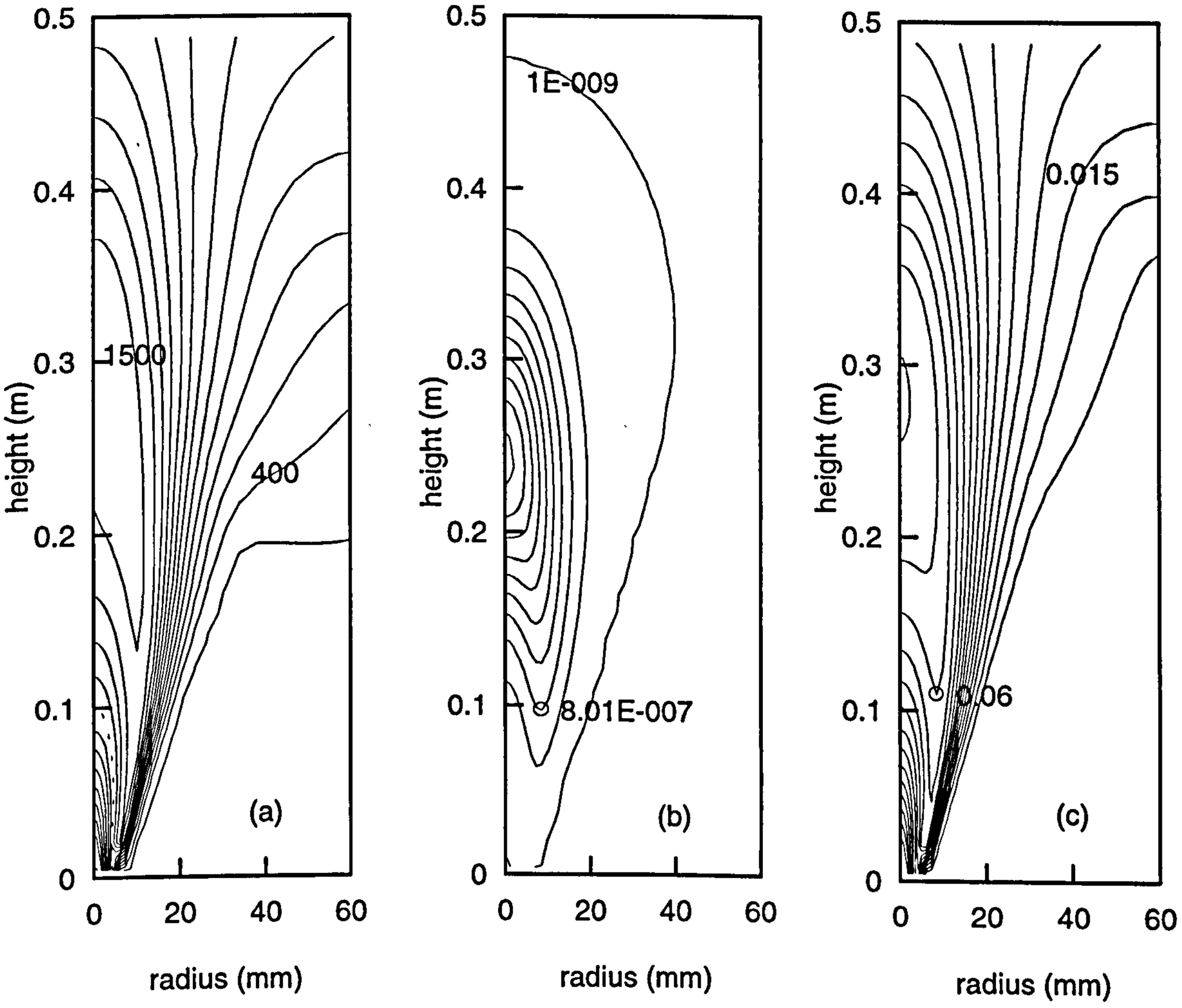

Fig. 5.21 Contour plots for 3 atm. flame with oxidation : (a) mean temperature (contour width = 100 K), (b) mean soot volume fraction (contour width = 4.0e-7), (c) mean mole fraction of CO_2 (contour width = 0.005).

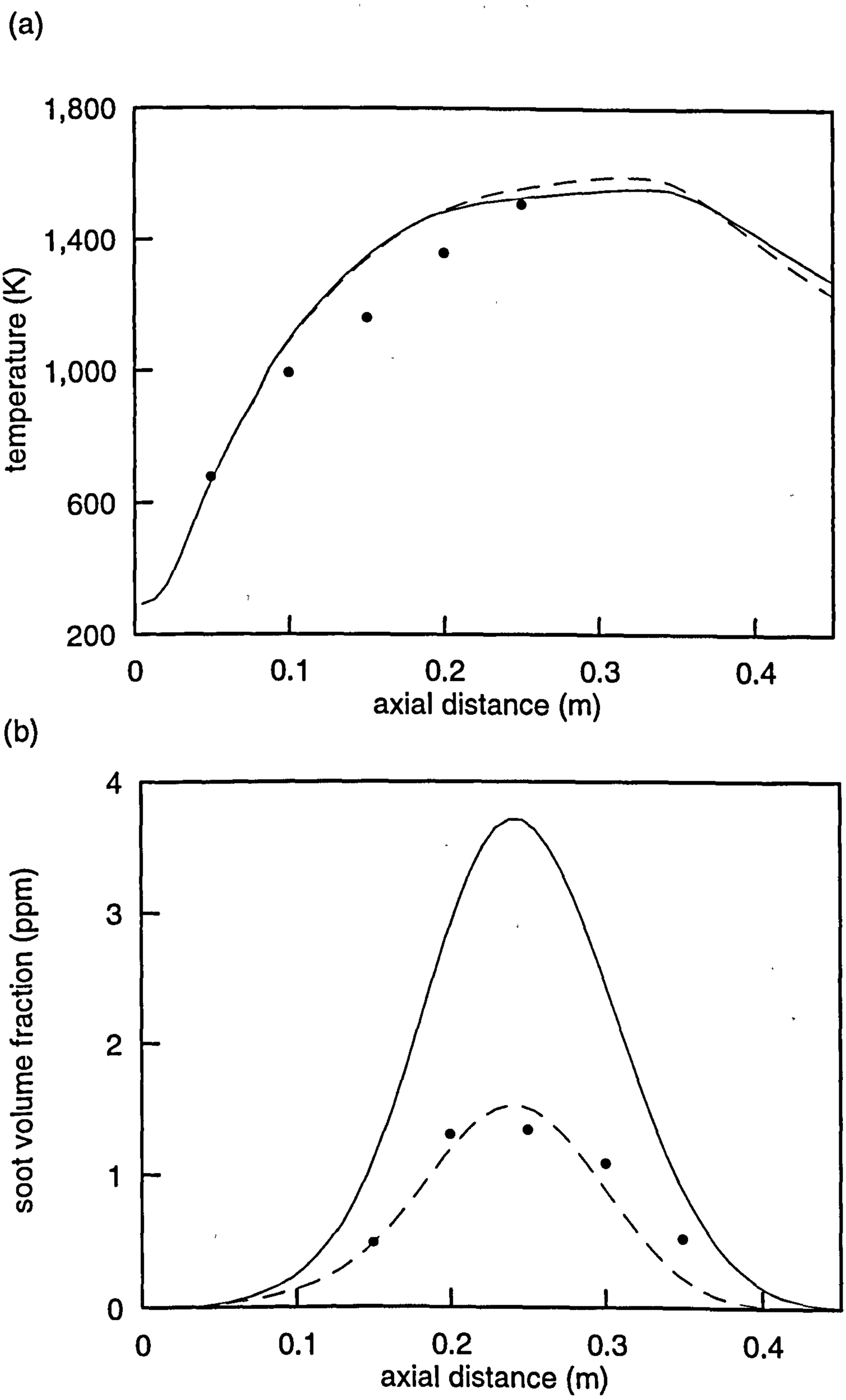

Fig. 5.22 Centre line variation of : (a) mean temperature; (b) mean soot volume fraction in 3 atm. flame (oxidation included). Experimental data shown as dot symbols; solid lines exclude turbulence-radiation interaction; dashed lines incorporate turbulent fluctuations into evaluation of black body intensity.

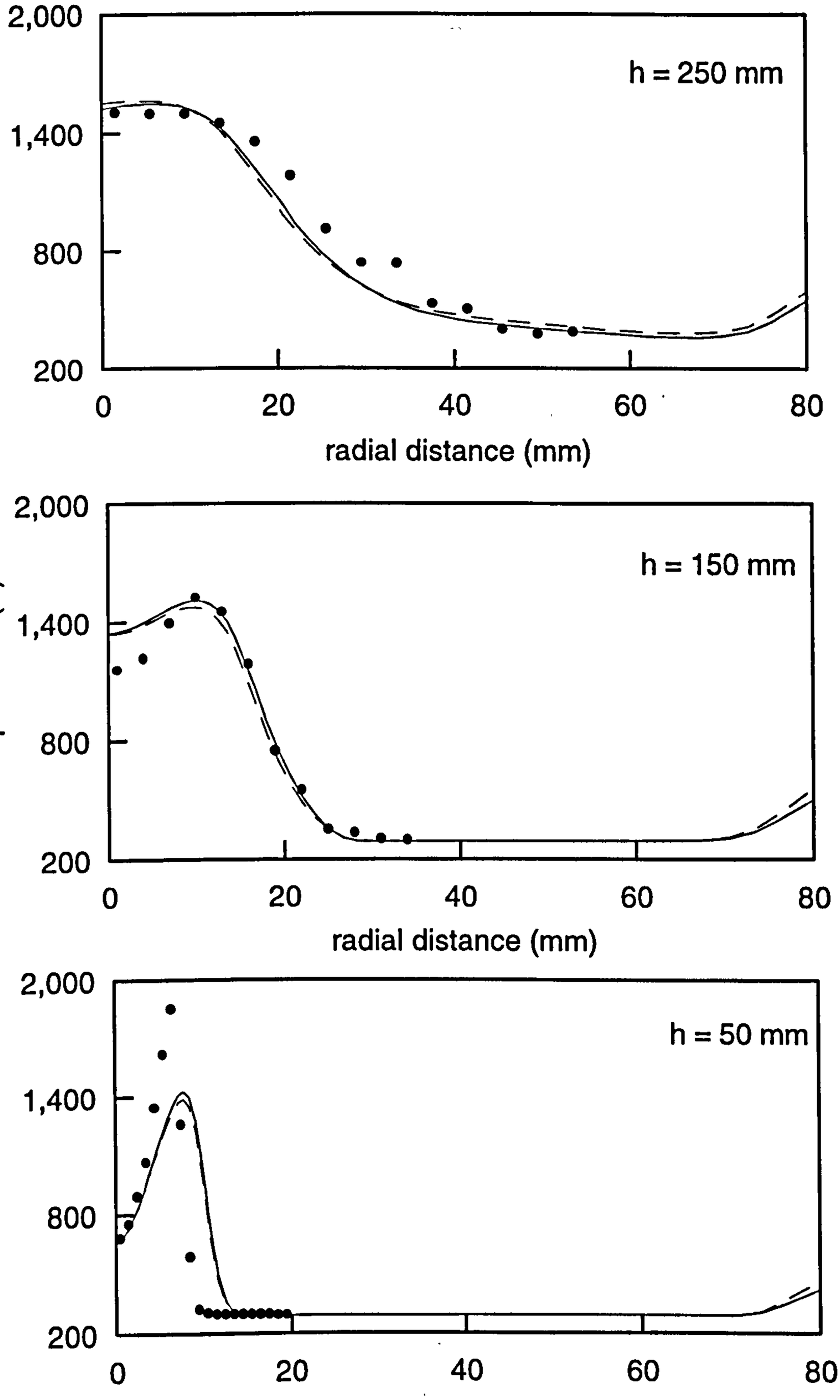

Fig. 5.23 Influence of including turbulence-radiation interaction on radial mean temperature profiles (3 atm. flame). Experimental data shown as dot symbols; solid lines exclude turbulence-radiation interaction; dashed lines incorporate turbulent fluctuations into evaluation of black body intensity.

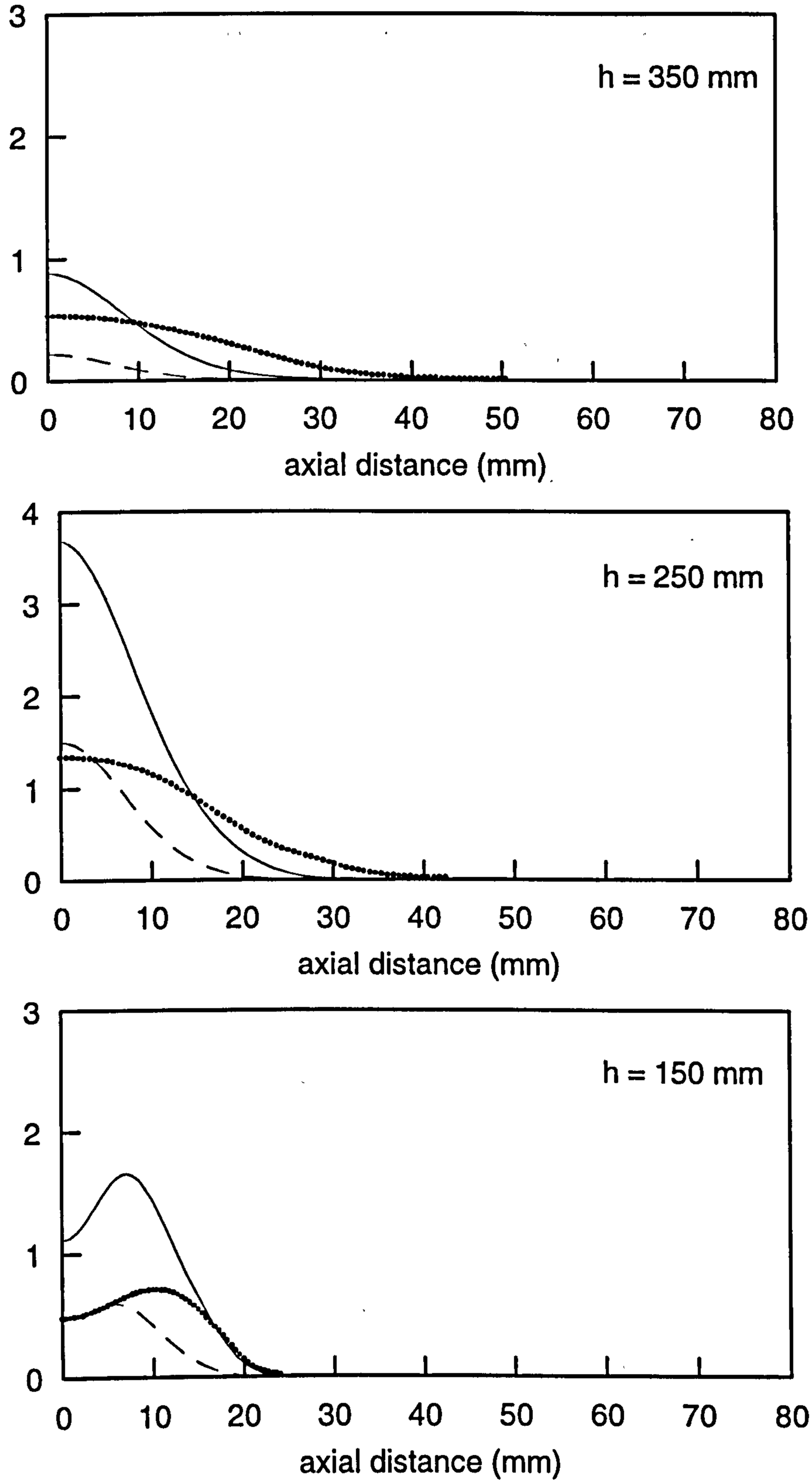

Fig. 5.24 Influence of turbulence-radiation interaction on radial mean soot volume fraction profiles (3 atm. flame). Experimental data shown as dot symbols; solid lines exclude turbulence-radiation interaction; dashed lines incorporate turbulent fluctuations into evaluation of black body intensity.

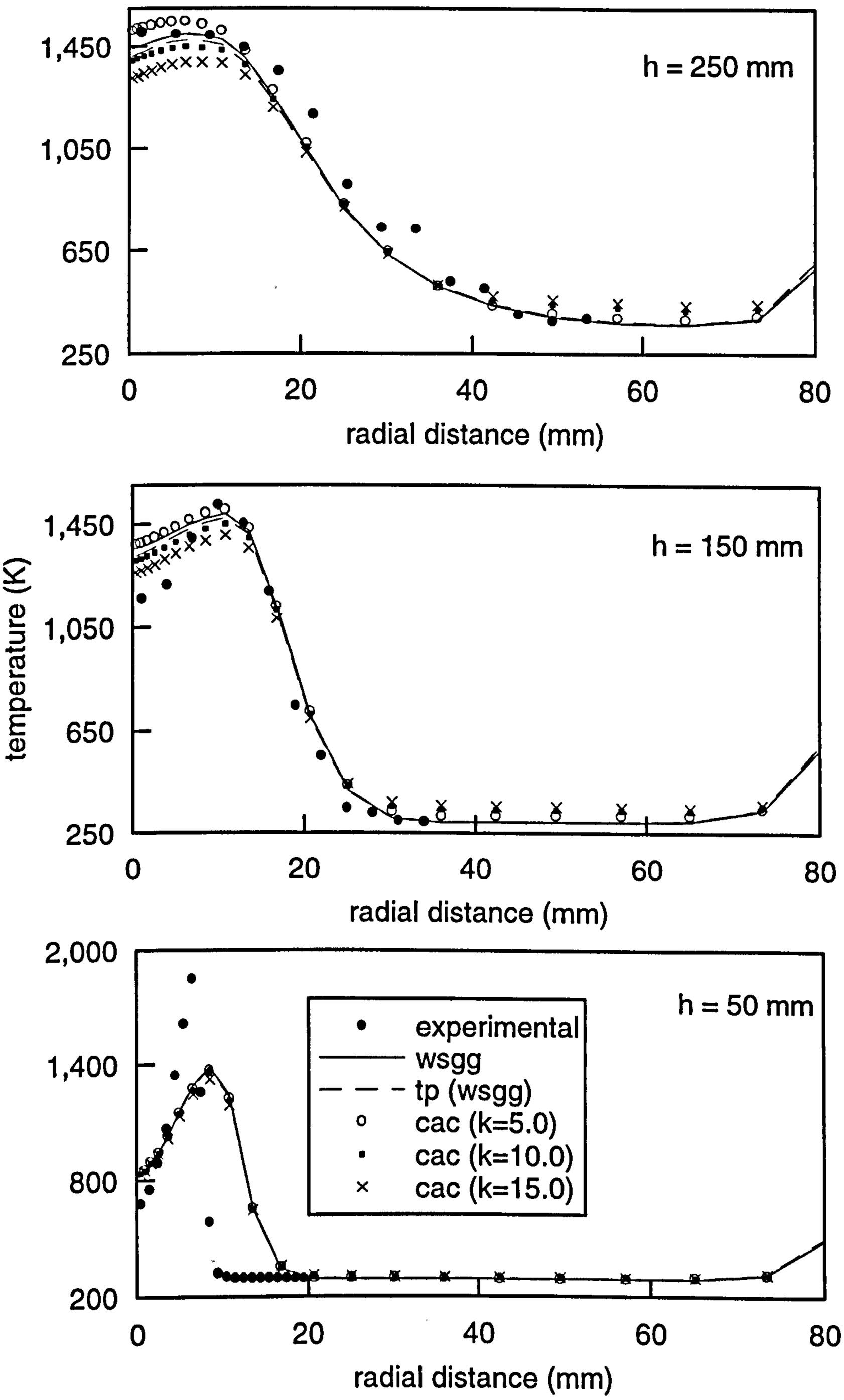

Fig. 5.25 Influence of different solutions to the RTE on radial mean temperature variation in 3 atm. flame.

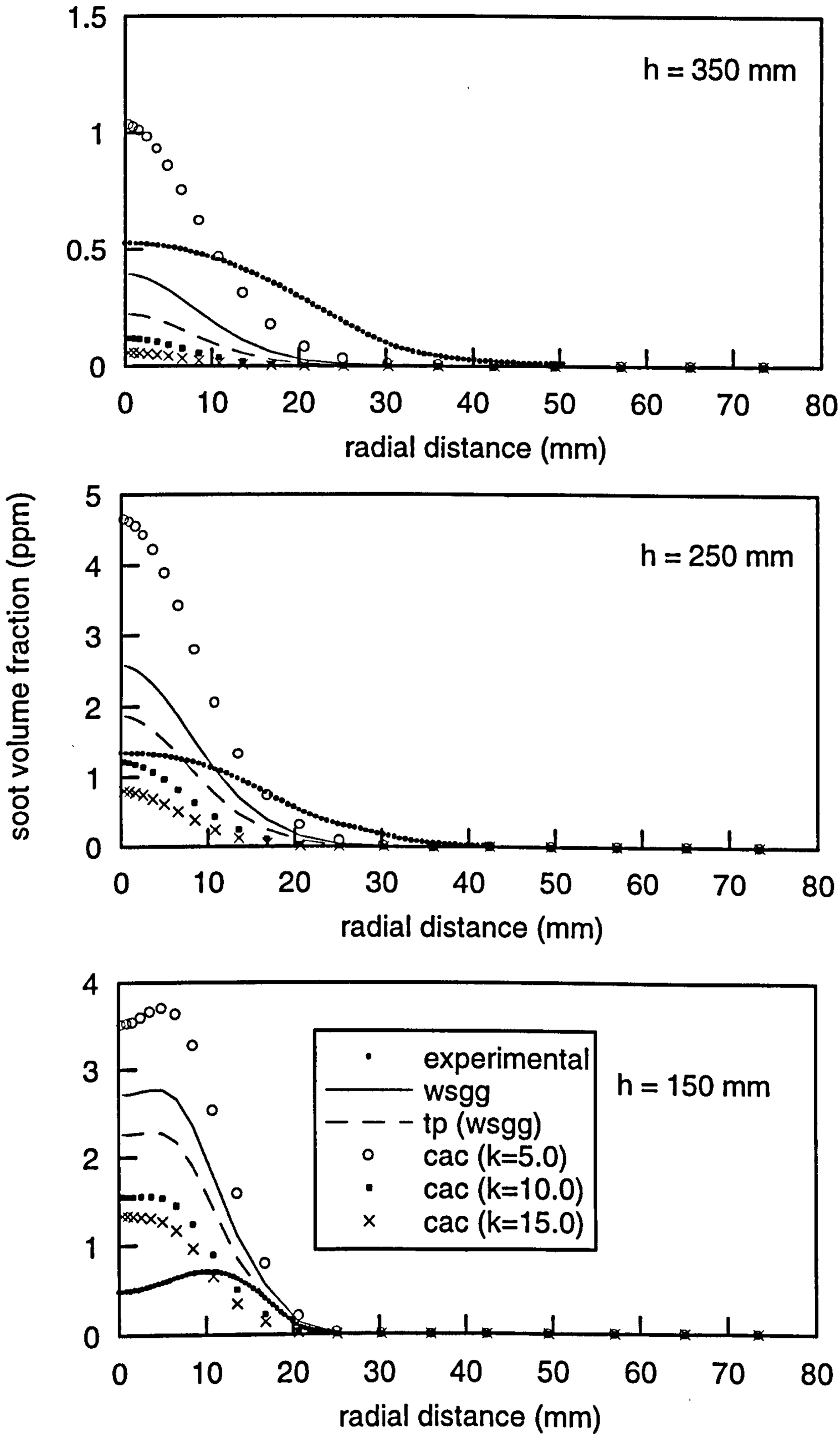

Fig. 5.26 Influence of different solutions to the RTE on radial mean soot volume fraction variation in 3 atm. flame.

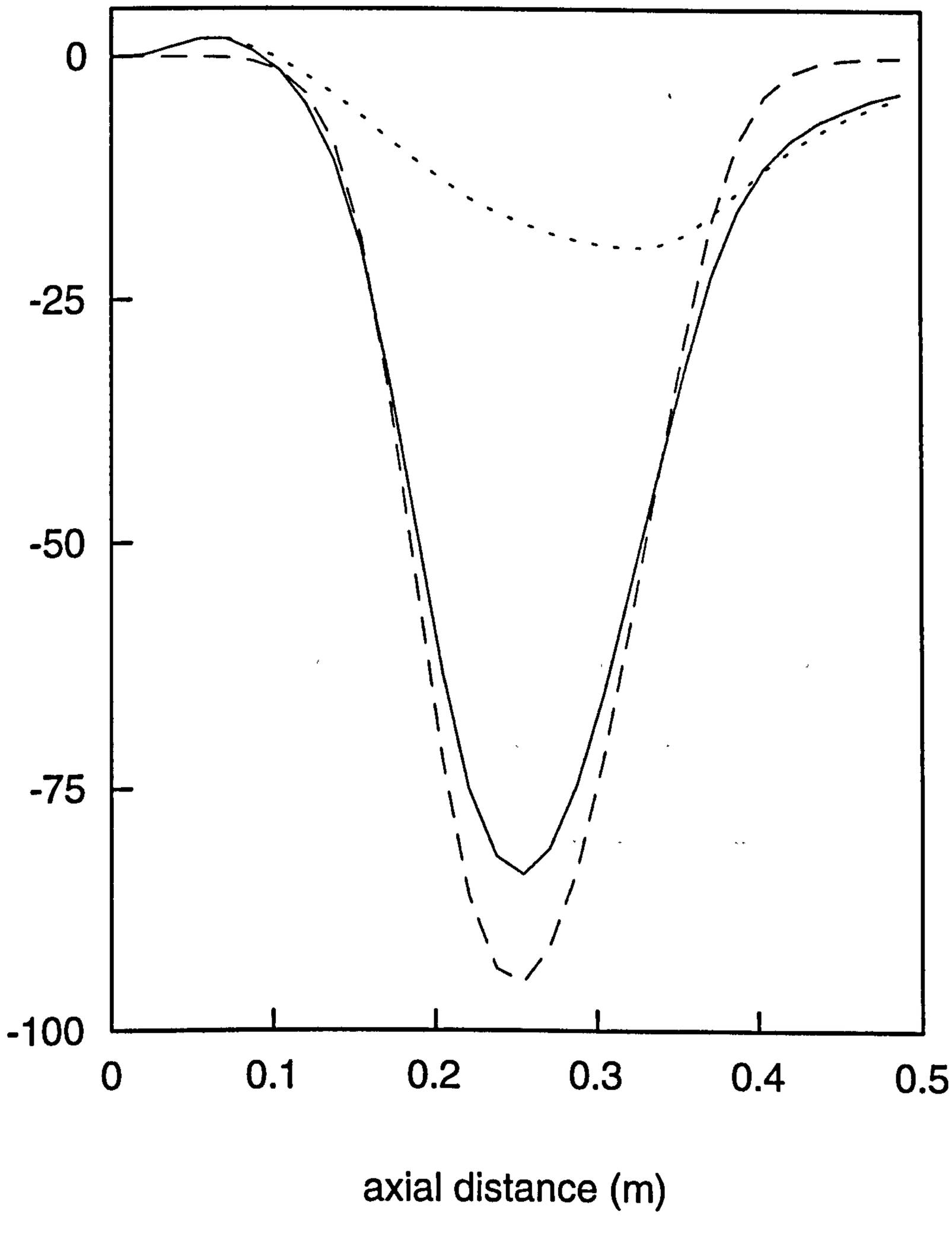

Fig. 5.27a Centre line variation of volumetric radiative flux in 3 atm. flame.

(b)

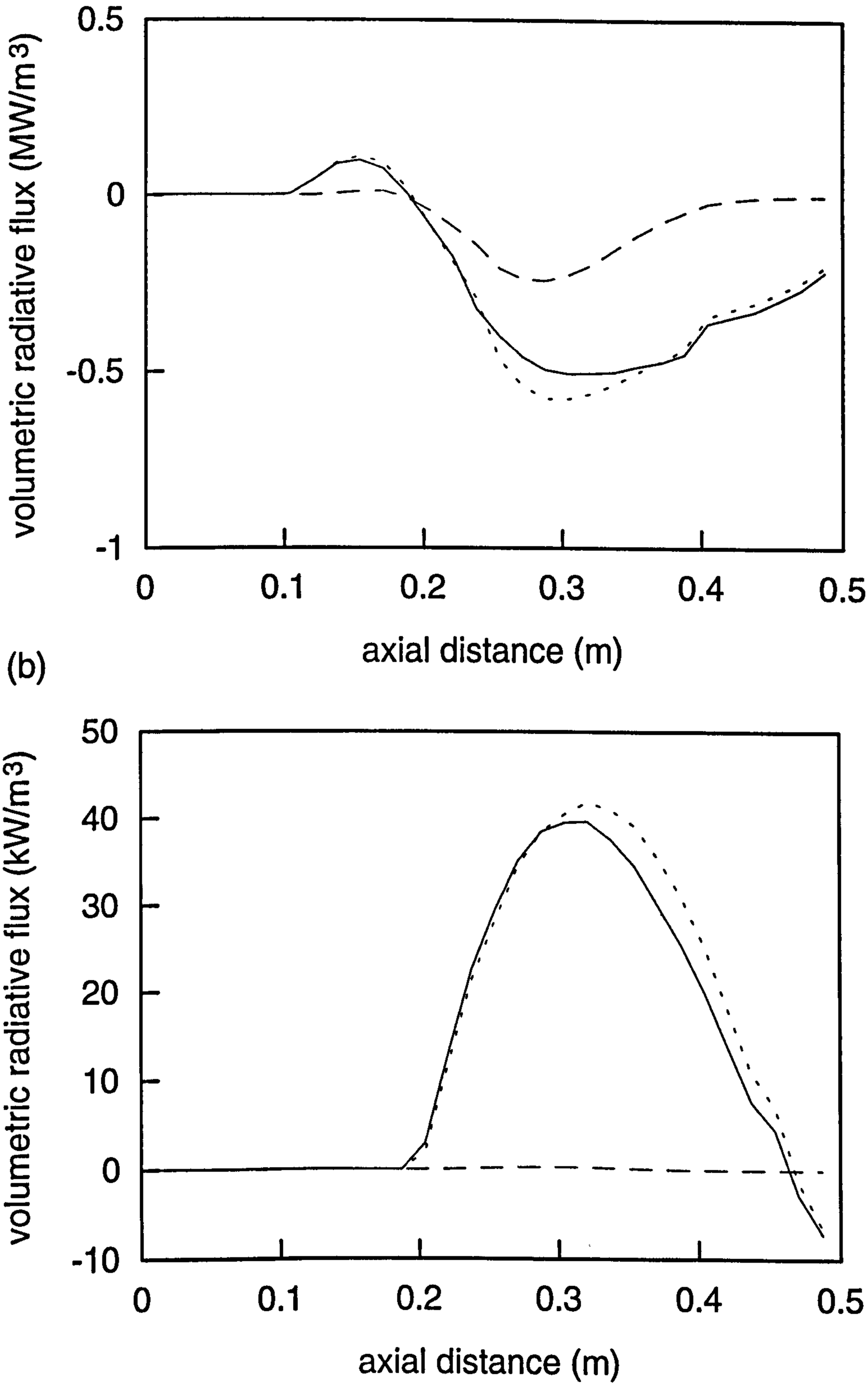

(b)

Fig. 5.27 Axial variation of volumetric radiative flux in 3 atm. flame at radii of : (b) 20.6 mm, and (c) 40.2 mm. For key, see Fig. 5.27a.

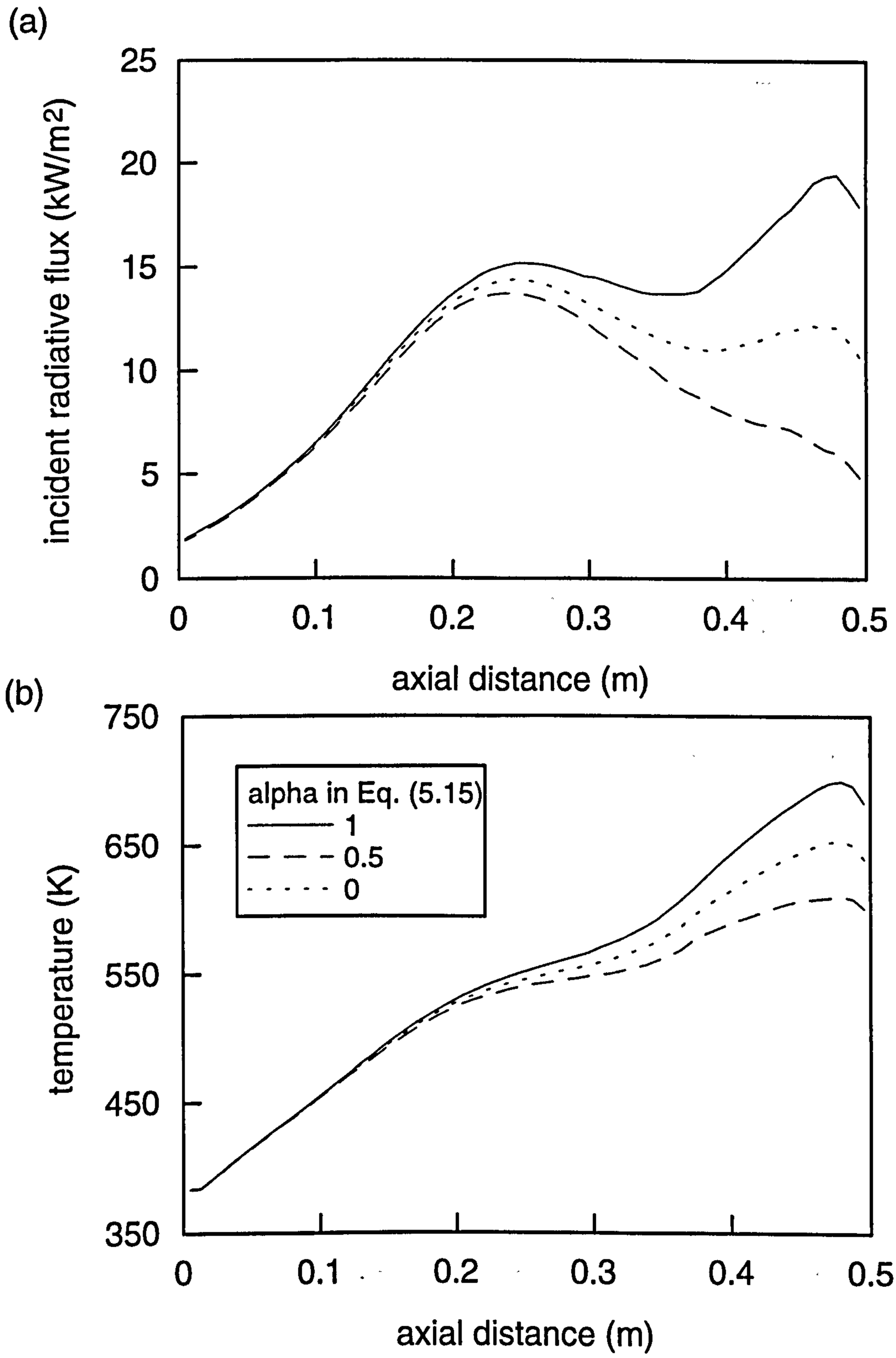

Fig. 5.28 Influence of radiation boundary condition applied at outflow boundary : (a) incident radiative flux to pyrex casing; (b) internal face temperature of pyrex casing.

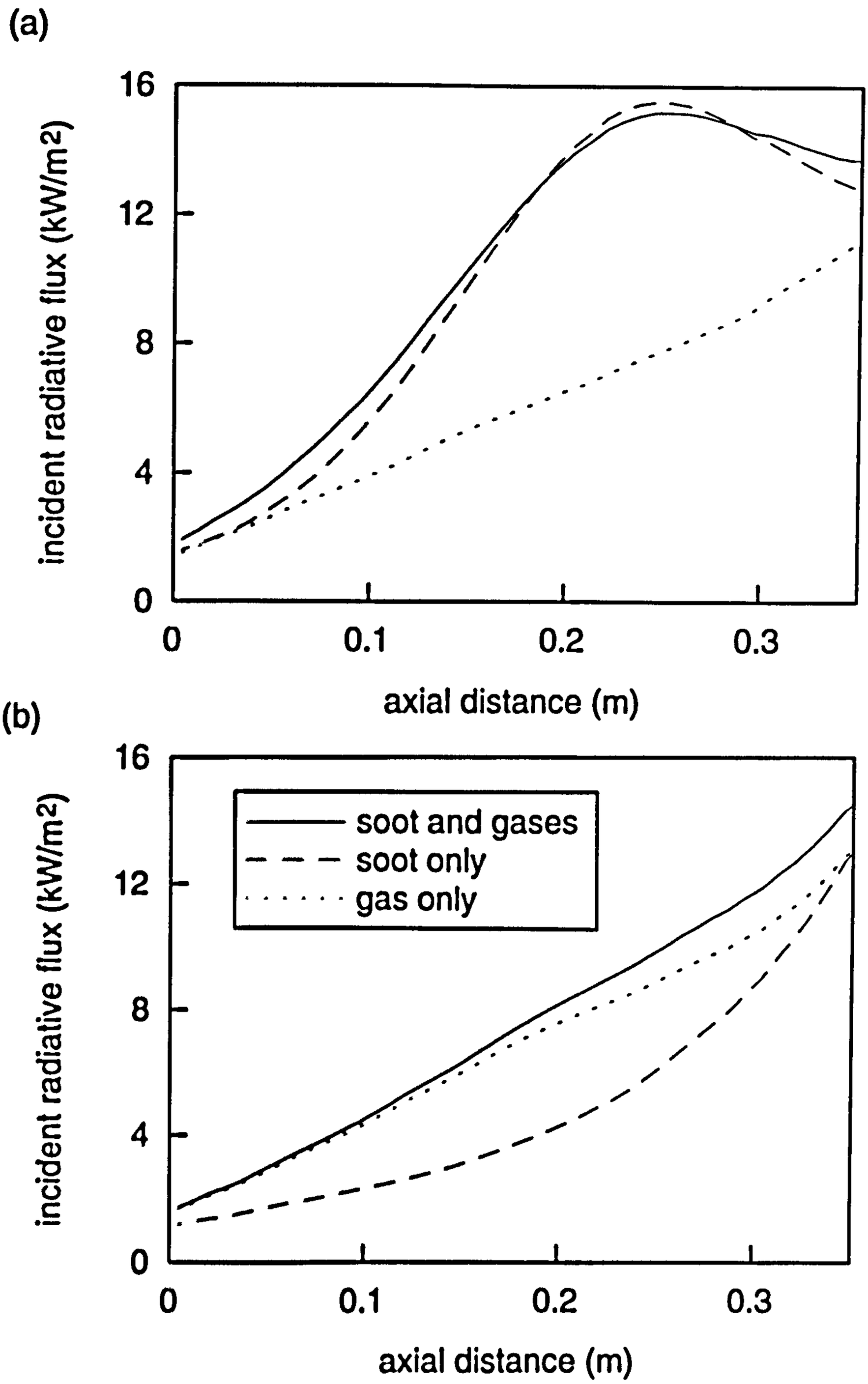

Fig. 5.29 Incident radiative flux to pyrex casing : (a) 3 atm. flame; (b) 1 atm. flame.

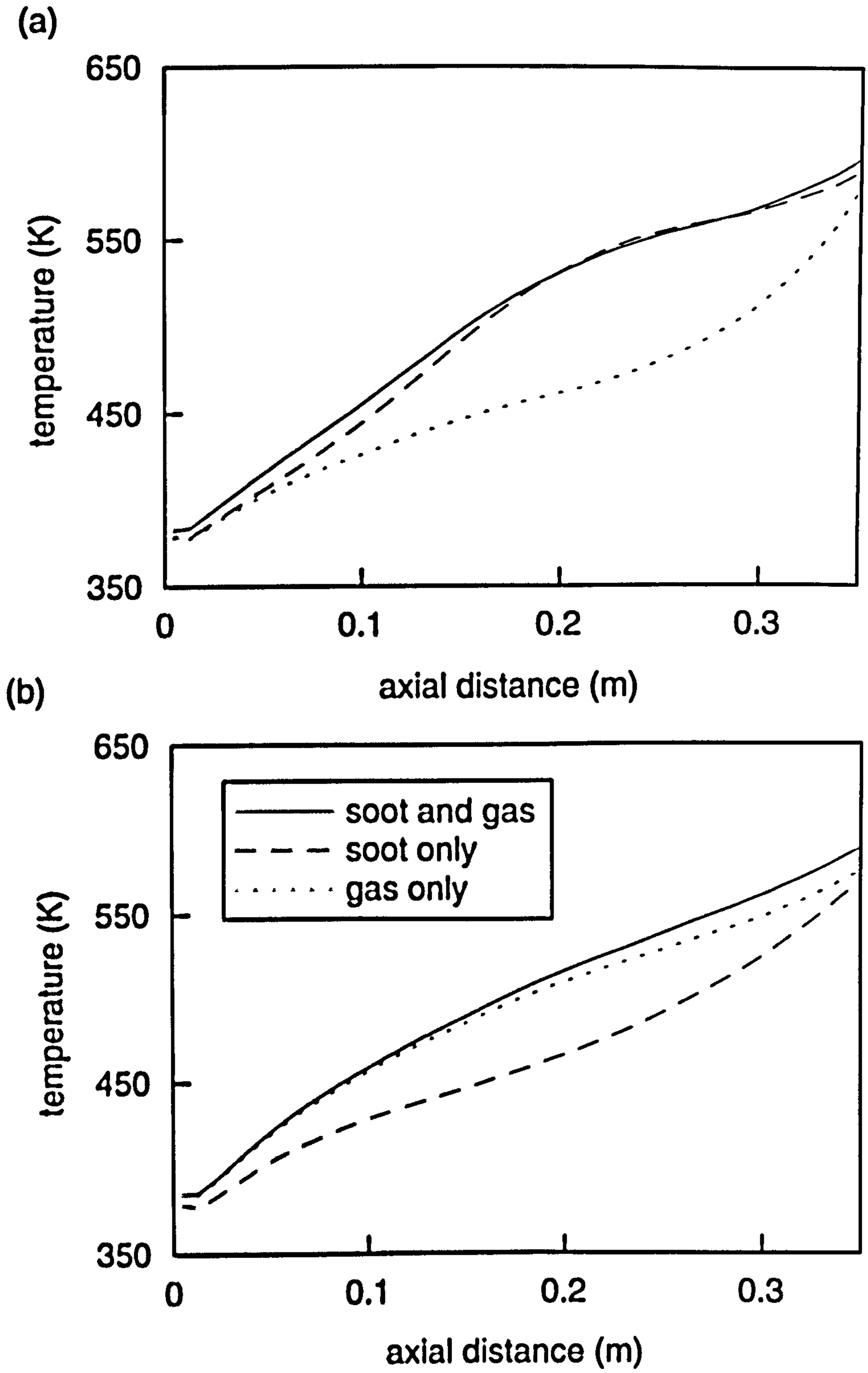

Fig. 5.30 Mean internal face temperature of pyrex casing : (a) 3 atm. flame; (b) 1 atm. flame.

Chapter 6

Conclusions and Recommendations for Future Work

Thermal radiation in combustion systems is a highly complex phenomenon dependent on numerous aspects of the associated environment. Likewise, the processes of soot formation and oxidation are governed by a multi-dimensional array of parameters. All these phenomena are intimately coupled by their strong mutual dependence on temperature, and by the influence of soot concentration on thermal radiation. More specifically, as soot particles form and grow, their radiation properties change. The consequent effect on radiative loss alters the temperature field, which simultaneously affects the mechanisms governing the evolution of these particles, and the subsequent levels of radiative exchange. In the foreseeable future, computational fluid dynamics is unlikely to accomplish detailed predictions, on an acceptable time scale, of these complex interactions as they occur in practical combustion systems. Nonetheless, increasingly less approximate methods must be developed.

Perennially, levels of computing power have determined the degree of approximation appropriate for a particular physical model. In the discrete transfer radiation model, originally recommended for its computational efficiency relative to other available models, incorporation of a detailed, spectrally resolved solution to the radiative transfer equation is likely to remain prohibitively expensive for some time. However, more approximate algorithms, perhaps not viable a few years ago, can now be realistically applied within a CFD simulation of combustion. Selection of the most suitable algorithm in terms of the accuracy afforded at an acceptable cost has constituted an important feature of this thesis. The soot formation (and

oxidation) model has not been scrutinised in an equivalent way, but has been adopted from parallel work conducted at Cranfield University. In common with the radiation model, however, the soot model is also characterised by global approximations employed to represent fine scale physical and chemical processes.

Before considering the consequences of harnessing these sub-models together in the simulation of experimental flames, along with the implications of this analysis for application to practical problems, a summary is now provided of the preceding chapters.

Following the introduction in chapter 1, many key elements commonly employed in the physical modelling of turbulent non-premixed combustion were identified in chapter 2. Whilst recognition was given to the status of advanced techniques, more detailed descriptions were provided of less sophisticated models. For example, constrained by current levels of computing power, many researchers still employ the $k-\varepsilon$ turbulence model coupled to an eddy break-up description of combustion heat release. Indeed, this simplified representation of turbulent combustion was employed in the simulation of experimental flames in chapter 5.

Chapters 3 and 4 focused on the modelling of thermal radiation in the discrete transfer radiation model (DTRM). Initially, a description of the method was presented including its implementation in general curvilinear co-ordinates. Then, issues relating to the optimisation of the DTRM were considered with special attention given to the directions in which rays can be launched from boundary surfaces. The potential benefit of generating a more uniform distribution of rays, by alternative strategies for discretising the solid angle hemisphere, was identified. Although significant potential errors accompany the conventional method of discretisation for low numbers of rays, this becomes of less concern as ray numbers are increased.

The second part of chapter 3 investigated solutions to the radiative transfer equation and methods for representing the radiative properties of typical combustion media. Attention was given to the faster, more

approximate algorithms including a constant absorption coefficient (CAC) solution, a total property (TP) solution in which radiative properties are evaluated on a cell-by-cell basis, and a weighted sum of gray gases (WSGG) solution. A (narrow band) differential banded transmissivity (DBT) solution was used as a benchmark against which comparisons were made. Emitting-absorbing media were considered comprising the principal molecular gases, CO_2 and H_2O, soot, and mixtures of these components. Treatment of gray boundaries was also included. The main conclusions to be drawn from this analysis concerned the diminution in performance of the TP solution with decreasing soot loading, and a general recommendation for the WSGG solution.

In chapter 4, less approximate differential solutions to the RTE were described, and a new algorithm was devised to better represent the source temperature dependence of absorption. Entitled the differential total absorptivity (DTA) solution, it sought to directly incorporate absorptivities into solution of the RTE. Relative to the WSGG solution, superior agreement with the DBT solution was achieved across a selection of one-dimensional layers. Performance of the WSGG solution was shown to deteriorate with increasing temperature range. However, the DTA solution is relatively expensive due to the need to compute differential expressions for each upstream element in all paths. Consequently, the WSGG solution is favoured for the diffusion flames simulated here since temperatures are considerably lower than 1800 K in most parts of the flow field.

A data set of scalar measurements of mixture fraction, temperature and soot volume fraction obtained for confined turbulent diffusion flames burning at 1 and 3 atm., was used in chapter 5 to assess numerous aspects of a methodology designed to model the intimate coupling between thermal radiation and soot formation (and oxidation) in a turbulent combusting environment. The effect of radiative loss on the temperature-dependent chemistry of soot nucleation, surface growth, coagulation and oxidation was accommodated through an extended flamelet approach. Radiative exchange

was computed using the discrete transfer radiation model with properties established from the local mean concentrations of CO_2, H_2O and soot. The WSGG solution to the radiative transfer equation was employed, including interaction with gray boundaries. Utilising an eddy break-up model of combustion heat release, temperature was determined from total enthalpy which was evaluated by solution of its steady state balance equation. Generally good agreement was obtained between prediction and experiment, although a significant weakness was identified in the evaluation of temperature from mean enthalpy. Thus, although the overall methodology conveniently permits the calculation of temperature in both fluid and solid media, it requires further validation, particularly in practical problems requiring fine resolution of solid boundaries.

Confidence in the prediction of soot concentration was largely restrained due to uncertainties associated with the universal representation of complex mechanisms, especially soot oxidation. Nonetheless, the trends of soot evolution with downstream distance were adequately reproduced.

Some interesting features concerning the relative contributions to radiative energy exchange by gaseous and particulate components were identified through comparison between the two flames. Also, the variation in performance of the total property solution to the radiative transfer equation for different soot loadings was confirmed. The relative insensitivity of temperature to radiation boundary conditions was demonstrated, this being largely due to the dominance of radiation by the flame. Turbulence-radiation interaction was briefly considered and found to produce a negligible effect on temperature, but was shown to have a more significant effect on soot yield, particularly for the more heavily sooting flame.

The results presented in chapter 5 successfully demonstrated the effectiveness of an approach for incorporating coupled thermal radiation and soot formation within an elliptic flowfield calculation of turbulent

combustion. Therefore, extension to more complex geometries of the finite volume CFD approach and the accompanying sub-models as described herein, is now envisaged. With the aid of embedded grids and/or grid refinement, it will be possible to accurately resolve the characteristics of a combustion source, without demanding unfeasible computer resources, as would be required if the same grid resolution were employed throughout the computational domain. However, such an approach would have to be used cautiously due to a number of weaknesses and uncertainties which warrant further investigation.

First, the method of temperature prediction from enthalpy requires additional validation. The inclusion of turbulent fluctuations would appear to be important, and enhancements to the high Reynolds number $k-\varepsilon$ turbulence model may be necessary. For example, buoyancy and low Reynolds number effects may require further attention. Turbulence-radiation interaction was briefly addressed in chapter 5, but a fuller treatment of all non-linear terms is warranted to further assess the significance of turbulent fluctuations in non-spectrally resolved solutions to the radiative transfer equation.

Second, a more universally applicable soot formation and oxidation model must be developed which does not require *ad hoc* scaling of parameters. Ideally, a model is needed capable of application to a wide range of fuels.

Modelling of the radiative transfer equation is more easily resolved than the mechanisms governing the evolution of soot particles. A number of algorithms are available possessing different degrees of approximation, and varying suitability to application in CFD prediction. However, each is limited by the accuracy of data they employ. For the weighted sum of gray gases solution, for example, it would be advantageous to generate coefficients for a selection of temperatures and pressure-path-lengths. In the differential total absorptivity solution, total property data is required across a wider range of all dependent parameters than currently available.

Indeed, application of solutions to the RTE in the DTRM, other than the constant absorption coefficient solution, require attention in this respect largely due to the possibility of generating a vast range of path lengths in the ray tracing procedure. Also, it would be useful to have more extensive validation of radiative property models across a range of total pressures.

Optimisation of the DTRM should be undertaken so as to minimise computational cost and the "ray effect". This could be achieved by increasing ray density in regions of large gradients, and decreasing the number of rays traversing regions of relative uniformity. Adaptive techniques would be useful, particularly in transient problems such as the spread of unwanted fires.

Although the analysis presented above demonstrated a relative insensitivity of flow field prediction to radiation boundary conditions, a more detailed representation of thermal properties is likely to be necessary in practical problems. Indeed, modelling the failure of window glass exposed to enclosure fires is expected to demand such detail. However, there are vast scale differences between a typical pane of glass and even a small room. Clearly, embedded grids are going to be required to model this type of problem. Whilst fine resolution calculations coupled to more coarsely defined regions are certainly feasible, both within boundaries and combustion zones, problems of computational cost, accuracy and grid independence still have to be addressed. Thus, CFD field modelling of practical problems incorporating detailed descriptions of these particular phenomena remains a particularly challenging task.

In its present form, the overall methodology assessed in this thesis for the simulation of turbulent non-premixed combustion, can be applied to practical problems. For example, it would now be particularly interesting to model smoke plumes, and smoke layers occurring in enclosure fires, and to further validate the modelling of radiative exchange in such environments. It would also be of interest to extend the methodology to transient problems, such as fire spread and the response of furnaces to changes in operating

conditions. Finally, whilst the recommendations made above for enhancements and extensions to the various physical sub-models would most likely be validated against relatively small scale laboratory data, the consequences for application to practical combustion problems would also require further research. At all times, reliable experimental data will be needed, and modelling strategies will be constrained by the level of computing power available.

References

Abbas, A. S. and Lockwood, F. C., 1985, Prediction of Soot Concentrations in Turbulent Diffusion Flames, *J. Inst. Energy*, pp. 112-115.

Abbas, A. S. and Lockwood, F. C., 1984, The Prediction of the Combustion and Heat Transfer Performance of a Refinery Heater, *Combust. Flame*, Vol. 58, pp. 91-101.

Abramowitz, M. and Stegun, I. A., 1972, *Handbook of Mathematical Functions*, Dover.

Adams, B. R. and Smith, P. J., 1995, Modelling Effects of Soot and Turbulence-Radiation Coupling on Radiative Transfer in Turbulent Gaseous Combustion, *Combust. Sci. Tech.*, Vol. 109, pp. 121-140.

Adams, B. R. and Smith, P. J., 1993, Three-dimensional Discrete-ordinates Modelling of Radiative Transfer in a Geometrically Complex Furnace, *Combust. Sci. Tech.*, Vol. 88, pp. 293-308.

Bai, X. S. and Fuchs, L., 1993, Calculation of Turbulent Combustion of Propane in Furnaces, *Int. J. Num. Meth. Fl.*, Vol. 17, pp. 221-239.

Benim, A. C., 1989, Finite Element Solution of an Enclosed Turbulent Diffusion Flame, *Int. J. Num. Meth. Fl.*, Vol. 9, pp. 289-303.

Bhattacharjee, S. and Grosshandler, W. L., 1990, A Simplified Model for Radiative Source Term in Combusting Flows, *Int. J. Heat Mass Trans.*, Vol. 33, No. 3, pp. 507-516.

Bhattacharjee, S. and Grosshandler, W. L., 1989, Effect of Radiative Heat Transfer on Combustion Chamber Flows, *Combust. Flame*, Vol. 77, pp. 347-357.

Bilger, R. W., 1993, Conditional Moment Closure for Turbulent Reacting Flow, *Phys. Fluids A*, Vol. 5, pp. 436-444.

Bilger, R. W. and Starner, S. H., 1983, A Simple Model for Carbon-Monoxide in Laminar and Turbulent Hydrogen Diffusions Flames, *Combust. Flame*, Vol. 51, pp. 155-176.

Bilger, R. W., 1976, Turbulent Jet Diffusion Flames, *Prog. Energy Combust. Sci.*, Vol. 1, pp. 87-109.

Bockhorn, H. (Ed.), 1994, *Soot Formation in Combustion (Mechanisms and Models)*, Springer Series in Chemical Physics 59, Springer-Verlag.

Bockhorn, H., 1989, Finite Chemical Reaction Rate and Local Equilibrium Effects in Turbulent Hydrogen-Air Diffusion Flames, *Twenty-Second Symposium (International) on Combustion,* The Combustion Institute, pp. 655-664.

Borghi, R., 1988, Turbulent Combustion Modelling, *Prog. Energy Combust. Sci.*, Vol. 14, pp. 245-292.

Borkowski, C. A. and Kaminski, D. A., 1994, Assessment of the P-1 Approximation in Cold-walled Enclosures with Internal Heat Generation, *Num. Heat Transfer*, Part B, Vol. 25, pp. 309-329.

Boussinesq, J., 1877, Theorie de l'ecoulement Tourbillant, *Mem. Pre. par. div. Sav.*, 23, Paris.

Bradley, D., Dixon-Lewis, G., Habik, G. and Mushi, E., 1984, The Oxidation of Graphite Powder in Flame Reaction Zones, *Twentieth Symposium (International) on Combustion*, The Combustion Institute, Pittsburgh, pp. 931-940.

Bressloff, N. W., Moss, J. B. and Rubini, P. A., 1996a, Assessment of a Differential Total Absorptivity Solution to the Radiative Transfer Equation as Applied in the Discrete Transfer Radiation Model, *Numerical Heat Transfer, Part B : Fundamentals*, Vol. 29, No. 3, pp. 381-397.

Bressloff, N. W., Moss, J. B. and Rubini, P. A., 1996b, CFD Prediction of Coupled Radiation Heat Transfer and Soot Production in Turbulent Flames, accepted for presentation at the Twenty-Sixth Symposium on Combustion.

Bressloff, N. W., Moss, J. B., Rubini, P.A., 1995, Application of a New Weighting Set for the Discrete Transfer Radiation Model, *Proceedings of the 3rd European Conference on Industrial Furnaces and Boilers*, Lisbon, Portugal.

Brizuela, E. A. and Bilger, R. W., 1996, On the Eddy Break-Up Coefficient, *Combust. Flame*, Vol. 104, pp. 208-212.

Brookes, S. J., 1996, Coupled Soot Production and Thermal Radiation from Turbulent Jet Flames, *Ph. D. Thesis*, Cranfield University (in preparation).

Buckius, R. O. and Tien, C. L., 1977, Infrared Flame Radiation, *Int. J. Heat Trans.*, Vol.20, pp.93-106.

Carvalho, M. d. G., 1995, Mathematical Modelling of Industrial Furnaces and Boilers, proceedings *Proceedings of the 3rd European Conference on Industrial Furnaces and Boilers*, Lisbon, Portugal.

Carvalho,M. G., Farias, T. and Fontes, P., 1991, Predicting Radiative Heat Transfer in Absorbing, Emitting, and Scattering Media Using the Discrete Transfer Method, *Fundamentals of Radiation Heat Transfer ASME*, HTD-Vol. 160, pp.17-26.

Carvalho, M. G. and Coelho, P. J., 1989, Heat Transfer in Gas Turbine Combustors, *J. Thermophysics*, Vol. 3, No. 2, pp. 123-131.

Chai, J. C, Parthasarathy, G. and Patankar, S. V., 1994, A Finite-Volume Radiation Heat Transfer Procedure for Irregular Geometries, *AIAA 94-2095*.

Chan, S. H., Pan, X. C. and Zhang, J., 1994, Two-Dimensional Nonstationary Causal Stochastic Model for Turbulence/Radiation Interactions in Flames, *Twenty-Fifth Symposium (International) on Combustion,* The Combustion Institute, pp. 1115-1123.

Chandrasekhar, S., 1950, *Radiative Transfer*, Clarendon Press, Oxford.

Chen, J.-Y. and Kollmann, W., 1994, *Comparison of Prediction and Measurement in Non-Premixed Turbulent Flames*, (eds. P. Libby and F. Williams), Turbulent Reacting Flows, Academic Press Ltd., London.

Chen, J.-Y., Kollmann, W. and Dibble, R. W., 1989, PDF Modelling of Turbulent Non-Premixed Methane Jet Flames, *Combust. Sci. Tech.*, Vol. 64, pp. 315-346.

Chen, C. H., Lan, C. Y. and Shan, D. Y., 1991, Turbulent Boundary-Layer Diffusion Flame - Effects of Probability Density Function, *AIAA J.*, Vol. 29, pp. 371-379.

Coelho, P. J. and Carvalho, M. G., 1985, Modelling of Soot Formation and Oxidation in Turbulent Diffusion Flames, *J. Thermo. Heat Trans.*, Vol. 9, No. 4, pp. 644-652.

Cox, G., 1977, On Radiant Heat Transfer from Turbulent Flames, *Comb. Sci. Tech.*, Vol. 17, pp. 75-78.

Crosbie, A. L. and Schrenker, R. G., 1984, Radiative Transfer in Two-Dimensional Rectangular Medium Exposed to Diffuse Reflection, *J. Quant. Spectrosc. Radiat. Transfer*, Vol. 31, pp. 339-372.

Crauford, N. L., Liew, S. K. and Moss, J. B., 1985, Experimental and Numerical Simulation of a Buoyant Fire, *Combust. Flame*, Vol. 61, pp. 63-77.

Cumber, P. S., 1995, Improvements to the Discrete Transfer Method of Calculating Radiative Heat Transfer, *Int. J. Heat Mass Transfer*, Vol. 38, No. 12, pp. 2251-2258.

Davis, R. W., Moore, E. F., Chen, L.-D., Roquemore, W. M., Vilimpoc, V. and Goss, L. P., 1994, A Numerical/Experimental Study of the Dynamic Structure of a Buoyant Jet Diffusion Flame, *Theoret. Comput. Fluid Dynamics*, Vol. 6, pp. 113-123.

De Ris, J., 1979, Fire Radiation - A Review, *Seventeenth Symposium (International) on Combustion*, The Combustion Institute, pp. 1003-1016.

Delaunay, B., 1934, Sur la Sphere Vide, *Bull. Acad. Sci. URSS, Class. Sci. Nat.*, pp. 793-800.

Denison, M. K. and Webb, B. W., 1995, The Spectral Line-Based Weighted-Sum-of-Gray-Gases Model in Nonisothermal Nonhomogeneous Media, *J. Heat Transfer*, Vol. 117, pp. 359-365.

Dibble, R. W., Kollmann, W., Farshchi, M. and Schifer, R. W., 1986, *Twenty-First Symposium (International) on Combustion,* The Combustion Institute, pp. 1329-1340.

Docherty, P. and Fairweather, M., 1988, Predictions of Radiative Transfer from Nonhomogeneous Combustion Products Using the Discrete Transfer Method, *Combust. Flame*, Vol. 71, pp. 79-87.

Dopazo, C., 1994, *Recent Developments in Pdf Methods*, (eds. P. Libby and F. Williams), Turbulent Reacting Flows, Academic Press Ltd., London.

Edwards, D. K. and Matavosian, R., 1984, Scaling Rules for Total Absorptivity and Emissivity of Gases, *J. Heat Trans.* Vol. 106, pp. 684-689.

Edwards, D. K., 1976, Molecular Gas Band Radiation, *Advances in Heat Transfer*, Vol. 12, Academic Press, New York, pp. 115-193.

Edwards, D. K. and Balakrishnan, A., 1973, Thermal Radiation by Combustion Gases, *Int. J. Heat Mass Trans.*, Vol. 16, pp. 25-40.

Edwards, D. K. and Menard, W. A., 1964, Comparison of Models for Correlation of Total Band Absorption, *Appl. Optics*, Vol. 3, pp. 621-625.

Elkaim, D., Reggio, M. and Camarero, R., 1993, Control Volume Finite-Element Solution of a Confined Turbulent Diffusion Flame, *Numerical Heat Transfer, Part A*, Vol. 23, pp. 259-279.

Fairweather, M., Jones, W. P., Ledin, H. S. and Lindstedt, R. P., 1992a, Predictions of Soot Formation in Turbulent Non-Premixed Propane Flmaes, *Twenty-Fourth Symposium (International) on Combustion*, The Combustion Institute, pp. 1067-1074.

Fairweather, M., Jones, W. P. and Lindstedt, R. P., 1992b, Predictions of Radiative Transfer from a Turbulent Reacting Jet in a Cross-Wind, *Combust. Flame*, Vol. 89, pp. 45-63.

Fenimore, C. P. and Jones, G. W., 1967, Oxidation of Soot by Hydroxyl Radicals, *J. Phys. Chem.*, Vol. 71, p. 593.

Felske, J. D. and Charalampopolous, T.T., 1982, Gray Gas Weighting Coefficients for Arbitrary Gas-Soot Mixtures, *Int. J. Heat Mass Transmissivity.*, Vol. 25, No. 12, pp. 1849-1855.

Felske, J. D. and Tien, C. L., 1973, Calculation of the Emissivity of Luminous Flames, *Combust. Sci. Tech.*, Vol. 7, pp. 25-31.

Fletcher, D. F., Kent, J. H., Apte, V. B. and Green, A. R., 1994, Numerical Simulations of Smoke Movement from a Pool Fire in a Ventilated Tunnel, *Fire Safety Journal*, Vol. 23, pp. 305-325.

FLUENT, 1993, Version 4.3, Fluent Inc., Lebanon.

Frenklach, M. and Wang, H., 1990, Detailed Modelling of Soot Particle Nucleation and Growth, *Twenty-Third Symposium (International) on Combustion*, The Combustion Institute, pp. 1559-1566.

Germano, M, Piomelli, U., Moin, P. and Cabot, W. H., 1991, *Phys. Fluids A*, Vol. 3, pp. 1760-1765.

Gibson, M. M. and Launder, B. E., 1978, Ground Effects on Pressure Fluctuations in the Atmosphere, *J. Fluid Mech.*, Vol. 86, pp. 491-511.

Gilyazetdinov, L. P., 1972, The Kinetics and Formation Mechanism of Carbon Black during the Thermal Decomposition of Hydrocarbons in the Gas Phase, *Khim. Tverd. Topl.*, Vol. 3, pp.103-111.

Giridharan, M. G., Lowry, S. and Krishnan, A., 1995, A Mutli-Block, BFC Radiation Model for Complex Geometries, *AIAA 95-2020.*

Givi, P., 1989, Model Free Simulations of Turbulent Reactive Flows, *Prog. Energ. Combust. Sci.*, Vol. 15, pp. 1-107.

Glassman, I., 1988, Soot Formation in Combustion Processes, *Twenty-Second Symposium (International) on Combustion*, The Combustion Institute, pp. 295-311.

Gore J. P.,. Ip U.-S and Sivathanu Y. R., 1992, Coupled Structure and Radiation Analysis of Acetylene/Air Flames, *J. Heat Trans.*, Vol. 114, pp. 487-493.

Gore, J. P. and Faeth, G. M., 1988, Structure and Radiation Properties of Luminous Turbulent Acetylene/Air Diffusion Flames, *J. Heat Trans.*, Vol. 110, pp. 173-181.

Gore, J. P. and Faeth, G. M., 1986, Structure and Spectral Radiation Properties of Turbulent Ethylene/Air Diffusion Flames, *Twenty-First Symposium (International) on Combustion*, The Combustion Institute, pp. 1521-1531.

Grosshandler, W. L., 1980, Radiative Heat Transfer in Nonhomogeneous Gases : A Simplified Approach, *Int. J. Heat Mass Transfer*, Vol. 23, pp. 1447-1459.

Grosshandler, W. L. and Modak, A. T., 1981, Radiation from Nonhomogeneous Combustion Products, *Eighteenth Symposium (International) on Combustion*, The Combustion Institute, pp. 601-609.

Haidekker, A., Charette, A. and Kocaefe, Y. S., 1994, Application of the Hybrid Zone/Monte Carlo Method to 3-D curvilinear Grids in Radiative Heat Transfer, *Int. J. Num. Meth. Eng.*, Vol. 37, pp.203-216.

Holen, J., Brostrom, M. and Magnussen, B. F., 1990, Finite Difference Calculation of Pool Fires, *Twenty-Third Symposium (International) on Combustion*, The Combustion Institute, pp. 1677-1683.

Honnery, D. R. and Kent, J. H., 1992, Soot Mass Growth Modelling in Laminar Diffusion Flames, *Twenty-Fourth Symposium (International) on Combustion*, The Combustion Institute, pp. 1041-1047.

Hottel, H. C. and Sarofim A. F., 1967, *Radiative Transfer*, McGraw-Hill, New York.

Hottel, H. C. and Egbert, R. B., 1942, *Trans. Am. Inst. Chem. Eng.*, Vol. 38, pp. 531-565.

Howell, J. R., Thermal Radiation in Participating Media : Past, Present, and Some Possible Futures, 1988, *J.Heat Transfer*, vol. 110, pp. 1220-1226.

Hubbard, G. L. and Tien, C. L., 1978, Infrared Mean Absorption Coefficients of Luminous Flames and Smoke, *J. Heat Transfer*, Vol. 100, pp. 235-239.

Hyde, D. J. and Truelove, J. S., 1977, The Discrete Ordinates Approximation for Multidimensional Radiant Heat Transfer in Furnaces, *AERE R-8502*, AERE Harwell, UK.

Jeng, S.-M., Faeth, G. M., 1984, Species Concentrations and Turbulence Properties in Buoyant Methane Diffusion Flames, *J. Heat Trans.*, Vol. 106, No. 4, pp. 721-727.

Jeng, S.-M., Lai, M.C. and Faeth, G. M., 1984, Nonluminous Radiation in Turbulent Buoyant Axisymmetric Flames, *Combust. Sci. Tech.*, Vol. 40, pp. 41-53.

Johnson, T. R. and Beer, J. M., 1973, *J. Inst. Fuel*, Vol. 46, pp. 301-309.

Jones, W. P., 1994, *Recent Developments in Pdf Methods*, (eds. P. Libby and F. Williams), Turbulent Reacting Flows, Academic Press Ltd., London.

Jones, W. P. and Whitelaw, J. H., 1982, Calculation Methods for Reacting Turbulent Flows : A Review, *Combust. Flame*, Vol. 48, pp. 1-26.

Jones, W. P., 1980, Models for Turbulent Flows with Variable Density, *VKI Lecture Series 1979-2, in Predicion Methods for Turbulent Flows*, W. Kollmann (ed.), Hemisphere Publishing Corp.

Jones, W. P. and Priddin, C., 1979, Prediction ofthe Flowfield and Local Gas Composition in Gas Turbine Combustors, *Seventeenth Symposium (International) on Combustion*, The Combustion Institute, pp. 399-409.

Jones, W. P. and Launder, B. E., 1972, The Prediction of Laminarization with a Two-equation Model of Turbulence, *Int. J. Heat Mass Transfer*, Vol. 15, pp. 301-314.

Kabashnikov, V. P. and Kmit, G. I., 1979, Influence of Turbulent Fluctuations on Thermal Radiation, *J. App. Spect.*, Vol. 31, pp.963-967.

Kahn, I. M. and Greaves, G., 1974, A Method for Calculating the Formation and Combustion of Soot in Diesel Engines, *Heat Transfer in Flames*, Afghan, N. H. and Beer, J. M. (eds.), Scripta Book Co.

Kaplan, C. R., Baek, S. W., Oran, E. S. and Ellzey, J. L., 1994, Dynamics of

a Strongly Radiating Unsteady Ethylene Jet Diffusion Flame, *Combust. Flame*, Vol. 96, pp. 1-21.

Kennedy, I. M., Kollmann, W. and Chen, J.-Y., 1990, A Model for Soot Formation in a Laminar Diffusion Flame, *Combust. Flame*, Vol. 81, pp. 73-85.

Kent, J. H. and Bilger, R. W., 1976, The Prediction of Turbulent Diffusion Flame Fields and Nitric Oxide Formation, *Sixteenth Symposium (International) on Combustion*, The Combustion Institute, pp. 1643-1656.

Kent, J. H. and Honnery, D. R., 1990, A Soot Formation Map for a Laminar Ethylene Diffusion Flame, *Combust. Flame*, Vol. 79, pp. 287-298.

Kent, J. H. and Honnery, D., 1987, Soot and Mixture Fraction in Turbulent Diffusion Flames, *Combust. Sci. Tech.*, Vol. 54, pp. 383-397.

Kent, J. H. and Wagner, H. Gg., 1984, Why do Diffusion Flames Emit Smoke?, *Combust. Sci. Tech.*, Vol. 41, pp. 245-269.

Kim, T. K., Menart, J. A., and Lee, H. S., 1991, Nongray Radiative Gas Analysis Using the S-N Discrete Ordinates Method, *J. Heat Transfer*, Vol. 113, pp.946-952.

Klassen, M., Gore, J. P., Sivathanu, Y. R., Hamins, A. and Kashiwagi, T., 1992, Radiative Heat Feedback in a Toluene Pool Fire, *Twenty-Fourth Symposium (International) on Combustion*, pp. 1713-1719.

Komornicki, W. and Tomeczek, J., 1992, Modification of the Wide-band Gas Radiation Model for Flame Calculation, *Int. J. Heat Mass Transfer*, Vol. 35, No. 7, pp. 1667-1672.

Kounalakis, M. E., Sivathanu, Y. R., and Faeth, G. M., 1991, Infrared Radiation Statistics of Nonluminous Turbulent Diffusion Flames, *J. Heat Trans.*, Vol. 113, pp. 437-445.

Kounalakis, M. E., Gore, J. P. and Faeth, G. M., 1988, Turbulence/Radiation Interactions in Nonpremixed Hydrogen/Air Flames, *Twenty-Second Symposium (International) on Combustion*, pp. 1281-1290.

Kuo, K. K., 1986, *Priciples of Combustion*, John Wiley and Sons, p. 516.

Lathrop,K. D., 1968, Ray Effects in Discrete Ordinates Equations, *Nuclear Sci. and Engineering* Vol. 32, pp. 357-369.

Launder, B. E., 1989, 2nd-Moment Closure - Present and Future - Review, *Int. J. Heat Fluid Flow*, Vol. 10, pp. 282-299.

Leckner, B., 1972, Spectral and Total Emissivity of Water Vapour and Carbon Dioxide, *Combust. Flame*, Vol. 19, pp. 33-48.

Lee, K. B., Thring, M. W. and Beer, J. M, 1962, On the Rate of Combustion of Soot in a Laminar Soot Flame, *Combust. Flame*, Vol. 6, pp. 137-145.

Lefevre, A. H., 1984, Flame Radiation in Gas Turbine Combustion Chambers, *Int. J. Heat Mass Transfer*, Vol. 27, No. 9, pp. 1493-1510.

Leung, K. M., Lindstedt, R. P. and Jone, W. P., 1991, A Simplified Reaction Mechanism for Soot Formation in Non-Premixed Flames, *Combust. Flame*, Vol. 87, Nos. 3-4, pp. 289-305.

Libby, P. A. and Bray, K. N. C., 1981, Counter-Gradient Diffusion in Premixed Turbulent Flames, *AIAA J.*, Vol. 19, pp. 205-213.

Libby, P. A. and Williams, F. A. (eds.), 1994, *Turbulent Reacting Flows*, pp. 1-61, Academic Press Ltd., London.

Liew, S. K., Bray, K. N. C. and Moss, J. B., 1984, A Stretched Laminar Flamelet Model of Turbulent Non-Premixed Combustion, *Comb. Flame*, Vol. 56, pp. 199-213.

Liew, S. K., 1983, Flamelet Models of Turbulent Non-Premixed Combustion, *Ph. D. Thesis*, University of Southampton, England.

Liew, S. K., Bray, K. N. C. and Moss, J. B., 1981, A Flamelet Model of Turbulent Non-Premixed Combustion, *Comb. Sci. Tech.*, Vol. 27, pp. 69-73.

Liu, J. and Tiwari, S. N., 1994, Investigation of Radiative Transfer in Nongray Gases using a Narrow Band Model and Monte Carlo Simulation, *J. Heat Transfer*, Vol. 116, pp. 160-166.

Lockwood, F. C. and Malalasekera, W. M. G., 1988, Flash Over, *Twenty-Second Symposium (International) on Combustion*, The Combustion Institute, Pittsburgh, pp. 1319-1328.

Lockwood, F. C. and Shah, N. G., 1981, A New Radiation Solution Method for Incorporation in General Combustion Prediction Procedures, *Eighteenth Symposium (International) on Combustion*, pp. 1405-1414, The Combustion Institute, Pittsburgh.

Lockwood, F. C. and Shah, N. G., 1976, An Improved Flux Model for the Calculation of Radiation Heat Transfer in Combustion Chambers, *Proceedings of the 16th National Heat Transfer Conference*, St. Louis, USA.

Lockwood, F. C. and Naguib, 1975, The Predictions in the Fluctuations in the Properties of Free, Round-jet Turbulent Diffusion Flames, *Combust. Flame*, Vol. 24, pp. 109-124.

Ludwig, C. B., Malkmus, W., Reardon, J. E., and Thomson, J. A. L., 1973, *Handbook of Infrared Radiation from Combustion Gases*, NASA SP-3080, Scientific and Technical Information Office, Washington, DC.

Magnussen, B. F., 1989, Modelling of No_x and Soot Formation by the Eddy Dissipation Concept, presented at the International Flame Research Foundation 1st Topic Oriented Meeting, Amsterdam, Holland.

Magnussen, B. F., Hjertager, B. H., Olsen, J. G. and Bhaduri, D., 1979, Effects of Turbulent Structure and Local Concentrations on Soot Formation and Combustion in C_2H_2 Flames, *Seventeenth Symposium (International) on Combustion*, Combustion Institute, pp. 1383-1393.

Magnussen, B. F. and Hjertager, B. H., 1976, On Mathematical Modelling of Turbulent Combustion with Special Emphasis on Soot Formation and Combustion, *Sixteenth Symposium (International) on Combustion*, Combustion Institute, pp. 719-729.

Markstein, G. H., 1974, Radiative Energy Transfer from Gaseous Diffusion Flames, *Fifteenth Symposium (International) on Combustion*, The Combustion Institute, pp. 1285-1294.

Majumdar, S., 1988, Role of Underrelaxation in Momentum Interpolation for Calculation of Flow with Nonstaggered Grids, Num. Heat Trans., Vol. 13, pp. 125-132.

Malalasekera, W. M. G. and James, E. H., 1995, Calculation of Radiative Heat Transfer in Three-Dimensional Complex Geometries, *Proceedings of the 30th National Heat Transfer Conference*, Vol. 13, ASME HTD-Vol. 315, pp. 53-61.

McBride, B. J., Gordon, S. and Martin, A. R., 1993, Coefficients for Calculating Thermodynamic and Transport Properties of Individual Species, *NASA TM4513*.

Melaaen, M. C., 1992, Calculation of Fluid Flows with Staggered and Nonstaggered Curvilinear Nonorthogonal Grids - The Theory, *Num. Heat Trans., Part B*, Vol. 21, pp. 1-19.

Mell, W. E., Nilsen, V., Kosaly, G. and Riley, J. J., 1993, Direct Numerical Simulation Investigation of the Conditional Moment Closure Model for Nonpremixed Turbulent Reacting Flows, *Combust. Sci. Tech.*, Vol. 91, Nos. 1-2, pp. 179-186.

Meng, F.L., McKenty, F., Camarero, R., 1993, Radiative heat transfer by the discrete transfer method using an unstructured mesh, *Nat. Heat Tran. Conf.*, HTD-Vol. 244, Radiative Heat Transfer : Theory and Applications, pp. 55-66.

Miller, J. H., Honnery, D. R. and Kent, J. H., 1992, Modelling the Growth of Polynuclear Aromatic Hydrocarbons in Diffusion Flames, *Twenty-Fourth Symposium (International) on Combustion*, The Combustion Institute, pp. 1031-1039.

Missaghi, M., Pourkashanian, M., Smedley, J. M., Williams, A. and Yap, L. T., A Computational of Soot Formation in Turbulent Diffusion Flames, *Proceedings of the Second Int. Conf. on Combustion Tech. for a Clean Environment*, Lisbon, Portugal, paper 34.2.

Modak, A. T., 1979, Radiation from Products of Combustion, *Fire Research*, Vol. 1, pp. 339-361.

Modest, M. F., 1993, *Radiative Heat Transfer*, Mc-Graw Hill, New York.

Modest, M. F., 1991, The Weighted-Sum-of_Gray-Gases Model for Arbitrary Solution Methods in Radiative Transfer, *J. Heat Transfer*, Vol. 113, pp. 650-656.

Moss, J. B., Stewart, C. D. and Young, K. J., 1995, Modelling Soot Formation and Burnout in a High Temperature Laminar Diffusion Flame Burning under Oxygen-Enriched Conditions, *Combust. Flame*, Vol. 101, pp. 491-500.

Moss, J. B., Stewart, C. D. and Syed, K. J., 1988, Flowfield Modelling of Soot Formation at Elevated Pressure, *Twenty-Second Symposium (International) on Combustion*, The Combustion Institute, pp. 413-423.

Mullins, J., Simmons, B. and Williams, A., 1987, Rates of Formation of Soot from Hydrocarbon Flames and its Destruction, *AGARD CP-422*, paper 23.

Nagle, J. and Strickland-Constable, R. F., 1962, Oxidation of Carbon between 1000°-2000°C, *Proceedings of the 5th Conference on Carbon*, Vol. 1, Pergamon, London, pp. 154-164.

Patankar, S. V., 1980, *Numerical Heat Transfer and Fluid Flow*, Hemisphere Publishing Corporation.

Peters, N., 1986, Laminar Flamelet Concepts in Turbulent Combustion, *Twenty-First Symposium (International) on Combustion*, The Combustion Institute, pp. 1231-1250.

Pope, S. B., 1991, Application of the Velocity-Dissipation PDF Model to Inhomogeneous Turbulent Flows, *Phys. Fluids A*, Vol. 3, No. 8, pp. 1947-1957.

Pope, S. B., 1985, PDF Methods for Turbulent Reactive Flows, *Prog. Energy Combust. Sci.*, Vol. 11, pp. 119-192.

Pope, S. B., 1981, A Monte Carlo Method for the PDF Equations of Turbulent Reactive Flow, *Combust. Sci. Tech.*, Vol. 25, pp. 159-174.

Pope, S. B., 1978, An Explanation of the Round-Jet/Plane-Jet Anomoly, *AIAA Journal*, Vol. 16, No. 3, pp. 279-281.

Puri, R., Moser, M., Santoro, R. J. and Smyth, K. C., 1992, Laser-Induced Fluorescence Measurements of OH Concentrations in the Oxidation Region of Laminar, Hydrocarbon Diffusion Flames, *Twenty-Fourth Symposium (International) on Combustion*, The Combustion Institute, Pittsburgh, pp. 1015-1022.

Raithby, G. D. and Chui, E. H., 1990, A Finite-Volume Method for Predicting Radiant Heat Transfer in Enclosures with Participating Media, *J. Heat Transfer*, Vol. 112, pp. 415-423.

Reynolds, W. C., 1990, The Potential and Limitations of Direct and Large Eddy Simulations, *Whither Turbulence. Turbulence at the Crossroads*, pp. 313-343, Springer-Verlag, Berlin.

Riley, J. J., Metcalfe, R. W. and Orszag, S. A., 1986, Direct Numerical Simulations of Chemically Reacting Mixing Layers, *Phys. Fluids*, Vol. 29, pp. 406-422.

Rodi, W, 1993, *Turbulence Models and their Application in Hydraulics, A State of the Art Review*, Delft, The Netherlands, IAHR.

Rodi, W., 1972, The Prediction of Free Turbulent Boundary Layers by Use of a Two-Equation Model of Turbulence, *Ph.D. Thesis*, University of London, UK.

Sarofim, A. F., 1986, Radiative Heat Transfer in Combustion : Friend of Foe, *Twenty-first Symposium (International) on Combustion*, The Combustion Institute, Pittsburgh, pp. 1-23.

Schneider, G. E. and Raw, M. J., 1987, Control Volume Finite-Element Method for Heat Transfer and Fluid Flow using Colocated Variables, 1. Computational Procedure, *Numerical Heat Transfer*, Vol. 11, pp. 363-390.

Selcuk, N., 1985, Exact Solutions for Radiative Heat Transfer in Box-Shaped Furnaces, *Journal of Heat Transfer*, vol. 107, pp. 648-655.

Sekar, B., Mukunda, H. S. and Carpenter, M. H., 1990, The Direct Simulation of High-Speed Mixing Layers Without and With Chemical Heat Release, *CFD Symposium on Aeropropulsion*, NASA Lewis Research Center, 24-26 April.

Shah, N. G., 1979, New Method of Computation Of Radiant Heat Transfer in Combustion Chambers, *Ph.D. Thesis*, Imperial College, London, England.

Siegel, R. and Howell, J. R., 1992, *Thermal Radiation Heat Transfer*, Hemisphere Publishing Corp., Washington, pp. 683-689.

Sivathanu, Y. R. and Gore, J. P., 1994, Coupled Radiation and Soot Kinetics in Laminar Acetylene/Air Diffusion Flames, *Combust. Flame*, Vol. 97, pp. 161-172.

Sivathanu, Y. R. and Gore, J. P. and Golinar, J., 1991, Transient Scalar Properties of Strongly Radiating Jet Flames, *Combust. Sci. Tech.*, Vol. 76, pp. 45-66.

Sivathanu, Y. R., Kounalakis, M. E. and Faeth, G. M., 1990, *Twenty-Third Symposium (International) on Combustion*, The Combustion Institute, Pittsburgh, pp. 1543-1550.

Sivathanu, Y. R. and Faeth, G. M., 1990, Soot Volume Fractions in the Overfire Region of Turbulent Diffusion Flames, *Combust. Flame*, Vol. 81, pp. 133-149.

Smith, T. F., Shen, Z. F. and Friedman, J. N., 1982, Evaluation of Coefficients for the Weighted Sum of Gray Gases Model, *J. Heat Transfer*, Vol. 104, pp. 602-608.

Song, Tae-Ho, 1993, Comparison of Engineering Models of Nongray Behaviour of Combustion Products, *Int. J. Heat Mass Trans.*, Vol. 36, No. 16, pp. 3975-3982.

Soufiani, A. and Djavdan, E., 1994, A Comparison between Weighted Sum of Gray Gases and Statistical Narrow-Band Radiation Models for Combustion Applications, *Combust. Flame*, Vol. 97, pp. 240-250.

Soufiani, A., Hartman, J. M., and Taine, J., 1985, Validity of Band-Model Calculations for CO_2 and H_2O Applied to Radiative Properties and Conductive-Radiative Transfer, *J. Quant. Spectroc. Radiat. Transfer*, Vol. 35, No. 3, pp. 243-257.

Soufiani, A. and Taine, J., 1985, Application of Statistical Narrow-band Model to Coupled Radiation and Convection at High Temperature, *Int. J. Heat Mass Transfer*, Vol. 30. No. 3, pp. 437-447.

Spalding, D. B., 1979, *Combustion and Mass Transfer*, Pergamon Press.

Spalding, D. B., 1977, *GENMIX - A General Program for Two-Dimensional Parabolic Phenomena*, Pergamon Press.

Spalding, D. B., 1971a, Mixing and Chemical Reaction in Steady Confined Turbulent Flames, *Thirteenth Symposium (International) on Combustion*, pp. 649-657, The Combustion Institute, Pittsburgh.

Spalding, D. B., 1971b, Concentration Fluctuations in a Round Turbulent Jet, *Chem. Eng. Sci.*, Vol. 110, pp. 173-181.

Speziale, C. G., 1991, Analytical Methods for the Development of Reynolds Stress Closures in Turbulence, *Ann. Rev. Fluid Mech.*, Vol. 23, pp. 107-157.

Steward, F. R. and Cannon, P., 1971, The Calculation of Radiative Heat Flux in a Cylindrical Furnace using the Monte Carlo Method, *Int. J. Heat Mass Transfer* Vol. 14, pp. 245-262.

Stewart, C. D., Syed, K. J. and Moss, J. B., 1991, Modelling Soot Formation in Non-Premixed Kerosene-Air Flames, *Combust. Sci. Tech.*, Vol. 75, Nos. 4-6, pp. 211-226.

Syed, K. J., 1990, Soot and Radiation Modelling in Buoyant Fires, *Ph. D. Thesis*, Cranfield University, England.

Syed, K. J., Stewart, C. D. and Moss, J. B., 1990, Modelling Soot Formation and Thermal Radiation in Buoyant Turbulent Diffusion Flames, *Twenty-Third Symposium (International) on Combustion*, The Combustion Institute, pp. 1533-1541.

Taine, J., 1983, A Line-by-Line Calculation of Low-Resolution Radiative Properties of CO_2-CO-Transparent Nonisothermal Gases Mixtures up to 3000K, *J. Quant. Spectroc. Radiat. Transfer*, Vol. 30, No. 4, pp. 371-379.

Taylor, P. B. and Foster, P. J., 1974, The Total Emissivities of Luminous and Non-Luminous Flames, *Int. J. Heat Mass Transfer*, Vol. 17, pp. 1591-1605.

Tennekes, H. and Lumley, J. L., 1972, *A First Cousre in Turbulence*, MIT Press, Cambridge.

Tesner, P. A., Snegiriova, T. D. and Knorre, V.G., 1971, Kinetics of Dispersed Carbon Formation, *Combust. Flame*, Vol. 17, No. 2, pp. 253-260.

Thynell, S. T. and Lin W.-Q., 1989, Radiation Transfer in Absorbing, Emitting Two-Dimensional Media Bounded by Reflecting Walls, *Nat. Heat Tran. Conf.*, HTD-Vol. 106, Heat Transfer Phenomena in Radiation, Combustion and Fires, pp. 9-16.

Tien, C. L. and Lee, S. C., 1982, Flame Radiation, *Prog. Energy Combust. Sci.*, Vol. 8, pp. 41-59.

Tong, T. W. and Skocypec, R. D., 1992, Summary on Comparison of Radiative Heat Transfer Solutions for a Specified Problem, *Proceedings of the 28th National Heat Transfer Conference*, ASME HTD-Vol. 203, Developments in Radiative Heat Transfer, pp. 253-264.

Traugott, S. C., 1968, On Grey Absorption Coefficients in Radiative Transfer, *J. Quant. Spectrosc. Radiat. Transfer*, Vol. 8, pp. 971-999.

Truelove, J. S., 1975, Zone Method for Radiative Heat Transfer Calculations, *HTFS DR33*, AERE, Harwell, Oxon, England.

Vandromme, D. and Kollmann, W., 1982, Second Order Closure for Variable Density Free Shear Layers, *Turbulent Shear Flows*, Vol. 3, pp. 275-290, Springer-Verlag, Berlin.

van Leer, B., 1974, Towards the Ultimate Conservative Difference Scheme. II. Monotonicity and Conservation Combined in a Second Order Scheme, *J. Comput. Phys.*, Vol. 14, pp. 361-370.

Villasenour, R. and Kennedy, I. M., 1992, Soot Formation and Oxidation in Laminar Diffusion Flames, *Twenty-Fourth Symposium (International) on Combustion*, The Combustion Institute, pp. 1023-1030.

Viskanta, R. and Menguc, M. P., 1987, Radiation Heat Transfer in Combustion Systems, *Prog. Energy Combust. Sci.*, Vol. 13, pp. 97-160.

Warnatz, J., 1981, The Structure of Laminar Alkane-, Alkene- and Acetylene Flames, *Eighteenth Symposium (International) on Combustion*, The Combustion Institute, pp. 369-384.

Weissman, W. and Benson, S. W., 1989, Mechanism of Soot Initiation in Methane Systems, *Prog. Energy Comb. Sci.*, Vol. 15, pp. 273-285.

Williams, F. A. and Fuhs, A. E., 1957, Apparent Emission Intensities from a Turbulent Flame Composed of Wrinkled Laminar Flames, *Jet Propulsion*, Vol. 27, pp. 1099-**.

Young, K. J. and Moss, J. B., 1995, *Combust. Sci. Tech.*, Vol. 105, pp. 33-53.

Young, K. J., 1993, Soot Formation in Turbulent, Vaporised Kerosine-Air Jet Flames at Elevated Pressure, *Ph. D. Thesis*, Cranfield University, England.

Yuen, W. W. and Tien, C. L., 1976, A Simple Calculation Scheme for the Luminous-Flame Emissivity, *Sixteenth Symposium (International) on Combustion*, The Combustion Institute, pp. 1481-1487.

Appendix A

Solutions to the Radiative Transfer Equation.

DBT	Differential banded transmissivity solution $i_n = \sum_{j=1}^{J}\left[i_{0,j}\bar{\tau}_{0\to n,j} + \sum_{r=1}^{n}\bar{i}_b\left(T_s,\nu_j\right)\left[\bar{\tau}_{r\to n,j}-\bar{\tau}_{r-1\to n,j}\right]\Delta\nu_j \right]$ where banded radiative properties are evaluated from the statistical narrow band model due to Ludwig et al (1974).
WSGG	Weighted sum of grey gases solution $i_n = \sum_{j=1}^{J}\left[i_{0,j}\prod_{r=1}^{n}\tau_{j,r} + \sum_{r=1}^{n}\left[a_j i_{b,j,r}\varepsilon_{j,r}\prod_{r'=r+1}^{n}\tau_{j,r'} \right]\right]$ where coefficients are used from an expression for the total emissivity : $\varepsilon^T = \sum_{n,n'} a_{m,n,n'}(T)\left\{1-exp\left[-k_{g,n}\left[p_w+p_c\right]-k_{p,n'}\rho_p\Phi\right]L\right\}$
CAC	Constant absorption coefficient solution $i_n = i_0\prod_{r=1}^{n}\tau_r + \sum_{r=1}^{n} i_{b,r}\varepsilon_r\prod_{r'=r+1}^{n}\tau_{r'}$ where $\varepsilon_r = \left[1-e^{-kpL}\right]$ is evaluated by assuming a constant absorption coefficient.

TP	Total property solution $i_n = i_0 \prod_{r=1}^{n} \tau_r + \sum_{r=1}^{n} i_{b,r} \varepsilon_r \prod_{r'=r+1}^{n} \tau_{r'}$ where $\varepsilon_r = \left[1 - e^{-kpL}\right]$ is evaluated by an absorption coefficient evaluated from a particular radiative property model.
DTT	Differential total transmissivity solution $i_n = i_0 \tau^T_{0\to n}\left(\overline{T}_{0\to n}, \overline{p}_{c,0\to n}, \overline{p}_{h,0\to n}, l_{0\to n}\right) + i_{p,n}$ $+ \sum_{r=1}^{n} i_b\left(T_{r-\frac{1}{2}}\right)\left[\tau^T_{r\to n}\left(\overline{T}_{r\to n}, \overline{p}_{c,r\to n}, \overline{p}_{h,r\to n}, l_{r\to n}\right)\right.$ $\left. - \tau^T_{r-1\to n}\left(\overline{T}_{r-1\to n}, \overline{p}_{c,r-1\to n}, \overline{p}_{h,r-1\to n}, l_{r-1\to n}\right)\right]$
DBA	Differential banded absorptance solution $i_n = i_{p,n} + \sum_{i=1}^{I}\sum_{j=1}^{J}\left[i_{0,j}\bar{\tau}_{0\to n,j} + \right.$ $\left.\sum_{r=1}^{n} \bar{i}_b\left(T_s, \nu_j\right)\left[\bar{\tau}_{p,r-1\to n} F_{r-1\to n,j} - \bar{\tau}_{p,r\to n} F_{r\to n,j}\right] - C\right]$ where the exponential wide band model is employed to evaluate black body fractions from absorptances.

DTA	Differential total absorptivity solution

(i) for gases

$$i_n = i_0\left[1-\alpha^T_{0\to n}\left(T_0,\overline{T}_{0\to n},\overline{p}_{c,0\to n},\overline{p}_{h,0\to n},l_{0\to n}\right)\right]$$

$$+\sum_{r=1}^{n} i_b\left(T_{r-\frac{1}{2}}\right)\left[\alpha^T_{r-1\to n}\left(T_{r-\frac{1}{2}},\overline{T}_{r-1\to n},\overline{p}_{c,r-1\to n},\overline{p}_{h,r-1\to n},l_{r-1\to n}\right)\right.$$

$$\left.-\alpha^T_{r\to n}\left(T_{r-\frac{1}{2}},\overline{T}_{r\to n},\overline{p}_{c,r\to n},\overline{p}_{h,r\to n},l_{r\to n}\right)\right]$$

(ii) for soot

$$i_{p,n} = i_0\left[1-\alpha^T_{0\to n}\left(T_0,\overline{\Phi}_{0\to n},l_{0\to n}\right)\right]$$

$$+\sum_{r=1}^{n} i_b\left(T_{r-\frac{1}{2}}\right)\left[\alpha^T_{r-1\to n}\left(T_{r-\frac{1}{2}},\overline{\Phi}_{r-1\to n},l_{r-1\to n}\right)\right.$$

$$\left.-\alpha^T_{r\to n}\left(T_{r-\frac{1}{2}},\overline{\Phi}_{r\to n},l_{r\to n}\right)\right]$$

(iii) for gas-soot mixtures

$$i_n = i_0\tau^T_{g,0\to n}\tau^T_{p,0\to n}$$

$$+\sum_{r=1}^{n} i_b\left(T_{r-\frac{1}{2}}\right)\left[\tau^T_{g,r\to n}\tau^T_{p,r\to n}-\tau^T_{g,r\to n-1}\tau^T_{p,r\to n-1}\right]$$

or

$$i_n = i_0\tau^T_{g,0\to n}\tau^T_{p,0\to n}+i_{p,n}$$

$$+\sum_{r=1}^{n} i_b\left(T_{r-\frac{1}{2}}\right)\left[\alpha^T_{g,r\to n-1}\tau^T_{p,r\to n-1}-\alpha^T_{g,r\to n}\tau^T_{p,r\to n}\right]$$